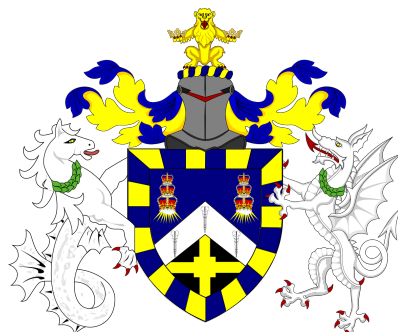


¹ ADVANCING NEUTRINO
² DETECTION AND TRIGGERING IN
³ DUNE



⁵ Francisco Martínez López

⁶ Submitted in partial fulfillment of the requirements
⁷ of the Degree of Doctor of Philosophy

⁸ School of Physical and Chemical Sciences

⁹ Queen Mary University of London

¹⁰ December 2023

¹¹ Statement of originality

- ¹² I, [insert name as recorded in QM records], confirm that the research included within
¹³ this thesis is my own work or that where it has been carried out in collaboration with, or
¹⁴ supported by others, that this is duly acknowledged below and my contribution indicated.
¹⁵ Previously published material is also acknowledged below.
- ¹⁶ I attest that I have exercised reasonable care to ensure that the work is original, and
¹⁷ does not to the best of my knowledge break any UK law, infringe any third party's
¹⁸ copyright or other Intellectual Property Right, or contain any confidential material.
- ¹⁹ I accept that the College has the right to use plagiarism detection software to check the
²⁰ electronic version of the thesis.
- ²¹ I confirm that this thesis has not been previously submitted for the award of a degree
²² by this or any other university.
- ²³ The copyright of this thesis rests with the author and no quotation from it or information
²⁴ derived from it may be published without the prior written consent of the author.
- ²⁵ Signature: [can be digital signature]
- ²⁶ Date:
- ²⁷ Details of collaboration and publications:
²⁸ [insert details here if applicable]

²⁹ Abstract

³⁰ Hello, here is some text without a meaning. This text should show what a printed text
³¹ will look like at this place. If you read this text, you will get no information. Really? Is
³² there no information? Is there a difference between this text and some nonsense like
³³ “Huardest gefburn”? Kjift – not at all! A blind text like this gives you information about
³⁴ the selected font, how the letters are written and an impression of the look. This text
³⁵ should contain all letters of the alphabet and it should be written in of the original
³⁶ language. There is no need for special content, but the length of words should match
³⁷ the language.

O time, thou must untangle this, not I.
It is too hard a knot for me to untie!

Twelfth Night

SHAKESPEARE

³⁸ Acknowledgements

³⁹ In principio fu la Maestra Manuela.

⁴⁰ A heartfelt thank you to . . . for accepting to be the referees of this thesis, and for
⁴¹ the thought-provoking discussions we shared. Their comments brought this manuscript
⁴² to a significant improvement.

⁴³ I feel privileged to have this many eminent researchers in my committee. A very big
⁴⁴ thank you for accepting to be part of it.

⁴⁵ Thank you to . . .

⁴⁶ Un ringraziamento va anche agli amici triestini di nascita, di adozione, o di passaggio,
⁴⁷ matematici, sballerine, o altro, oggi sparpagliati per il mondo a formare una famiglia
⁴⁸ grazie alla quale uno non si sente mai troppo solo e lontano da tutti. Tanto siamo
⁴⁹ dappertutto.

⁵⁰ In particolare grazie a . . .

⁵¹ Prima di giungere ai ringraziamenti più personali, . . .

⁵² Contents

⁵³	Statement of originality	3
⁵⁴	Abstract	5
⁵⁵	Acknowledgements	9
⁵⁶	List of Figures	15
⁵⁷	List of Tables	29
⁵⁸	1 Introduction	31
⁵⁹	2 Neutrino physics	33
⁶⁰	2.1 Neutrinos in the SM	33
⁶¹	2.2 Neutrino oscillations	34
⁶²	2.2.1 Oscillations in vacuum	35
⁶³	2.2.2 Oscillations in matter	36
⁶⁴	2.2.3 Current status of neutrino oscillations	37
⁶⁵	2.3 Open questions in the neutrino sector	38
⁶⁶	3 The Deep Underground Neutrino Experiment	41
⁶⁷	3.1 Overview	41
⁶⁸	3.2 Physics goals of DUNE	43
⁶⁹	3.3 Far Detector	45
⁷⁰	3.3.1 Horizontal Drift	46
⁷¹	3.3.2 Vertical Drift	49

CONTENTS

72	3.3.3 FD Data Acquisition System	51
73	3.4 Near Detector	52
74	3.4.1 ND-LAr	54
75	3.4.2 TMS/ND-GAr	55
76	3.4.3 PRISM	56
77	3.4.4 SAND	58
78	3.5 LBNF beamline	58
79	4 ND-GAr	61
80	4.1 Requirements	61
81	4.2 Reference design	62
82	4.2.1 HPgTPC	62
83	4.2.2 ECal	63
84	4.2.3 Magnet	64
85	4.2.4 Muon system	65
86	4.3 GArSoft	65
87	4.3.1 Event generation	65
88	4.3.2 Detector simulation	66
89	4.3.3 Reconstruction	67
90	5 FWTPG offline software	71
91	6 Matched Filter approach to induction wire Trigger Primitives	73
92	6.1 Motivation	73
93	6.2 Signal-to-noise ratio definition	75
94	6.3 Low-pass FIR filter design	77
95	6.4 Matched filters	80
96	6.5 Using simulated samples	86
97	6.5.1 Angular dependence	92
98	6.5.2 Distortion and peak asymmetry	94

CONTENTS

99	6.5.3 Hit sensitivity	97
100	7 DM searches with neutrinos from the Sun	107
101	7.1 Motivation	107
102	7.2 Gravitational capture of DM by the Sun	107
103	7.3 Neutrino flux from DM annihilations	114
104	7.4 Computing limits from solar neutrino fluxes	115
105	7.5 Example: Kaluza-Klein Dark Matter	119
106	7.6 High energy DM neutrino signals	123
107	7.6.1 DIS events	125
108	7.6.2 Single proton QEL events	130
109	7.6.3 Results	133
110	7.7 Example: Leptophilic Dark Matter	135
111	8 Particle ID in GArSoft	141
112	8.1 dE/dx measurement in the TPC	142
113	8.1.1 Energy calibration	144
114	8.1.2 Truncated dE/dx mean	154
115	8.1.3 Mean dE/dx parametrisation	157
116	8.1.4 Particle identification	161
117	8.2 Muon and pion separation in the ECal and MuID	161
118	8.2.1 Track-ECal matching	164
119	8.2.2 Feature selection and importance	168
120	8.2.3 Hyperparameter optimisation	171
121	8.2.4 Probability calibration	171
122	8.2.5 Performance	171
123	8.3 ECal time-of-flight	171
124	8.3.1 Arrival time estimations	171
125	8.3.2 Proton and pion separation	171
126	8.4 Charged pion decay in flight	171

CONTENTS

127	8.4.1 Track breakpoints	179
128	8.5 Neutral particle identification	179
129	8.5.1 ECal clustering	179
130	8.5.2 π^0 reconstruction	182
131	9 Conclusions	185
132	A An appendix	187
133	Bibliography	189

¹³⁴ List of Figures

¹³⁵	3.1 Schematic diagram of the DUNE experiment and the LBNF beamline [1].	42
¹³⁶	3.2 Schematic diagram showing the operating principle of a LArTPC with wire readout	46
¹³⁸	3.3 Proposed design for the FD-1 and FD-2 modules following the HD principle.	47
¹³⁹	3.4 Schematic representation of an APA frames showing the U, V, X and G wires.	48
¹⁴¹	3.5 A PDS module containing 24 X-ARAPUCAs and the location of the modules on the APAs.	48
¹⁴³	3.6 Proposed design for the FD-3 module following the VD principle.	49
¹⁴⁴	3.7 Schematic representation of the electrode strip configuration for a top and bottom CRU.	50
¹⁴⁶	3.8 Detailed diagram of the DUNE FD DAQ system. Figure taken from Ref. [2].	51
¹⁴⁸	3.9 Representation of the ND hall in Phase II, showing the different subcomponents.	53
¹⁴⁹	3.10 Schematic representation of the external components of ND-LAr, including the cryostat and the PRISM movable system and detailed drawing of one ArgonCube module.	54
¹⁵²	3.11 Schematic view of the TMS detector, highlighting its main parts.	55
¹⁵³	3.12 Cross section of the ND-GAr geometry, showing the HPgTPC, ECal and magnet.	56

LIST OF FIGURES

155	3.13	Predicted beam muon neutrino flux at the ND location for different off-axis positions.	57
156	3.14	Schematic longitudinal section of the LBNF beamline at Fermilab.	58
158	3.15	Predicted neutrino fluxes at the FD in FHC mode and RHC mode.	59
159	4.1	Diagram of the ALICE TPC, showing the two drift chambers, inner and outer field cages and readout chambers.	63
161	4.2	Diagram of the ALICE TPC, showing the two drift chambers, inner and outer field cages and readout chambers.	64
163	6.1	<i>Schematic representation of an APA. The black lines represent the APA steel frame. The green and magenta lines correspond to the direction of the U and V induction wires respectively. The blue lines indicate the direction of the X collection wires and the wire shielding G.</i>	74
167	6.2	<i>Left panel: Zoomed unfiltered waveform corresponding to channel 7840 from the ProtoDUNE-SP raw data capture <code>felix-2020-07-17-21:31:44</code> (blue line). The green dashed lines mark the region $\pm 3\sigma_{\text{raw}}$. The resulting noise waveform is also shown (red line). Top right panel: ADC distribution for channel 7840, where the green shaded region represents $\pm \sigma_{\text{raw}}$. Bottom right panel: noise ADC distribution for channel 7840, where the green shaded region represents $\pm \sigma_{\text{noise}}$.</i>	75
174	6.3	<i>Left panel: Zoomed filtered waveform corresponding to channel 7840 from the ProtoDUNE-SP raw data capture <code>felix-2020-07-17-21:31:44</code> (blue line). The filter used was the current implementation of the low-pass FIR filter in <code>dtp-firmware</code>. The green dashed lines mark the region $\pm 3\sigma_{\text{raw}}$. The resulting noise waveform is also shown (red line). Top right panel: ADC distribution for channel 7840 after filtering, where the green shaded region represents $\pm \sigma_{\text{raw}}$. Bottom right panel: noise ADC distribution for channel 7840 after filtering, where the green shaded region represents $\pm \sigma_{\text{noise}}$</i>	77

LIST OF FIGURES

182	6.4 Power spectrum in decibels for the current implementation of the low-pass	
183	FIR filter in <code>dtp-firmware</code> (blue line), compared to the response of an	
184	optimal filter obtained using the Parks-McClellan algorithm for the same	
185	pass-band (red line). Also for comparison I include the spectrum of the	
186	optimal filter when taking only the integer part of the coefficients (red	
187	dashed line)	78
188	6.5 Relative change in the S/N for the ProtoDUNE-SP raw data capture	
189	<code>felix-2020-07-17-21:31:44</code> , using different values of the cutoff frequency	
190	f_c and the transition width δf . The optimal Chebyshev filters were applied	
191	using just the integer part of the coefficients given by the Parks-McClellan	
192	algorithm.	79
193	6.6 Distribution of the relative change of the S/N on the different wire planes	
194	from the ProtoDUNE-SP raw data capture <code>felix-2020-07-17-21:31:44</code>	
195	after the optimal Chebyshev filter was applied. The filter was computed	
196	with the Parks-McClellan algorithm using a cutoff of $f_c = 0.068 \text{ ticks}^{-1}$	
197	and a transition width $\delta f = 0.010 \text{ ticks}^{-1}$	80
198	6.7 Left panel: Zoomed match filtered waveform corresponding to channel 7840	
199	from the ProtoDUNE-SP raw data capture <code>felix-2020-07-17-21:31:44</code>	
200	(blue line). The filter used was directly extracted from the data, being	
201	the 32 values around the first peak in the original waveform. The green	
202	dashed lines mark the region $\pm 3\sigma_{\text{raw}}$. The resulting noise waveform is	
203	also shown (red line). Top right panel: ADC distribution for channel 7840	
204	after match filtering, where the green shaded region represents $\pm \sigma_{\text{raw}}$.	
205	Bottom right panel: noise ADC distribution for channel 7840 after match	
206	filtering, where the green shaded region represents $\pm \sigma_{\text{noise}}$	81
207	6.8 Relative improvement in the S/N for the raw data capture <code>felix-2020-07-17-21:31:44</code> ,	
208	using the matched filter following the parametrisation in Eq. (6.17). The	
209	black crosses in both panels denote the location of the maximum ratio value.	84

LIST OF FIGURES

210	6.9 Left panel: Optimal matched filter coefficients for the U (blue line) and V (red line) planes. The filters were computed with our parametrisation in Eq. (6.17) for the parameter values $\delta = 0.035$, $\sigma = 0.191$ and $\delta = 0.018$, $\sigma = 0.191$ respectively. Right panel: Distribution of the relative change of the S/N on the two induction wire planes from the ProtoDUNE-SP raw data capture <i>felix-2020-07-17-21:31:44</i> after their respective optimal matched filters were applied.	87
217	6.10 Left panel: distributions of the particles track length in the liquid argon for the generated $E_k = 100$ MeV monoenergetic samples, electrons (blue), muons (red), protons (green) and neutral pions (purple). Right panel: distribution of the length of the longest photon in the neutral pion sample after the decay process $\pi^0 \rightarrow \gamma\gamma$	88
222	6.11 Left panel: schematic representation of the two new rotated reference frames used in this analysis (denoted as prime and double prime), viewed from the yz plane. The magenta stack of lines represent the wires in the U plane, whereas the green lines correspond to the wires in the V plane. Right panel: 3D representation of the momentum of one of the generated monoenergetic muons (red arrow) in the original reference frame (black lines), along with the new reference frame used for the U plane waveforms (blue lines). In the yz plane I added the projection of these three.	90
230	6.12 Distributions of the mean S/N improvement per event for the corresponding sample after applying the matched filters. Here I separated the change in the U plane (blue) and the V plane (red) channels. From top left to the right: muon, electron, proton and neutral pion. All the events have a fixed kinetic energy of $E_k = 100$ MeV.	91

LIST OF FIGURES

LIST OF FIGURES

255	6.16 Left panel: peak asymmetry distribution for the case of the monoenergetic	
256	$E_k = 100$ MeV muon sample. Each value corresponds to a single bipolar	
257	signal peak from a channel in any event. The blue distribution represents	
258	the peaks on U plane channels, whereas the red corresponds to signal peaks	
259	in V wires. Right panel: relation between the mean peak asymmetry per	
260	event with the S/N for U channel waveforms from the $E_k = 100$ MeV	
261	muon sample. The top subplot shows the decimal logarithm of the mean	
262	S/N for the raw (red) and the matched filtered (blue) waveforms. The	
263	bottom subplot contains the mean S/N improvement ratio after the matched	
264	filter was applied.	96
265	6.17 Raw data display in the plane time (in firmware ticks) vs. offline channel	
266	number for an $E_k = 100$ MeV electron event. The produced true hits are	
267	superimposed (black boxes) as well as the hits comming from the standard	
268	hit finder chain (blue circles) and the hit finder using the matched filter	
269	(green triangles).	98
270	6.18 Dependence of the precision (blue), sensitivity (red) and F_1 (green) scores	
271	on the threshold values used in the hit finder, for the FIR (left panel)	
272	and matched filter (right panel) cases. The results were obtained after	
273	matching the hits to the true hits in the case of the isotropic muon sample	
274	with kinetic energy in the range 5 to 100 MeV, taking only into account	
275	the induction plane channels. The points represent the mean value while	
276	the error bars indicate one standard deviation around that mean value. . .	100

LIST OF FIGURES

- 277 6.19 *Dependence of the averaged hit sensitivity on the kinetic energy of the*
278 *events for the matched filter (blue) and standard (red) hits, for the case of*
279 *the muon (left panel) and electron (right panel) samples, separated between*
280 *U (top plots) and V (bottom plots) induction wire planes. The top subplots*
281 *contain the hit sensitivities for the two hit finder alternatives, while the*
282 *bottom subplots show the ratio between the two. The horizontal lines sit at*
283 *the mean value and represent the size of the energy bins, while the vertical*
284 *error bars indicate one standard deviation around that mean value.* 102
- 285 6.20 *Distributions of the hit sensitivity in the U (top panels) and V (bottom*
286 *panels) planes versus the hit sensitivity in the X plane, both for the*
287 *standard hits (left panels) and the matched filter hits (right panels), in the*
288 *case of the electron sample and a threshold of 30 ADC.* 103
- 289 6.21 *Top panels: standard residual plots of the hit sensitivities between the X*
290 *and U planes. Bottom panels: quantile-quantile plots of the hit sensitivity*
291 *standard residuals between the X and U planes. In all cases, the left*
292 *panel corresponds to the standard hits while the right panel represents the*
293 *matched filter case, all from the electron sample with a 30 ADC threshold.* 104
- 294 7.1 *Input solar parameters used in our capture rate computation as functions*
295 *of the Sun's radius, from left to right: temperature (with respect to the*
296 *temperature at the core), mass (in solar masses) and electron number*
297 *density (with respect to the electron density at the core). All quantities*
298 *shown correspond to the standard solar model BS2005-OP [3].* 111
- 299 7.2 *Capture rates as a function of the DM mass for the DM-electron interactions*
300 *(red lines), SD DM-nucleons interactions (green lines) and SI DM-nucleons*
301 *interactions (blue lines). Solid lines represent the values computed in this*
302 *work while the dashed lines are the one given in Ref. [4]. All the rates*
303 *are shown for a choice of scattering cross section of $\sigma_i = 10^{-40} \text{ cm}^2$.* . . 112

LIST OF FIGURES

304	7.3 <i>NuWro computed $\nu_\mu - {}^{40}\text{Ar}$ charged-current scattering cross section as a function of the neutrino energy E_μ. The black line shows to the total cross section, whereas the others correspond to the different contributions (in red quasi-elastic scattering, in green resonant pion exchange, in blue deep inelastic scattering and in purple meson exchange current).</i>	116
309	7.4 <i>Expected atmospheric neutrino flux as a function of the neutrino energy E_ν at Homestake at solar minimum, taken from Ref. [5]. The blue solid (dashed) line correspond to muon neutrinos (antineutrinos) and the red solid (dashed) line correspond to electron neutrinos (antineutrinos)</i>	118
313	7.5 Feynman diagrams for B^1B^1 annihilation into SM fermions.	120
314	7.6 Feynman diagrams for B^1B^1 annihilation into a Higgs boson pair. . . .	120
315	7.7 <i>Computed spectra of muon neutrinos at the DUNE FD site from B^1 annihilations in the Sun for three different values of M_{LKP}, plotted in relative energy units for legibility.</i>	121
318	7.8 <i>Projected 90% confidence level upper limit for DUNE (400 kT yr) on the spin- dependent B^1-proton scattering cross section as a function of M_{LKP} (green dots). I also show the previous limits from IceCube [6] (blue line) and Antares [7] (red line) on the LKP cross section. The shaded area represents the disfavoured region (at 95% confidence level) on the mass of the LKP from LHC data [8]</i>	122
324	7.9 <i>Computed spectra of muon neutrinos at the DUNE FD site from $\tau^+\tau^-$ (left panel) and $b\bar{b}$ (right panel) annihilations in the Sun for the DM masses $m_{\text{DM}} = 10$ GeV (red line), 50 GeV (green line) and 100 GeV (blue line), plotted in relative energy units.</i>	123
328	7.10 <i>Distribution of the muon neutrino energies from the $\tau^+\tau^-$ (left panel) and $b\bar{b}$ (right panel) annihilation channels, for $m_{\text{DM}} = 10$ GeV, separated by CC interaction type: QEL (blue), MEC (orange), RES (green) and DIS (red)</i>	125

LIST OF FIGURES

<p>332 7.11 <i>Distributions of θ_μ (left panel), θ_j (central panel) and θ_{plane} (right panel)</i> 333 <i>for the $b\bar{b}$ sample with $m_{DM} = 10$ GeV (blue) and the atmospheric</i> 334 <i>background (red).</i></p> <p>335 7.12 <i>Left panel: signal efficiencies (blue lines) and background rejections (red</i> 336 <i>lines) for events passing the cuts $\theta < \theta_{cut}$ for the jet (solid lines) and</i> 337 <i>muon (dashed lines) angles. Right panel: signal efficiency (blue line) and</i> 338 <i>background rejection (red line) for events passing the cut $\theta_{plane} < \theta_{cut}$ for</i> 339 <i>the momentum conservation plane deviation.</i></p> <p>340 7.13 <i>Signal efficiencies for the $\tau^+\tau^-$ (blue line) and $b\bar{b}$ (red line) DIS samples</i> 341 <i>as functions of the DM mass, m_{DM}, obtained by applying the optimal</i> 342 <i>angular cuts $\theta_\mu < 27^\circ$, $4^\circ < \theta_j < 26^\circ$ and $\theta_{plane} < 3.5^\circ$.</i></p> <p>343 7.14 <i>Distributions of $\cos \theta_\mu$ (left panel), $\cos \theta_p$ (central panel) and $\cos \theta_N$</i> 344 <i>(right panel) for the $\tau^+\tau^-$ QEL sample with $m_{DM} = 5$ GeV (blue) and</i> 345 <i>the atmospheric background (red).</i></p> <p>346 7.15 <i>Left panel: value of the loss function for the training sample (blue line)</i> 347 <i>and accuracy for the validation sample (red line) versus the number of</i> 348 <i>iterations for the MLP classifier training. Right panel: distributions of the</i> 349 <i>predicted probabilities assigned by the MLP classifier to the test sample</i> 350 <i>for the $\tau^+\tau^-$ QEL signal with $m_{DM} = 5$ GeV (blue) and the atmospheric</i> 351 <i>background (red).</i></p> <p>352 7.16 <i>Signal efficiencies for the $\tau^+\tau^-$ (blue line) and $b\bar{b}$ (red line) single proton</i> 353 <i>QEL samples as functions of the DM mass, m_{DM}, obtained by requiring a</i> 354 <i>minimum predicted probability from the MLP classifier of 0.97 in order to</i> 355 <i>achieve a background rejection greater than 99.8%.</i></p>	<p>126</p> <p>127</p> <p>129</p> <p>130</p> <p>131</p> <p>132</p>
---	---

LIST OF FIGURES

356	7.17 Projected 90% confidence level upper limit for DUNE (400 kT yr) on 357 the spin-dependent DM-nucleon scattering cross section as a function of 358 m_{DM} , for the annihilation channels $\tau^+\tau^-$ (blue) and $b\bar{b}$ (red) separated 359 by interaction type (up triangles denote DIS interactions whereas down 360 triangles represent QEL interactions). I also show the previous limits 361 from IceCube [9] (solid lines) and the projected sensitivities for Pingu [10] 362 (dashed lines) and Hyper-Kamiokande [11] (dash-dotted lines), as well 363 as the direct detection limits from PICASSO [12] (solid green line) and 364 PICO-60 C ₃ F ₈ [13] (dashed green line).	134
365	7.18 Left panel: Projected 90% confidence level sensitivity of DUNE (400 kT 366 yr) to the scale Λ of an EFT containing only leptophilic DM axial-axial 367 interactions (blue line). Right panel: . In both cases the corresponding 368 limits from DarkSide-50 [14] (dotted green line) and XENON1T [15] 369 (dashed red line) are also shown, together with the configurations for which 370 the correct relic density is achieved (black line), all for the coupling values 371 $c_A^e = 10^3$ and $c_A^\nu = 10^{-2}$	138
372	8.1 Left panel: distribution of the fraction of Geant4-level energy deposits per 373 track with residual range less than 20% of the total track length, for the 374 isotropic proton sample. Right panel: distribution of the ionisation per 375 unit length of the energy deposits in the proton sample after removing 376 the tracks with less than 30% of their energy deposits in the last 20% of 377 the track.	145
378	8.2 Left panel: distribution of the reconstructed ionisation charge per unit 379 length for our MC stopping proton sample. The different colors indicate 380 how many consecutive dQ/dx pairs were grouped together. Right panel: 381 distribution of the median change in dQ/dx per track after $N_{group} = 4$ 382 clusters were reclustered together.	146

LIST OF FIGURES

383	8.3 Distribution of the Geant4-simulated energy losses per unit length versus	
384	residual range for the stopping proton sample. The overlaid points	
385	represent the fitted most probable value of the dE/dx distribution in each	
386	residual range bin, whereas the curve is their best fit to the Bragg-Kleeman	
387	formula from Eq. (8.4).	148
388	8.4 Fitted most probable dQ/dx values for each dE/dx bin (red points),	
389	obtained from the stopping proton sample. The overlaid curve (black	
390	line) represents the best fit to the logarithmic calibration function from	
391	Eq. (8.5).	149
392	8.5 Fitted most probable dQ/dx values for each dE/dx bin for three different	
393	ADC bit limits, 10 (blue points), 12 (default, yellow points) and 16-bit	
394	(red points).	151
395	8.6 Top panel: area normalised dE/dx distributions for the true (solid grey)	
396	and the reconstructed energy deposits in the stopping proton sample,	
397	both after applying the calibration (blue) and the calibration and the	
398	normalisation correction (yellow). Also shown is the distribution obtained	
399	by applying a correction factor to the dQ/dx values but not the calibration	
400	(red). Bottom panel: fractional residuals for the uncorrected (blue),	
401	corrected (yellow) and uncalibrated (red) samples.	152
402	8.7 Left panel: fractional residuals between the true and the corrected dE/dx	
403	means (blue) and the 60% truncated means (yellow), for each event in the	
404	stopping proton sample. Right panel: fractional residuals between the	
405	true and the uncorrected (blue), corrected (yellow) and uncalibrated (red)	
406	dE/dx 60% truncated means, for each event in the stopping proton sample.	154
407	8.8 Estimated values of the mean dE/dx bias (left panel) and resolution	
408	(right panel) obtained using the corrected data from the stopping proton	
409	sample, for different values of the truncation factor.	155
410	8.9 Examples of the truncated mean dE/dx LanGauss fits for various $\beta\gamma$	
411	bins, from a simulated FHC neutrino sample.	157

LIST OF FIGURES

412	8.10 Resulting one and two dimensional projections of the posterior probability distributions of the ALEPH $\langle dE/dx \rangle$ parameters obtained by fitting the 60% truncated mean dE/dx values from a FHC neutrino sample in ND-GAr. The vertical dashed lines in the 1D distributions represent the 16th, 50th and 84th percentiles.	158
417	8.11 Truncated mean dE/dx obtained for the FHC neutrino sample as a function of the $\beta\gamma$ product (upper panel). Also shown are the fitted most probable values for each $\beta\gamma$ bin (red points) and the best fit obtained using the ALEPH parametrisation (black line). The residuals resulting from the fit are shown in the lower panel.	159
422	8.12 Distribution of the 60% truncated mean dE/dx versus reconstructed momentum for the FHC neutrino sample. The black lines indicate the predictions of the ALEPH parametrisation for electrons, muons, charged pions and protons.	160
426	8.13 Estimated values of the mean dE/dx bias (left panel) and resolution (right panel) obtained for the true protons in a FHC neutrino sample.	161
428	8.14 Momentum distribution for the primary muon in ν_μ CC $N\pi^\pm$ interactions inside the fiducial volume of ND-GAr (blue line), compared to the post FSI charged pion spectrum (red line).	162
431	8.15 Distributions of energy deposits in the ECal for a muon (left) and a charged pion (right) with similar momenta. The energy is projected onto the plane perpendicular to the principal component of the hits, and the positions are relative to the center of the interaction.	163
435	8.16 Left panel: comparison between the precision (blue), sensitivity (yellow) and F_1 score (red) obtained for the default (horizontal lines) and new algorithms, both with the χ^2 -based direction estimator (squares) and cheating the directions (circles), for different values of the χ^2 cut. Right panel: comparison of the performance of the new algorithm when applying the cluster t_0 correction (squares) and when (circles).	165

LIST OF FIGURES

441	8.17 Schematics of a possible option to deal with track-ECal associations in non-zero t_0 neutrino interaction events, trying to correct for the drift direction uncertainty in a cluster-by-cluster basis using the cluster time, $t_{cluster}$	167
445	8.18 Left panel: number of non-decaying, decaying and decaying in the fiducial volume pions for a MC sample of 10^5 , $p = 500$ MeV isotropic positively charged pions inside the TPC. Right panel: event display for a positive pion decaying inside the fiducial volume, with a single reconstructed track for the pion and muon system.	172
450	8.19 Values of $\chi_k^{2(FB)}$ (top left panel), F_k (top right panel), $D_k^{1/R}$ (bottom left panel) and D_k^ϕ (bottom right panel) versus position along the drift direction for a reconstructed track in a positive pion decay event. The vertical red dashed line indicates the true location of the decay point. . .	174
454	8.20 Fractional residual distributions of the true and reconstructed decay position along the drift coordinate, using the position of the maximum of $\chi_k^{2(FB)}$ (left panel) and F_k (right panel) as estimates of the decay position. Also shown are double Gaussian fits to these points (red lines). .	175
458	8.21 Distributions of the extreme values of $\chi_k^{2(FB)}$ (top left panel), F_k (top right panel), $D_k^{1/R}$ (bottom left panel) and D_k^ϕ (bottom right panel) for non-decaying reconstructed pion tracks (blue) and tracks which include the decay inside the fiducial volume (red).	177
462	8.22 Left panel: distributions of the predicted probabilities assigned by the BDT classifier to a test sample of decaying pion+muon tracks (blue) and non-decaying pion tracks (red). Left: signal efficiency versus background acceptance (ROC curve) obtained from the BDT for the test sample. .	178
466	8.23 Left panel: dependence of the decay position finding resolution on the true value of the decay angle for the $\chi_k^{2(FB)}$ (red) and F_k (blue) methods. Right panel: signal efficiency (blue line) and background rejection (red line) from the BDT classifier versus true decay angle.	178

LIST OF FIGURES

470	8.24 Mean values of the F_1 -score marginal distributions for the different	
471	free parameters of the new clustering algorithm, with the error bars	
472	representing one standard deviation around the mean. The F_1 -score	
473	values were computed for the 6561 possible parameter configurations	
474	using 1000 ν_μ CC interaction events.	181
475	8.25 Left panel: distributions of the number of ECal clusters per photon from	
476	π^0 decays for the standard (red) and new (blue) clustering algorithms.	
477	Right panel: reconstructed invariant mass distributions for photon pairs	
478	from single π^0 events using the standard (red) and new (blue) ECal	
479	clustering algorithms.	183

⁴⁸⁰ List of Tables

⁴⁸¹	2.1	Summary of neutrino oscillation parameters determined in the Neutrino Global Fit of 2020 [16]	38
⁴⁸²			
⁴⁸³	3.1	Summary of the two-phased plan for DUNE	43
⁴⁸⁴	3.2	Exposure and time required to achieve the different physics milestones of the two phases	44
⁴⁸⁵			
⁴⁸⁶	6.1	<i>Characteristic parameters of the two monoenergetic muon events selected, relative to the U plane: projected angles in the xz' and $y'z'$ planes, S/N values for the raw and filtered waveforms, mean improvement of the S/N and peak asymmetry.</i>	95
⁴⁸⁷			
⁴⁸⁸			
⁴⁸⁹			
⁴⁹⁰	8.1	Calibration parameters obtained from the fit of the ND-GAr simulated stopping proton sample to the calibration function from Eq. (8.5). The fits were performed for the 10, 12, and 16-bit ADC limits.	151
⁴⁹¹			
⁴⁹²			
⁴⁹³	8.2	Summary of parameters and sampled values used in the optimisation of the clustering algorithm.	181
⁴⁹⁴			

⁴⁹⁵ Chapter 1

⁴⁹⁶ Introduction

497 **Chapter 2**

498 **Neutrino physics**

499 Ever since they were postulated in 1930 by Wolfgang Pauli to explain the continuous
500 β decay spectrum [17] and later found by Reines and Cowan at the Savannah River
501 reactor in 1953 [18], neutrinos have had a special place among all other elementary
502 particles. They provide a unique way to probe a wide range of quite different physics,
503 from nuclear physics to cosmology, from astrophysics to colliders. Moreover, there is
504 compelling evidence to believe that the study of neutrinos may be key to unveil different
505 aspects of physics beyond the SM, difficult to test elsewhere.

506 In this Chapter I will review the basics of neutrino physics, from its role within the
507 SM to the main open questions related to the neutrino sector, paying special attention
508 to the phenomenology of neutrino oscillations.

509 **2.1 Neutrinos in the SM**

510 By definition, in the SM there are no right-handed neutrino fields. A direct implication
511 of this fact is that neutrinos are strictly massless within the SM. This follows from the
512 experimental observation that all neutrinos produced via weak interactions are pure
513 left-handed helicity states (and similarly antineutrinos are pure right-handed states).
514 The hypothetical existence of right-handed neutrinos could be indirectly inferred from
515 the observation of non-zero neutrino masses, nevertheless the existence neutrino masses

Chapter 2. Neutrino physics

516 is not a sufficient condition for the existence of such fields.

517 In the SM neutrinos appear in three flavours, namely ν_e , ν_μ and ν_τ . These are
518 associated with the corresponding charged leptons e , μ and τ , in such a way that the
519 charged current part of the Lagrangian coupling them is diagonal. As in the electroweak
520 theory neutrinos are coupled to the Z boson in a universal way, by measuring the so-called
521 invisible decay width of the Z we have an estimate of the number of light (i.e. lighter
522 than the Z boson) neutrino flavours. This number was measured by LEP in a combined
523 analysis of $e^+e^- \rightarrow \mu^+\mu^-$ and $e^+e^- \rightarrow$ hadrons to be $N_\nu = 2.9840 \pm 0.0082$ [19].

524 2.2 Neutrino oscillations

525 The evidence for neutrino oscillation [20], and therefore the existence of non-zero neutrino
526 masses, constitutes one of the groundbreaking discoveries of modern Physics and has
527 acted as driving force for Beyond the Standard Model (BSM) Physics. The minimal
528 extension of the Standard Model (SM) we can do to address these phenomena is
529 introducing distinct masses for at least two of the neutrinos. This way, we are left with
530 three neutrino mass eigenstates ν_1 , ν_2 and ν_3 , with masses m_1 , m_2 and m_3 respectively,
531 which in general will not coincide with the flavour eigenstates ν_e , ν_μ and ν_τ .

532 The way to relate these two sets of neutrino eigenstates is via a 3×3 unitary matrix,
533 called the Pontecorvo-Maki-Nakagawa-Sakata (PMNS) matrix [21, 22], as:

$$|\nu_\alpha\rangle = \sum_{i=1}^3 U_{\alpha i}^* |\nu_i\rangle, \quad (2.1)$$

534 where the Greek index α denotes the flavour $\{e, \mu, \tau\}$ and the Latin index i the associated
535 masses $\{1, 2, 3\}$. This leptonic mixing matrix may be parametrized in terms of 6
536 parameters, 3 of which are mixing angles θ_{12} , θ_{13} and θ_{23} , one CP-violating phase δ_{CP}

2.2. Neutrino oscillations

537 and 2 Majorana phases α and β :

$$U = \begin{pmatrix} 1 & 0 & 0 \\ 0 & c_{23} & s_{23} \\ 0 & -s_{23} & c_{23} \end{pmatrix} \begin{pmatrix} c_{13} & 0 & s_{13}e^{-i\delta_{CP}} \\ 0 & 1 & 0 \\ -s_{13}e^{-i\delta_{CP}} & 0 & c_{13} \end{pmatrix} \begin{pmatrix} c_{12} & s_{12} & 0 \\ -s_{12} & c_{12} & 0 \\ 0 & 0 & 1 \end{pmatrix} \begin{pmatrix} 1 & 0 & 0 \\ 0 & e^{i\alpha} & 0 \\ 0 & 0 & e^{i\beta} \end{pmatrix}, \quad (2.2)$$

538 where $c_{ij} \equiv \cos \theta_{ij}$ and $s_{ij} \equiv \sin \theta_{ij}$. This matrix is analogous to the Cabibbo-Kobayashi-
539 Maskawa (CKM) matrix in the quark sector. If neutrinos are Dirac fermions, we can
540 drop the Majorana phases in the PMNS matrix. But, in any case, these phases play no
541 role on the neutrino oscillations.

542 2.2.1 Oscillations in vacuum

543 Consider the case where a neutrino of flavour α is produced at $t = 0$, and then it
544 propagates through vacuum. Such a state will evolve in time according to the relation:

$$|\nu_\alpha(t)\rangle = \sum_{i=1}^3 U_{\alpha i}^* e^{-iE_i t} |\nu_i(t=0)\rangle, \quad (2.3)$$

545 as the mass eigenstates are also eigenstates of the free Hamiltonian. Now, if we express
546 the mass eigenstates as a superposition of flavour eigenstates, the last expression can be
547 rewritten as:

$$|\nu_\alpha(t)\rangle = \sum_{i=1}^3 U_{\beta i} e^{-iE_i t} U_{\alpha i}^* |\nu_\beta\rangle. \quad (2.4)$$

548 This way, the probability for the neutrino to transition from flavour α to flavour β
549 will be given by:

$$P(\nu_\alpha \rightarrow \nu_\beta) = |\langle \nu_\beta | \nu_\alpha(t) \rangle|^2 = \left| \sum_{i=1}^3 U_{\beta i} e^{-iE_i t} U_{\alpha i}^* \right|^2. \quad (2.5)$$

550 A usual approximation to take at this point is to consider ultra-relativistic neutrinos,
551 i.e. $E \approx |\vec{p}|$, so we can write the dispersion relations as:

$$E_i = \sqrt{p^2 + m_i^2} \approx E + \frac{m_i^2}{2E}, \quad (2.6)$$

Chapter 2. Neutrino physics

552 so we can write the oscillation probability as:

$$\begin{aligned} P(\nu_\alpha \rightarrow \nu_\beta) &= \sum_{i,j} U_{\alpha i}^* U_{\beta i} U_{\alpha j} U_{\beta j}^* e^{-i \frac{\Delta m_{ij}^2}{2E} t} \\ &= \delta_{\alpha\beta} - 4 \sum_{i < j} \Re [U_{\alpha i}^* U_{\beta i} U_{\alpha j} U_{\beta j}^*] \sin^2 \left(\frac{\Delta m_{ij}^2}{4E} t \right) \\ &\quad + 2 \sum_{i < j} \Im [U_{\alpha i}^* U_{\beta i} U_{\alpha j} U_{\beta j}^*] \sin \left(\frac{\Delta m_{ij}^2}{2E} t \right), \end{aligned} \quad (2.7)$$

553 where Δm_{ij}^2 is the difference of the squared masses of the j th and i th neutrino mass
 554 eigenvalues. At this point, it is usual to write the phase responsible for the oscillations
 555 as (under the approximate assumption $t \approx L$):

$$\Delta_{ij} \equiv \frac{\Delta m_{ij}^2}{4E} L \simeq 1.27 \frac{\Delta m_{ij}^2}{(\text{eV}^2)} \frac{L}{(\text{km})} \frac{(\text{GeV})}{E}. \quad (2.8)$$

556 Notice that, in the case of antineutrinos the only difference would be the sign of the
 557 last term in the oscillation probability. This way, one can write the CP asymmetry as:

$$\begin{aligned} A_{CP}^{\alpha\beta} &= P(\nu_\alpha \rightarrow \nu_\beta) - P(\bar{\nu}_\alpha \rightarrow \bar{\nu}_\beta) \\ &= 4 \sum_{i < j} \Im [U_{\alpha i}^* U_{\beta i} U_{\alpha j} U_{\beta j}^*] \sin 2\Delta_{ij}. \end{aligned} \quad (2.9)$$

558 2.2.2 Oscillations in matter

559 When neutrinos propagate through matter, their oscillation can be affected in mainly
 560 two ways. First, neutrinos can inelastically scatter with nuclei, thus destroying the
 561 coherent propagation of their quantum state. Nevertheless, in most cases this effect is
 562 negligible (even in very dense mediums like the core of the Sun). Second, neutrinos can
 563 also experience coherent or forward scatterings, that can affect their oscillation but not
 564 lose the coherent propagation of the state.

565 The first proposed model to account for neutrino oscillations in matter was proposed
 566 by Mikhaev, Smirnov and Wolfenstein (MSW) [23]. It relies on the fact that, as the
 567 only charged lepton present in ordinary matter is the electron, electron neutrinos can

2.2. Neutrino oscillations

568 undergo both charged and neutral-current interactions with matter whereas for muon
569 and tau neutrinos just neutral currents are possible.

570 2.2.3 Current status of neutrino oscillations

571 A wide range of neutrino experiments provide experimental input to the neutrino
572 oscillation framework, both using natural or synthetic neutrino sources. The results
573 from one of the neutrino global fit analyses, shown in Tab. 2.1¹, summarise well our
574 current understanding of the different oscillation parameters.

575 **Solar neutrino experiments** detect neutrinos produced in thermonuclear reactions
576 inside the Sun, mainly from the so-called *pp* chain and the CNO cycle. These neutrinos
577 have a typical energy in the range from 0.1 to 20 MeV. These experiments (Homestake
578 [24], GALLEX [25], SAGE [26], Borexino [27], Super-Kamiokande [28] and SNO [29])
579 provide the best sensitivities to θ_{12} and Δm_{21}^2 .

580 **Atmospheric neutrino experiments** detect the neutrino flux produced when
581 cosmic rays scatter with particles in Earth's atmosphere. These collisions generate particle
582 showers that eventually produce electron and muon neutrinos (and antineutrinos). Their
583 energies range from few MeV to about 10^9 GeV. Experiments, like Super-Kamiokande
584 [30] and IceCube [31] use atmospheric neutrinos to measure oscillations and are specially
585 sensitive to θ_{23} and Δm_{32}^2 .

586 **Reactor neutrino experiments** look for the $\bar{\nu}_e$ spectrum produced by nuclear
587 reactors, with energies in the MeV scale. Depending on the distance to the source,
588 long-baseline experiments like KamLAND [32] are sensitive to the solar mass splitting
589 Δm_{21}^2 whereas much shorter baseline experiment such as RENO [33] or DayaBay [34]
590 measure θ_{13} and Δm_{31}^2 .

591 **Accelerator experiments** measure neutrino fluxes generated in particle accelerators.
592 Usually mesons are produced in the accelerator to be focused into a beam, then some
593 decay to muon neutrinos and the rest are absorbed by a target. Depending on the

¹These are the results reported during M. Tórtola's talk at Neutrino 2024 (see this link). I need to keep an eye and see if they publish these or other updated results in the near future.

Chapter 2. Neutrino physics

Table 2.1: Summary of neutrino oscillation parameters determined in the Neutrino Global Fit of 2020 [16].

Parameter	Best fit $\pm 1\sigma$	3σ range
Δm_{21}^2 [eV $^2 \times 10^{-5}$]	$7.55^{+0.22}_{-0.20}$	6.98 – 8.19
$ \Delta m_{31}^2 $ [eV $^2 \times 10^{-3}$] (NO)	$2.51^{+0.02}_{-0.03}$	2.43 – 2.58
$ \Delta m_{31}^2 $ [eV $^2 \times 10^{-3}$] (IO)	$2.41^{+0.03}_{-0.02}$	2.34 – 2.49
$\sin^2 \theta_{12}/10^{-1}$	3.04 ± 0.16	2.57 – 3.55
$\sin^2 \theta_{23}/10^{-1}$ (NO)	$5.64^{+0.15}_{-0.21}$	4.23 – 6.04
$\sin^2 \theta_{23}/10^{-1}$ (IO)	$5.64^{+0.15}_{-0.18}$	4.27 – 6.03
$\sin^2 \theta_{13}/10^{-2}$ (NO)	$2.20^{+0.05}_{-0.06}$	2.03 – 2.38
$\sin^2 \theta_{13}/10^{-2}$ (IO)	$2.20^{+0.07}_{-0.04}$	2.04 – 2.38
δ_{CP}/π (NO)	$1.12^{+0.16}_{-0.12}$	0.76 – 2.00
δ_{CP}/π (IO)	$1.50^{+0.13}_{-0.14}$	1.11 – 1.87

594 configuration one can obtain a beam made of mostly neutrinos or antineutrinos. The
 595 typical energies of these neutrinos are in the GeV range. Experiments such as NOvA
 596 [35], T2K [36], MINOS [37], OPERA [?] and K2K [38] (and in the future DUNE [39])
 597 are primarily sensitive to θ_{13} , θ_{23} and Δm_{32}^2 . Also, in the coming years DUNE [39] and
 598 Hyper-Kamiokande [40] will be sensitive to δ_{CP} .

599 2.3 Open questions in the neutrino sector

600 A crucial question that remains open these days, and is of vital importance for oscillation
 601 phenomena, is whether the mass eigenvalue ν_3 is the heaviest (what we call normal
 602 ordering) or the lightest (referred to as inverted ordering) of the mass eigenstates. In
 603 other words, this means that we do not know the sign of Δm_{32}^2 , so we can either have
 604 $m_1 < m_2 < m_3$ (NO) or $m_3 < m_1 < m_2$ (IO).

605 Another big puzzle is related to the value of δ_{CP} . Nowadays it is poorly constrained,
 606 with all values between π and 2π being consistent with data. A prospective measurement
 607 different from $\delta_{CP} = 0, \pi$ will predict CP-violation in the leptonic sector, and thus

2.3. Open questions in the neutrino sector

contribute along with the one measured in the quark sector to the total amount of CP-violation. Although it is true that these two contributions by themselves are not enough to explain the matter anti-matter asymmetry in our universe, the amount of CP-violation in the leptonic sector can be key to explain such imbalance.

Both of these questions, because of their nature, could be understood thanks to future oscillation experiments.

Notwithstanding, there are other mysteries that can not be unveiled just by conducting oscillation experiments, as certain quantities do not influence these phenomena. Among these there is the question of the absolute values of the neutrino masses. Depending on the value of the lightest of the neutrino masses we can have different mass spectra, from hierarchical $m_1 \ll m_2 < m_3$ (NO) or $m_3 \ll m_1 < m_2$ (IO) to quasi-degenerate $m_1 \simeq m_2 \simeq m_3$.

Other open question concerns the nature itself of the neutrinos. If neutrinos are Dirac particles then their mass term can be generated through the usual Higgs mechanism by adding right-handed neutrino fields. However, if they are Majorana particles and therefore their own antiparticles, there is no need to add extra fields to have the mass term in the Lagrangian. Experiments like SuperNEMO [?], SNO+ [?] and NEXT [?], which search for neutrino-less double beta decay, will be able to determine whether neutrinos are Dirac or Majorana.

627 Chapter 3

628 The Deep Underground Neutrino
629 Experiment

630 The Deep Underground Neutrino Experiment (DUNE) is a next generation long-baseline
631 neutrino experiment [1]. It will aim to address several questions in neutrino physics,
632 study neutrinos from astrophysical sources and search for beyond the standard model
633 physics.

634 This chapter reviews the main goals of the DUNE experiment, the design of the far
635 detector modules and their data acquisition (DAQ) system, and the role that the near
636 detector plays in the physics program of DUNE.

637 3.1 Overview

638 The main physics goals of DUNE are:

- 639 • measure the neutrino mass hierarchy, the amount of CP violation in the leptonic
640 sector and the θ_{23} octant,
- 641 • detect rare low energy neutrino events, like neutrinos from supernova bursts, and
- 642 • search for proton decay and other beyond the standard model phenomena.

Chapter 3. The Deep Underground Neutrino Experiment

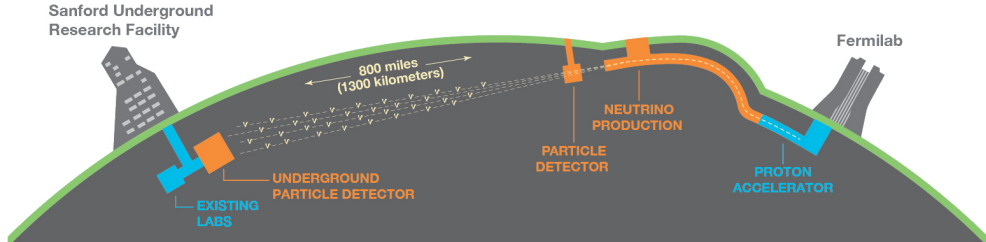


Figure 3.1: Schematic diagram of the DUNE experiment and the LBNF beamline [1].

The design of DUNE has been tailored with these goals in mind. It will consist of two neutrino detectors. A near detector (ND) complex will be placed in Fermilab, 574 m downstream of the neutrino production point, whereas a larger far detector (FD) will be built in the Sandford Underground Research Facility (SURF), South Dakota, approximately 1300 km away. Fig. 3.1 shows a simplified view of the various components of DUNE (not to scale).

The beam neutrinos to be used in DUNE will be provided by the LBNF beamline, the multi-megawatt wide-band neutrino beam planned for Fermilab. First, an intense proton beam is extracted from the Fermilab Main Injector. Then, these protons with energies between 60 GeV and 120 GeV collide with a high-power production target and produce charged mesons. Two magnetic horns allow to focus the mesons and perform a sign selection (thus having the capability to switch between neutrino and antineutrino mode). Soon after that, the mesons decay and produce neutrinos (or antineutrinos) which are then aimed to SURF.

Before arriving to the FD, the neutrino beam meets the ND complex, which serves as the experiment's control. Its role is to measure the unoscillated neutrino energy spectra. From these we can predict the unoscillated spectra at the FD, which can be compared to the spectra measured at the FD in order to extract the oscillation parameters. Therefore, the design of the DUNE ND is mainly driven by the needs of the oscillation physics program.

The liquid Argon time projection chamber (LArTPC) technology has been chosen for

3.2. Physics goals of DUNE

Table 3.1: Summary of the two-phased plan for DUNE. Adapted from Ref. [41].

Parameter	Phase I	Phase II	Benefit
FD mass	20 kt fiducial	40 kt fiducial	FD statistics
Beam power	up to 1.2 MW	2.4 MW	FD statistics
ND config.	ND-LAr, TMS, SAND	ND-LAr, ND-GAr, SAND	Systematic constraints

the FD modules of DUNE. Its four modules will record neutrino interactions from the accelerator-produced beam arriving at predictable times. As it also aims at recording rare events, the FD requires trigger schemes which can deal with both kinds of physics, and also maximum uptime.

DUNE is planned to be built using a staged approach consisting on two phases, which are summarised in Tab. 3.1. Phase I consists of a FD with 50% of the total fiducial mass, a reduced version of the ND complex and a 1.2 MW proton beam. It will be sufficient to achieve some early physics goals, like the determination of the neutrino mass ordering. For its Phase II, DUNE will feature the full four FD modules, a more capable ND and a 2.4 MW proton beam. The physics milestones for the two phases are given in Tab. 3.2, in a staging scenario which assumes that Phase II is completed after 6 years of operation.

A summary of the DUNE science program can be found in the DUNE FD Technical Design Report (TDR) Volume I [1]. For a detailed discussion on the two-phased approach the reader is referred to the DUNE Snowmass 2021 report [41].

3.2 Physics goals of DUNE

As noted in the literature (see for instance Ref. [16] for a review), the parameter space of the neutrino oscillation phenomena within the three-flavour picture is quite constrained by current experimental data. However, there are still crucial open questions, like the mass ordering, the value of δ_{CP} or the θ_{13} octant. One of the main goals of DUNE is to shed some light on the values of these parameters [42].

To address these questions DUNE can look to the subdominant oscillation channel

Chapter 3. The Deep Underground Neutrino Experiment

Table 3.2: Exposure and time required to achieve the different physics milestones of the two phases. The predictions assume a Phase II staging scenario where FD modules 3 and 4 are deployed in years 4 and 6 and both the beam and ND are upgraded after 6 years. Adapted from Ref. [41].

Stage	Physics milestone	Exposure (kt-MW-years)	Years (staged)
Phase I	5σ MO ($\delta_{CP} = -\pi/2$)	16	1-2
	5σ MO (100% of the δ_{CP} values)	66	3-5
	3σ CPV ($\delta_{CP} = -\pi/2$)	100	4-6
Phase II	5σ CPV ($\delta_{CP} = -\pi/2$)	334	7-8
	δ_{CP} resolution of 10 degrees ($\delta_{CP} = 0$)	400	8-9
	5σ CPV (50% of the δ_{CP} values)	646	11
	3σ CPV (75% of the δ_{CP} values)	936	14
	$\sin^2(2\theta_{13})$ resolution of 0.004	1079	16

686 $\nu_\mu \rightarrow \nu_e$ ($\bar{\nu}_\mu \rightarrow \bar{\nu}_e$) and study the energy dependence of the ν_e ($\bar{\nu}_e$) appearance probability.

687 When we focus on the antineutrino channel $\bar{\nu}_\mu \rightarrow \bar{\nu}_e$ there is a change in the sign of δ_{CP} ,
 688 thus introducing CP-violation. Moreover, due to the fact that there are no positrons in
 689 the composition of Earth, there is a sign difference for the matter effect contribution
 690 when looking to the antineutrino channel. This asymmetry is proportional to the baseline
 691 length L and is sensitive to the sign of Δ_{31} , and thus to the neutrino mass ordering.

692 Another of the main physics goals of DUNE is the search for baryon-number violating
 693 processes. Specifically, it will try to answer the question of whether protons are stable
 694 or not. There is no symmetry argument that forbids protons from decaying, but its
 695 apparent stability seems to suggest that baryon number is conserved [43]. However,
 696 proton decay is a usual feature of grand-unified theories, where electromagnetic, weak
 697 and strong interactions are unified above a certain energy scale [44].

698 As the energy deposition scale for this kind of searches is nearly the same as the one
 699 for long-baseline neutrino oscillations, DUNE will be able to look for them. It has several
 700 advantages over other experiments, such as excellent imaging and particle identification,
 701 which can be translated to lower backgrounds.

702 The last of the main objectives of DUNE is the detection of neutrinos originated in
 703 supernovae explosions, what is called a supernova neutrino burst (SNB). These neutrinos
 704 carry with them information about the core-collapse process, from the progenitor to the

3.3. Far Detector

explosion and the remnant; but also may have information about new exotic physics. So far, the only neutrino events ever recorded from such a process were a few dozens of $\bar{\nu}_e$ events from the 1987A supernova located in the Magellanic Cloud, 50 kpc away from Earth [45, 46].

DUNE aims to collect also some SNB events. Although these are quite rare, as the expected supernovae explosion events are about one every few decades for our galaxy and Andromeda, the long lifetime of the experiment (around a few decades as well) makes it reasonable to expect some. Nowadays the main sensitivity to SNB of most experiments is to the $\bar{\nu}_e$ through inverse beta decay. One of the advantages of DUNE is its expected sensitivity to ν_e , since the dominant channel will be ν_e CC scattering.

Moreover, due to the stringent requirements that the main physics goals set for DUNE, it will allow also to perform searches for all kind of BSM physics. Among others, DUNE will be able to look for: active-sterile neutrino mixing, non-unitarity of the PMNS matrix, non-standard interactions, Lorentz and CPT violations, neutrino trident production, light-mass DM, boosted DM and heavy neutral leptons. The reader is referred to the DUNE FD TDR Volume II [42] for a full discussion of the physics scope of DUNE.

3.3 Far Detector

The so-called DUNE FD complex will sit 1.5 km underground at SURF, South Dakota. Two caverns will host the four FD modules, two of them per cavern, each embedded in cryostats of dimensions 18.9 m (w) \times 17.8 m (h) \times 65.8 m (l). A central, smaller cavern will host the cryogenic system.

Three out of the four modules will be liquid argon (LAr) time projection chamber detectors, often refer to as LArTPCs, with a LAr fiducial mass of at least 10 kt each. The first and second FD modules, FD-1 and FD-2, will use a Horizontal Drift (HD) technology, whereas the third module, FD-3, will have a Vertical Drift (VD) direction. The technology for the fourth module is still to be decided,

Chapter 3. The Deep Underground Neutrino Experiment

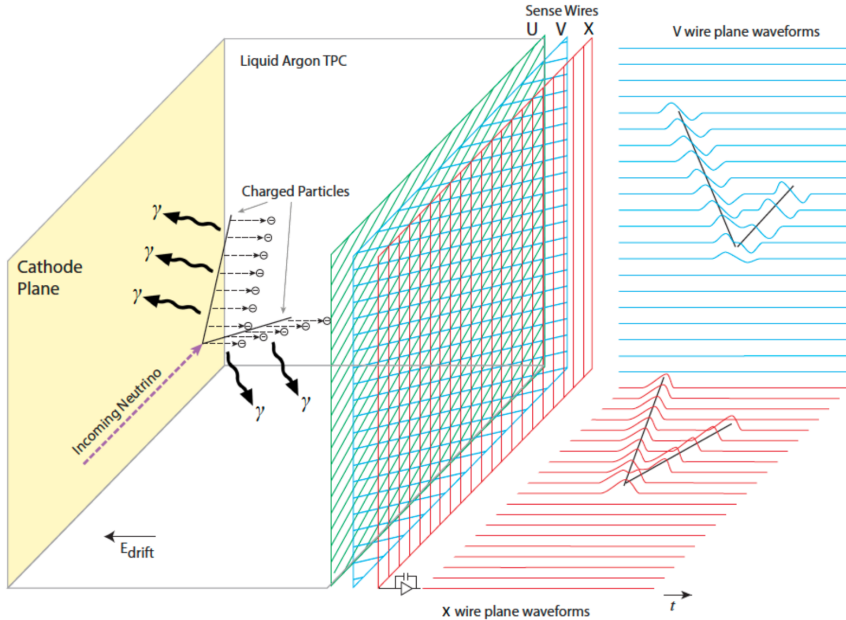


Figure 3.2: Schematic diagram showing the operating principle of a LArTPC with wire readout. Figure taken from Ref. [1].

For each event, with energies ranging from a few MeV to several GeV, these detectors collect both the scintillation light and the ionisation electrons created when the charged particles produced in neutrino-nucleus interactions ionise the argon nuclei. In both HD and VD designs the characteristic 128 nm scintillation light of argon is collected by a photon detection system (PDS). This light will indicate the time at which electrons start to drift, thus enabling reconstruction over the drift coordinate when compared to the time when the first ionisation electron arrives to the anode. Reconstruction of the topology in the transverse direction is achieved using the charge readout. Fig. 3.2 illustrates the detection principle described, for the case of a HD detector with a wire readout.

3.3.1 Horizontal Drift

Within the HD design the ionisation electrons produced as charged particles traverse the LAr drift horizontally towards the anode planes, made out of three layers of wire readout, due to the effect of an electric field. This design, previously known as single-phase (SP), was tested by the ProtoDUNE-SP detector at CERN. The prototype collected data from

3.3. Far Detector

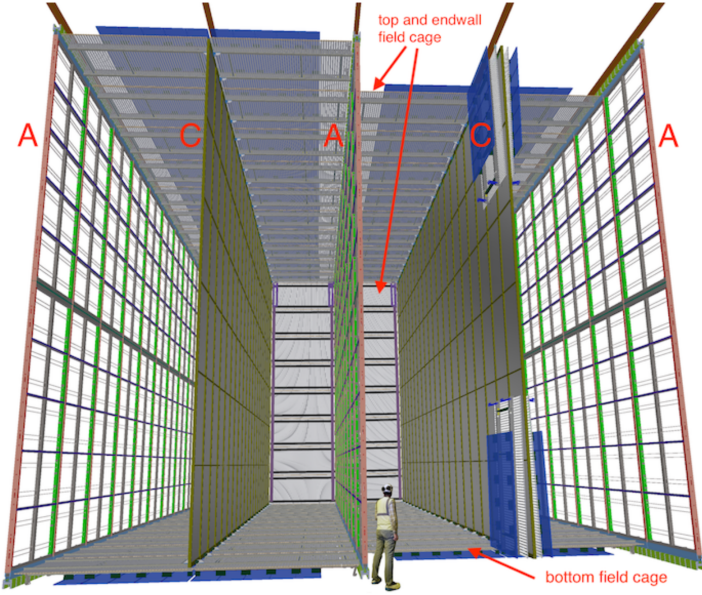


Figure 3.3: Proposed design for the FD-1 and FD-2 modules following the HD principle. Figure taken from Ref. [1].

747 a hadron beam and cosmic rays, providing high-quality data sets for calibration studies
 748 and proving the excellent performance of this design.

749 Each FD HD detector module is divided in four drift regions, with a maximum drift
 750 length of 3.5 m, by alternating anode and cathode walls. The surrounding field cage
 751 ensures the uniformity of the 500 V/cm horizontal electric field across the drift volumes.
 752 The three anode walls, which constitute the charge readout of the detector, are built by
 753 stacking anode plane assemblies (APAs), 2 high times 25 wide. The design of the HD
 754 modules is shown in Fig. 3.3.

755 Each APA is made of 2560 active wires arranged in three layers, plus an extra grid
 756 layer, wrapped around a metal frame. The two induction wire planes, U and V, sit at
 757 $\pm 35.7^\circ$ to the vertical on each side of the APA. The collection and shielding plane wires,
 758 X and G, run parallel to the vertical direction. The ionisation electrons drift past the
 759 induction planes, generating bipolar signals on those wires, and are collected by the
 760 collection plane, producing a monopolar positive signal. The spacing between the wires
 761 is ~ 5 mm, and it defines the spatial resolution of the APA.

762 The front-end readout electronics, or cold electronics as they are immerse in the LAr,

Chapter 3. The Deep Underground Neutrino Experiment

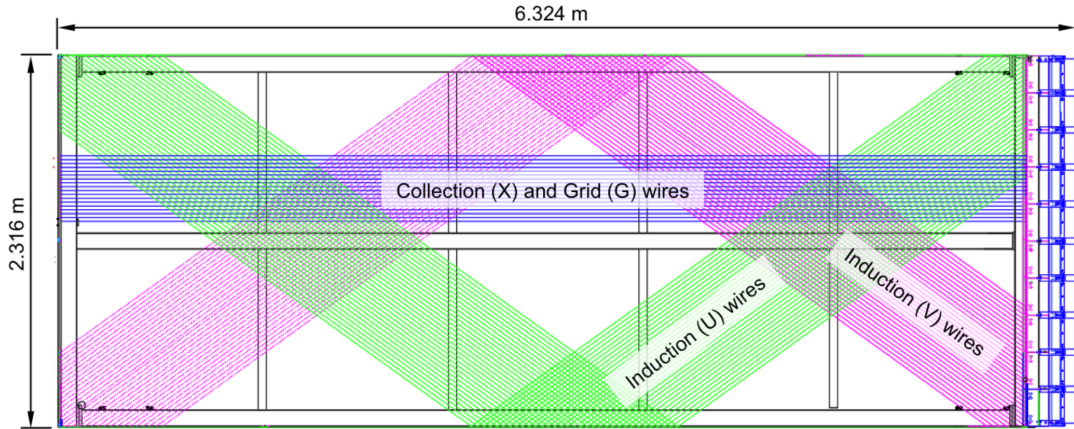


Figure 3.4: Schematic representation of an APA. The black lines represent the APA steel frame. The green and magenta lines correspond to the direction of the U and V induction wires respectively. The blue lines indicate the direction of the X collection wires and the wire shielding G. Figure taken from Ref. [1].

763 are attached to the top of the up APAs and the bottom of the down APAs. Mounted on
 764 the front-end mother boards we have a series of ASICs that digitize the signals from the
 765 collection and induction planes. Each wire signal goes to a charge-sensitive amplifier,
 766 then there is a pulse-shaping circuit and this is followed by the analogue-to-digital
 767 converter. This part of the process happens inside the LAr to minimise the number of
 768 cables penetrating the cryostat. The digitised signals come out finally via a series of
 769 high-speed serial links to the warm interface boards (WIBs), from where the data is sent
 770 to the back-end DAQ through optical fibers.

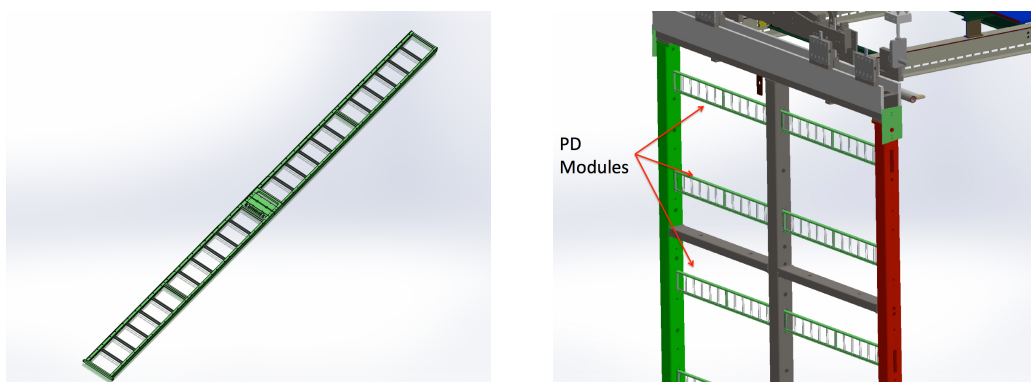


Figure 3.5: A PDS module containing 24 X-ARAPUCAs (left) and the location of the modules on the APAs (right). Figure taken from Ref. [1].

3.3. Far Detector

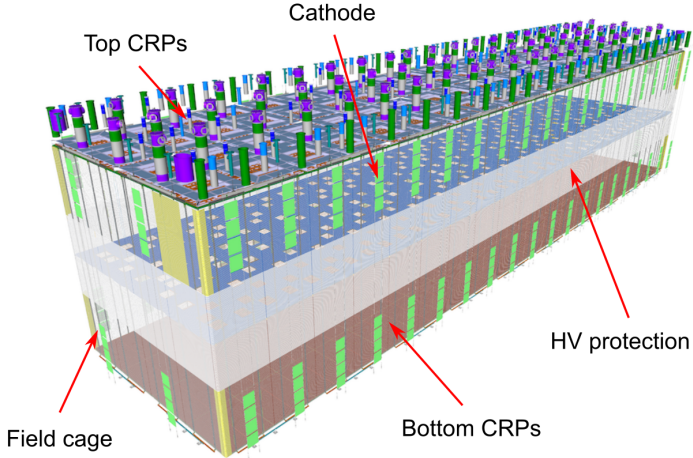


Figure 3.6: Proposed design for the FD-3 module following the VD principle. Figure adapted from Ref. [47].

771 The PDS uses modules of X-ARAPUCA devices, mounted on the APA frames
 772 between the wire planes. Each X-ARAPUCA consists of layers of dichroic filter and
 773 wavelength-shifter. They shift the VUV scintillation light into the visible spectrum,
 774 sending then the visible photons to silicon photomultiplier (SiPM) devices. The PDS
 775 modules are $209\text{ cm} \times 12\text{ cm} \times 2\text{ cm}$ bars, containing 24 X-ARAPUCAs. There are 10
 776 of these PDS modules per APA. Fig. 3.5 shows a PDS module (left) and the placement
 777 of the modules on the APAs (right).

778 **3.3.2 Vertical Drift**

779 In the VD case the ionisation electrons will drift vertically until they meet a printed
 780 circuit board-based (PCB) readout plane. It is based on the original dual-phase (DP)
 781 design deployed at CERN, known as ProtoDUNE-DP, used a vertical drift design with
 782 an additional amplification of the ionization electrons using a gaseous argon (GAr) layer
 783 above the liquid phase. The VD module incorporates the positive features of the DP
 784 design without the complications of having the LAr-GAr interface.

785 The current design of the FD VD module counts with two drift chambers with a
 786 maximum drift distance of 6.5 cm. A cathode plane splits the detector volume along the

Chapter 3. The Deep Underground Neutrino Experiment

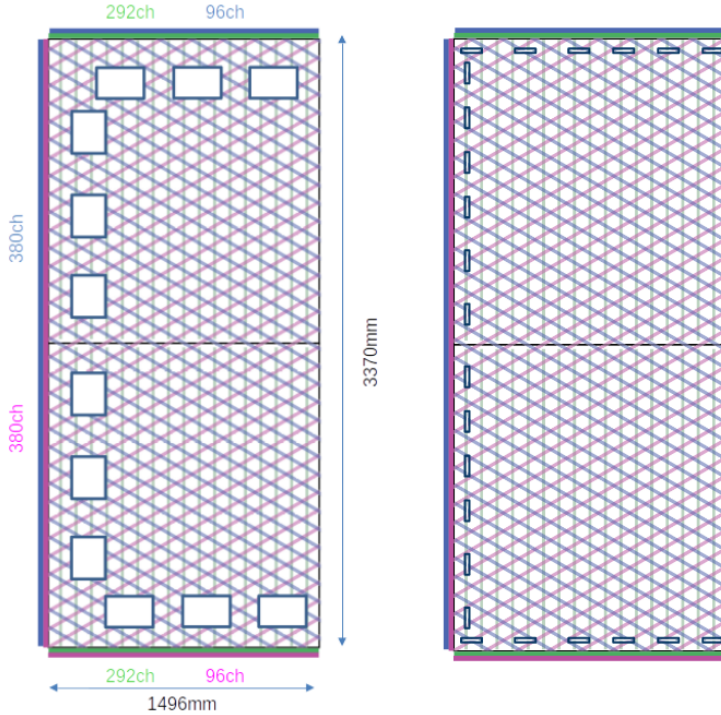


Figure 3.7: Schematic representation of the electrode strip configuration for a top (left) and bottom (right) CRU. Figure taken from Ref. [47].

drift direction while the two anode planes are connected to the bottom and top walls of the detector. The layout of the VD module is shown in Fig. 3.6. Compared with the HD design, the VD option offers a slightly larger instrumented volume and a more cost-effective solution for the charge readout.

As in the HD design, each drift volume features a 500 V/cm electric field and a field cage that ensures its uniformity. The anode planes are arrays of $3.4\text{ m} \times 3\text{ m}$ charge-readout planes (CRPs). These are formed by a pair of charge-readout units (CRUs), which are built from two double-sided perforated PCBs, with their perforations aligned. The perforations allow the drift electrons to pass between the layers.

The PCB face opposite to the cathode has a copper guard plane which acts as shielding, while its reverse face is etched with electrode strips forming the first induction plane. The outer PCB has electrode strips on both faces, the ones facing the inner PCB form the second induction plane while the outermost ones form the collection plane. Fig. 3.7 shows the layout of the electrode strips for the top (left) and bottom (right) CRUs.

3.3. Far Detector

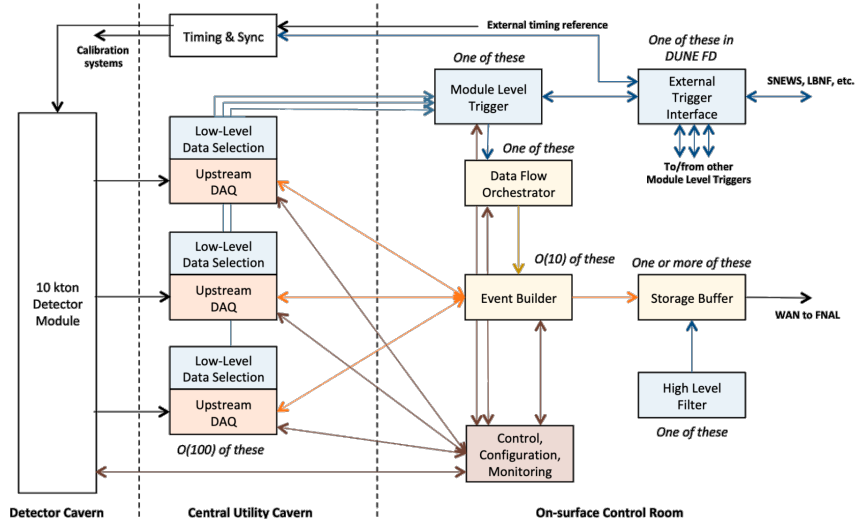


Figure 3.8: Detailed diagram of the DUNE FD DAQ system. Figure taken from Ref. [2].

801 The magenta and blue lines represent the first and second induction planes respectively,
802 and the green lines correspond to the collection plane.

803 The PDS in the VD module will use the same X-ARAPUCA technology developed
804 for the HD design. The plan is to place the PDS modules on the cryostat walls and on
805 the cathode, in order to maximise the photon yield.

806 3.3.3 FD Data Acquisition System

807 The task of the data acquisition (DAQ) system is to receive, process and store data from
808 the detector modules. In the case of DUNE the DAQ architecture is designed to work
809 for all FD modules interchangeably, except some aspects of the upstream part which
810 may depend on the specific module technology.

811 The enormous sample rate and the number of channels in TPC and PD readouts
812 will produce a very large volume of data. These pose really strong requirements and
813 challenges to the DUNE FD DAQ architecture. It will be required to read out data of
814 the order of ten thousand or more channels at rates of a few MHz. In order to cope
815 with the huge data volume, segmented readouts and compression algorithms are used to
816 reduce the data rate to manageable levels.

Chapter 3. The Deep Underground Neutrino Experiment

817 The DAQ system of the DUNE FD is composed of five different subsystems. The
818 first one is the upstream DAQ, which receives the raw data from the detector, buffers it
819 and perform some low-level pre-processing. The minimally processed data is then fed
820 into a hierarchical data selection system, which then performs a module level trigger
821 decision. In case of a positive decision a trigger command is produced and executed by
822 the data flow orchestrator, located in the back-end (BE) DAQ subsystem. Subsequently
823 the DAQ BE retrieves the relevant data from the buffers located in the upstream DAQ,
824 adds all the data into a cohesive record and saves it to permanent storage. Watching
825 over all the other subsystems we also have the control, configuration and monitoring
826 subsystem and the time and synchronization subsystem. Fig. 3.8 shows a schematic
827 diagram of the DAQ system, showing the different subsystems and their relations.

828 A notorious challenge for the DUNE DAQ system comes from its broad physics
829 goals. We must be prepared to process events spanning a wide range of time windows
830 (from 5 ms in the case of beam and cosmic neutrinos and nucleon decay to 100 s in the
831 case of SNBs) and therefore this requires a continuous readout of the detector modules.
832 Moreover, because of the off-beam measurements we need to ensure the capabilities
833 of online data processing and self-triggering. Having this into account, together with
834 the technical constraints, the DUNE FD DAQ faces a series of challenges: it needs to
835 be fault tolerant and redundant to reduce downtime, accommodate new components
836 while it keeps serving the operational modules, have large upstream buffers to handle
837 SNB physics, be able to support a wide range of readout windows and last reduce the
838 throughput of data to permanent storage to be at most 30 PB/year.

839 3.4 Near Detector

840 In order to estimate the oscillation parameters we measure the neutrino energy spectra
841 at the FD. This reconstructed energy arises from a convolution of the neutrino flux, cross
842 section, detector response and the oscillation probability. Using theoretical and empirical
843 models to account for the other effects, one can extract the oscillation probability using

3.4. Near Detector

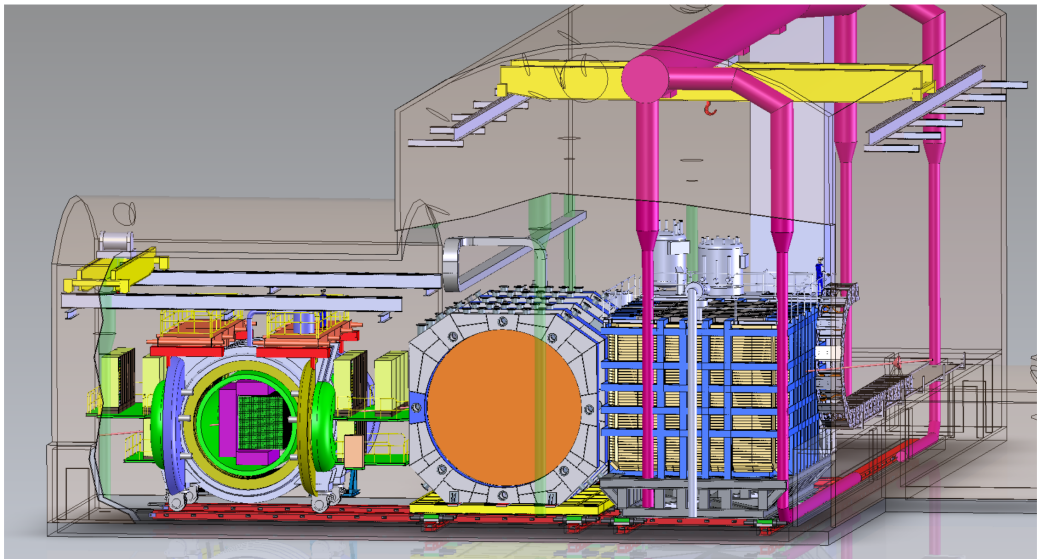


Figure 3.9: Representation of the ND hall in Phase II, showing the different subcomponents. From right to left, in the direction of the beam, we have ND-LAr, ND-GAr and SAND. Figure taken from Ref. [48].

844 the measurement. However, these models have associated a number of uncertainties that
845 are then propagated to the oscillation parameters.

846 One of the main roles of the ND is to measure the neutrino interaction rates before
847 the oscillation effects become relevant, i.e. close to the production point. By measuring
848 the ν_μ and ν_e energy spectra, and that of their corresponding antineutrinos, at the ND
849 we can constrain the model uncertainties. A complete cancellation of the uncertainties
850 when taking the ratio between the FD and ND measurements is not possible, as that
851 would require both detectors to have identical designs and the neutrino fluxes to be
852 the same. Because of the distance, the flux probed by the FD will have a different
853 energy and flavour composition than that at the ND, as neutrinos oscillate and the beam
854 spreads. The differences in the flux also determine the design of the detectors, therefore
855 the ND is limited in its capability to match the FD design.

856 Nevertheless, having a highly capable ND DUNE can minimise the systematic
857 uncertainties affecting the observed neutrino energy. The ND data can be used to
858 tune the model parameters by comparison with the prediction. Then, one uses the
859 tuned model to predict the unoscillated FD spectra. Comparing the prediction with the

Chapter 3. The Deep Underground Neutrino Experiment

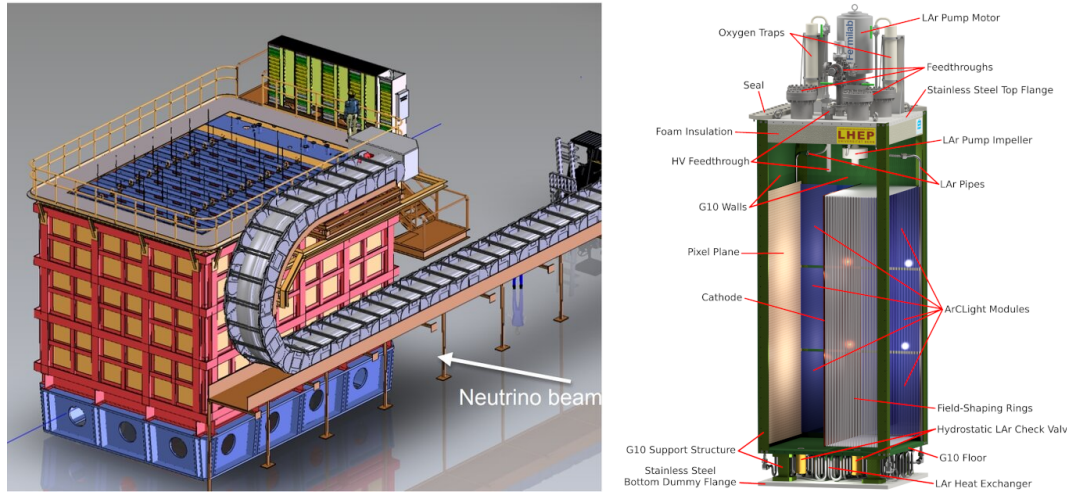


Figure 3.10: Schematic representation of the external components of ND-LAr, including the cryostat and the PRISM movable system (left) and detailed drawing of one ArgonCube module (right). Figure adapted from Ref. [1].

860 measured spectra it is possible to extract the oscillation parameters.

861 Additionally, the ND will have a physics program of its own. In particular, it will
 862 measure neutrino cross sections that will then be used to constrain the model used in
 863 the long-baseline oscillation analysis. It will also be used to search for BSM phenomena
 864 such as heavy neutral leptons, dark photons, millicharged particles, etc.

865 The DUNE ND can be divided in three main components, a LArTPC known as ND-
 866 LAr, a magnetised muon spectrometer, which will be the Temporary Muon Spectrometer
 867 (TMS) in Phase I and ND-GAr in Phase II, and the System for on-Axis Neutrino
 868 Detection (SAND). The layout of the Phase II DUNE ND can be seen in Fig. 3.9. The
 869 first two components of the ND will be able to move off-axis, in what is called the
 870 Precision Reaction-Independent Spectrum Measurement (PRISM) concept. More details
 871 on the purpose and design of the ND can be found in the DUNE ND Conceptual Design
 872 Report (CDR) [48].

873 3.4.1 ND-LAr

874 ND-LAr is a LArTPC, as the ND needs a LAr component in order to reduce cross
 875 section and detector systematic uncertainties in the oscillation analysis. However, its

3.4. Near Detector

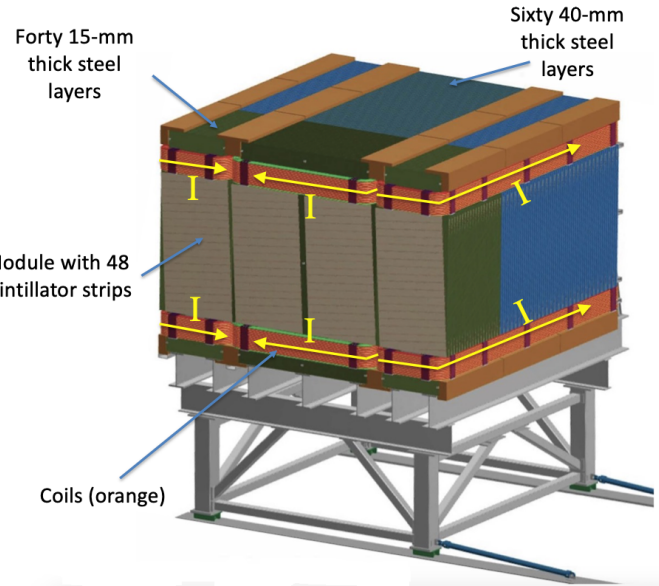


Figure 3.11: Schematic view of the TMS detector, highlighting its main parts. Figure adapted from Ref. [1].

876 design differs significantly from those proposed for the FD modules. Because of the
 877 high event rates at the ND, approximately 55 neutrino interaction events per $10 \mu\text{s}$ spill,
 878 ND-LAr will be built in a modular way. Each of the modules, based on the ArgonCube
 879 technology, is a fully instrumented, optically isolated TPC with a pixelated readout.
 880 The pixelisation allows for a fully 3D reconstruction and the optical isolation reduces
 881 the problems due to overlapping interactions. Fig. 3.10 shows a representation of the
 882 external parts of ND-LAr (left) and a detailed diagram of an ArgonCube module (right).

883 With a fiducial mass of 67 t and dimensions $7 \text{ m} (\text{w}) \times 3 \text{ m} (\text{h}) \times 5 \text{ m} (\text{l})$, ND-LAr
 884 will be able to provide high statistics and contain the hadronic systems from the beam
 885 neutrino interactions, but muons with a momentum higher than 0.7 GeV will exit the
 886 detector.

887 3.4.2 TMS/ND-GAr

888 In order to accurately estimate the neutrino energy, the momentum of the outgoing
 889 muons needs to be determined. That is the reason why a muon spectrometer is needed
 890 downstream of ND-LAr.

Chapter 3. The Deep Underground Neutrino Experiment

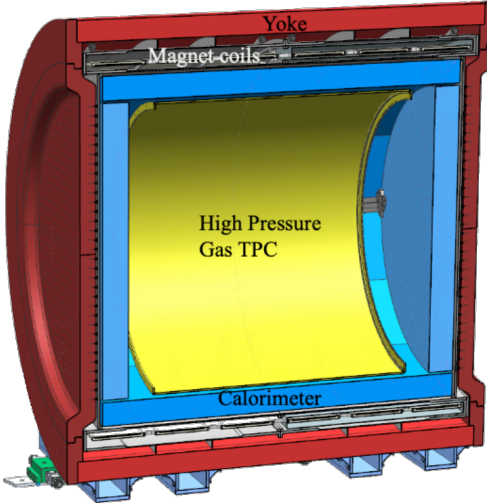


Figure 3.12: Cross section of the ND-GAr geometry, showing the HPgTPC, ECal and magnet. Figure adapted from Ref. [1].

891 In Phase I that role will be fulfilled by TMS. It is a magnetised sampling calorimeter,
892 with alternating steel and plastic scintillator layers. Fig. 3.11 shows a schematic view of
893 the TMS detector. The magnetic field allows a precise measurement of the sign of the
894 muon, so one can distinguish between neutrino and antineutrino interactions.

895 After the Phase II upgrade, TMS will be replaced with ND-GAr. This detector is
896 a magnetised, high-pressure GAr TPC (often denoted as HPgTPC) surrounded by an
897 electromagnetic calorimeter (ECal) and a muon tagger. A cross section of its geometry
898 can be seen in Fig. 3.12. ND-GAr will be able to measure the momenta of the outgoing
899 muons while also detect neutrino interactions inside the GAr volume. This allows
900 ND-GAr to constrain the systematic uncertainties even further, as it will be able to
901 accurately measure neutrino interactions at low energies thanks to the lower tracking
902 thresholds of GAr.

903 3.4.3 PRISM

904 In general, the observed peak neutrino energy of a neutrino beam decreases as the
905 observation angle with respect to the beam direction increases. This feature has been
906 used in other long-baseline neutrino experiments, like T2K (2.5° off-axis) and NOvA

3.4. Near Detector

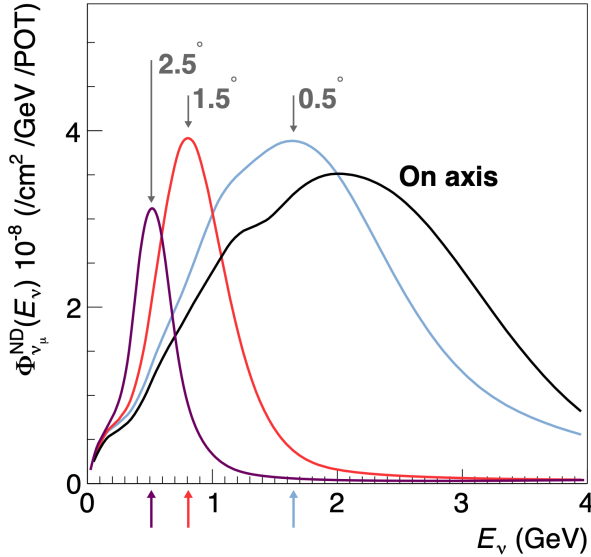


Figure 3.13: Predicted beam muon neutrino flux at the ND location for different off-axis positions. Figure taken from Ref. [48].

(0.8° off-axis), in order to achieve narrower energy distributions. The DUNE PRISM concept exploits this effect using a movable ND. Within PRISM both ND-LAr and the muon spectrometer (TMS in Phase I and ND-GAr in Phase II) can be moved up to 3.2° off-axis, equivalent to move the detectors 30.5 m laterally through the ND hall.

This allows to record additional data samples with different energy compositions. Fig. 3.13 compares the on-axis muon neutrino flux at the ND with the fluxes at different off-axis positions. As the off-axis position increases the neutrino flux becomes closer to a monoenergetic beam with a lower peak energy. These samples can be used to perform a data-driven determination of the relation between true and reconstructed neutrino energy, in order to reduce the dependence on the interaction model. The off-axis samples are linearly combined to produce a narrow Gaussian energy distribution centered on a target true energy. From the combination coefficients one can build a sample of reconstructed neutrino events that will determine the energy mapping.

The PRISM samples can also be used to form a flux at the ND location similar in shape to the oscillated flux measured by the FD. This method can be used to extract the oscillation parameters with minimal input from the neutrino interaction model.

Chapter 3. The Deep Underground Neutrino Experiment

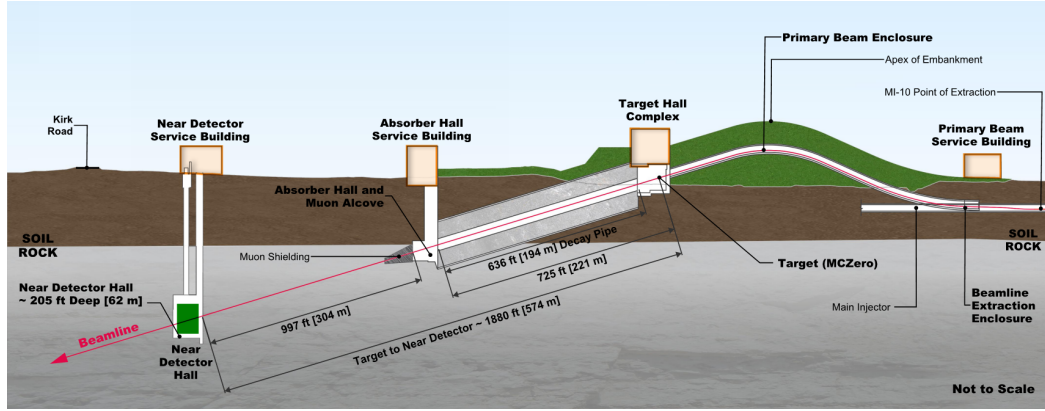


Figure 3.14: Schematic longitudinal section of the LBNF beamline at Fermilab (not to scale). Figure taken from Ref. [49].

923 3.4.4 SAND

924 The role of SAND is to monitor the beam stability by measuring the on-axis neutrino
 925 energy spectra. As the PRISM program requires that ND-LAr and its downstream
 926 muon spectrometer spend about half of the time in off-axis positions, it is not possible
 927 to monitor the stability with the movable detectors. Moreover, for the success of PRISM
 928 it is essential to have a stable beam configuration, or, at least, a quick assessment and
 929 modeling of the distortions.

930 The SAND detector is magnetised, and it counts with an inner low density tracker,
 931 a LAr target with optical readout and surrounding sampling calorimeter.

932 3.5 LBNF beamline

933 The Long-Baseline Neutrino Facility (LBNF) project is responsible for producing the
 934 neutrino beam for the DUNE detectors. A detailed discussion of the LBNF program
 935 can be found in the DUNE/LBNF CDR Volume III [49].

936 The LBNF beamline will provide a high-intensity neutrino beam within the adequate
 937 energy range in order to meet the long-baseline oscillation physics goals of DUNE. A
 938 schematic diagram of the longitudinal section of the LBNF beamline is shown in Fig.
 939 3.14. First, a beam of $60 - 120$ GeV protons is extracted from the Fermilab Main

3.5. LBNF beamline

940 Injector. This beam is aimed towards the target area, where it collides with a cylindrical
 941 graphite target to produce pions and kaons.

942 The diffuse, secondary beam of particles is focused by a pair of magnetic horns.
 943 These select the positively charged particles when operated in Forward Horn Current
 944 (FHC) mode, or the negatively charged ones when the current is reversed, also known as
 945 Reverse Horn Current (RHC) mode. The focused secondary beam then enters a 194 m
 946 decay pipe where the pions and kaons will predominantly produce $\mu^+\nu_\mu$ pairs when in
 947 FHC mode (or $\mu^-\bar{\nu}_\mu$ in RHC mode).

948 At the end of the decay pipe a hadron absorber removes the undecayed hadrons and
 949 muons from the beam, which reduces the ν_e ($\bar{\nu}_e$) and $\bar{\nu}_\mu$ (ν_μ) contamination coming
 950 from the μ^+ (μ^-) decays. The resulting neutrino flux at the FD is shown in Fig. 3.15,
 951 both for FHC (left) and RHC (right) modes. These predictions show the intrinsic $(\bar{\nu}_e)$
 952 contamination and wrong sign component from wrong sign and neutral meson decays,
 953 as well as muons decaying before reaching the absorber.

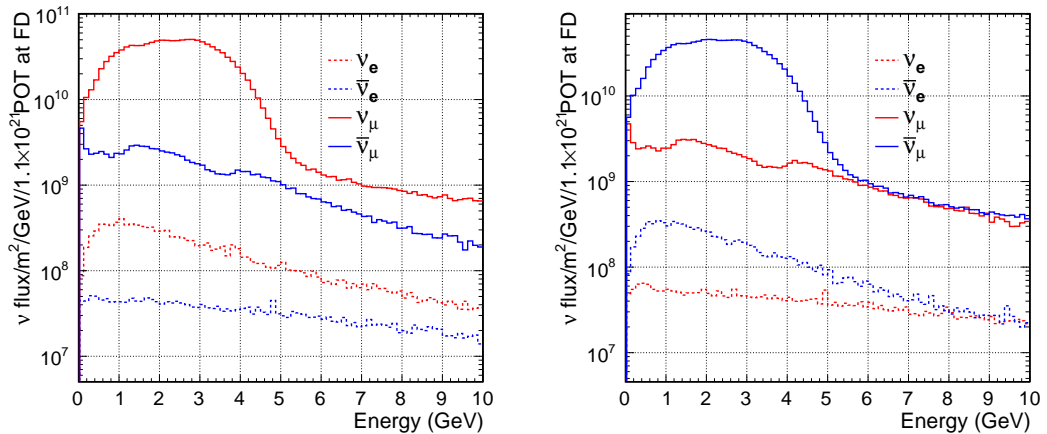


Figure 3.15: Predicted neutrino fluxes at the FD in FHC mode (left panel) and RHC mode (right panel). Figures taken from Ref. [42].

954 **Chapter 4**

955 **ND-GAr**

956 ND-GAr is a magnetised, high-pressure gaseous argon TPC (HPgTPC), surrounded by
957 an electromagnetic calorimeter (ECal) and a muon detector (commonly refer to as μ ID).
958 A detailed discussion on the requirements, design, performance and physics of ND-GAr
959 can be found in the DUNE ND CDR [48] and the ND-GAr whitepaper (cite).

960 In DUNE Phase II ND-GAr will fulfill the role of TMS, measuring the momentum
961 and sign of the charged particles exiting ND-LAr. Additionally, it will be able to measure
962 neutrino interactions inside the HPgTPC, achieving lower energy thresholds than those
963 of the ND and FD LArTPCs. By doing so ND-GAr will allow to constrain the relevant
964 systematic uncertainties for the LBL analysis even further.

965 The goal of the present chapter is to review the requirements that the physics program
966 of DUNE impose on ND-GAr, present the current status of its design and describe the
967 GArSoft package, its simulation and reconstruction software.

968 **4.1 Requirements**

969 The primary requirement for ND-GAr is to the measure the momentum and charge of
970 muons from ν_μ and $\bar{\nu}_\mu$ CC interactions in ND-LAr, in order to measure their energy
971 spectrum. To achieve the sensitivity to the neutrino oscillation parameters described
972 in the DUNE FD TDR Volume II [42] ND-GAr should be able to constrain the muon

Chapter 4. ND-GAr

973 energy within a 1% uncertainty or better. The main constraint will come from the
974 calibration of the magnetic field, performed using neutral kaon decays in the HPgTPC.

975 Another requirement for ND-GAr is the precise measurement of neutrino interactions
976 on argon for the energies relevant to the neutrino oscillation program. The goal is to
977 constrain the cross section systematic uncertainties in the regions of phase space that
978 are not accessible to ND-LAr. This requires the kinematic acceptance for muons in
979 ND-GAr to exceed that of ND-LAr, being comparable to the one observed in the FD.

980 ND-GAr should also be able to the relationship between true and reconstructed energy
981 from neutrino interactions on argon with low thresholds, being sensitive to particles that
982 are not observed or may be misidentified in ND-LAr. In particular, ND-GAr needs to
983 have low tracking thresholds in order to measure the spectrum of pions and protons
984 produced in final-state interactions (FSI). It also must be able to accurately measure
985 the pion multiplicity in 1, 2 and 3 pions final states, to inform the pion mass correction
986 in the LArTPCs.

987 4.2 Reference design

988 The final design of ND-GAr is still under preparation. However, a preliminary baseline
989 design was in place at the time of the ND CDR. This section summarises the main
990 features of that design, as it is also the one used for the default geometry in our simulation.
991 A DUNE Phase II whitepaper, discussing the different options under consideration for
992 the ND-GAr design, is in progress.

993 4.2.1 HPgTPC

994 The reference design for the ND-GAr HPgTPC follow closely that of the ALICE TPC.
995 It is a cylinder with a central high-voltage cathode, generating the electric field for
996 the two drift volumes, with a maximum drift distance of 2.5 m each. The anodes will
997 be instrumented with charge readout chambers. The original design repurposed the
998 multi-wire proportional readout chambers of ALICE, however the current R&D efforts

4.2. Reference design

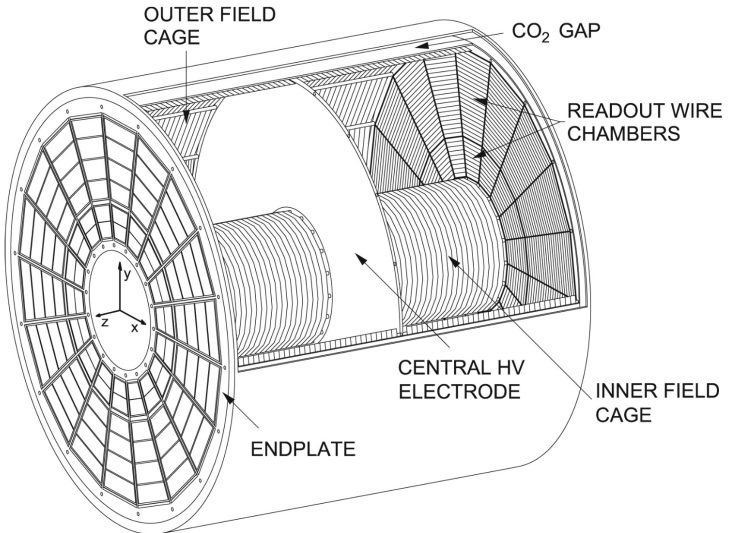


Figure 4.1: Diagram of the ALICE TPC, showing the two drift chambers, inner and outer field cages and readout chambers. Figure taken from Ref. [1].

999 focus on a gas electron multiplier option instead. Fig. 4.1 shows a schematic diagram of
 1000 the ALICE TPC design. The basic ND-GAr geometry will resemble this, except for the
 1001 inner field cage.

1002 It will use a 90-10 molar fraction argon-CH₄ mixture at 10 bar. With this baseline
 1003 gas mixture light collection is not possible, as the quenching gas absorbs most of the
 1004 VUV photons. Additional R&D efforts are underway, to understand if different mixtures
 1005 allow for the light signal to be used to provide a t_0 while maintaining stable charge gain.

1006 4.2.2 ECal

1007 The main role of the ND-GAr ECal is the calorimetric measurement of the electron
 1008 energies and the reconstruction of photons, in particular those from neutral pion decays.
 1009 Also, the ECal is able to provide a t_0 timestamp for neutrino interactions, by associating
 1010 its activity to the tracks in the HPgTPC. The ECal will also be able to perform
 1011 neutron reconstruction using time of flight and reject external backgrounds, thanks to
 1012 its sub-nanosecond time resolution.

1013 The ECal design features three independent subdetectors, two end caps at each side
 1014 and a barrel surrounding the HPgTPC. Each of the detectors is divided in modules,

Chapter 4. ND-GAr

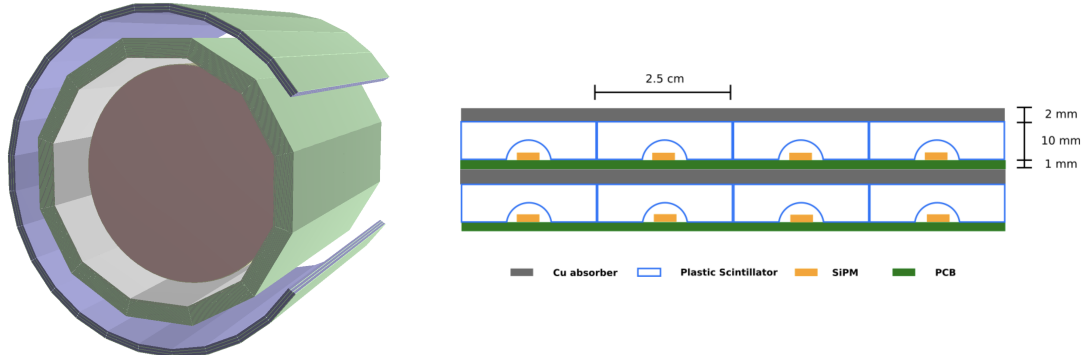


Figure 4.2: View of the 12-sided ECal barrel and outer muon tagger geometries (left) and layout of the ECal tile layers for the 2 mm Cu, 10 mm scintillator option (right). Figure adapted from Ref. [1].

which combine alternating layers of plastic scintillator and absorber material readout by SiPMs. The inner scintillator layers consist of $2.5 \times 2.5 \text{ cm}^2$ high-granularity tiles, whereas the outer ones are made out of 4 cm wide cross-strips spanning the whole module length. The current barrel geometry consists of 8 tile layers and 34 strip layers, while the end caps feature 6 and 36 respectively. The thickness of the scintillator layers is 7 mm and 5 mm for the Pb absorber layers. The 12-sided geometry of the ECal barrel (left) and the layout of the tile layers (left)¹ can be seen in Fig. 4.2.

4.2.3 Magnet

The ND-GAr magnet design, known as the Solenoid with Partial Yoke (SPY), consists of two coupled solenoids with an iron return yoke. The idea behind the design is to have a solenoid as thin as possible, as well as a return yoke mass distribution that minimises the material budget between ND-LAr and ND-GAr. The magnet needs to provide a 0.5 T field in the direction perpendicular to the beam, parallel to the drift electric field. It needs to host the pressure vessel and the surrounding ECal, which points to an inner diameter of $\sim 6.4 \text{ m}$.

The solenoid is a single layer coil, based on niobium titanium superconducting

¹The figure shows the layout of the tile layers for a previous design with 2 mm Cu absorber and 10 mm plastic scintillator, as mentioned in the text the current choice is 5 mm Pb absorber and 7 mm scintillator.

4.3. GArSoft

1031 Rutherford cable. The total length of the coil is 7.5 m. The bobbin will be split in four
1032 segments grouped in pairs with two identical cryostats, connected in series. The iron
1033 yoke features an aperture in the upstream side to allow the muons coming from ND-LAr.
1034 Still, its material will be enough to reduce the magnetic field reaching SAND, and also
1035 stop the charged pions produced inside the HPgTPC.

1036 4.2.4 Muon system

1037 The design of the ND-GAr muon system is still in a preliminary stage. Its role is to
1038 distinguish between muons and pions punching through the ECal. This is especially
1039 important for wrong-sign determination, to separate these from neutral current events.

1040 In its current form, the muon system consists of three layers of longitudinal sampling
1041 structures. It alternates 10 cm Fe absorber slabs with 2 cm plastic scintillator strips.
1042 The transverse granularity required is still under study.

1043 4.3 GArSoft

1044 GArSoft is a software package developed for the simulation and reconstruction of events
1045 in ND-GAr. It is inspired by the LArSoft toolkit used for the simulation of LArTPC
1046 experiments, like the DUNE FD modules. It is based on `art`, the framework for event
1047 processing in particle physics experiments [?]. Other of its main dependencies are `ROOT`,
1048 `NuTools`, `GENIE` and `Geant4`. It allows the user to run all the steps of a generation-
1049 simulation-reconstruction workflow using FHiCL configuration files.

1050 4.3.1 Event generation

1051 The standard generator FHiCLs in GArSoft run the event generation and particle
1052 propagation simulation (i.e. Geant4) in the same job by default. However, it is possible
1053 to split them up if needed. The current version of GArSoft provides five different event
1054 generators, each of them producing `simb::MCTruth` products defined in `NuTools`. The
1055 available modules are:

Chapter 4. ND-GAr

- 1056 • **SingleGen**: particle gun generator. It produces the specified particles with a given
1057 distribution of momenta, initial positions and angles.
 - 1058 • **TextGen**: text file generator. The input file must follow the `hepevt` format², the
1059 module simply copies this to `simb::MCTruth` data products.
 - 1060 • **GENIEGen**: GENIE neutrino event generator. The module runs the neutrino-nucleus
1061 interaction generator using the options specified in the driver FHiCL file (flux file,
1062 flavour composition, number of interactions per event, t_0 distribution, ...). Current
1063 default version is `v3_04_00`.
 - 1064 • **RadioGen**: radiological generator. It produces a set list of particles to model
1065 radiological decays. Not tested.
 - 1066 • **CRYGen**: cosmic ray generator. The module runs the CRY event generator with a
1067 configuration specified in the FHiCL file (latitude and altitude of detector, energy
1068 threshold, ...). Not tested.
- 1069 The module `GArG4` searches for all the generated `simb::MCTruth` data products, using
1070 them as inputs to the Geant4 simulation with the specified detector geometry. A constant
1071 0.5 T magnetic field along the drift coordinate is assumed. The main outputs of this step
1072 are `simb::MCParticle` objects for the generated Geant4 particles, `gar::EnergyDeposit`
1073 data products for the energy deposits in the HPgTPC and `gar::CaloDeposit` data
1074 products for the energy deposits in the ECal and muon system.

1075 4.3.2 Detector simulation

- 1076 The standard detector simulation step in GArSoft is all run with a single FHiCL, but
1077 the different modules can be run independently as well. First the `IonizationReadout`

²In brief, each event contains at least two lines. The first line contains two entries, the event number and the number of particles in the event. Each following line contains 15 entries to describe each particle. The entries are: status code, pdg code for the particle, entry of the first mother for this particle, entry of the second mother for this particle, entry of the first daughter for this particle, entry of the second daughter for this particle, x component of the particle momentum, y component of the particle momentum, z component of the particle momentum, energy of the particle, mass of the particle, x component of the particle initial position, y component of the particle initial position, z component of the particle initial position and time of the particle production.

4.3. GArSoft

1078 module simulates the charge readout of the HPgTPC, and later the `SiPMReadout` module
1079 runs twice, once for the ECal and then for the muon system, with different configurations.

1080 The `IonizationAndScintillation` module collects all the `gar::EnergyDeposit`
1081 data products, to compute the equivalent number of ionization electrons for each energy
1082 deposit. The `ElectronDriftAlg` module simulates the electron diffusion numerically
1083 both in the longitudinal and transverse directions and applies an electron lifetime
1084 correction factor. The induced charge on the nearest and neighbouring readout pads
1085 is modeled using the provided pad response functions. The digitisation of the data is
1086 then simulated with the `TPCReadoutSimAlg` module. By default, the ADC sampling
1087 rate used is 50.505 MHz. The resulting raw waveforms for each channel are stored with
1088 zero-suppression, in order to save memory and CPU time. The algorithms keep blocks
1089 of ADC values above a certain threshold, plus some adjustable additional early and late
1090 tick counts. The results of these three steps are `gar::raw::RawDigit` data products.

1091 For the ECal and the muon system the `SiPMReadout` module calls either the
1092 `ECALReadoutSimStandardAlg` or `MuIDReadoutSimStandardAlg` modules. These take
1093 all the `gar::CaloDeposit` data products in the corresponding detector and do the
1094 digitisation depending on whether the hit was in a tile or strip layer. They include single
1095 photon statistics, electronic noise, SiPM saturation and time smearing. The resulting
1096 objects are `gar::raw::CaloRawDigit` data products.

1097 4.3.3 Reconstruction

1098 The reconstruction in GArSoft is also run as a single job by default. It first runs the hit
1099 finding, clustering, track fitting and vertex identification in the HPgTPC, followed by
1100 the hit finding and clustering in the ECal and muon system. After those it produces the
1101 associations between the associations between the tracks and the ECal clusters.

1102 Focusing first on the HPgTPC reconstruction, the `CompressedHitFinder` module
1103 takes the zero-suppressed ADCs from the `gar::raw::RawDigit` data products. The
1104 reconstructed hits largely correspond to the above threshold blocks, however the hit
1105 finder identifies waveforms with more than one maximum, diving them in multiple hits

Chapter 4. ND-GAr

1106 if they dip below a certain threshold. The data products produced are of the form
1107 `gar::rec::Hit`. These are the inputs to the clustering of hits in the `TPCHitCluster`
1108 module. Hits close in space and time are merged, and the resulting centroids are found.
1109 This module outputs `gar::rec::TPCClusters` objects and associations to the input
1110 hits.

1111 The following step prior to the track fitting is pattern recognition. The module
1112 called `tpcvecchitfinder2` uses the `gar::rec::TPCClusters` data products to find track
1113 segments, typically called vector hits. They are identified by performing linear 2D fits
1114 to the positions of the clusters in a 10 cm radius, one fit for each coordinate pair. A
1115 3D fit defines the line segment of the vector hit, using as independent variable the one
1116 whose sum of (absolute value) slopes in the 2D fits is the smallest. The clusters are
1117 merged to a given vector hit if they are less than 2 cm away from the line segment. The
1118 outputs are `gar::rec::VecHit` data products, as well as associations to the clusters. The
1119 `tpcpatrec2` module takes the `gar::rec::VecHit` objects to form the track candidates.
1120 The vector hits are merged together if their direction matches, their centers are within
1121 60 cm and their direction vectors point roughly to their respective centers. Once
1122 the clusters of vector hits are formed they are used to make a first estimation of the
1123 track parameters, simply taking three clusters along the track. The module produces
1124 `gar::rec::Track` data products and associations between these tracks and the clusters
1125 and vector hits.

1126 The track is fitted by means of a Kalman filter in the `tpctrackfit2` module, using
1127 the position along the drift direction as the independent variable. Two different fits are
1128 performed per track, a forward and a backwards fit, each starting from one of the track
1129 ends. The Kalman filter state vector ($y, z, R, \phi, \tan\lambda$) is estimated at each point along
1130 the track using a Bayesian update. The track parameters reported in the forward and
1131 backwards fits are the ones computed at the opposite end where the fit started. The
1132 main outputs of the track fit are the `gar::rec::Track` objects. Additionally, the module
1133 stores the fitted 3D positions along the track in the `gar::rec::TrackTrajectory` data
1134 products and the total charge and step sizes for each point also get stored in the form of

4.3. GArSoft

1135 `gar::rec::TrackIonization` objects.

1136 After the tracking step, the `vertexfinder1` module looks at the reconstructed
1137 `gar::rec::Track` products, creating vertex candidates with the track ends that are
1138 within 12 cm of each other. The vertices are then fitted using linear extrapolations from
1139 the different track ends associated. The results are `gar::rec::Vertex` data products,
1140 and associations to the tracks and corresponding track ends.

1141 For the ECal and muon tagger, the `SiPMHitFinder` module runs twice with different
1142 configurations, adapted to the particular capabilities of both. The module simply takes
1143 the `gar::raw::CaloRawDigit` products, applies a calibration factor to convert the ADC
1144 counts to MeV and for the strip layer hits it calculates the position along the strip using
1145 the times recorded of both SiPMs. This module produces `gar::rec::CaloHit` data
1146 products. Next, these objects are used as inputs to the `CaloClustering` module. It
1147 merges the hits based on a simple nearest neighbours (NN) algorithm. For the resulting
1148 clusters it also computes the total energy and position of the centroid. The results are
1149 stored as `gar::rec::Cluster` data products, with associations to the hits.

1150 The last step in the reconstruction is associating the reconstructed tracks in the
1151 HPgTPC to the clusters formed in the ECal and muon system. The `TPCECALAssociation`
1152 module checks first the position of the track end points, considering only the points
1153 that are at least 215 cm away from the cathode or have a radial distance to the center
1154 greater than 230 cm. The candidates are propagated up to the radial position, in the
1155 case of clusters in the barrel, or the drift coordinate position, for the end cap cluster, of
1156 the different clusters in the collection using the track parameters computed at the end
1157 point. The end point is associated to the cluster if certain proximity criteria are met.
1158 This module creates associations between the tracks, the end points and the clusters.
1159 The criteria for the associations are slightly different for the ECal and the muon tagger.

₁₁₆₀ Chapter 5

₁₁₆₁ FWTPG offline software

1162 Chapter 6

1163 Matched Filter approach to
1164 induction wire Trigger Primitives

1165 6.1 Motivation

1166 The filter implemented in the firmware of the upstream DUNE FD DAQ is a 32nd-order
1167 low-pass finite impulse-response (FIR) filter. The output of such filter for a discrete
1168 system can be written as:

$$y[i] = \sum_{j=0}^N h[j]x[i-j], \quad (6.1)$$

1169 where N is the order of the filter, y is the output sequence, x is the input sequence and h
1170 is the set of coefficients of the filter. The current implementation within `dtp-firmware`
1171 [50] uses a set of 16 non-zero integer coefficients.

1172 Filtering is a vital step in the hit finder chain. It helps to suppress the noise and
1173 enhance the signal peaks with respect to the noiseless baseline. A good filtering strategy
1174 allows us to use lower thresholds when forming the trigger primitives (TPs) and thus
1175 increasing the sensitivity of our detector to low energy physics events. In such events,
1176 the hits produced by the ionisation electrons tend to have lower amplitudes than those
1177 of interest to the baseline physics programme of the DUNE experiment.

1178 This is particularly important for the induction planes. In general, signal peaks in

Chapter 6. Matched Filter approach to induction wire Trigger Primitives

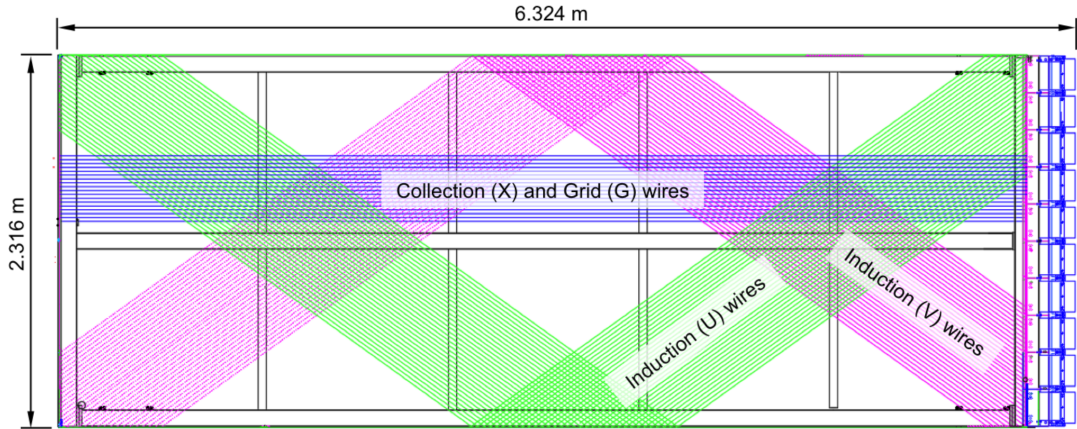


Figure 6.1: Schematic representation of an APA. The black lines represent the APA steel frame. The green and magenta lines correspond to the direction of the U and V induction wires respectively. The blue lines indicate the direction of the X collection wires and the wire shielding G.

the induction wires have smaller amplitude than the ones in the induction plane. This, together with the fact that the pulse shapes are bipolar, reduces our capacity to detect the hits on these channels. The inefficiency of detecting TPs in the induction planes (denoted as U and V planes) lead trigger algorithms to focus mainly on the TPs from the collection plane (so-called X plane). As a result, the possibility of making trigger decisions based on the coincidence of TPs across the three wire planes remains nowadays unexploited in DUNE. Fig. 6.1 shows a schematic view of an anode plane assembly (APA), with the different wire plane orientations highlighted.

A possible improvement of the current hit finder chain could require optimising the existing or choosing a new filter implementation. A filter strategy which improves the induction signals may be able to enhance the detection efficiency of TPs from the induction planes and ideally make it comparable to that of the collection plane.

The goal is to implement a better finite-impulse response filter design and to evaluate its performance relative to the current filter. To do so, we need to take into account the limitations of the firmware: the FIR filter shall have maximum 32 coefficients (so-called taps) whose values are 12-bit unsigned integers. Although it is technically possible to include non-integer coefficients, it would be a technical challenge as we have 40 FIR

6.2. Signal-to-noise ratio definition

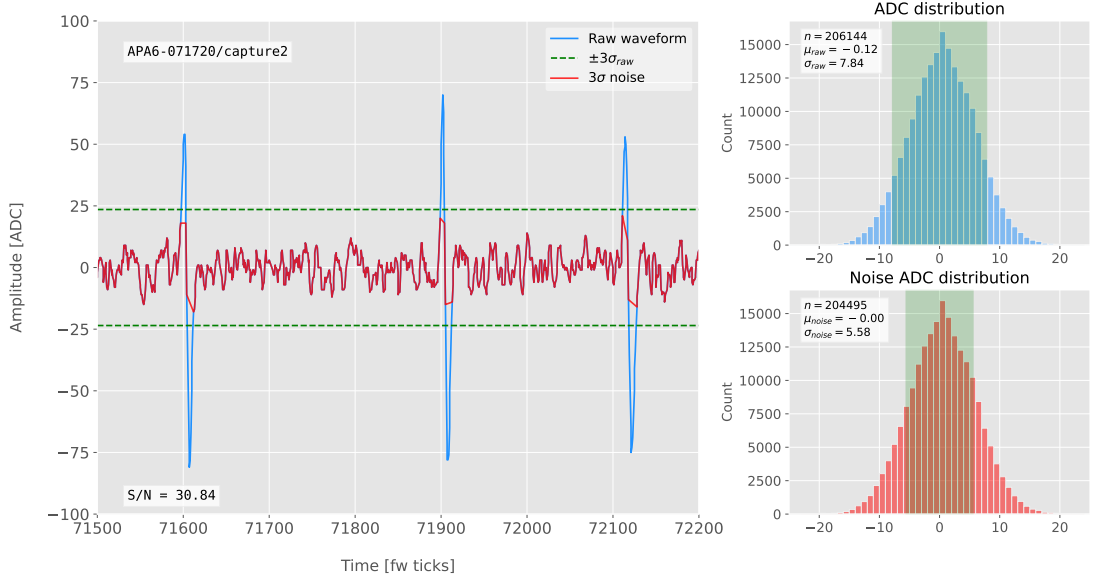


Figure 6.2: Left panel: Zoomed unfiltered waveform corresponding to channel 7840 from the ProtoDUNE-SP raw data capture `felix-2020-07-17-21:31:44` (blue line). The green dashed lines mark the region $\pm 3\sigma_{\text{raw}}$. The resulting noise waveform is also shown (red line). Top right panel: ADC distribution for channel 7840, where the green shaded region represents $\pm \sigma_{\text{raw}}$. Bottom right panel: noise ADC distribution for channel 7840, where the green shaded region represents $\pm \sigma_{\text{noise}}$.

1196 instances per APA, as there are 4 FIR per optical link and 10 optical links per APA.
 1197 With these restrictions, the task is to provide a set of 32 coefficients which yield an
 1198 optimal filter performance for the induction wires.

1199 6.2 Signal-to-noise ratio definition

1200 I introduce the signal to noise ratio (S/N) as a measure of the FIR filter performance
 1201 and demonstrate how to extract its value for a set of ProtoDUNE-SP data. The S/N
 1202 metrics allow us to compare different filter implementations and serve as a basis for more
 1203 detailed studies presented later in this document. Specifically, I use the ADC capture
 1204 `felix-2020-07-17-21:31:44` (data capture taken for firmware validation purposes). I
 1205 defined S/N as the height of the signal peaks relative to the size of the noise peaks.
 1206 To quantify this quantity channel by channel one first need to estimate the standard
 1207 deviation of the ADC data for each channel, σ_{ADC} . Then, I define the corresponding

Chapter 6. Matched Filter approach to induction wire Trigger Primitives

noise waveform to be the ADC values in the range $\pm 3\sigma_{ADC}$. From this new noise data one can estimate again the mean and standard deviation, μ_{noise} and σ_{noise} , so I can write the S/N for any given channel as:

$$S/N = \frac{\max [ADC] - \mu_{noise}}{\sigma_{noise}}, \quad (6.2)$$

where $\max [ADC]$ is simply the maximum ADC value found in the corresponding channel.

One can apply this definition of the S/N with a waveform from one of the channels of the data capture¹. Fig. 6.2 shows a zoomed region of the waveform corresponding to channel 7840 (blue line), where one can clearly see three signal peaks and continuous additive noise (we actually see 6 peaks, 3 positive and 3 negative, but, because by design for induction channels the expected signal pulse shapes are bipolar, I treat them as a collection of 3 individual signal peaks). I estimated the standard deviation of this raw waveform to be $\sigma_{raw} = 7.84$ ADC, so I am able to define the noise waveform (red line) as the ADC values in the range ± 23.52 ADC. This way one obtains $\mu_{noise} = 0$ and $\sigma_{noise} = 5.58$ ADC, which gives $S/N = 30.84$.

We can repeat this calculation now for the corresponding filtered waveform (using the current firmware FIR filter). In Fig. 6.3 I plotted the same time window for the filtered waveform from channel 7840 (blue line). In this case, the standard deviation of the waveform is larger than before, giving $\sigma_{raw} = 10.99$ ADC. The resulting noise waveform (red line) results from selection the ADC values in the range ± 32.91 ADC, giving now $\mu_{noise} = -0.47$ ADC and $\sigma_{noise} = 7.03$ ADC. Finally, one obtains $S/N = 24.68$. Notice that the value of S/N decreases after the filtering. Clearly, one can see that the noise baseline has increased by a factor of 1.35 when we applied the FIR filter and at the same time the amplitude of the signal peaks has remained almost unchanged, leading to this poorer S/N value.

¹All the original work was done within the `dtp-simulation` package [51], which offers a variety of tools to read raw data and emulate the TPG block (pedestal subtraction, filtering and hit finder). However, the results shown in this report were re-worked later using the C++ based `dtpemulator` package [52]. Its main purpose is the emulation of the TPG block and, in the same way as its predecessor, it has been cross-checked against the current firmware implementation.

6.3. Low-pass FIR filter design

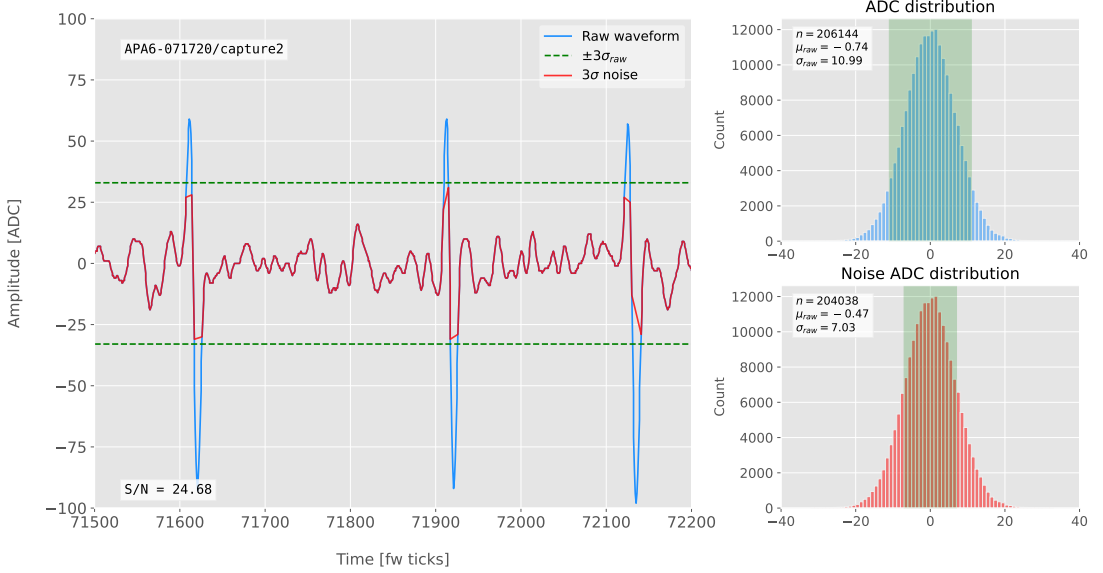


Figure 6.3: Left panel: Zoomed filtered waveform corresponding to channel 7840 from the ProtoDUNE-SP raw data capture `felix-2020-07-17-21:31:44` (blue line). The filter used was the current implementation of the low-pass FIR filter in `dtp-firmware`. The green dashed lines mark the region $\pm 3\sigma_{\text{raw}}$. The resulting noise waveform is also shown (red line). Top right panel: ADC distribution for channel 7840 after filtering, where the green shaded region represents $\pm \sigma_{\text{raw}}$. Bottom right panel: noise ADC distribution for channel 7840 after filtering, where the green shaded region represents $\pm \sigma_{\text{noise}}$

1231 6.3 Low-pass FIR filter design

1232 In general, when one uses a method to optimize the frequency response of a digital filter,
 1233 such as the Parks-McClellan algorithm, one finds a set of N real coefficients that give
 1234 the best response for the specified pass-band and order of the filter [53].

1235 In our case, as the sampling frequency is defined as 1 ticks^{-1} , the Nyquist frequency
 1236 will simply be $1/2 \text{ ticks}^{-1}$. The current implementation of the filter seems to have as
 1237 pass-band the range $[0, 0.1] \text{ ticks}^{-1}$. This can be seen in Fig. 6.4, where I show the
 1238 power spectrum, in decibels, of such filter implementation (blue solid line). For instance,
 1239 the Park-McClellan algorithm finds the optimal Chebyshev FIR filter taking as input
 1240 the boundaries of the target pass-band and stop-band, which can be written in the form:

$$\left\{ \begin{array}{l} [0, f_c] \\ [f_c + \delta f, f_N] \end{array} \right. , \quad (6.3)$$

Chapter 6. Matched Filter approach to induction wire Trigger Primitives

where f_c is the cut-off frequency, δf is the transition width and f_N is the aforementioned Nyquist frequency. A similar behaviour to the one in the current filter can be obtained by setting $f_c = 0$ and $\delta f = 0.1 \text{ ticks}^{-1}$. The response of the resulting filter is also shown in Fig. 6.4 (blue solid line). Notice that the suppression of the stop-band is enhanced for this optimal filter. For comparison I included the power response of the filter obtained by taking the integer part of the coefficients resulting from the Parks-McClellan method (red dashed line). One can see that it does not suppress that much the stop-band, in a similar way to the current implementation of the filter.

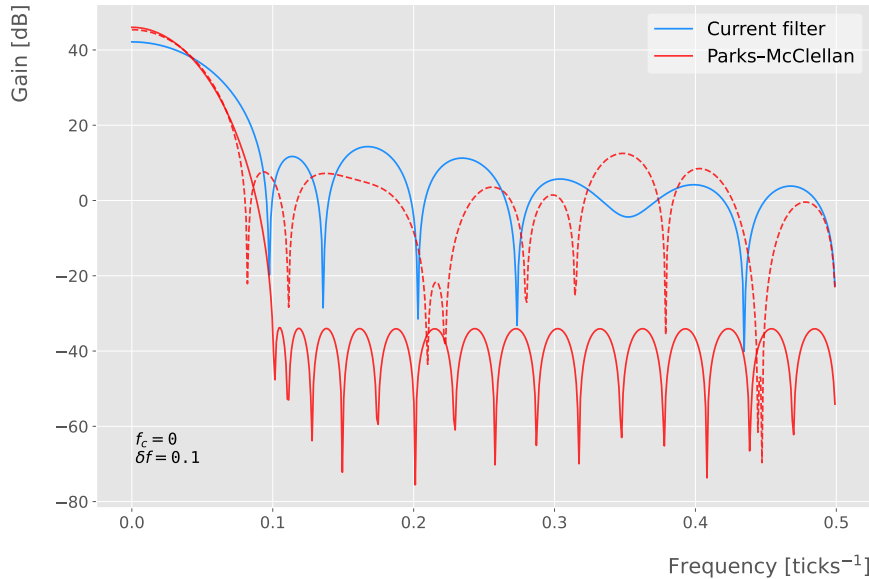


Figure 6.4: Power spectrum in decibels for the current implementation of the low-pass FIR filter in `dtp-firmware` (blue line), compared to the response of an optimal filter obtained using the Parks-McClellan algorithm for the same pass-band (red line). Also for comparison I include the spectrum of the optimal filter when taking only the integer part of the coefficients (red dashed line).

At this point, I tried to improve the performance of the FIR filter using the Parks-McClellan method, i.e. maximize the overall S/N, using the available data captures. I did so by varying the values of the two quantities that parametrize the pass-band and stop-band, the cut-off frequency f_c and the transition width δf .

Fig. 6.5 shows the average relative change in the S/N (i.e. the ratio between the value of the S/N after and before the filtering) for capture `felix-2020-07-17-21:31:44`,

6.3. Low-pass FIR filter design

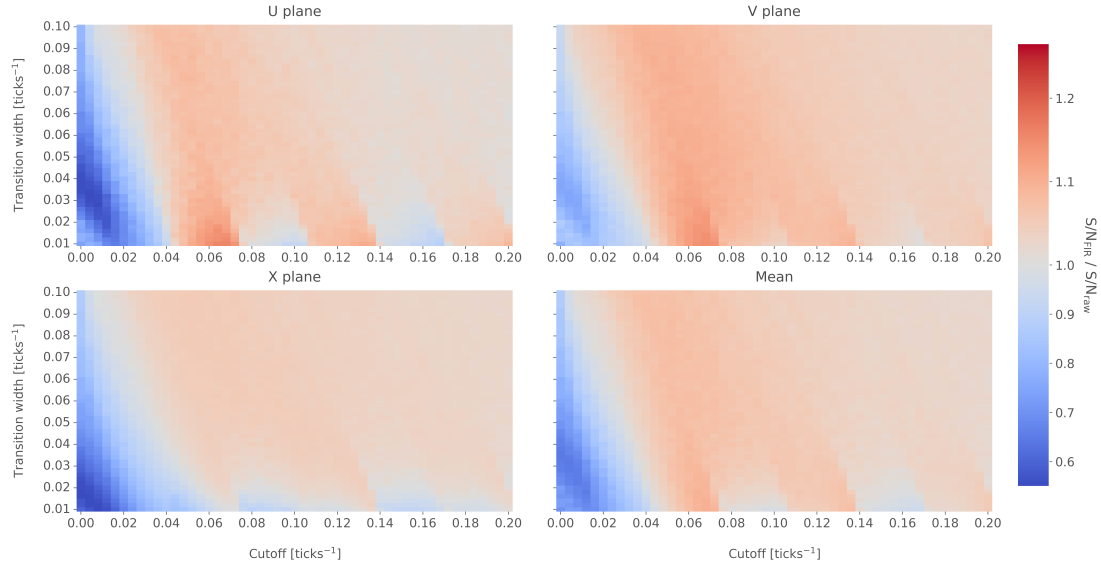


Figure 6.5: Relative change in the S/N for the ProtoDUNE-SP raw data capture `felix-2020-07-17-21:31:44`, using different values of the cutoff frequency f_c and the transition width δf . The optimal Chebyshev filters were applied using just the integer part of the coefficients given by the Parks-McClellan algorithm.

when using filters designed with the Parks-McClellan algorithm for the specified values of the cut-off frequency f_c and the transition width δf , restricted to integer values for the filter coefficients. One can clearly distinguish different regions where we get an improvement of up to a factor of 1.35 for the U plane. For large values of $f_c + \delta f$ the ratio tends to 1, as expected (in that limit the width of the stop-band goes to 0, meaning that no frequencies are filtered out and thus the waveform remains the same).

Using the configuration which gives the best mean performance for the three planes (see bottom right panel of Fig. 6.5), i.e. $f_c = 0.068 \text{ ticks}^{-1}$ and $\delta f = 0.010 \text{ ticks}^{-1}$, we can see how such filter affects the different channels. Fig. 6.6 shows the distribution of the S/N improvement values for all the channels in the raw ADC capture `felix-2020-07-17-21:31:44`, separated by wire plane, after the optimal Chebyshev filter was applied. One can see that there is a clear improvement for both U and V induction wire planes, obtaining a mean change of 1.25 and 1.30 for them respectively. However, in the case of the collection plane X the mean of this distribution is roughly 1, meaning that a good fraction of channels in that plane get a slightly worse S/N after the

Chapter 6. Matched Filter approach to induction wire Trigger Primitives

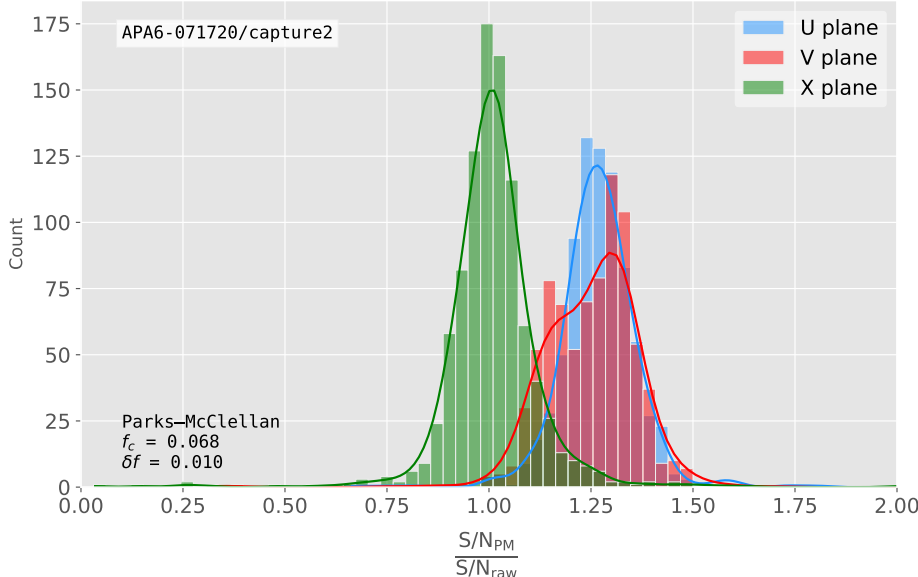


Figure 6.6: Distribution of the relative change of the S/N on the different wire planes from the ProtoDUNE-SP raw data capture *felix-2020-07-17-21:31:44* after the optimal Chebyshev filter was applied. The filter was computed with the Parks-McClellan algorithm using a cutoff of $f_c = 0.068 \text{ ticks}^{-1}$ and a transition width $\delta f = 0.010 \text{ ticks}^{-1}$.

filter is applied. In any case, this is not a big issue as the S/N for collection channels is usually much higher than the one for induction channels.

The results I obtained optimising the low pass filter with the Parks-McClellan method are promising. Nonetheless, the improvement found is rather marginal so I wondered if there could be an alternative approach to the filtering problem which yields better outputs. At this point, I found a possible alternative in matched filters. By construction, this kind of filters offer the best improvement on the S/N.

6.4 Matched filters

In the context of signal processing, a matched filter is the optimal linear filter for maximising the signal-to-noise ratio (S/N) in the presence of additive noise, obtained by convolving a conjugated time-reversed known template with an unknown signal to detect the presence of the template in the signal [54].

Given a known signal sequence $s(t)$ and another (a priori unknown) noise sequence

6.4. Matched filters

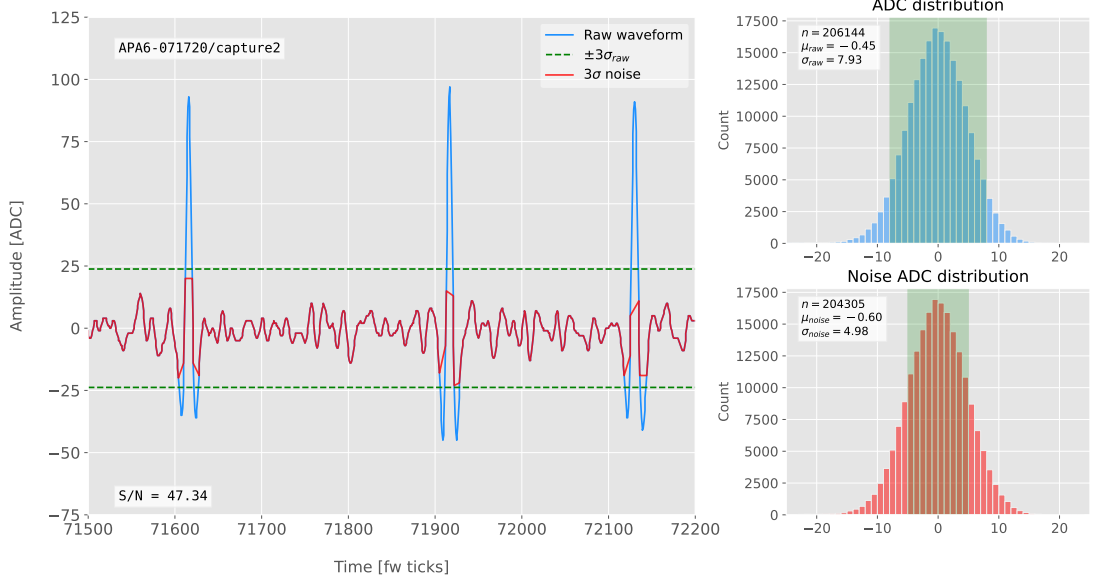


Figure 6.7: Left panel: Zoomed match filtered waveform corresponding to channel 7840 from the ProtoDUNE-SP raw data capture *felix-2020-07-17-21:31:44* (blue line). The filter used was directly extracted from the data, being the 32 values around the first peak in the original waveform. The green dashed lines mark the region $\pm 3\sigma_{\text{raw}}$. The resulting noise waveform is also shown (red line). Top right panel: ADC distribution for channel 7840 after match filtering, where the green shaded region represents $\pm \sigma_{\text{raw}}$. Bottom right panel: noise ADC distribution for channel 7840 after match filtering, where the green shaded region represents $\pm \sigma_{\text{noise}}$

1283 $n(t)$, the input signal can be written as:

$$x(t) = s(t) + n(t). \quad (6.4)$$

1284 Now, considering a linear time-invariant filter, whose impulse-response function I
1285 will refer to as $h(t)$, one can write the output signal as:

$$\begin{aligned} y(t) &= x(t) * h(t) \\ &= (s(t) + n(t)) * h(t) \\ &= y_s(t) + y_n(t), \end{aligned} \quad (6.5)$$

1286 where $y_s(t)$ and $y_n(t)$ are simply the outputs of the filter due to the signal and the noise
1287 components respectively.

Chapter 6. Matched Filter approach to induction wire Trigger Primitives

1288 The goal of the matched filter is to detect the presence of the signal $s(t)$ in the input
 1289 sample $x(t)$ at a certain time t_0 , which effectively means we need to maximise the S/N.
 1290 This way, what one wants is to have a filter which gives a much bigger output when the
 1291 known signal is present than when it is not. Putting it in other words, the instantaneous
 1292 power of the signal output $y_s(t)$ should be much larger than the average power of the
 1293 noise output $y_n(t)$ at some time t_0 .

1294 For the case of the filtered signal, one can easily re-write it as an inverse Fourier
 1295 transform:

$$y_s(t) = \frac{1}{2\pi} \int_{-\infty}^{\infty} d\omega H(\omega)S(\omega)e^{i\omega t}, \quad (6.6)$$

1296 where $H(\omega)$ and $S(\omega)$ are the Fourier transforms of the impulse-response function (i.e.
 1297 the transfer function of the filter) and of the input signal, respectively.

1298 Now focusing on the noise, we can use the Wiener-Khinchin theorem [55] to write
 1299 the mean power of the noise after filtering as:

$$E|y_n(t)|^2 = \frac{1}{2\pi} \int_{-\infty}^{\infty} d\omega |H(\omega)|^2 S_n(\omega), \quad (6.7)$$

1300 where $S_n(\omega)$ is the power spectral density of the noise.

1301 Having these, one can write the instantaneous S/N at time t_0 as:

$$\begin{aligned} \left(\frac{S}{N} \right)_{t_0} &= \frac{|y_s|^2}{E|y_n(t)|^2} \\ &= \frac{1}{2\pi} \frac{\left| \int_{-\infty}^{\infty} d\omega H(\omega)S(\omega)e^{i\omega t_0} \right|^2}{\int_{-\infty}^{\infty} d\omega |H(\omega)|^2 S_n(\omega)}. \end{aligned} \quad (6.8)$$

1302 Once we have this expression, we need to find the upper limit of it to determine what
 1303 would be the optimal choice for the transfer function. One can use the Cauchy-Schwarz
 1304 inequality, which in the present case takes the form:

$$\left| \int_{-\infty}^{\infty} dx f(x)g(x) \right|^2 \leq \int_{-\infty}^{\infty} dx |f(x)|^2 + \int_{-\infty}^{\infty} dx |g(x)|^2, \quad (6.9)$$

6.4. Matched filters

1305 for any two analytical functions $f(x)$ and $g(x)$. One can prove that making the choice:

$$\begin{aligned} f(x) &= H(\omega) \sqrt{S_n(\omega)} e^{i\omega t_0}, \\ g(x) &= \frac{S(\omega)}{\sqrt{S_n(\omega)}}, \end{aligned} \quad (6.10)$$

1306 leads to the following upper bound for the S/N:

$$\left(\frac{S}{N} \right)_{t_0} \leq \frac{1}{2\pi} \int_{-\infty}^{\infty} d\omega \frac{|S(\omega)|^2}{S_n(\omega)}. \quad (6.11)$$

1307 From Eqs. (6.8), (6.9) and (6.10) one can also derive the form of the transfer function

1308 such that the upper bound is exactly reached [56]:

$$H(\omega) \propto \frac{S^*(\omega) e^{-i\omega t_0}}{S_n(\omega)}. \quad (6.12)$$

1309 From this last expression we can clearly see the way the matched filter acts. As the
1310 transfer function is proportional to the Fourier transform of the signal it will try to only
1311 pick the frequencies present in the signal [57].

1312 The matched filter transfer function can be greatly simplified if the input noise is
1313 Gaussian. In that case, the power spectral density of the noise is a constant, so it can be
1314 re-absorbed in the overall normalisation of the transfer function. Moreover, considering
1315 that the input signal is a real function, one can simply set $S^*(\omega) = S(-\omega)$, which gives:

$$H(\omega) \propto S(-\omega) e^{-i\omega t_0}. \quad (6.13)$$

1316 For a discrete signal, one can think of the input and impulse-response sequences as
1317 vectors of \mathbb{R}^N . Then, the matched filter tries to maximise the inner product of the signal
1318 and the filter while minimising the output due to the noise by choosing a filter vector
1319 orthogonal to the later. In the case of additive noise, that leads to the impulse-response
1320 vector:

$$h = \frac{1}{\sqrt{s^\dagger R_n^{-1} s}} R_n^{-1} s, \quad (6.14)$$

Chapter 6. Matched Filter approach to induction wire Trigger Primitives

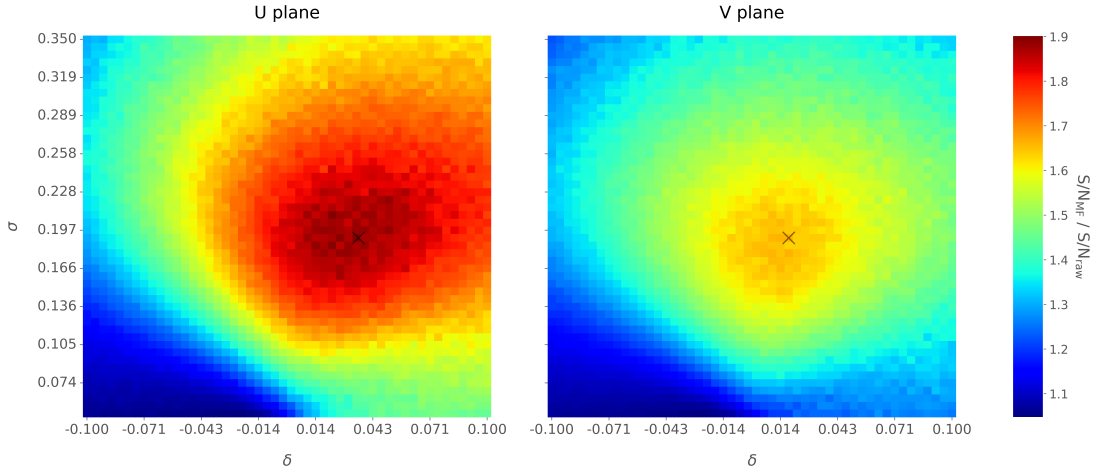


Figure 6.8: Relative improvement in the S/N for the raw data capture `felix-2020-07-17-21:31:44`, using the matched filter following the parametrisation in Eq. (6.17). The black crosses in both panels denote the location of the maximum ratio value.

1321 where s is a reversed signal template sequence of length N equal to the order of the filter
 1322 and R_n is the covariance matrix associated with the noise sequence n . For the Gaussian
 1323 noise case, the covariance matrix is simply the unit matrix, so the above expression
 1324 simplifies again to:

$$h = \frac{s}{|s|}. \quad (6.15)$$

1325 For this first stage of the study, I use a definition of the S/N per channel given by:

$$\text{S/N} = \frac{\max [ADC] - \mu_{noise}}{\sigma_{noise}}, \quad (6.16)$$

1326 where the subscript *noise* refers to a subset of the data obtained by only taking into
 1327 account waveform values within a $\pm 3\sigma$ range around the mean of the data and $\max [ADC]$
 1328 is the maximum of the original waveform. This definition is further discussed in App.
 1329 6.2, where I also show examples of its application to raw data and to a waveform filtered
 1330 with the current low-pass FIR filter.

1331 To test whether this choice of filter is appropriate one needs to choose a signal
 1332 template. As an example of how a matched filter would affect our signal, I simply took
 1333 the filter coefficients to be the 32 ADC values around a signal peak present in the data.

6.4. Matched filters

1334 In Fig. 6.7 (left panel) I plotted a zoomed region for channel 7840 in the raw data capture
1335 `felix-2020-07-17-21:31:44`, after applying the matched filter described before (blue
1336 line). When compared to the raw and FIR filtered case (see App. 6.2), after applying
1337 the match filter the standard deviation of the noise waveform (red line) decreases and at
1338 the same time the signal peaks are enhanced. This leads to an improvement of the S/N
1339 by a factor of 1.92 when compared to the raw waveform.

1340 In order to obtain the matched filter that is more suitable for our data, I explored
1341 different configurations of signal templates. In order to perform this exploration, I
1342 parametrised the signal using the bipolar function:

$$f(x) = -A(x + \delta) e^{-x^2/\sigma^2}, \quad (6.17)$$

1343 where the parameter δ controls the asymmetry between the positive and negative peaks
1344 and σ controls their width. The amplitude parameter A is set such that it keeps the
1345 height of the biggest peak to be less than 200 ADC in absolute value.

1346 As this parametrisation is only adequate for bipolar signals I will focus exclusively
1347 on the induction channels. Also, the optimal configurations I found for the U and V
1348 plane will be kept separate, i.e. I will have two sets of coefficients that will be applied to
1349 either the U and V planes of wires. I do so as I found this was the choice giving the
1350 best performance. Even so, as I will discuss, the differences are not very pronounced. In
1351 case it is not technically possible to separate channels in the firmware according to the
1352 wire plane they come from and use different sets of filter coefficients for them, we can
1353 just find a common unique set of coefficients. In such case, I do not expect our results
1354 to change dramatically.

1355 In Fig. 6.8 I present the results of our parameter scan, for channels in the induction
1356 planes U (left panel) and V (right panel). For each configuration of σ and δ the resulting
1357 matched filter was applied to all channels in the corresponding plane within the data
1358 capture `felix-2020-07-17-21:31:44`, the S/N improvement was computed with respect
1359 to the raw waveforms and then the S/N mean value was kept as a score for such filter.

Chapter 6. Matched Filter approach to induction wire Trigger Primitives

1360 One can see that the improvement obtained for the U plane is in general higher than the
1361 one for the V plane. In any case, I got substantially higher ratios than the ones obtained
1362 for the low-pass FIR filters. For the optimal configurations I attained improvements up
1363 to a factor of 1.85 for the U plane and 1.65 for the V plane.

1364 The sets of optimal matched filter coefficients were obtained for the parameters
1365 $\delta = 0.035$, $\sigma = 0.191$ for the U plane and $\delta = 0.018$, $\sigma = 0.191$ for the V plane. I
1366 show these two sets of coefficients in Fig. 6.9 (left panel). Also in Fig. 6.9 (right
1367 panel) I plot the distribution of the S/N improvement after the optimal match filters
1368 for the U and V were applied to the corresponding channels in the raw data capture
1369 `felix-2020-07-17-21:31:44`. As mentioned before, the mean improvement achieved
1370 for the U plane channels is slightly bigger than the one for the V channels. Note, however,
1371 that the spread of the distribution for the V plane is also smaller than the one for the U
1372 plane.

1373 I also performed a similar scan for the case of a low-pass FIR filter using the Parks-
1374 McClellan algorithm. In that case, the parameters to check were the cutoff frequency
1375 and the transition width of the filter. A summary of the results is given in App. 6.3.

1376 Overall, one can see that the improvements on the S/N are much more significant in
1377 the case of the matched filter than it is for the low-pass FIR filters. The analysis of this
1378 and other raw data captures from ProtoDUNE-SP suggest that matched filters increase
1379 the S/N of induction channels by a factor of 1.5 more than the optimal low-pass FIR
1380 filters.

1381 Although these results are by themselves great points in favour of the matched
1382 filter, more studies are needed to completely assess the robustness of this approach. I
1383 proceeded then to test the matched filter with simulated data samples.

1384 6.5 Using simulated samples

1385 In order to further test the matched filter, the next step was to generate and process
1386 data samples using *LArSoft* [58]. In this way, one can control the particle content of

6.5. Using simulated samples

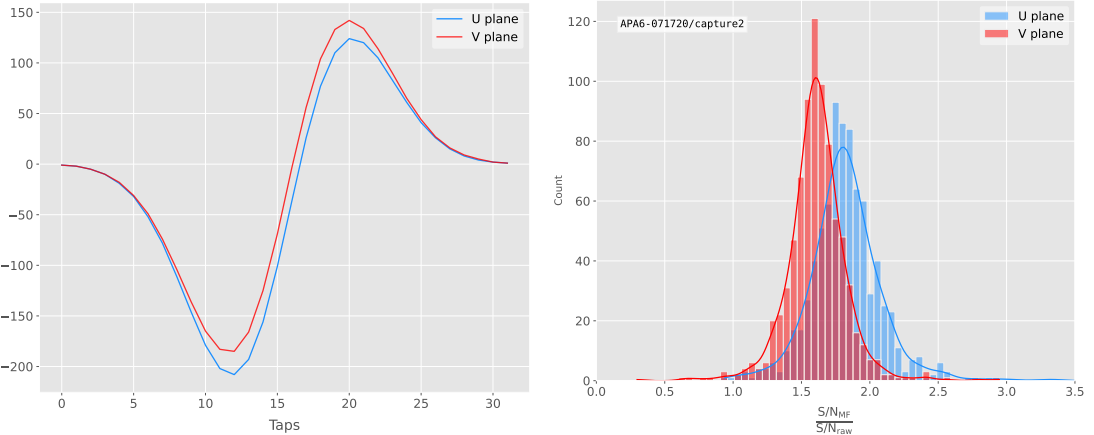


Figure 6.9: Left panel: Optimal matched filter coefficients for the U (blue line) and V (red line) planes. The filters were computed with our parametrisation in Eq. (6.17) for the parameter values $\delta = 0.035$, $\sigma = 0.191$ and $\delta = 0.018$, $\sigma = 0.191$ respectively. Right panel: Distribution of the relative change of the S/N on the two induction wire planes from the ProtoDUNE-SP raw data capture *felix-2020-07-17-21:31:44* after their respective optimal matched filters were applied.

1387 the samples, the orientation of the tracks and their energy, and therefore see how the
1388 matched filter behaves in various situations.

1389 To begin with, I prepared different monoenergetic and isotropic samples containing
1390 a single particle per event. Each sample contains a different particle species, namely
1391 electrons, muons, protons and neutral pions all with a kinetic energy of $E_k = 100$ MeV.
1392 I chose these because of the fairly different topologies they generate in the liquid argon,
1393 ranging from shower-like to track-like. The procedure I followed to generate the samples
1394 and process them is discussed in detail in App. ??.

1395 These were generated with the single particle gun and the Geant4 stage of the
1396 *LArSoft* simulation [58] was performed with the standard configuration for the DUNE
1397 FD 10kt module.

1398 For simplicity, I restricted the particles to start drifting in a single TPC volume
1399 (in this case TPC 0), so I can focus exclusively on the signals coming from one APA.
1400 The chosen kinetic energy for all the particles in my first trial is $E_k = 100$ MeV, so a
1401 necessary check is to see if all our tracks will be typically contained in one TPC volume.
1402 Fig. 6.10 (left panel) shows the distributions of the track lengths in the liquid argon

Chapter 6. Matched Filter approach to induction wire Trigger Primitives

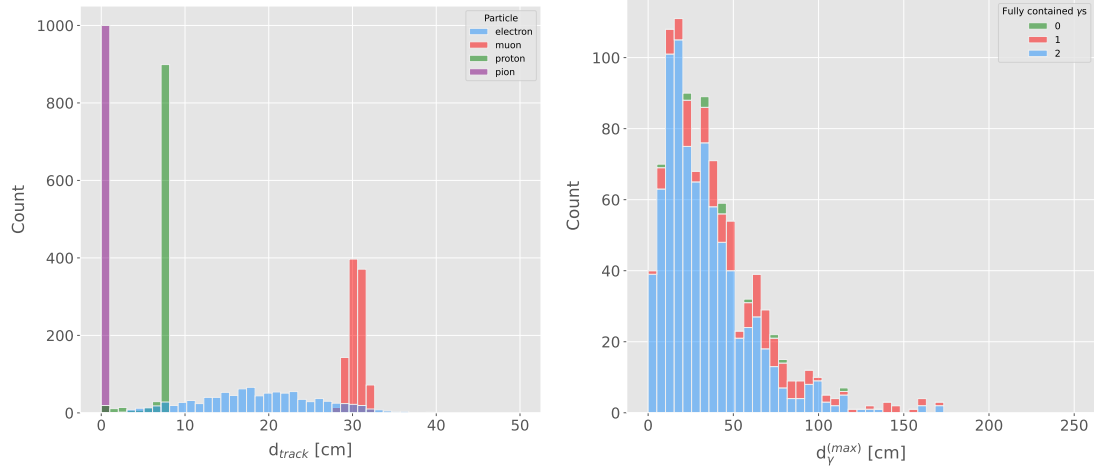


Figure 6.10: Left panel: distributions of the particles track length in the liquid argon for the generated $E_k = 100$ MeV monoenergetic samples, electrons (blue), muons (red), protons (green) and neutral pions (purple). Right panel: distribution of the length of the longest photon in the neutral pion sample after the decay process $\pi^0 \rightarrow \gamma\gamma$.

of all generated particles with $E_k = 100$ MeV. One can see that, in the case of the track-like particles (i.e. muons and protons), their length distributions are quite sharp and centered at relatively low distances (30 and 8 cm, respectively). For electrons, the distribution is quite broad but it does not extend past ~ 30 cm. The case of neutral pions can be misleading, as they decay promptly the track length associated with the true Monte Carlo particle is always < 1 cm. In Fig. 6.10 (right panel) I show the effective length distribution of the longest photon after the pion decays as $\pi^0 \rightarrow \gamma\gamma$, highlighting the number of fully contained photons in the TPC volume per event (either zero, one or both). One can see that the vast majority of events has both photons contained and that just a negligible number of them has none of them contained in the TPC volume. In any case, for the sake of caution, I will only keep the pion events with both photons contained.

Once I have prepared a sample at the Geant4 level, I need to process it through the detector simulation. In order to make adequate estimations of the noise levels and run the filtering and hit finder as I did with the ProtoDUNE data, one needs to turn off the default zero-suppression of the waveforms produced by the simulation. At this first stage I am only concerned with the waveforms with the noise added, so I keep the noise

6.5. Using simulated samples

addition option as true in the configuration. However, for studies related to the hit finder performance one will also need to store the noiseless waveforms in order to retrieve the truth information of the hits. I will discuss this approach next.

After the detector simulation stage, one needs to extract the no zero-suppressed noisy waveforms, along with their offline channel numbers, and store them in a certain format to be analysed later. To reduce the amount of data that will go for processing, I used the information from the Geant4 step of the simulation to select only the active channels, i.e. the channels where some ionisation electrons arrive. Moreover, as said previously, I only extract the waveforms from APA 0 and exclusively the ones coming from induction channels. The resulting ROOT file contains a tree with two branches, one containing the waveforms for each event and channel and the other with the corresponding offline channel numbers.

Finally, to extract the truth values for the orientation of the tracks and the energies of the particles I used a modified analysis module. This gives a ROOT file with a single tree, containing several branches with different information such as the components of the initial momentum of the particles, initial and final xyz location, track length, etc.

For the analysis of the resulting waveforms and truth values I used a custom set of Python libraries (available at [??]). Among other functionalities, these enable the user to read the ROOT files, export the raw data as pandas objects, apply the filters and compute the S/N of both the raw and filtered signals. So far, the default configuration for the filtering uses the set of optimal matched filter coefficients that I found using the ProtoDUNE data samples.

Additionally, for the analysis of the samples it was necessary to use two different reference frames, to study separately the signals coming from the U and V induction wire planes. As I am focussing on a single APA, the U and V wires have a different orientation in the yz plane. In the case of U wires, these are tilted 35.7° clockwise from the vertical (y direction), whereas the V wires are at the same angle but in the counter clockwise direction. Because of this, the best option is to deal with two new coordinate systems rotated by $\pm 35.7^\circ$ along the x axis, so the new y' and y'' directions are aligned with the

Chapter 6. Matched Filter approach to induction wire Trigger Primitives

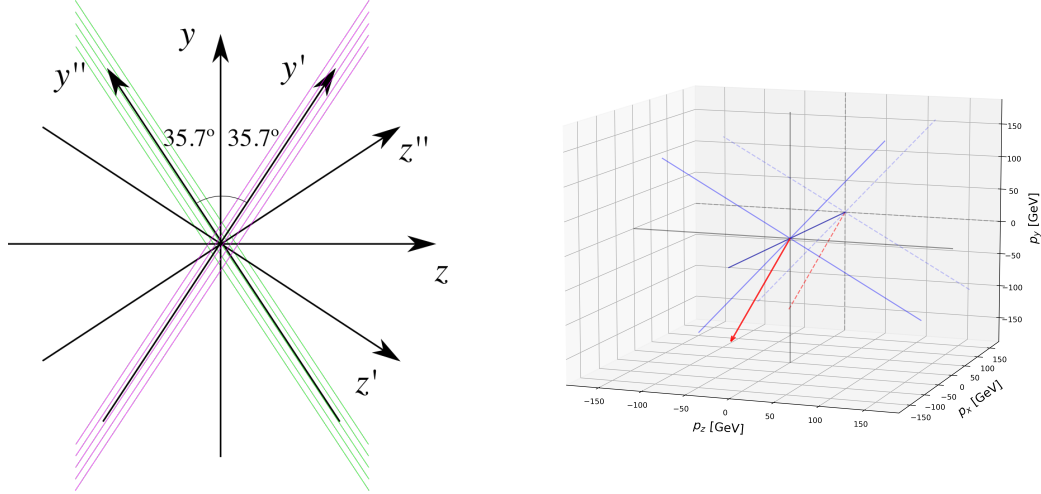


Figure 6.11: Left panel: schematic representation of the two new rotated reference frames used in this analysis (denoted as prime and double prime), viewed from the yz plane. The magenta stack of lines represent the wires in the U plane, whereas the green lines correspond to the wires in the V plane. Right panel: 3D representation of the momentum of one of the generated monoenergetic muons (red arrow) in the original reference frame (black lines), along with the new reference frame used for the U plane waveforms (blue lines). In the yz plane I added the projection of these three.

1449 U and V induction wires. Fig. 6.11 (left panel) shows a schematic representation of
 1450 the original reference frame together with the two rotated ones (denoted by primed and
 1451 double primed). This way, one can easily understand how parallel was a track to the
 1452 wires in the two induction planes. Fig. 6.11 (right panel) shows a 3D representation of
 1453 the momentum of a track (red arrow) in the original reference frame (black lines), along
 1454 with the new reference frame for U wires (blue lines). I added the projection in the yz
 1455 plane of this three, to show the usefulness of the new reference frame to tell whether a
 1456 track is parallel or normal to the wires in the induction plane.

1457 Fig. 6.12 shows the distribution of the average S/N improvement per event when one
 1458 applies the optimal matched filters. I produced separate distributions for the channels
 1459 in the U (red) and V (blue) induction wire planes. Notice that the S/N distributions
 1460 for the track-like particles, i.e. muons (top left panel) and protons (bottom left panel),
 1461 have significantly larger mean values than the distributions of the shower like particles,
 1462 i.e. electrons (top right panel) and neutral pions (bottom right panel). An important

6.5. Using simulated samples

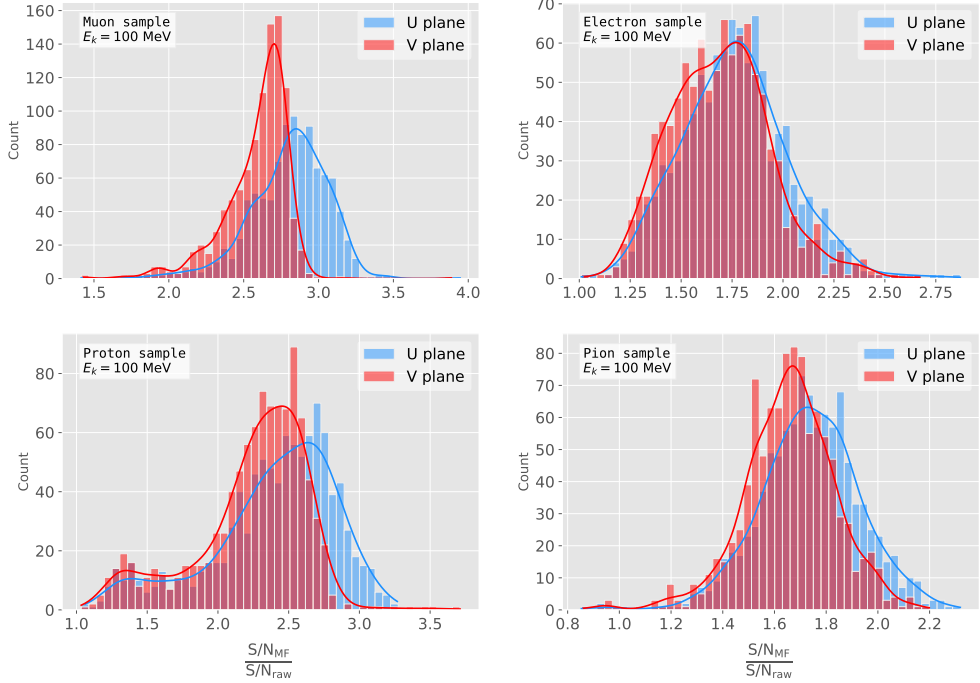


Figure 6.12: Distributions of the mean S/N improvement per event for the corresponding sample after applying the matched filters. Here I separated the change in the U plane (blue) and the V plane (red) channels. From top left to the right: muon, electron, proton and neutral pion. All the events have a fixed kinetic energy of $E_k = 100 \text{ MeV}$.

difference between these results and the ones seen before for ProtoDUNE data is that, overall, the improvements that I get for simulated data are bigger. This could be due either to the default noise model used in the *LArSoft* simulation or to the simulated hits having higher energy than the ones in the recorded data. Nonetheless, the concluding message is that the previously optimised matched filters give an overall significant improvement of the S/N for the different samples.

About the convention I followed for the plots and results, in the case of the raw and filtered S/N of each event in the sample I simply took the average of the quantities over all the active channels in the event. That is, if a certain event has N_{chan} active channels these two quantities are computed as:

$$(S/N_{fir})_{event} = \frac{\sum_{i=0}^{N_{chan}} (S/N_{fir})_i}{N_{chan}},$$

$$(S/N_{raw})_{event} = \frac{\sum_{i=0}^{N_{chan}} (S/N_{raw})_i}{N_{chan}}. \quad (6.18)$$

Chapter 6. Matched Filter approach to induction wire Trigger Primitives

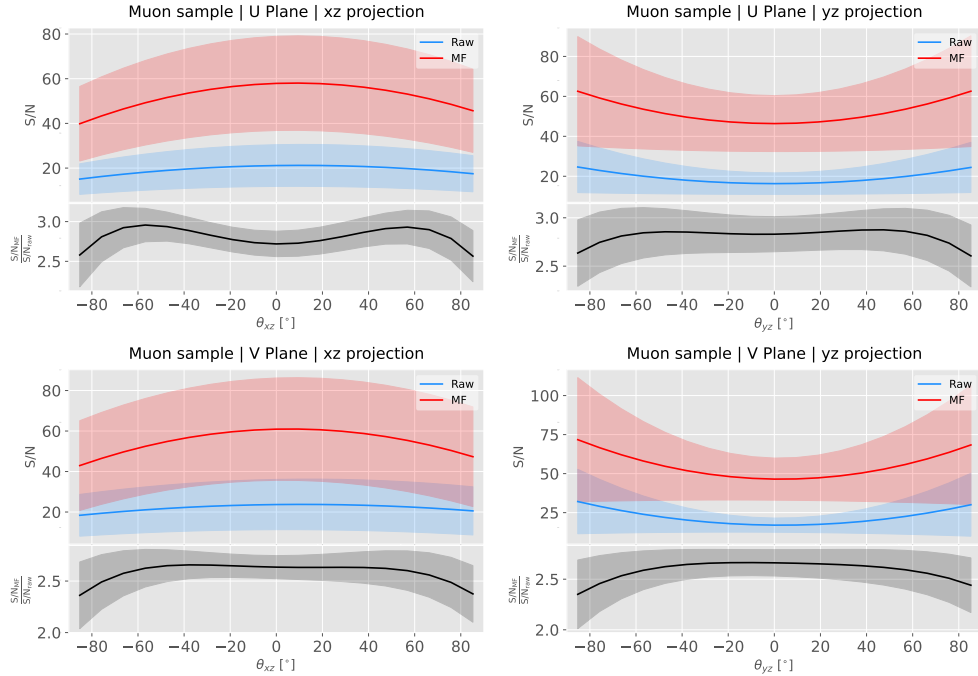


Figure 6.13: Angular dependence of the mean S/N and the S/N improvement, for the different monoenergetic samples considered (from top to bottom: electrons, muons, protons and neutral pions). The two columns on the left represent the values for the U plane waveforms. The top subplots show the mean S/N for raw (green) and filtered (red) waveforms whereas the bottom subplots depict the averaged S/N improvement (black).

1473 However, for the ratio of the raw and filtered S/N (what I called the S/N improvement)
 1474 per event I am not just taking the ratio of the previous two quantities but computing
 1475 the average of the individual ratios per channel in the event:

$$\left(\frac{S/N_{fir}}{S/N_{raw}} \right)_{event} = \frac{\sum_{i=0}^{N_{chan}} \left(\frac{S/N_{fir}}{S/N_{raw}} \right)_i}{N_{chan}}, \quad (6.19)$$

1476 and so:

$$\left(\frac{S/N_{fir}}{S/N_{raw}} \right)_{event} \neq \frac{(S/N_{fir})_{event}}{(S/N_{raw})_{event}}. \quad (6.20)$$

1477 6.5.1 Angular dependence

1478 Having these monoenergetic samples, one can also study the angular dependence of the
 1479 performance of the matched filter. This is an important point, as it is a well established
 1480 fact that for certain configurations (an extreme case configuration being signals normal

6.5. Using simulated samples

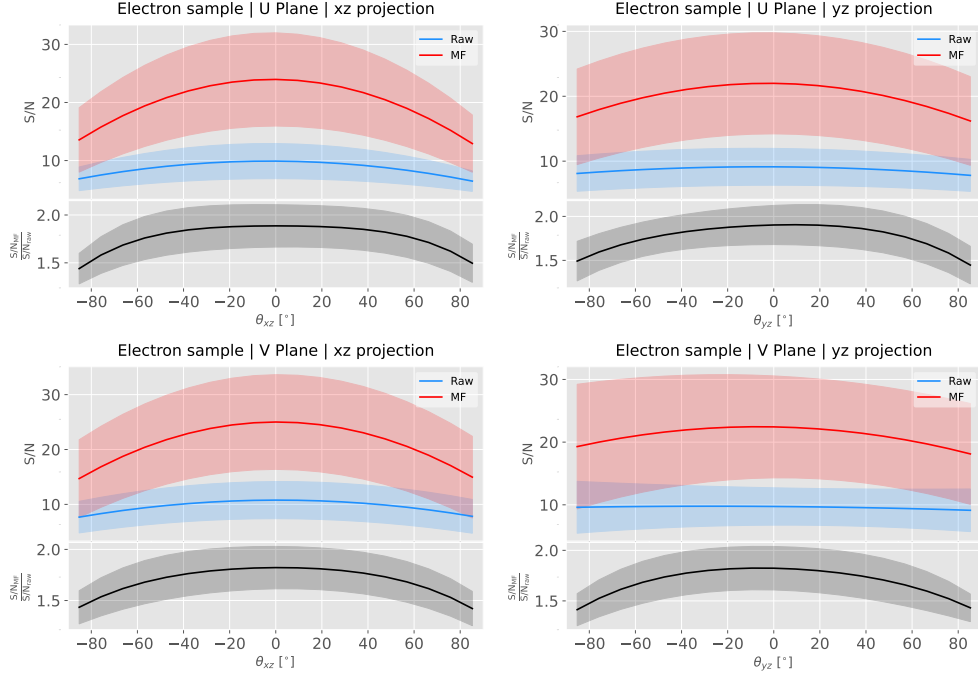


Figure 6.14: Angular dependence of the mean S/N and the S/N improvement, for the different monoenergetic samples considered (from top to bottom: electrons, muons, protons and neutral pions). The two columns on the left represent the values for the U plane waveforms. The top subplots show the mean S/N for raw (green) and filtered (red) waveforms whereas the bottom subplots depict the averaged S/N improvement (black).

to the wire plane and perpendicular to the induction wires at the same time) the S/N is much lower than average as the corresponding waveforms are severely distorted. In this sense, I am interested to see how the matched filter behaves for these cases and how the S/N improvement on those compare to the average.

Fig. 6.13 shows the angular dependence of the S/N for the monoenergetic $E_k = 100$ MeV isotropic muons, for the different induction wire planes and projections. The angles for each event are given by the components of the initial value of the momentum of the particles, taking the angles of the projections on the xz and yz planes with respect to the z axis (more accurately, one needs to compute these angles twice for each event, a pair for the $xy'z'$ coordinate system and the other for the $xy''z''$). The top row shows the dependence on the angles corresponding to the U plane, i.e. $\theta_{xz'}$ and $\theta_{y'z'}$, whereas the bottom row shows the angular dependence viewed from the V plane, $\theta_{xz''}$ and $\theta_{y''z''}$. In each plot, the top subplot represents the mean values of the S/N for the raw (blue) and

Chapter 6. Matched Filter approach to induction wire Trigger Primitives

1494 matched filtered (red) signals, and the bottom subplot the averaged S/N improvement
1495 (black). The solid lines represent the mean value obtained for the corresponding angular
1496 value, whereas the semitransparent bands represent one standard deviation around the
1497 mean at each point.

1498 As expected, the S/N is in general higher when tracks are parallel to the APA (i.e.
1499 $\theta_{xz} \sim 0$) and lower when it is normal to the plane ($\theta_{xz} \sim \pm 90^\circ$). In the same way, tracks
1500 parallel to the wires ($\theta_{yz} \sim \pm 90^\circ$) tend to have higher S/N than those perpendicular to
1501 these ($\theta_{yz} \sim \pm 0$).

1502 Fig. 6.14 shows the corresponding angular dependence information for the $E_k =$
1503 100 MeV electrons sample. Notice that, in this case, the S/N behaviour discussed above
1504 does not hold. A possible explanation can be that, because most hits in these events
1505 are produced by the secondary particles generated in the EM shower, the signal peaks
1506 whose S/N ratios were computed do not correspond to the directional information of
1507 the primary electron.

1508 6.5.2 Distortion and peak asymmetry

1509 As a little case of study, I selected two of the simulated $E_k = 100$ MeV monoenergetic
1510 muon events. With respect to the U induction plane, one is parallel to the APA (low
1511 $\theta_{xz'}$) and to the wires (high $\theta_{y'z'}$) and the other is normal to the APA plane (high $\theta_{xz'}$)
1512 and perpendicular to the wires (low $\theta_{y'z'}$). As expected from the results on the angular
1513 dependence discussed above, the former has a higher S/N (before and after the filtering)
1514 when compared to the latter. An interesting thing to notice about these two samples
1515 is that, even though one has a much bigger S/N than the other, it is the one with the
1516 smallest S/N the one that got the biggest averaged S/N improvement. In Table 6.1
1517 I included all the relevant parameters of these two $E_k = 100$ MeV muon events I am
1518 considering, namely, the angles with respect to the $xy'z'$ reference frame, the values of
1519 the S/N, the S/N improvement and also the so-called peak asymmetry Δ_{peak} that I will
1520 discuss next.

1521 One can try to understand better what is going on with these two events by looking

6.5. Using simulated samples

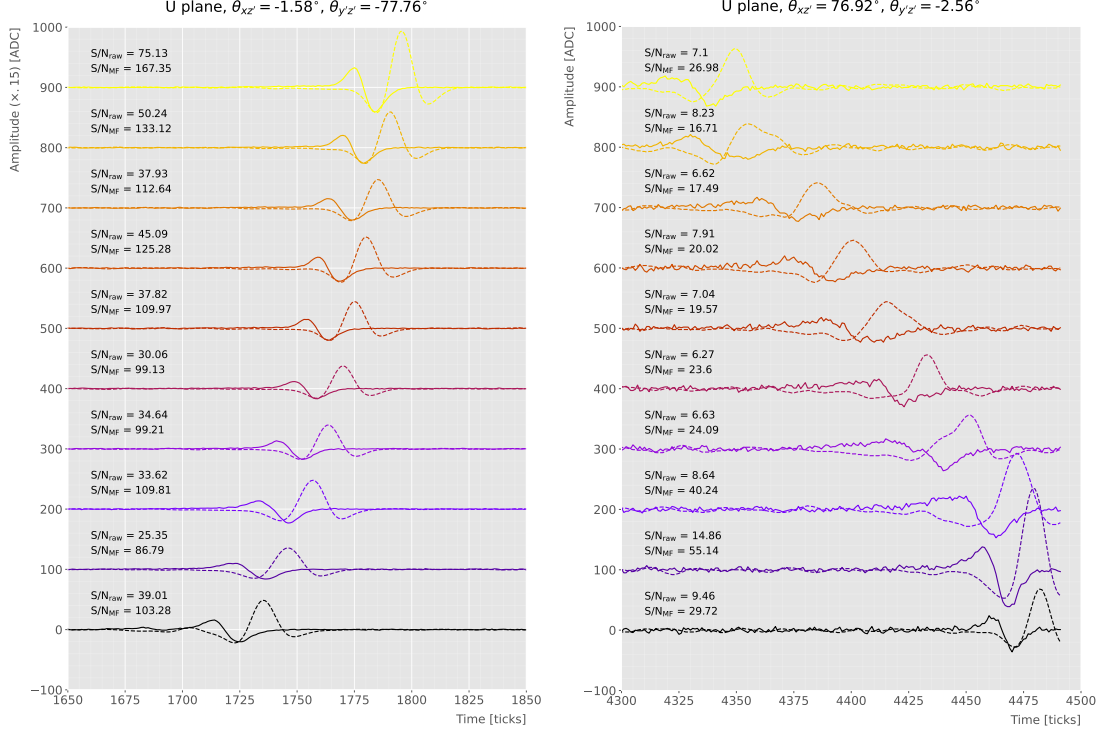


Figure 6.15: Selected consecutive waveforms corresponding to two monoenergetic $E_k = 100$ MeV muon events, one is parallel to the APA and to the wires in the U plane (left panel) and the other is normal to the APA plane and perpendicular to the U plane wires (right panel). The solid lines represent the raw waveforms whereas the dashed lines correspond to the waveforms after the matched filter was applied. The waveforms on the left panel have been scaled by a factor of 0.15 to have similar amplitude to the ones on the right panel.

Table 6.1: Characteristic parameters of the two monoenergetic muon events selected, relative to the U plane: projected angles in the xz' and $y'z'$ planes, S/N values for the raw and filtered waveforms, mean improvement of the S/N and peak asymmetry.

	θ_{xz}' (°)	$\theta_{y'z}'$ (°)	S/N _{raw}	S/N _{MF}	$\frac{S/N_{MF}}{S/N_{raw}}$	Δ_{peak} (ADC)
High ("parallel")	-1.58	-77.76	41.65	112.44	2.83	-35.73
Low ("normal")	76.92	-2.56	8.07	25.46	3.12	-10.38

at the raw and filtered data from some of their active channels. Fig. 6.15 shows a selection of consecutive raw and filtered U plane waveforms from the event with high S/N (left panel) and the one with low S/N (right panel). Notice that to show both collections of waveforms at a similar scale I had to apply a factor of 0.15 to the waveforms with high S/N. Additionally, next to each waveform I included the values of the raw and

Chapter 6. Matched Filter approach to induction wire Trigger Primitives

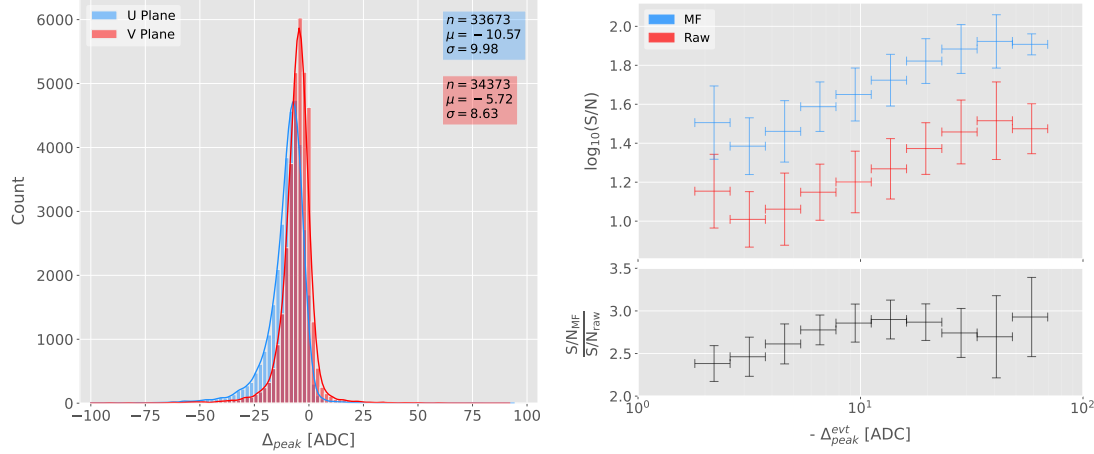


Figure 6.16: Left panel: peak asymmetry distribution for the case of the monoenergetic $E_k = 100$ MeV muon sample. Each value corresponds to a single bipolar signal peak from a channel in any event. The blue distribution represents the peaks on U plane channels, whereas the red corresponds to signal peaks in V wires. Right panel: relation between the mean peak asymmetry per event with the S/N for U channel waveforms from the $E_k = 100$ MeV muon sample. The top subplot shows the decimal logarithm of the mean S/N for the raw (red) and the matched filtered (blue) waveforms. The bottom subplot contains the mean S/N improvement ratio after the matched filter was applied.

1527 matched filtered S/N for the corresponding channel. The first thing to notice in this plot
 1528 is that the amplitude of the signal peaks from the normal track have a much smaller
 1529 amplitude, and also appear quite distorted when compared to the others. On the other
 1530 hand, although the matched filtered S/N is still smaller, the relative improvement is
 1531 bigger than in the parallel case.

1532 A way I found to quantify the difference between the shapes within these two events
 1533 is their different peak asymmetry. One can define the peak asymmetry as the (signed)
 1534 difference between the positive and the negative peaks of the bipolar shape, i.e.:

$$\Delta_{peak} \equiv h_+ - h_-, \quad (6.21)$$

1535 where both heights h_+ and h_- are positive defined. Fig. 6.16 (left panel) shows the
 1536 distribution of this peak asymmetry for all the waveforms corresponding to channels
 1537 in the U (blue) and V (red) planes for the monoenergetic muon sample. One can
 1538 see that these distributions are clearly shifted to negative values (with mean values

6.5. Using simulated samples

1539 $\mu_{\Delta}^U = -10.57$ ADC and $\mu_{\Delta}^V = -5.72$ ADC respectively). It is interesting to notice
1540 that the peak asymmetry value of the sample with high S/N sits at the left tail of the
1541 distribution whereas the corresponding value of the sample with low S/N lies around
1542 the mean.

1543 Now, one can try to correlate the peak asymmetry with the S/N and the S/N change
1544 per event. Fig. 6.16 (right panel) shows the result of comparing (minus) the mean
1545 peak asymmetry per event to the averaged raw (red) and matched filtered (blue) S/N
1546 per event (top subplot). The horizontal lines sit at the mean value obtained in the fit
1547 and represent the width of the $-\Delta_{peak}$ bins used, while the vertical lines indicate one
1548 standard deviation around that mean value. Notice that, when taking decimal logarithm
1549 on both, there is an approximate linear relation between these quantities, except for
1550 peak asymmetry values bigger than -5 ADC where the S/N remains constant.

1551 Also, in the bottom subplot of Fig. 6.16 (right panel) I show the relation between
1552 the peak asymmetry and the mean S/N improvement. In this case, one see that there is
1553 a maximum at $\Delta_{peak} \sim -10$ ADC. As mentioned previously, this is also the value of the
1554 mean of the peak asymmetry distribution. In fact, it is expected that our filter favours
1555 the signal peaks with the most common values of the peak asymmetry, as this was one
1556 of the features I target in our filter coefficient optimisation through the parameter δ .

1557 These results suggest that events with poorer values of the mean S/N, usually
1558 associated to non-favourable track orientations, tend to have smaller values of the mean
1559 peak asymmetry (in absolute value). Nonetheless, because our matched filters have
1560 been optimised to account for these asymmetries, the improvement on the S/N for these
1561 events is sizeable if not better than the one for events which already had a high S/N.

1562 6.5.3 Hit sensitivity

1563 One of the advantages of the matched filter, directly related to increasing the S/N, is
1564 the capability of picking hits that before fell below the threshold. For instance, Fig. 6.17
1565 shows the raw ADC data from an example event (electron, $E_k = 100$ MeV) with the
1566 produced true hits superimposed (black boxes), together with the hits produced by the

Chapter 6. Matched Filter approach to induction wire Trigger Primitives

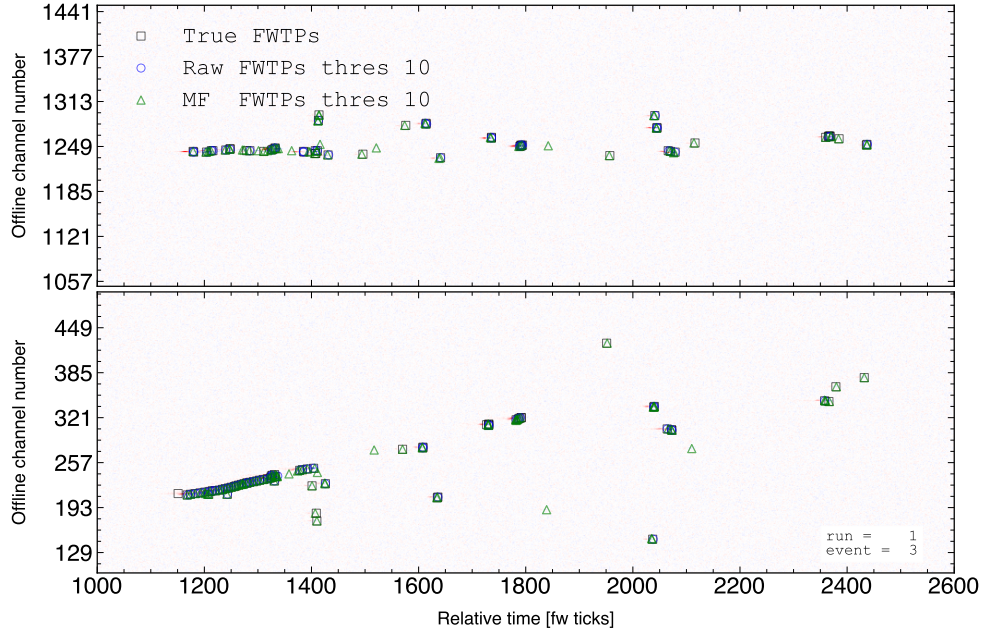


Figure 6.17: Raw data display in the plane time (in firmware ticks) vs. offline channel number for an $E_k = 100$ MeV electron event. The produced true hits are superimposed (black boxes) as well as the hits coming from the standard hit finder chain (blue circles) and the hit finder using the matched filter (green triangles).

standard hit finder chain (blue circles), i.e. using the current FIR filter, and the hits obtained using the matched filters (green triangles). Both the standard and the matched filter hit finders were run with a threshold of 10 ADC. Notice that the standard hits match well the true ones at the initial part of the event (where we have a track-like object), but they miss most of the hits produced by the EM shower at later times. On the other hand, the hits produced with the matched filter have a better agreement with the true hits even for the more diffuse shower activity.

Notwithstanding that now I get more hits with this combination of matched filter and low threshold as a results of the enhancement of the signal peaks relative to the noise level, it is also true that I pick some spurious hits not related to any real activity if one lowers the thresholds too much. Therefore, some optimisation of the threshold is needed. Basically one will need to make a trade-off between precision and sensitivity.

Having this in mind, I tried to compare the produced hits one gets from the standard hit finder and the ones resulting from applying the matched filter with the true hits.

6.5. Using simulated samples

1581 By running the hit finders on our samples with different values of the threshold one
1582 can understand, for instance, how low one can set the threshold without getting mostly
1583 spurious hits and then evaluate the gains obtained from this.

1584 Because now I am also interested in seeing how the hit sensitivity changes with the
1585 energy, I prepared new isotropic samples with the same types of particles as before
1586 (muons, electrons, protons and neutral pions) but with a flat kinetic energy distribution
1587 ranging from 5 to 100 MeV.

1588 In order to estimate the hit sensitivity, given a certain sample, one needs to recover
1589 the set of true hits to be able to compare these with the ones produced. To do so,
1590 a modification in the procedure I was using to extract the raw waveforms is needed.
1591 For this kind of study I run the detector simulation in two steps, first I produce the
1592 waveforms without noise and extract them in the same format I used for the raw data,
1593 then the noise is added and the noisy waveforms are then written to a file as well.

1594 To have a better comparison between the true hits and the ones produced from
1595 the raw waveforms after applying the two filters, I applied also the FIR filter and the
1596 matched filters to the noiseless waveforms and then I run the hit finder with a minimal
1597 threshold (in this case I used 1 ADC) on these noiseless filtered waveforms. In this way
1598 I generated two sets of true hits, I will refer to them as standard true hits (with the
1599 current/default FIR filter) and matched filter true hits respectively. This allows a more
1600 precise matching between the different groups of hits produced, as it will account for
1601 any delays and distortions introduced by the FIR and the matched filters.

1602 In the case of the raw waveforms (with noise), I run the hit finder on them, with
1603 different values of the threshold, after applying either the FIR or the matched filters. I
1604 will name them simply standard hits and matched filter hits respectively. Then, I match
1605 the generated hits to the true hits (the standard hits with the standard true hits and
1606 the matched filter hits with the matched filter true hits). The matching is performed by
1607 comparing the channel number and the timestamp of the hits. To count as a match,
1608 I require that all hits with the same channel number and timestamp have overlapping
1609 hit windows, i.e. the time windows between their hit end and hit start times need to

Chapter 6. Matched Filter approach to induction wire Trigger Primitives

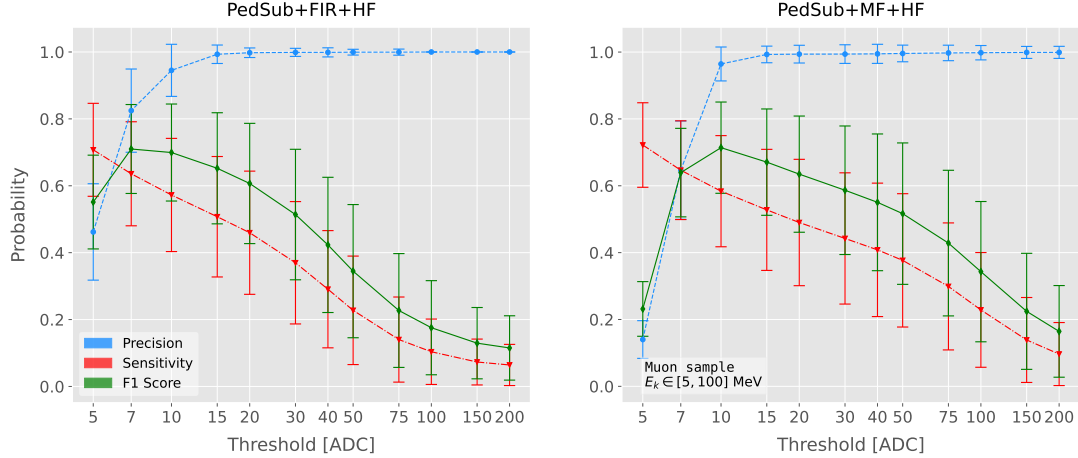


Figure 6.18: Dependence of the precision (blue), sensitivity (red) and F_1 (green) scores on the threshold values used in the hit finder, for the FIR (left panel) and matched filter (right panel) cases. The results were obtained after matching the hits to the true hits in the case of the isotropic muon sample with kinetic energy in the range 5 to 100 MeV, taking only into account the induction plane channels. The points represent the mean value while the error bars indicate one standard deviation around that mean value.

overlap. If more than one hit in one of the groups have hit overlap with the same hit in the other group I only count the hit with closer hit peak time value.

The generation of the samples, the procedure to produce the standard hits (with the default FIR filter) and matched filter hits and the matching of these with the true hits is described in detail in App. ??.

To quantify the performance of the two hit finder approaches, I use a classical method from statistical classification known as confusion matrix [59]. This is basically a way of sorting the outputs of a binary classifier, considering the true values of the classification and the predicted values. It divides the outputs in four categories: true positive (TP, both true and predicted values are 1), false negative (FN, true value is 1 but predicted is 0), false positive (FP, true value is 0 but predicted is 1) and true negative (TN, both true and predicted values are 0)).

The contents of the confusion matrix allow us to compute other derived scores to judge the performance of our classifiers. In this study, I will make use of three of these

6.5. Using simulated samples

1624 metrics, namely the precision or positive predictive value:

$$\text{PPV} = \frac{\text{TP}}{\text{TP} + \text{FP}}, \quad (6.22)$$

1625 the sensitivity or true positive rate:

$$\text{TPR} = \frac{\text{TP}}{\text{TP} + \text{FN}}, \quad (6.23)$$

1626 and the F_1 score [60]:

$$F_1 = \frac{2\text{TP}}{2\text{TP} + \text{FP} + \text{FN}}, \quad (6.24)$$

1627 which is the harmonic mean of the precision and the sensitivity.

1628 In our specific case I am not going to make use of the true negative value, as its
1629 definition in this context can be ambiguous because one does not have clear instances in
1630 the classification process. This way, I will only count the number of true positives as the
1631 total amount of hits I can match between true and raw populations, the number of false
1632 negatives will be the number of missing true hits and the false positive the number of
1633 hits which do not match any true hit.

1634 In Fig. 6.18 I show the precision (blue), sensitivity (red) and F_1 (green) scores I
1635 obtained for different values of the threshold used in the hit finder for the case of the
1636 muon sample. Because the matched filters are only applied to induction channels, I only
1637 consider here hits coming from the U and V planes. The panel on the left corresponds
1638 to the scores I got when I ran the hit finder on the FIR filtered waveforms, whereas the
1639 right panel contains the scores for the matched filter case. The points are centered at
1640 the threshold value used and represent the mean value obtained for each score using all
1641 the generated events, while the error bars indicate one standard deviation around the
1642 mean value.

1643 One can see that the precision for the matched filter case is lower when the thresholds
1644 are very low, as the noise baseline is slightly amplified, but then rises to high values
1645 quicker than for the FIR case. The other difference one can spot is that the sensitivity

Chapter 6. Matched Filter approach to induction wire Trigger Primitives

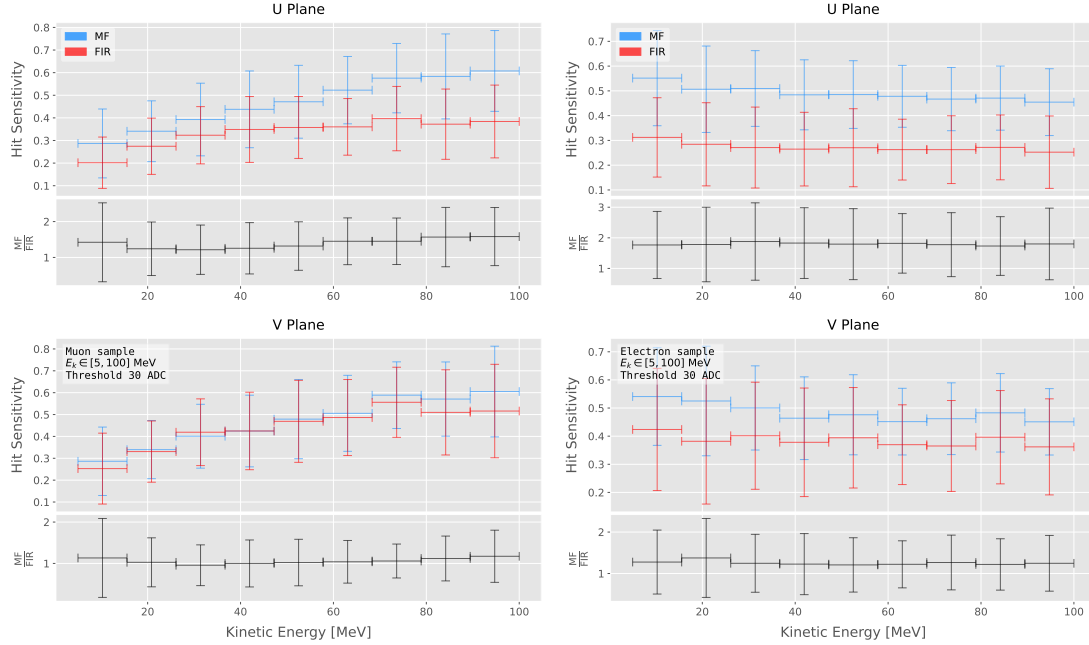


Figure 6.19: Dependence of the averaged hit sensitivity on the kinetic energy of the events for the matched filter (blue) and standard (red) hits, for the case of the muon (left panel) and electron (right panel) samples, separated between U (top plots) and V (bottom plots) induction wire planes. The top subplots contain the hit sensitivities for the two hit finder alternatives, while the bottom subplots show the ratio between the two. The horizontal lines sit at the mean value and represent the size of the energy bins, while the vertical error bars indicate one standard deviation around that mean value.

in the FIR case starts dropping faster at around the same threshold values where the precision stabilizes around 1, while in contrast for the matched filter this rapid decrease starts at higher threshold values. A similar scan for the same thresholds was performed for the electron sample in the same energy range, yielding similar results.

In Fig. 6.19 I show the averaged hit sensitivity versus the kinetic energy of the events, both for the matched filter hits (blue) and the standard hits (red). The left panel corresponds to the muon sample, whereas the one on the right corresponds to the electron sample, both with kinetic energies between 5 and 100 MeV. In each panel the top plot corresponds to hits in the U plane, while the bottom plot contains the same information for the V plane. Each plot contains two subplots, the one on the top shows the hit sensitivity values for the matched filter and standard hits separate, while the bottom subplot depicts the ratio between the matched filter and standard sensitivities.

6.5. Using simulated samples

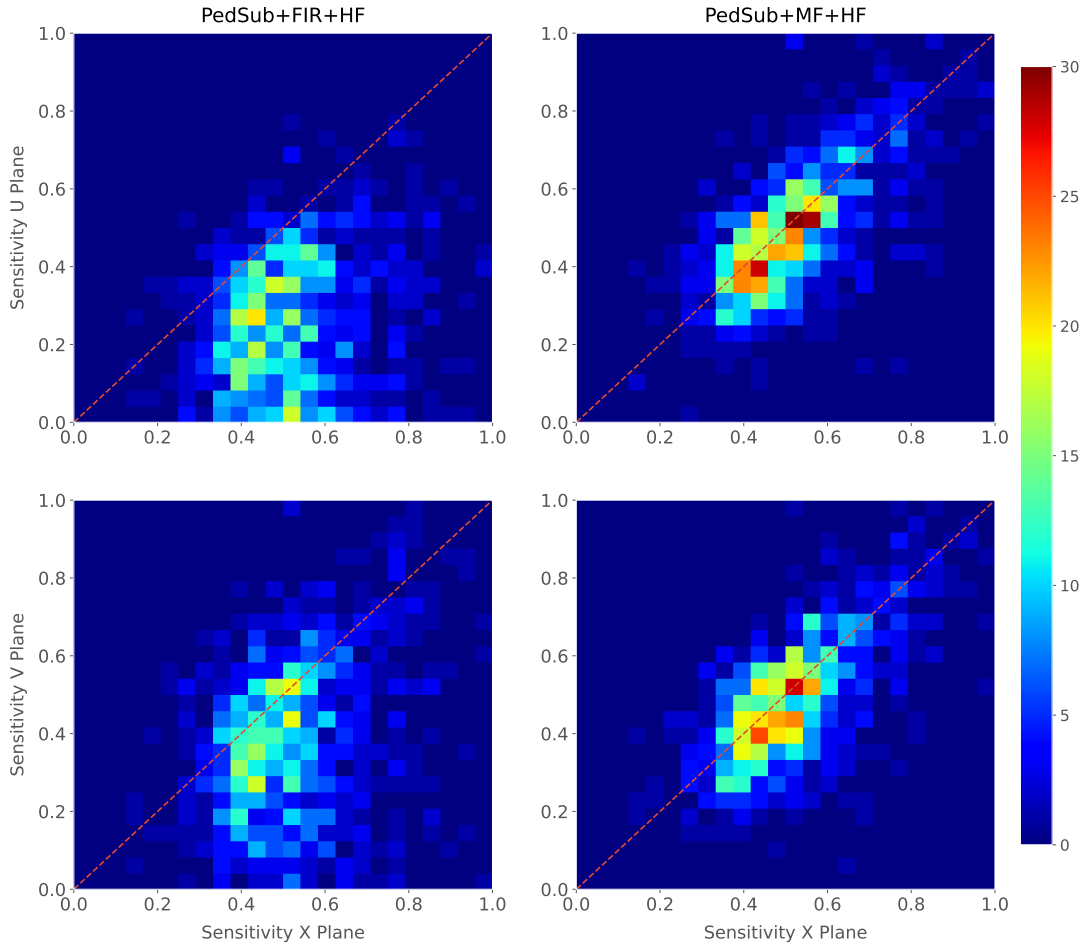


Figure 6.20: Distributions of the hit sensitivity in the U (top panels) and V (bottom panels) planes versus the hit sensitivity in the X plane, both for the standard hits (left panels) and the matched filter hits (right panels), in the case of the electron sample and a threshold of 30 ADC.

1658 The horizontal lines are placed at the mean value obtained in the fit and represent the
 1659 width of the E_k bins used, while the vertical error bars indicate one standard deviation
 1660 around that mean value. In both cases the threshold used was 30 ADC, as I required
 1661 the precision to be higher than 0.99 for both matched filter and standard cases.

1662 One can see that, in general, the improvements are better for the U than for the V
 1663 plane. While for the U channels I achieved a mean improvement of 50% and 80% for
 1664 muons and electrons respectively, the improvement in the V plane is stalled at 10% and
 1665 25%. Nevertheless, if I look at the sensitivities for the matched filter hits in both planes
 1666 one can see these have similar mean values for each energy bin, while on the contrary

Chapter 6. Matched Filter approach to induction wire Trigger Primitives

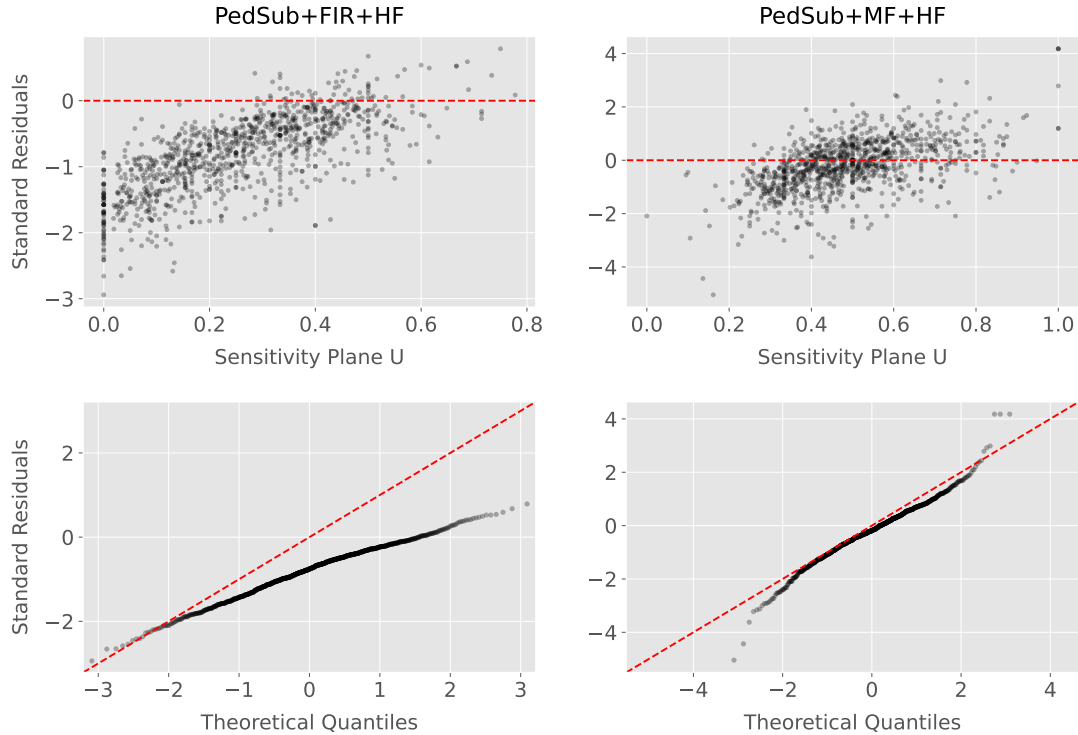


Figure 6.21: Top panels: standard residual plots of the hit sensitivities between the X and U planes. Bottom panels: quantile-quantile plots of the hit sensitivity standard residuals between the X and U planes. In all cases, the left panel corresponds to the standard hits while the right panel represents the matched filter case, all from the electron sample with a 30 ADC threshold.

for the standard hits the sensitivity remains relatively high for the V plane. This way, it looks there was a less significant gain because the hit sensitivity was already high.

Another interesting observation is the different behaviors for muons and electrons. While hit sensitivity for muons grows significantly with energy, in the case of electrons this slightly decreases the higher the kinetic energy of the event is. In any case, when it comes to the improvement on the sensitivities, this remains almost constant in all cases.

Furthermore, we can look at how the concurrence of hits between the different wire planes has changed. For any given event, I expect to have a similar number of hits in the three planes. As the ionisation electrons need to cross the U and V planes prior to reach the collection plane X they will induce current in those wire planes. A way to check the concurrence of hits across planes is looking at the relation between the hit sensitivities for each individual event. One cannot expect the sensitivities to be exactly equal across

6.5. Using simulated samples

1679 planes, but ideally they should be normally distributed around the diagonal.

1680 Fig. 6.20 shows the hit sensitivity in the U (top panels) and V (bottom panels)
1681 planes versus the hit sensitivity in the X plane, for the case of the standard hits (left
1682 panels) and the matched filter hits (right panels). All plots were generated for the
1683 electron sample and a threshold of 30 ADC. From these one can see a clear trend,
1684 when I use the standard hit finder chain the sensitivities in the induction planes are
1685 systematically lower than the hit sensitivity in the X plane, i.e. most of the points sit
1686 below the diagonal (red dashed line). In contrast, when the matched filters are applied,
1687 the majority of the events are distributed around the diagonal. This points out that the
1688 concurrence of hits across planes has improved.

1689 To exemplify the improvement I obtained, one can consider the residuals of the hit
1690 sensitivities for the X and U planes. Assuming the diagonal hypothesis, i.e. given a
1691 dataset of the form (x, y) for any x I take the predicted y value to be equal to the value
1692 of x , I can compute the standard residuals for the hit sensitivities in U given the ones for
1693 X. In Fig. 6.21 (top panels) I show these standard residuals against the corresponding
1694 values of the hit sensitivity in the U plane, for our electron sample with kinetic energy
1695 between 5 and 100 MeV. If I compare the scatter points in the case of the standard
1696 hits (left panel) and the matched filter hits (right panel), I see that the residuals of the
1697 standard hit finder case follow a certain pattern and their mean deviates from 0.

1698 To see clearly if the residuals are normally distributed, in Fig. 6.21 (bottom panels)
1699 I plot the corresponding quantile-quantile plot for both the standard (left panel) and
1700 matched filter (right panel) standard residuals. One can clearly see that the points for
1701 the standard case follow a strongly non-linear pattern, suggesting that the residuals
1702 do not follow a normal distribution. In contrast, for the matched filter hits the points
1703 conform to a roughly linear path, implying that in this case the normality condition is
1704 fulfilled.

1705 All these results hint at the fact that the concurrence of hits across the wire planes
1706 can be strengthened by applying the matched filters.

1707 **Chapter 7**

1708 **DM searches with neutrinos from
1709 the Sun**

1710 **7.1 Motivation**

1711 The idea of detecting neutrino signals coming from the Sun’s core to probe DM is not new.
1712 The main focus of these searches has usually been high-energy neutrinos originated from
1713 DM annihilations into heavy particles [61–64], although recent studies have proposed to
1714 look at the low-energy neutrino flux arising from the decay of light mesons at rest in the
1715 Sun [65–68] previously thought undetectable.

1716 In this chapter I try to demonstrate the capability of DUNE to constrain different
1717 DM scenarios. I used the neutrino fluxes arising from DM annihilations in the core
1718 of the Sun to compute the projected limits that DUNE would be able to set on the
1719 annihilation rates in the Sun and the DM scattering cross sections.

1720 **7.2 Gravitational capture of DM by the Sun**

1721 The Sun and the centre of the Earth are possible sources of DM annihilations, specially
1722 interesting because of their proximity. Their gravitational attraction ensured the capture
1723 of DM from the local halo through repeated scatterings of DM particles crossing them.

Chapter 7. DM searches with neutrinos from the Sun

1724 Only neutrinos produced from DM annihilations can escape the dense interior of these
1725 objects. Therefore, neutrino telescopes are the most useful experimental layouts to
1726 pursue DM searches from their cores.

1727 The neutrino flux from DM annihilations inside the Sun depends on the DM capture
1728 rate, which is proportional to the DM scattering cross section, and the annihilation rate,
1729 which is proportional to the velocity-averaged DM annihilation cross-section. The total
1730 number of DM particles inside the Sun follows the Boltzmann equation [65]:

$$\frac{dN_{DM}}{dt} = C_{\odot} - A_{\odot} N_{DM}^2, \quad (7.1)$$

1731 where C_{\odot} and A_{\odot} are the total Sun DM capture and annihilation rates respectively.
1732 In this expression I neglected the evaporation term, proportional to N_{DM} , which only
1733 contribute for $m_{DM} \lesssim 4$ GeV [69]. As the current threshold of neutrino telescopes is
1734 a few GeV, this region falls below the probed range but can be important in future
1735 low-energy projects.

1736 This equation has an equilibrium solution:

$$N_{DM}^{eq} = \sqrt{\frac{C_{\odot}}{A_{\odot}}}, \quad (7.2)$$

1737 which represents the amount of DM inside the Sun if the capture and annihilation have
1738 reached equilibrium. As the Sun is approximately 4.6 Gyr old, it is usually assumed that
1739 equilibrium has been achieved. Therefore, the anomalous neutrino flux from the Sun
1740 would only depend on the DM scattering cross section, enabling us to set limits on this
1741 quantity. If one does not assume equilibrium, some assumptions on the DM annihilation
1742 cross section are necessary to extract predictions from neutrino signals.

1743 Here, I am going to consider three possible scenarios for the DM interactions: DM
1744 scattering off electrons, spin-dependent (SD) and spin-independent interactions off nuclei.
1745 For the case of these last two, the cross sections will be given in terms of the SD and
1746 SI elastic scattering DM cross section off protons (assuming that DM interactions off

7.2. Gravitational capture of DM by the Sun

1747 protons and neutrons are identical), σ_p^{SD} and σ_p^{SI} , as [4, 65]:

$$\sigma_i^{\text{SD}} = \left(\frac{\tilde{\mu}_{A_i}}{\tilde{\mu}_p} \right)^2 \frac{4(J_i + 1)}{3J_i} |\langle S_{p,i} \rangle + \langle S_{n,i} \rangle|^2 \sigma_p^{\text{SD}}, \quad (7.3)$$

$$\sigma_i^{\text{SI}} = \left(\frac{\tilde{\mu}_{A_i}}{\tilde{\mu}_p} \right)^2 A_i^2 \sigma_p^{\text{SI}}, \quad (7.4)$$

1748 where $\tilde{\mu}_{A_i}$ is the reduced mass of the DM-nucleus i system, $\tilde{\mu}_p$ is the reduced mass of
1749 the DM-proton system, A_i and J_i the mass number and total angular momentum of
1750 nucleus i and $\langle S_{p,i} \rangle$ and $\langle S_{n,i} \rangle$ the expectation value of the spins of protons and neutrons
1751 averaged over all nucleons, respectively (see Ref. [70] for a review on spin expectation
1752 values).

1753 Since the Sun is mainly composed of Hydrogen, the capture of DM from the halo
1754 is expected to occur mainly through spin-dependent scattering. However, since the
1755 spin-independent cross section is proportional to the square of the atomic mass, heavy
1756 elements can contribute to the capture rate (even though they constitute less than 2%
1757 of the mass of the Sun). Heavy elements can also contribute to the spin-dependent cross
1758 section if the DM has also momentum-dependent interactions.

1759 DM particles can get captured by the Sun if after repeated scatterings off solar
1760 targets their final velocity is lower than the escape velocity of the Sun. In the limit of
1761 weak cross sections, this capture rate can be approximately written as [4]:

$$C_{\odot}^{\text{weak}} = \sum_i \int_0^{R_{\odot}} dr 4\pi r^2 \int_0^{\infty} du_{\chi} \frac{\rho_{\chi}}{m_{\chi}} \frac{f_{v_{\odot}}(u_{\chi})}{u_{\chi}} \omega(r) \int_0^{v_e(r)} dv R_i^-(\omega \rightarrow v) |F_i(q)|^2, \quad (7.5)$$

1762 where the summation extends over all possible nuclear targets. In this expression, R_{\odot}
1763 is the radius of the Sun, ρ_{χ} is the local DM density, m_{χ} the mass of the DM particle,
1764 $f_{v_{\odot}}(u_{\chi})$ the DM velocity distribution seen from the Sun's reference frame, $R_i^-(\omega \rightarrow v)$
1765 is the differential rate at which a DM particle with velocity v scatters a solar target of
1766 mass m_i to end up with a velocity ω and $|F_i(q)|$ is the nuclear form factor of target i .

1767 The differential scattering rate takes a rather simple form when considering velocity-

Chapter 7. DM searches with neutrinos from the Sun

1768 independent and isotropic cross sections. In that case, this quantity is given by [4, 71]:

$$R_i^-(\omega \rightarrow v) = \frac{2}{\sqrt{\pi}} \frac{\mu_{i,+}^2}{\mu_i} \frac{v}{\omega} n_i(r) \sigma_i \left[\chi(-\alpha_-, \alpha_+) + \chi(-\beta_-, \beta_+) e^{\mu_i(\omega^2 - v^2)/u_i^2(r)} \right], \quad (7.6)$$

1769 where μ_i is the ratio between the DM mass and the mass of target i , $\mu_{i,\pm}$ is defined as:

$$\mu_{i,\pm} \equiv \frac{\mu_i \pm 1}{2}, \quad (7.7)$$

1770 $n_i(r)$ is the density profile of target i in the solar medium, $u_i(r)$ is the most probable

1771 velocity of target i given by:

$$u_i(r) = \sqrt{\frac{2T_\odot(r)}{m_i}}, \quad (7.8)$$

1772 where $T_\odot(r)$ is the temperature of the Sun, the quantities α_\pm and β_\pm are defined as:

$$\alpha_\pm \equiv \frac{\mu_{i,+}v \pm \mu_{i,-}\omega}{u_i(r)}, \quad (7.9)$$

$$\beta_\pm \equiv \frac{\mu_{i,-}v \pm \mu_{i,+}\omega}{u_i(r)}, \quad (7.10)$$

1773 and the function $\chi(a, b)$ is a Gaussian integral of the form:

$$\chi(a, b) \equiv \int_a^b dx e^{-x^2}. \quad (7.11)$$

1774 Finally, if one assumes the DM halo velocity distribution in the galactic rest frame

1775 to be a Maxwell-Boltzmann distribution, one can write the halo velocity distribution for

1776 an observer moving at the speed of the Sun with respect to the DM rest frame as:

$$f_{v_\odot}(u_\chi) = \sqrt{\frac{3}{2\pi}} \frac{u_\chi}{v_\odot v_d} \left(e^{-\frac{3(u_\chi - v_\odot)^2}{2v_d^2}} - e^{-\frac{3(u_\chi + v_\odot)^2}{2v_d^2}} \right), \quad (7.12)$$

1777 where:

$$\omega^2 = u_\chi + v_e(r)^2, \quad (7.13)$$

1778 is the DM velocity squared, v_\odot the relative velocity of the Sun from the DM rest frame

7.2. Gravitational capture of DM by the Sun

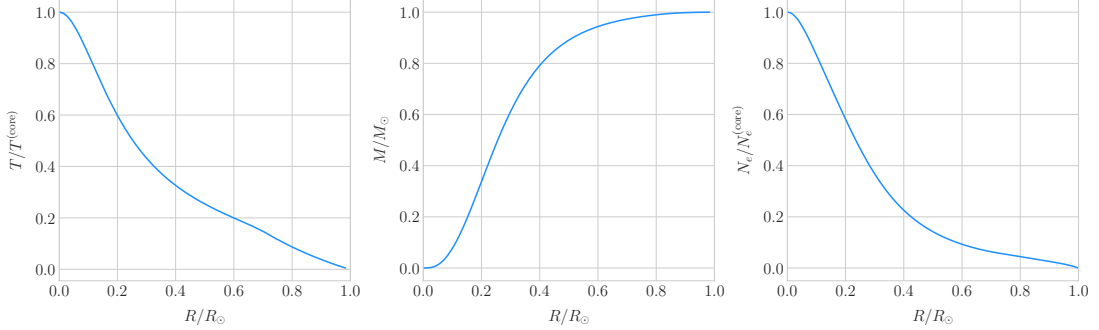


Figure 7.1: Input solar parameters used in our capture rate computation as functions of the Sun's radius, from left to right: temperature (with respect to the temperature at the core), mass (in solar masses) and electron number density (with respect to the electron density at the core). All quantities shown correspond to the standard solar model BS2005-OP [3].

and $v_d \simeq \sqrt{3/2}v_\odot$ the velocity dispersion.

For the case of strong scattering cross section, Eq. (7.5) ceases to be valid, as it escalates indefinitely with the cross section. In that limit, the capture rate saturates to the case where the probability of interaction is equal to one, which can be written as:

$$C_\odot^{\text{geom}} = \pi R_\odot^2 \left(\frac{\rho_\chi}{m_\chi} \right) \langle v \rangle \left(1 + \frac{3}{2} \frac{v_e^2(R_\odot)}{v_d^2} \right) \xi(v_\odot, v_d), \quad (7.14)$$

where $v_d = \sqrt{8/3\pi}v_\odot$ is the mean velocity in the DM rest frame and the factor $\xi(v_\odot, v_d)$ accounts for the suppression due to the motion of the Sun:

$$\xi(v_\odot, v_d) = \frac{v_d^2 e^{-\frac{3v_\odot^2}{2v_d^2}} + \sqrt{\frac{\pi}{6}} \frac{v_d}{v_\odot} (v_d^2 + 3v_e^2(R_\odot) + 3v_\odot^2) \text{Erf} \left(\sqrt{\frac{3}{2}} \frac{v_\odot}{v_d} \right)}{2v_d^2 + 3v_e^2(R_\odot)}. \quad (7.15)$$

Having these into account, one can write the total capture rate as a combination of both contributions, allowing a smooth transition between the two, as:

$$C_\odot = C_\odot^{\text{weak}} \left(1 - e^{C_\odot^{\text{geom}}/C_\odot^{\text{weak}}} \right). \quad (7.16)$$

I computed the capture rate from Eq. (7.16) in the case of interactions with electrons. To do so, I used the standard solar model BS2005-OP [3]. Fig. 7.1 shows the

Chapter 7. DM searches with neutrinos from the Sun

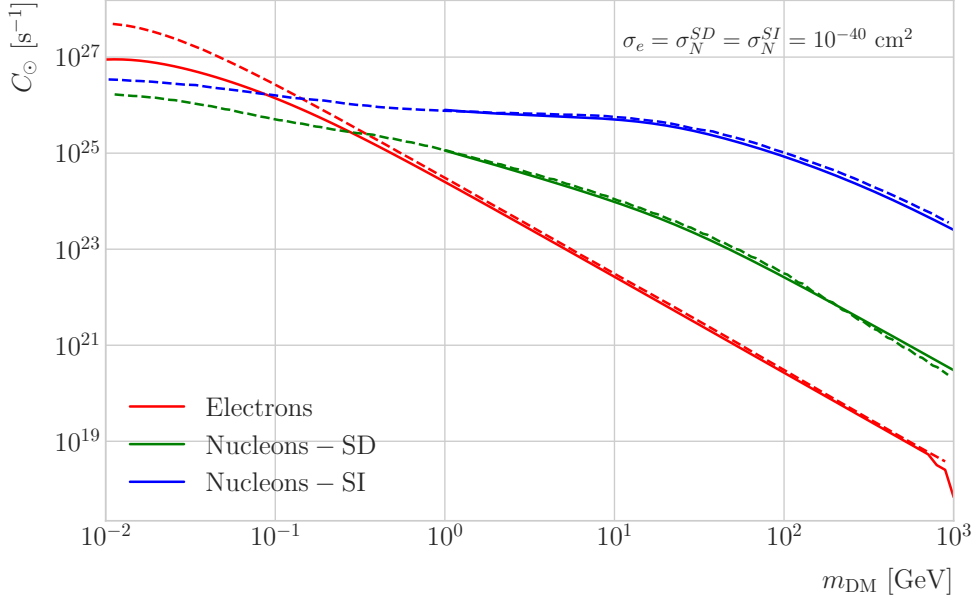


Figure 7.2: Capture rates as a function of the DM mass for the DM-electron interactions (red lines), SD DM-nucleons interactions (green lines) and SI DM-nucleons interactions (blue lines). Solid lines represent the values computed in this work while the dashed lines are the one given in Ref. [4]. All the rates are shown for a choice of scattering cross section of $\sigma_i = 10^{-40} \text{ cm}^2$.

1789 three parameters from the solar model that are needed for the computation, the solar
 1790 temperature (left panel), mass (central panel) and electron density (right panel) profiles.

1791 For the case of the interactions off nuclei, the computations are more convoluted
 1792 as one needs to add up the contributions of the different most abundant nuclei in
 1793 the Sun. Also, in contrast to the electron scenario where the form factor is trivially
 1794 $|F_e(q)|^2 = 1$, for any nucleus i one would need to consider some appropriate nuclear
 1795 density distribution (either a Gaussian approximation, a Woods-Saxon distribution, etc)
 1796 which would complicate the calculations even further.

1797 That is the reason why, at this stage of our study, I decided to take an alternative
 1798 approach to the computation of the DM-nucleus capture rates. I used the **DarkSUSY**
 1799 software, that allows us to compute these quantities performing a full numerical
 1800 integration over the momentum transfer of the form factors. The default standard
 1801 solar model used by **DarkSUSY** is BP2000¹ [72].

¹This is what they say in their manual, but I fear it is somewhat outdated. It appears to me this

7.2. Gravitational capture of DM by the Sun

1802 In Fig. 7.2 I show the results I obtained for the capture rates, for the case of
 1803 interactions off electrons (red solid line), SD (green solid line) and SI (blue solid line)
 1804 interactions of nucleons. In all cases I used a value of the scattering cross sections of
 1805 $\sigma_i = 10^{-40} \text{ cm}^2$. Note here one of the limitations of the **DarkSUSY** approach, one can
 1806 not extend the computation below $m_{\text{DM}} = 1 \text{ GeV}$. Nevertheless, this is not something
 1807 to worry about in this case, as I will discuss next. As a comparison, I added also the
 1808 values computed in Ref. [4] (same color scheme, dashed lines). One can see there is good
 1809 agreement between these and the **DarkSUSY** computation of the SD and SI interactions
 1810 for $m_{\text{DM}} \geq 1 \text{ GeV}$. In this regime their computations also matches quite well our
 1811 result for the electron capture rate. However, these start to differ significantly below
 1812 $m_{\text{DM}} = 1 \text{ GeV}$, being their estimate up to a factor of 5 bigger than ours for low masses.

1813 Let us comment briefly about the assumption I made before about not including
 1814 an evaporation term in the Boltzmann equation. If I include this term in the equation
 1815 (which will be proportional to the number of DM particles) the equilibrium solution
 1816 takes the form:

$$N_{\text{DM}}^{eq} = \sqrt{\frac{C_{\odot}}{A_{\odot}}} \frac{1}{\kappa + \frac{1}{2} E_{\odot} \tau_{eq}}, \quad (7.17)$$

1817 where E_{\odot} is the total evaporation rate, τ_{eq} is the equilibrium time in the absence of
 1818 evaporation:

$$\tau_{eq} = \frac{1}{\sqrt{C_{\odot} A_{\odot}}}, \quad (7.18)$$

1819 and κ is defined as:

$$\kappa \equiv \sqrt{1 + \left(\frac{E_{\odot} \tau_{eq}}{2} \right)^2}. \quad (7.19)$$

1820 Now, it is easy to proof that in case evaporation dominates $\kappa \gg 1$ and therefore:

$$N_{\text{DM}}^{eq} \simeq \frac{C_{\odot}}{E_{\odot}}. \quad (7.20)$$

1821 In contrast, if evaporation is irrelevant $\kappa \simeq 1$ and one recovers Eq. (7.2).

model is relatively old and do not see why they are not using others like [3]. Maybe one can double-check in the code to make sure.

Chapter 7. DM searches with neutrinos from the Sun

1822 In this way, one can define the evaporation mass as the mass for which the number
1823 of DM particles in equilibrium approaches Eq. (7.20) at 10% level:

$$\left| N_{DM}^{eq}(m_{\text{evap}}) - \frac{C_{\odot}(m_{\text{evap}})}{E_{\odot}(m_{\text{evap}})} \right| = 0.1 N_{DM}^{eq}(m_{\text{evap}}). \quad (7.21)$$

1824 This can be regarded as the minimum testable mass one can reach using the annihilation
1825 products of the DM in the Sun.

1826 It was reported in Ref. [4] that, in the case of both SD and SI DM interactions
1827 off nuclei, this value ranges from 2 to 4 GeV depending on the specific scattering
1828 cross section value, compatible with the usual assumptions in the literature. What is
1829 interesting is the case of the electron capture. It was found that, when one applies a
1830 cutoff in the velocity distribution of the DM trapped in the Sun slightly below the escape
1831 velocity, the evaporation mass for the DM-electron interaction decreases remarkably. For
1832 a moderate choice of $v_c(r) = 0.9v_e(r)$ one gets an evaporation mass of around 200 to
1833 600 MeV. This possibility opens a region of the parameter space that could be tested
1834 with neutrino detectors.

1835 7.3 Neutrino flux from DM annihilations

1836 When WIMPs annihilate inside the Sun a flux of high-energy neutrinos is expected from
1837 heavy quarks, gauge bosons and $\tau^+\tau^-$ final states, which decay before losing energy
1838 in the dense solar medium, as they will produce a continuum spectra up to $E_{\nu} \sim m_{\chi}$
1839 (in the case of direct annihilation to neutrinos one would have a line at $E_{\nu} = m_{\chi}$) [66].
1840 This kind of signal has been extensively studied in the literature, allowing to put strong
1841 limits on the SD WIMP-proton cross section for large m_{χ} . However, the number of
1842 high-energy neutrinos per WIMP annihilation is small and the spectrum depends on the
1843 unknown final state. Moreover, background rejection is easier for large m_{χ} but neutrinos
1844 with $E_{\nu} \gtrsim 100$ GeV are significantly attenuated by interactions in the Sun.

1845 Nevertheless, most WIMP annihilation final states eventually produce a low-energy
1846 neutrino spectrum. In this case one does not just consider the more massive final

7.4. Computing limits from solar neutrino fluxes

1847 states but also annihilations into e^+e^- , $\mu^+\mu^-$ and light quarks [65]. In particular, light
 1848 mesons would be produced and stopped in the dense medium, thus decaying at rest and
 1849 producing a monoenergetic neutrino signal. The decay-at-rest of kaons will produce
 1850 a $E_\nu = 236$ MeV ν_μ while in the case of pions one would have a $E_\nu = 29.8$ MeV ν_μ .
 1851 In practice only K^+ and π^+ contribute to these signals, as K^- and π^- are usually
 1852 Coulomb-captured in an atomic orbit and get absorbed by the nucleus. There is also a
 1853 low-energy neutrino signal coming from muon decays, which are produced in kaon or
 1854 pion decays, leptonic decays of other hadrons and heavy leptons or even directly from
 1855 WIMP annihilations, which can decay at rest and contribute to the previous low-energy
 1856 neutrino flux with a well known spectrum below 52.8 MeV.

1857 These monoenergetic MeV neutrinos were previously considered undetectable but,
 1858 due to the large yield, the known spectra and the modern advances in the detector
 1859 technology, these low-energy neutrino flux can be a good probe of the SD WIMP-proton
 1860 cross-section in standard solar WIMP capture scenario, as it is sensitive to low WIMP
 1861 masses and insensitive to the particular final state. A good place to look for these signals
 1862 are next-generation neutrino experiments such as DUNE.

1863 7.4 Computing limits from solar neutrino fluxes

1864 In order to use the neutrino fluxes from DM annihilations in the Sun, the first thing I
 1865 need to do is to determine the expected number of atmospheric background events, for
 1866 a given exposure, after directionality selection has been applied. I can write this number
 1867 as:

$$N_B = \eta_B \int d\Omega \int_{E_{min}}^{E_{max}} dE_\nu \frac{d^2\Phi_{atm}^\mu}{dE_\nu d\Omega} \times \left(A_{eff}^{(\mu)}(E_\nu) T \right), \quad (7.22)$$

1868 where η_B is the background efficiency, E_{min} and E_{max} the minimum and maximum
 1869 energies to integrate over, $d^2\Phi_{atm}^\mu/dE_\nu d\Omega$ the differential flux of atmospheric muon
 1870 neutrinos, $A_{eff}^{(\mu)}$ is the effective area of DUNE to muon neutrinos and T is the exposure
 1871 time. The effective area can be expressed as the product of the neutrino-nucleus scattering
 1872 cross section and the number of nuclei in the fiducial volume of the detector. This way

Chapter 7. DM searches with neutrinos from the Sun

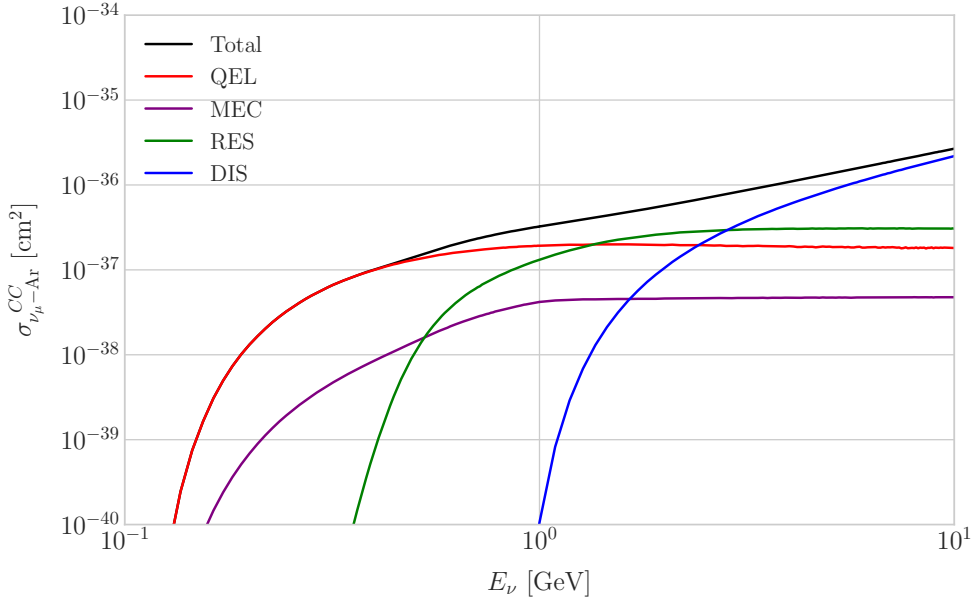


Figure 7.3: *NuWro* computed $\nu_\mu - {}^{40}\text{Ar}$ charged-current scattering cross section as a function of the neutrino energy E_μ . The black line shows to the total cross section, whereas the others correspond to the different contributions (in red quasi-elastic scattering, in green resonant pion exchange, in blue deep inelastic scattering and in purple meson exchange current).

1873 for DUNE I can write:

$$A_{eff}^{(\mu)}(E_\nu) = (6.0 \times 10^{-10} \text{ m}^2) \left(\frac{\sigma_{\nu - \text{Ar}}^{(\mu)}(E_\nu)}{10^{-38} \text{ cm}^2} \right) \left(\frac{M_{target}}{40 \text{ kT}} \right), \quad (7.23)$$

1874 where $\sigma_{\nu - \text{Ar}}^{(\mu)}$ is the $\nu_\mu - {}^{40}\text{Ar}$ charged-current scattering cross section. In Fig. 7.3 I
 1875 show the computed value of this cross section as a function of the neutrino energy E_ν ,
 1876 in the range of interest both for the atmospheric background and signal events. It was
 1877 computed using the NuWro Monte Carlo neutrino event generator [73], including the
 1878 charged-current contributions of the quasi-elastic scattering (red line), resonant pion
 1879 exchange (green line), deep inelastic scattering (blue line) and meson exchange current
 1880 (purple line).

1881 The background rejection will depend on the resolution of the detector and the
 1882 selection one applies on the events. A geometry argument can be used to estimate
 1883 the maximum background rejection one can achieve in this case, considering one can

7.4. Computing limits from solar neutrino fluxes

1884 efficiently discriminate all events coming from a direction different from that of the
 1885 Sun. In that case, the optimal background efficiency will simply be the relative angular
 1886 coverage of the Sun. Taking the angular diameter of the Sun as seen from the Earth to
 1887 be 0.5° , I have:

$$\eta_B^{(opt)} \approx \frac{\pi \left(\frac{0.5}{2}\right)^2}{360 \times 180} \simeq 3.03 \times 10^{-6}. \quad (7.24)$$

1888 This value will give a very optimistic estimate of the number of background events.
 1889 However, it can be regarded as an lower limit, as it represents the best case scenario.

1890 In Fig. 7.4 I show the fluxes of atmospheric neutrinos at the Homestake mine during
 1891 solar minimum, taken from Ref. [5]. The values are averaged over the two angular
 1892 directions. In blue I have the flux of muon neutrinos while in red I indicate the flux
 1893 of electron neutrinos. Additionally, the dashed lines correspond to both antineutrino
 1894 species.

1895 Using these values for the muon neutrino and the corresponding total CC cross
 1896 section, one can compute the number of expected background events by integrating over
 1897 the given energy range (as in this case the angular integral is trivial). As for the energy
 1898 range to integrate over, I choose the range for DUNE specified in [42], $E_{min} = 10^{-1}$ GeV
 1899 and $E_{max} = 10$ GeV. Taking all these into account, I found the number of background
 1900 events to be:

$$N_B \simeq \eta_B \times (3.827 \times 10^4) \times \left(\frac{\text{exposure}}{400 \text{ kT yr}} \right). \quad (7.25)$$

1901 In order to estimate the sensitivity of DUNE to this kind signal, one can consider a
 1902 hypothetical data set where the number of observed neutrinos is taken to be the expected
 1903 number of background events rounded to the nearest integer, $N_{obs} = \text{round}(N_B)$ [74].
 1904 Now, if I assume that the number of signal and background events seen by DUNE are
 1905 given by Poisson distributions with means equal to the expected number of signal and
 1906 background events, N_S and N_B , one can denote by N_S^{90} to the number of expected
 1907 signal events such that the probability of having an experimental run with a number of
 1908 events greater than N_{obs} is 90%. This number can be obtained as the numerical solution

Chapter 7. DM searches with neutrinos from the Sun

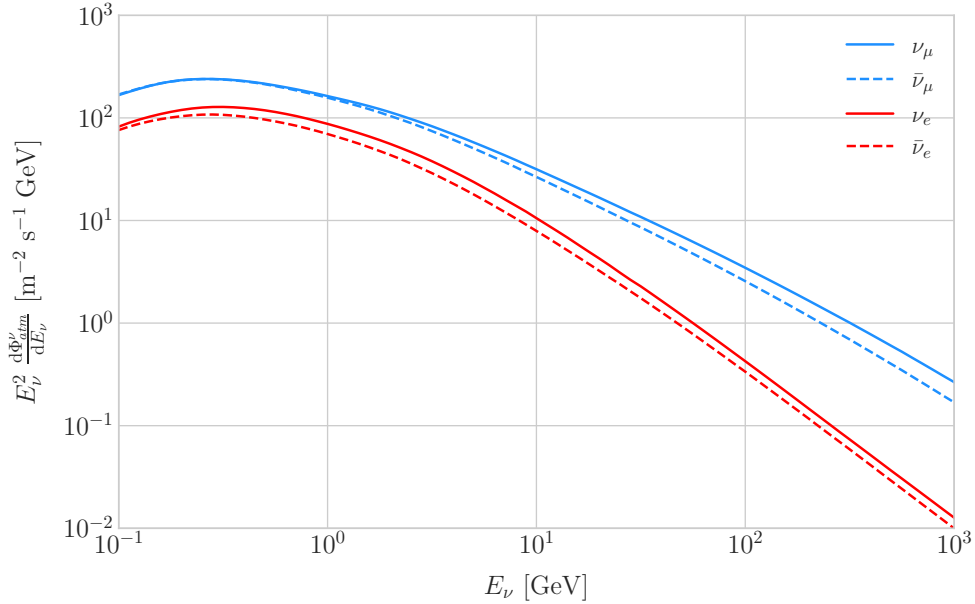


Figure 7.4: Expected atmospheric neutrino flux as a function of the neutrino energy E_ν at Homestake at solar minimum, taken from Ref. [5]. The blue solid (dashed) line correspond to muon neutrinos (antineutrinos) and the red solid (dashed) line correspond to electron neutrinos (antineutrinos).

1909 to the equation:

$$1 - \frac{\Gamma(N_{obs} + 1, N_S^{90} + N_B)}{N_{obs}!} = 0.9, \quad (7.26)$$

1910 where $\Gamma(x, y)$ is the upper incomplete gamma function.

1911 The number of signal events is related to the neutrino flux from DM annihilations in
 1912 a similar way as the background events to the atmospheric neutrino flux. In this case I
 1913 have:

$$N_S = \eta_S \Gamma_A^{eq} \int_{z_{min}}^{z_{max}} dz \frac{dN_\nu}{dAdN_A dz} \times (A_{eff}^\mu(z)T), \quad (7.27)$$

1914 where η_S is the signal efficiency, Γ_A^{eq} is the total annihilation rate of DM particles at
 1915 equilibrium, $\Gamma_A^{eq} = A_\odot (N_{DM}^{eq})^2$, z_{min} and z_{max} the minimum and maximum relative
 1916 energies to integrate over (in such a way that $z_{min,max} \leq E_{min,max}/m_{DM}$ for each m_{DM})
 1917 and $dN_\nu/dAdN_A dz$ the muon neutrino flux per DM annihilation in the Sun.

1918 Knowing N_S^{90} one can use the relation in Eq. (7.27) to obtain $\Gamma_A^{eq,90}$ for different
 1919 values of the DM mass. From there I can directly translate those values into the

7.5. Example: Kaluza-Klein Dark Matter

1920 upper limits for DUNE on the DM scattering cross sections, for a given exposure. The
1921 relation between the annihilation rate and the DM-nucleon cross section comes from the
1922 equilibrium condition through the solar DM capture rate. The details of the evolution
1923 of the number of DM particles inside the Sun and the computation of the capture rates
1924 are discussed in App. 7.2.

1925 7.5 Example: Kaluza-Klein Dark Matter

1926 Even though there are plenty of BSM theories which provide viable dark matter
1927 candidates, Kaluza-Klein type of models [75, 76] within the universal extra dimensions
1928 (UED) paradigm naturally predict the existence of a massive, stable particle that can
1929 play the role of the dark matter. In the UED scenario all the SM fields can propagate
1930 in one or more compact extra dimensions [77], as opposed to the idea of brane worlds
1931 [78, 79], where just gravity can propagate in the bulk while SM particles live at fixed
1932 points.

1933 Furthermore, in UED there is no violation of the translational invariance along the
1934 extra dimensions, thus leading to degenerate KK modes masses and also the conservation
1935 of the KK number in the effective four dimensional theory. At loop level, radiative
1936 corrections and boundary terms shift the masses of the KK modes and break KK
1937 number conservation into a KK parity. As a result, this theory only contains interactions
1938 between an even number of odd KK modes and therefore the lightest among the first KK
1939 excitations will be stable. This particle is usually denoted as the lightest Kaluza-Klein
1940 particle (LKP) and its mass is proportional to $1/R$, being R the size of the extra
1941 dimension.

1942 A viable DM candidate needs to be electrically neutral and non-baryonic, therefore
1943 good candidates among the first Kaluza-Klein excitations would be the KK neutral
1944 gauge bosons and the KK neutrinos [80]. Another possible candidate is the first KK
1945 excitation of the graviton, which receives negligible radiate contributions and therefore
1946 has a mass almost equal to $1/R$, but it has been shown that the lightest eigenstate from

Chapter 7. DM searches with neutrinos from the Sun

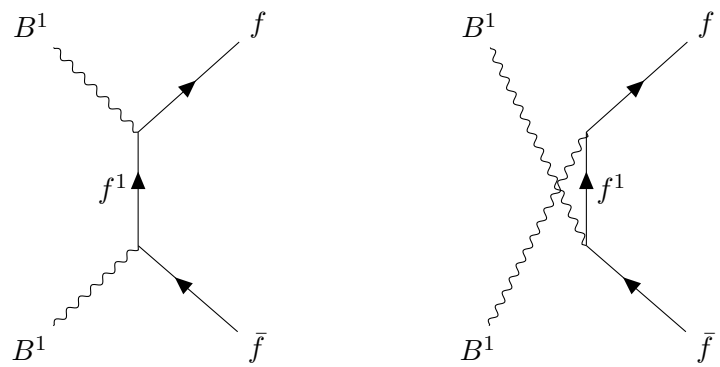


Figure 7.5: Feynman diagrams for B^1B^1 annihilation into SM fermions.

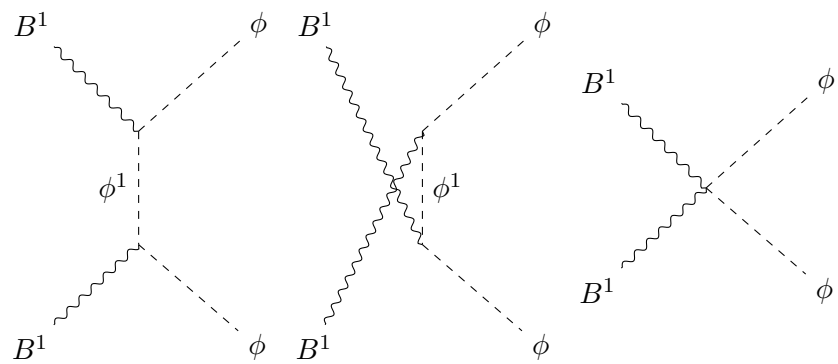


Figure 7.6: Feynman diagrams for B^1B^1 annihilation into a Higgs boson pair.

7.5. Example: Kaluza-Klein Dark Matter

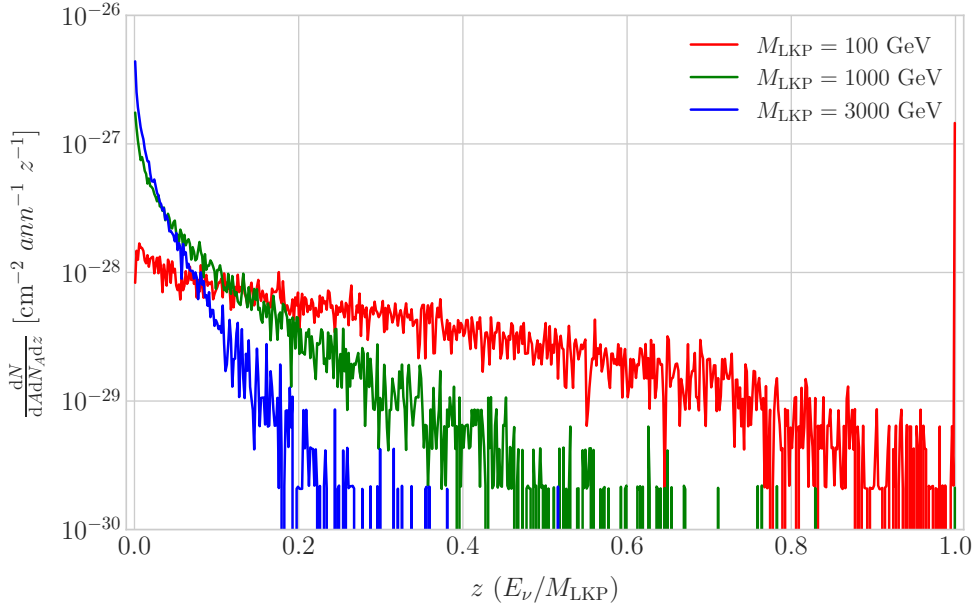


Figure 7.7: Computed spectra of muon neutrinos at the DUNE FD site from B^1 annihilations in the Sun for three different values of M_{LKP} , plotted in relative energy units for legibility.

the mixing of the gauge mass states (B^1, W_3^1) would be lighter, as B^1 and W_3^1 receive negative radiative corrections [81]. It is also understood that, when these corrections become sizeable, the eigenstates become approximately pure B^1 and W_3^1 states as the Weinberg mixing angle grows small with the KK number [81]. In that case, the LKP can be well-approximated as being entirely B^1 .

I need to compute the neutrino flux produced by the annihilations of the LKP in the core of the Sun, taking into account their propagation in the solar medium, as well as neutrino oscillations. To this end I used `WimpSim` [82, 83] to generate one million annihilation events in the Sun over a time span of four years and propagate them to the DUNE FD location ($44^\circ 20' \text{ N}, 103^\circ 45' \text{ W}$), for different values of M_{LKP} . In Fig. 7.7 I show the obtained muon neutrino spectra arriving to the detector from LKP annihilations in the Sun, per unit area and per annihilation, plotted in relative energy units for different values of the mass. As one could expect the spectra get steeper the higher is the mass, due to the absorption of high-energy neutrinos in the solar medium. Also, one can see the peak at $z = 1$ due to the direct annihilation into neutrinos $\chi\chi \rightarrow \nu\bar{\nu}$.

Chapter 7. DM searches with neutrinos from the Sun

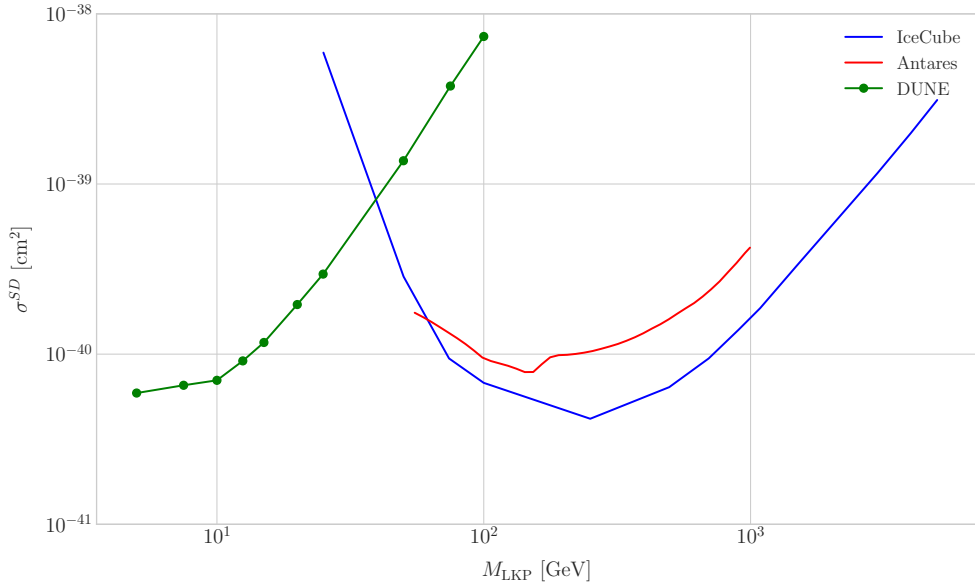


Figure 7.8: Projected 90% confidence level upper limit for DUNE (400 kT yr) on the spin-dependent B^1 -proton scattering cross section as a function of M_{LKP} (green dots). I also show the previous limits from IceCube [6] (blue line) and Antares [7] (red line) on the LKP cross section. The shaded area represents the disfavoured region (at 95% confidence level) on the mass of the LKP from LHC data [8].

Now, one can estimate the sensitivity of DUNE to this particular model by using the methods I previously discussed. To begin with, I will use the optimistic estimation of the background efficiency in Eq. (7.24) to get our upper bound. Using it, one can directly compute the number of expected background events to be $N_B = 0.1101$ for an exposure of 400 kT yr. Then, Eq. (7.26) give us a value of $N_S^{90} = 2.20$ for the 90% exclusion number of expected signal events. By using the NuWro generated cross sections and the computed neutrino fluxes from B^1 annihilations in the Sun I can estimate the limits on the SD and SI DM-nucleus cross section using the relation in Eq. (7.2) and the capture rates I computed with DarkSUSY.

In Fig. 7.8 I show the projected sensitive for DUNE on the spin-dependent B^1 -proton scattering cross section versus the mass of the DM particle, for a exposure of 400 kT yr (green dots). I also include the previous results from IceCube [6] (blue line) and Antares [7] (red line). The shaded area represents the disfavoured region from combined searches for UED by ATLAS and CMS [8].

7.6. High energy DM neutrino signals

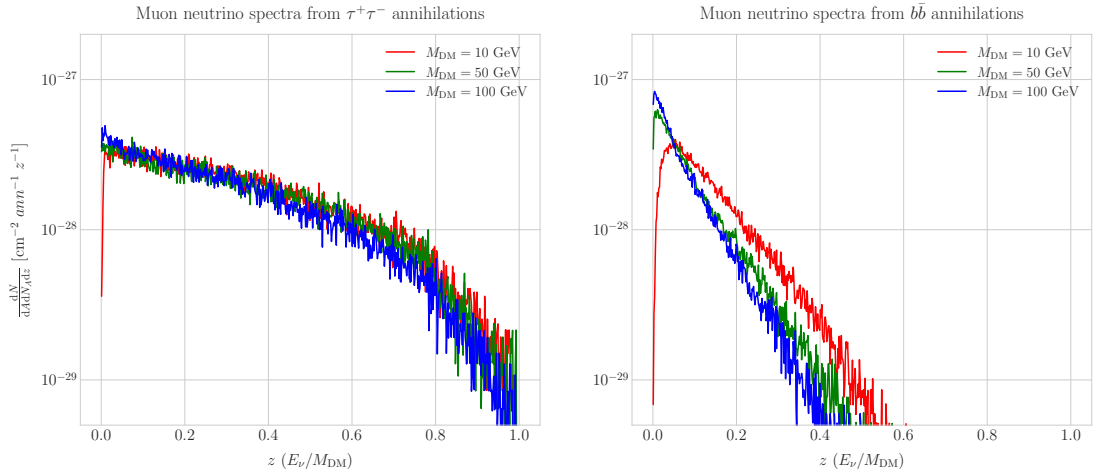


Figure 7.9: Computed spectra of muon neutrinos at the DUNE FD site from $\tau^+\tau^-$ (left panel) and $b\bar{b}$ (right panel) annihilations in the Sun for the DM masses $m_{\text{DM}} = 10 \text{ GeV}$ (red line), 50 GeV (green line) and 100 GeV (blue line), plotted in relative energy units.

From the experimental point of view, this estimation lacked a detailed simulation of the detector response and thus this must be consider as a mere optimistic sensitivity computation. However, it shows the potential of DUNE to constrain this kind of exotic scenarios, showing the region where it will be in a position to compete with other neutrino telescopes. A more detailed analysis is needed if I am to make a realistic estimation. Even though the region of the parameter space where DUNE would be sensitive to this particular model is quite constrained by collider searches [8] and other rare decay measurements [84, 85], it still constitutes an alternative indirect probe.

7.6 High energy DM neutrino signals

To have better estimates on the capability of the DUNE FD to constrain the parameter space of DM using solar neutrino fluxes, I need to start accounting for the detector resolution effects and the topologies of the different signatures. As a starting point, I will focus on specific annihilation channels. For the case of DUNE, the relevant ones are mainly the hard channels $\tau^+\tau^-$ and $\nu\bar{\nu}$ and the soft channel $b\bar{b}$. These are the open annihilation channels for relatively low mass WIMPs that will actually give neutrino fluxes. Other channels, like W^+W^- and ZZ , are open for more massive WIMPs, but

Chapter 7. DM searches with neutrinos from the Sun

1992 those will produce usually a higher energy neutrino flux that will be out of reach for
1993 DUNE (usually the maximum neutrino energy is taken to be $E_{max} = 10$ GeV).

1994 In Fig. 7.9 I show the `WimpSim` [82, 83] generated muon neutrino spectra at the
1995 DUNE FD location ($44^\circ 20' N, 103^\circ 45' W$) from $\tau^+\tau^-$ (left panel) and $b\bar{b}$ (right panel)
1996 annihilations in the core of the Sun, for different DM masses. Here, one can clearly see
1997 the meaning of the previous distinction between hard and soft channels. For the same
1998 DM mass value, the muon neutrino spectrum from the $\tau^+\tau^-$ channel is more flat and
1999 reaches higher energies than the one from the $b\bar{b}$ channel, which drops faster.

2000 In this case, I prepared two sets of files, one for $\tau^+\tau^-$ and the other for $b\bar{b}$, for DM
2001 masses in the range from 5 to 100 GeV (actually for $b\bar{b}$ the first mass point I took is
2002 7.5 GeV, as a WIMP with $m_{DM} = 5$ GeV can not kinematically self annihilate into $b\bar{b}$).
2003 Then, I prepared the `WimpSim` output fluxes in a specific way to use them as inputs to
2004 `NuWro`, which simulates the neutrino interaction with the argon.

2005 Because `WimpSim` outputs an event list together with the fluxes, I can use the former
2006 to generate the events. The direction of these is given in terms of the azimuth and
2007 altitude angles viewed from the specified location, so first I need to convert these into the
2008 DUNE FD coordinates. Once I have done it, each event can be processed with `NuWro`.
2009 To increase the number of samples and optimise the computation time, I generate 100
2010 interactions (i.e. `NuWro` events) for each `WimpSim` event². I restrict the event generation
2011 to charged current interactions, but I allow all the different contributions to the CC
2012 cross section, i.e. quasielastic scattering (QEL), meson exchange current process (MEC),
2013 resonant pion production (RES) and deep inelastic scattering (DIS). I just take into
2014 account the CC contribution because I am only interested in final states with charged
2015 leptons, as we have better chances of reconstructing the kinematics of CC events.

2016 For the atmospheric fluxes I follow a similar procedure, only that this time I do not
2017 have a set of events but the fluxes binned in azimuth and altitude angles. This way, I
2018 transform these to DUNE coordinates and process the fluxes for each bin separated with

²This also solves a problem related with the generation of the neutrino interactions in `NuWro`, as if you only produce one event each time you launch `NuWro` it will always produce an interaction of the dominant interaction type for that particular energy.

7.6. High energy DM neutrino signals

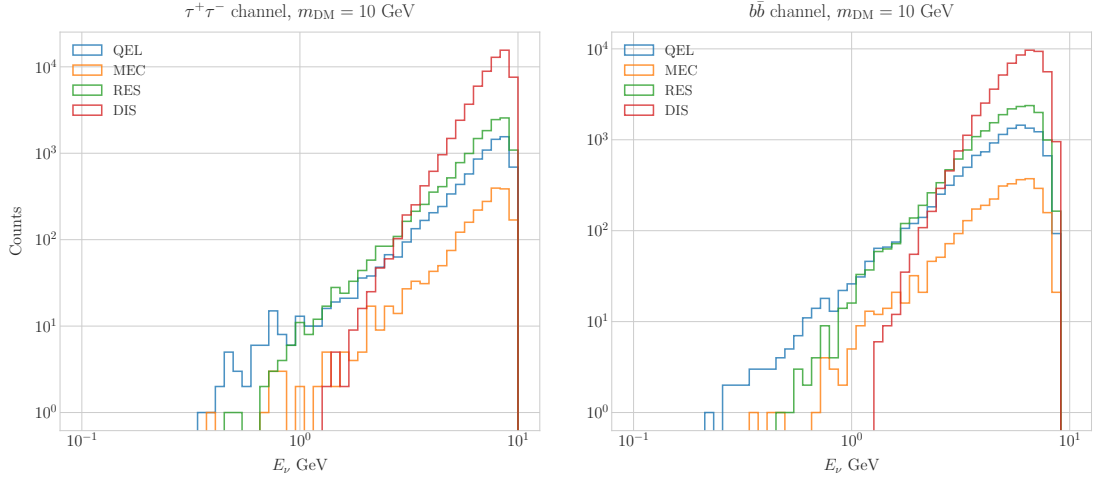


Figure 7.10: Distribution of the muon neutrino energies from the $\tau^+\tau^-$ (left panel) and $b\bar{b}$ (right panel) annihilation channels, for $m_{\text{DM}} = 10 \text{ GeV}$, separated by CC interaction type: QEL (blue), MEC (orange), RES (green) and DIS (red).

2019 NuWro.

2020 At this point, I have two sets of events with different energies and final states.
 2021 In Fig. 7.10 one can see the distribution of the muon neutrino energies for the case
 2022 $m_{\text{DM}} = 10 \text{ GeV}$, both for the $\tau^+\tau^-$ (left panel) and $b\bar{b}$ (right panel) channels, separated
 2023 by interaction. One can clearly see that there are different energy regimes where the
 2024 primary interaction type is different. This leads to a plurality of event topologies,
 2025 therefore making it difficult to implement a general approach to the selection of events
 2026 in detriment of the background. As a way to proceed, I decided to split our samples,
 2027 based on the different interaction modes and contents of the final state, into a CC DIS
 2028 sample and a single proton CC QEL sample.

2029 **7.6.1 DIS events**

2030 To begin with, I consider the high energy part of the spectrum. In this region DIS events
 2031 dominate, i.e. interactions of the form $\nu_\mu + q_d(\bar{q}_u) \rightarrow \mu^- + q_u(\bar{q}_d)$. Therefore, our final
 2032 estates will contain a muon and a hadronic jet from the fragmentation of the outgoing
 2033 quark. As all these events have $E_\nu \gtrsim 1 \text{ GeV}$ the momentum transfer to the remnant
 2034 nucleus is negligible, for this reason the neutrino energy can be effectively reconstructed

Chapter 7. DM searches with neutrinos from the Sun

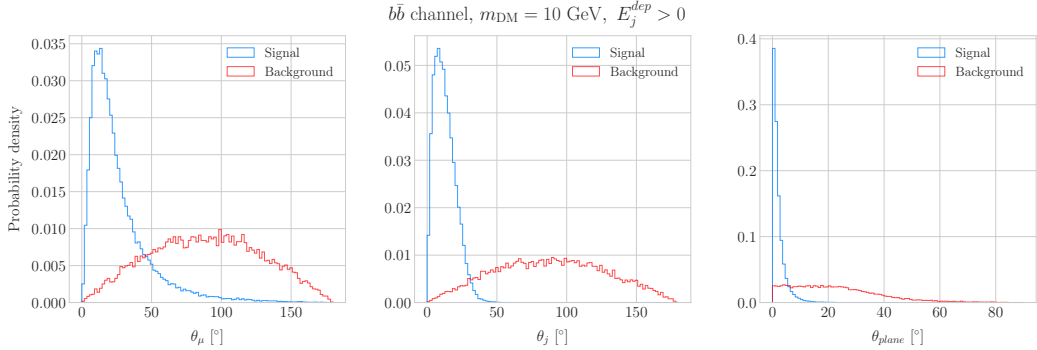


Figure 7.11: Distributions of θ_μ (left panel), θ_j (central panel) and θ_{plane} (right panel) for the $b\bar{b}$ sample with $m_{\text{DM}} = 10 \text{ GeV}$ (blue) and the atmospheric background (red).

2035 just taking into account the momenta of the muon and the jet. This technique was
 2036 successfully used in Ref. [86] to select monoenergetic DM solar neutrino events from $\nu\bar{\nu}$
 2037 annihilation channels.

2038 Using momentum conservation one sees that the plane generated by the momenta
 2039 of the muon and the jet needs to also contain the momentum of the neutrino. As we
 2040 are interested in neutrinos coming from the Sun, the momentum of the neutrino can be
 2041 regarded as known beforehand. This will allow us to define the angle of the outgoing
 2042 muon and jet with respect to the incoming neutrino. Moreover, one can also use that
 2043 information to reject poorly reconstructed jets, checking for deviations of these from the
 2044 momentum conservation plane.

2045 To account for the limited angular resolution of the detector, I smeared the momenta
 2046 of the muons and hadrons. In a liquid argon TPC muons are expected to be tracked with
 2047 high precision, therefore I take the associated angular resolution to be 1° . In the case of
 2048 jets, it is expected that for the hadrons dominating the cascade a detector like DUNE
 2049 has an angular resolution between 1° to 5° [42], so I take the latter, more conservative,
 2050 estimate.

2051 As a first selection step, I will just take into account particles with kinetic energies
 2052 above the detection threshold of DUNE. For muons and photons the specified threshold
 2053 energy is 30 MeV, for charged pions 100 MeV and for other hadrons 50 MeV [42]. This
 2054 way, if the outgoing muon in a certain event has an energy lower than the required

7.6. High energy DM neutrino signals

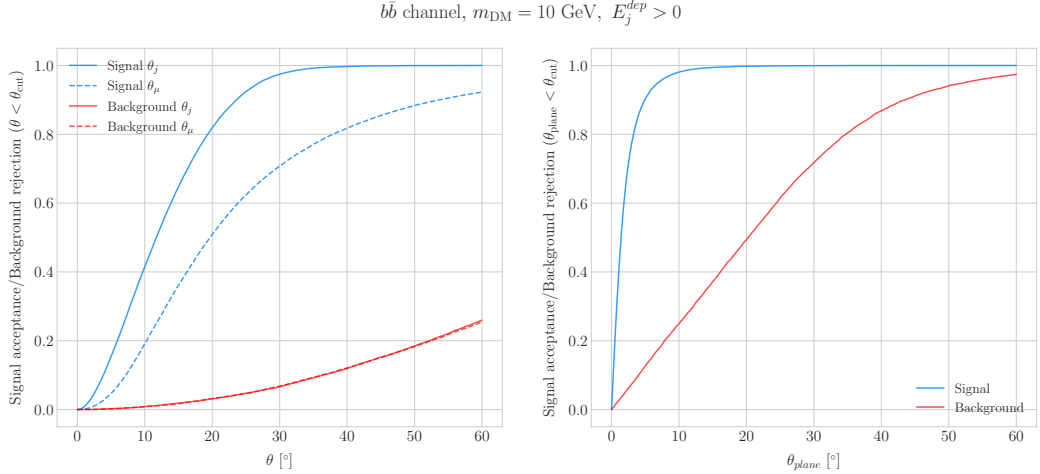


Figure 7.12: Left panel: signal efficiencies (blue lines) and background rejections (red lines) for events passing the cuts $\theta < \theta_{\text{cut}}$ for the jet (solid lines) and muon (dashed lines) angles. Right panel: signal efficiency (blue line) and background rejection (red line) for events passing the cut $\theta_{\text{plane}} < \theta_{\text{cut}}$ for the momentum conservation plane deviation.

threshold I will drop such event. For the case of hadrons and photons, I will only require to have at least one particle above the energy threshold, so then one can compute the jet momentum using the (smeared) momenta of the N particles above threshold as:

$$\vec{p}_j = \sum_{i=1}^N \vec{p}_i. \quad (7.28)$$

Additionally, I will also define an estimation of the deposited hadronic energy as:

$$E_j^{\text{dep}} = m_{^{39}\text{Ar}} - m_{^{40}\text{Ar}} + \sum_{i=1}^N \sqrt{|\vec{p}_i|^2 + m_i^2}. \quad (7.29)$$

This quantity is useful to select events with enough hadronic visible energy in the detector. For events where most of the hadronic energy is scattered across plenty of hadrons with individual energies below the detection threshold, this estimation will give $E_j^{\text{dep}} \leq 0$. In these cases it could be expected that the jet momentum is poorly reconstructed, and therefore I require events to pass the cut $E_j^{\text{dep}} > 0$.

For the events I can compute the angles for the muon and jet with respect to the

Chapter 7. DM searches with neutrinos from the Sun

2065 incoming neutrino as:

$$\cos \theta_\mu = \hat{p}_\nu \cdot \hat{p}_\mu, \quad (7.30)$$

$$\cos \theta_j = \hat{p}_\nu \cdot \hat{p}_j, \quad (7.31)$$

2066 and the deviation from the momentum conservation plane as:

$$\sin \theta_{plane} = \left| \frac{\hat{p}_\mu \times \hat{p}_\nu}{|\hat{p}_\mu \times \hat{p}_\nu|} \cdot \hat{p}_j \right|. \quad (7.32)$$

2067 In Fig. 7.11 I show some distributions of these quantities for the case of the $b\bar{b}$ sample
 2068 with $m_{DM} = 10$ GeV (blue histograms) and for the atmospheric backgrounds (red).
 2069 In order to select the atmospheric events I followed the same criteria as for the signal
 2070 events. However, because in the signal case I used the true direction of the neutrino
 2071 as input, as it should be that of the Sun at that time and therefore known, in the
 2072 atmospheric case I used a set of solar positions as our ansatz for the neutrino direction.
 2073 From the distributions, one can see that the muon and the jet for the signal events are
 2074 predominantly forward and also that the deviations from the momentum conservation
 2075 plane are peaked at zero, as one should expect.

2076 Now, I can start applying cuts to maximise our signal selection efficiency while at
 2077 the same time I try to minimise the amount of atmospheric background events passing
 2078 the selection. To this end, I will need to find some lower and upper cuts for θ_j and
 2079 θ_μ and an upper bound for θ_{plane} . In Fig. 7.12 I show how upper bound cuts in the
 2080 different angular variables affect the signal efficiency (blue lines) and the background
 2081 rejection (red lines). Notice that the signal efficiency behaves in a quite different way
 2082 when I apply cuts in the jet and the muon angles. On the contrary, the cuts on both
 2083 variables have a similar effect on the background rejection.

2084 In order to obtain the optimal set of cuts, I perform a multidimensional scan. I
 2085 do this separately for the $\tau^+\tau^-$ and the $b\bar{b}$ samples. For each case, I scan the possible
 2086 cuts for each mass point and then I take the mean value of the signal efficiency for

7.6. High energy DM neutrino signals

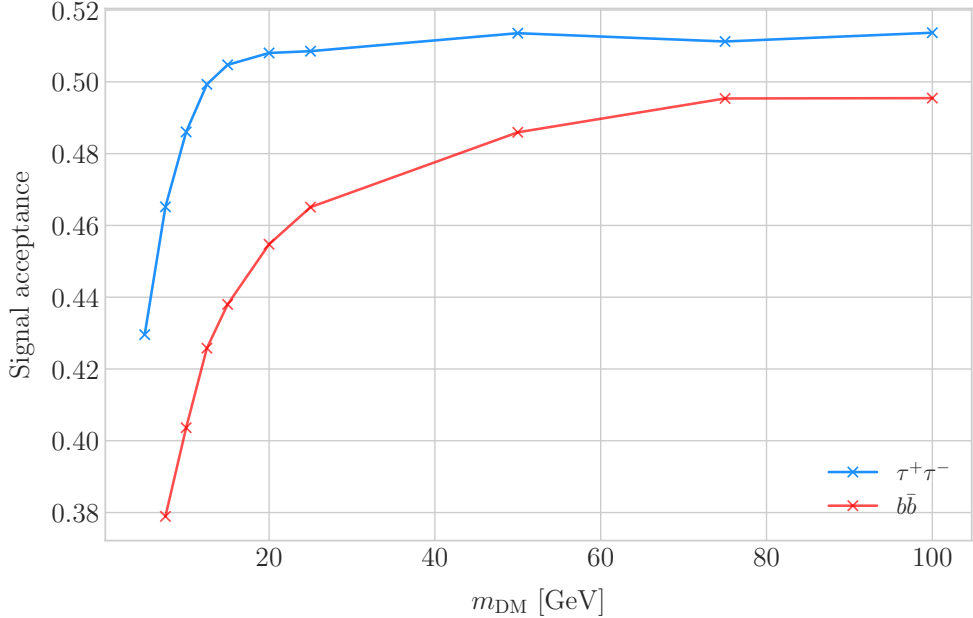


Figure 7.13: Signal efficiencies for the $\tau^+\tau^-$ (blue line) and $b\bar{b}$ (red line) DIS samples as functions of the DM mass, m_{DM} , obtained by applying the optimal angular cuts $\theta_\mu < 27^\circ$, $4^\circ < \theta_j < 26^\circ$ and $\theta_{\text{plane}} < 3.5^\circ$.

2087 each configuration, to get the mean efficiency for each set of cuts. I do a similar scan
 2088 for the atmospheric sample independently. Then, I take the sets of cuts such that
 2089 the background rejection achieved is greater than 99.8% and search for the one which
 2090 maximises the $\tau^+\tau^-$ and $b\bar{b}$ sample mean efficiencies. I found that with the cuts $\theta_\mu < 27^\circ$,
 2091 $4^\circ < \theta_j < 26^\circ$ and $\theta_{\text{plane}} < 3.5^\circ$ I get a background rejection of 99.80% while achieving
 2092 a 49.40% and 44.92% mean signal efficiencies for the $\tau^+\tau^-$ and $b\bar{b}$ signals respectively.

2093 In Fig. 7.13 I show the signal efficiencies as a function of the DM mass for the $\tau^+\tau^-$
 2094 (blue line) and the $b\bar{b}$ (red line) DIS events, after applying the cuts discussed above, as
 2095 well as the energy threshold and hadronic visible energy selections. One can see that
 2096 the efficiency grows with the mass, as annihilations of more massive DM particles will
 2097 produce a neutrino spectrum centered at higher energies, where DIS events dominate.
 2098 Notice also that the efficiency is higher for the $\tau^+\tau^-$ case at every mass point, as in
 2099 general this channel produces neutrinos at higher energies than the corresponding $b\bar{b}$
 2100 channel.

Chapter 7. DM searches with neutrinos from the Sun

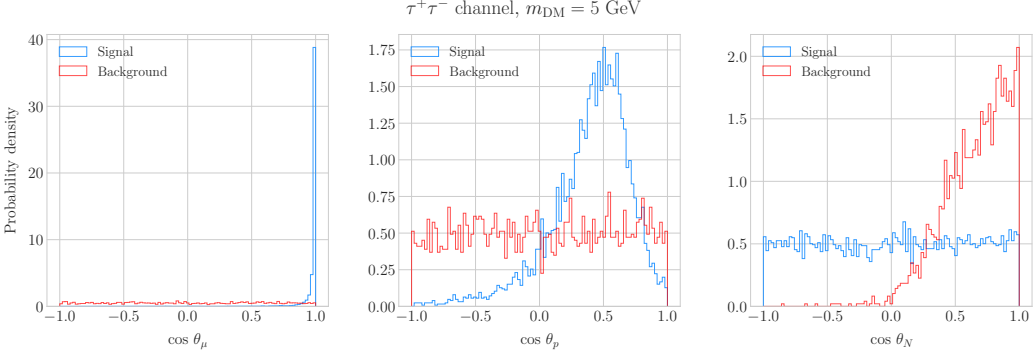


Figure 7.14: Distributions of $\cos \theta_\mu$ (left panel), $\cos \theta_p$ (central panel) and $\cos \theta_N$ (right panel) for the $\tau^+\tau^-$ QEL sample with $m_{\text{DM}} = 5$ GeV (blue) and the atmospheric background (red).

2101 7.6.2 Single proton QEL events

2102 Now, one can try to explore the low energy tail of the neutrino energy distributions. This
 2103 regime is dominated by the QEL interactions, i.e. events of the type $\nu_\mu + n \rightarrow \mu^- + p$.
 2104 In this case, as the typical energies are $E_\nu \lesssim 1$ GeV, the momentum transfer to the
 2105 remnant nucleus is sizeable. Therefore, I can not make the approximation I did before
 2106 and assume that the momentum of the muon and the proton will give an adequate
 2107 estimation of the reconstructed neutrino energy.

2108 In any case, as before, I can take the direction of the incoming neutrino as known.
 2109 That way, one can estimate the energy of the neutrino as:

$$E_\nu^{reco} = E_\mu + E_p + m_{^{39}\text{Ar}} - m_{^{40}\text{Ar}}, \quad (7.33)$$

2110 and using momentum conservation I can write the momentum of the remnant nucleus
 2111 as:

$$\vec{p}_N = \hat{p}_\nu (E_\mu + E_p + m_{^{39}\text{Ar}} - m_{^{40}\text{Ar}}) - \vec{p}_\mu - \vec{p}_p. \quad (7.34)$$

2112 As in the previous case, I need to drop the events where the muon or the proton fall
 2113 below the kinetic energy detection threshold [42]. Also, I again apply a smearing to the
 2114 momenta of the particles, a 1% for muons and 5% for protons.

2115 Having done that, one can compute the following angular variables for our selected

7.6. High energy DM neutrino signals

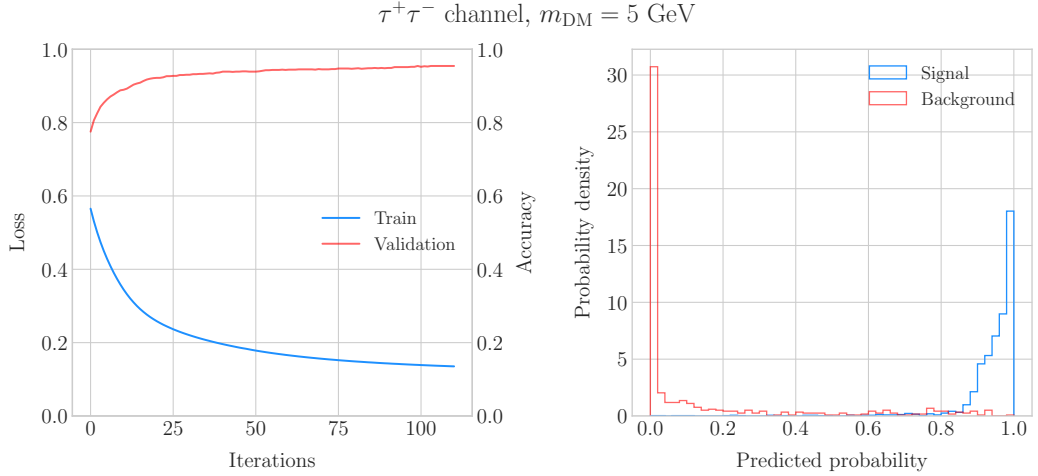


Figure 7.15: Left panel: value of the loss function for the training sample (blue line) and accuracy for the validation sample (red line) versus the number of iterations for the MLP classifier training. Right panel: distributions of the predicted probabilities assigned by the MLP classifier to the test sample for the $\tau^+\tau^-$ QEL signal with $m_{\text{DM}} = 5 \text{ GeV}$ (blue) and the atmospheric background (red).

2116 events:

$$\cos \theta_\mu = \hat{p}_\nu \cdot \hat{p}_\mu, \quad (7.35)$$

$$\cos \theta_p = \hat{p}_\nu \cdot \hat{p}_p, \quad (7.36)$$

$$\cos \theta_N = \hat{p}_\nu \cdot \hat{p}_N. \quad (7.37)$$

2117 Fig. 7.14 shows the distributions of these angular variables for the $\tau^+\tau^-$ QEL
 2118 sample with $m_{\text{DM}} = 5 \text{ GeV}$ (blue) and the atmospheric background (red). Again, for
 2119 the atmospheric events I used a random solar position as the ansatz for the incoming
 2120 neutrino direction. Notice that now, opposed to the DIS case where the signal had very
 2121 sharp distributions for the variables considered, the shapes of the angular distributions
 2122 for signal and background are not that much different.

2123 This effectively means that the usual approach of applying simple angular cuts would
 2124 not work as well as in the previous situation. Therefore, as a possible solution, I tried to
 2125 use a multilayer perceptron (MLP) classifier to separate between signal and background
 2126 events. Thus, the power of the hypothesis test will serve as an estimate of the signal

Chapter 7. DM searches with neutrinos from the Sun

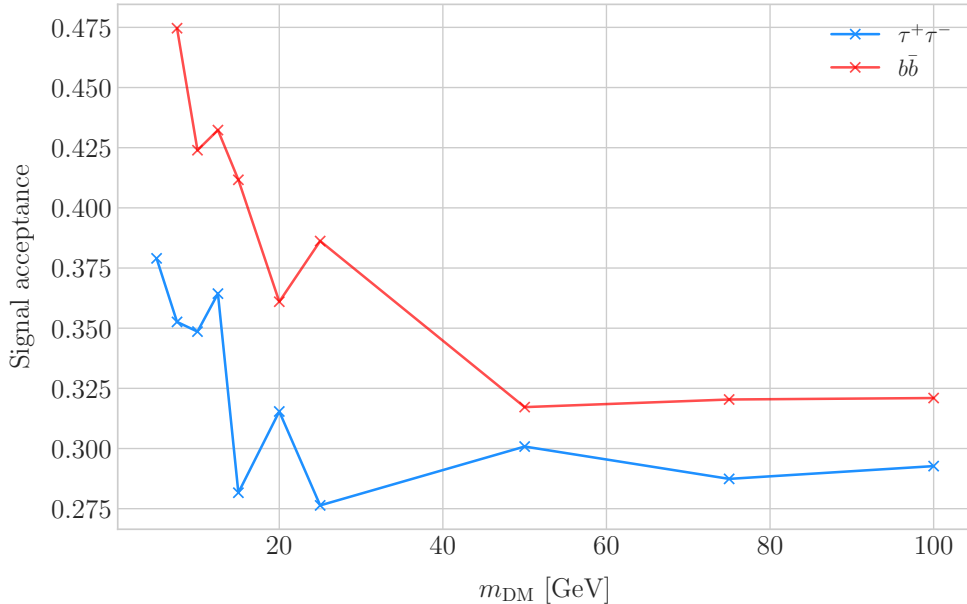


Figure 7.16: Signal efficiencies for the $\tau^+\tau^-$ (blue line) and $b\bar{b}$ (red line) single proton QEL samples as functions of the DM mass, m_{DM} , obtained by requiring a minimum predicted probability from the MLP classifier of 0.97 in order to achieve a background rejection greater than 99.8%.

efficiency, and in the same way one can take the size of the test to be our background rejection.

For each DM mass value and channel, as well as for the background sample, I divide our events into training, validation and test samples. The input variables for the classifier were the reconstructed neutrino energy from Eq. (7.33) and the angular variables defined in Eqs. (7.35 - 7.37). I used the MLP classifier implemented in `scikit-learn` [87], with a total of five hidden layers, the rectified linear unit activation function and adaptive learning rate. In order to account for fluctuations due to artifacts in the training process I repeated the training a thousand times for each sample, redefining each time the training, validation and test subsets, so one can take as our signal efficiency and background rejection the mean values of the powers and sizes of the tests.

The results of one of these training processes for the $\tau^+\tau^-$ QEL signal with $m_{\text{DM}} = 5$ GeV is shown in Fig. 7.15. On the left panel I show the loss function values (blue) and accuracy (red) at each iteration for the training and the validation samples respectively.

7.6. High energy DM neutrino signals

2141 The training stops either when the maximum number of iterations is reached (1000 in
2142 this case) or when the accuracy for the validation sample reaches a certain tolerance
2143 (I chose 10^{-4} as our tolerance). On the right panel I have the distributions for the
2144 predicted probability by the model, separated in true signal (blue) and background
2145 (red) events, for the test sample. One can see that both populations are well separated,
2146 obtaining a power of 44.97% and a size of 0.17% when I require a predicted probability
2147 greater than 0.97.

2148 Applying this criteria for each sample, I obtain the mean signal efficiencies shown in
2149 Fig. 7.16. Notice that the efficiencies for the channel $\tau^+\tau^-$ (blue line) are consistently
2150 lower than the ones for the $b\bar{b}$ channel (red line). This can be due to the fact that, for
2151 each DM mass point, the neutrino spectrum coming from the $b\bar{b}$ annihilation channel is
2152 centered at lower energies when compared to the $\tau^+\tau^-$ spectrum. This directly translates
2153 into more low energy neutrinos undergoing QEL interactions, which give signals that
2154 can be easily separated from the atmospheric background. This explanation also help us
2155 understand why in both cases the signal acceptance drops when the DM mass increases.
2156 In all cases, the background rejection took values between 99.8% to 99.9%. I will assume
2157 a 99.8% background rejection value in all cases to keep our estimation conservative.

2158 7.6.3 Results

2159 In order to estimate the DM-nucleon cross section sensitivities in the present case I need
2160 again to compute the expected number of background events. As I am now separating
2161 events by interaction type Eq. (7.25) does not hold anymore, as in that case I integrated
2162 over the total neutrino-argon cross section. In this instance, the expected background
2163 events for DIS events is approximately given by:

$$N_B^{DIS} \simeq \eta_B^{DIS} \times (4.655 \times 10^3) \times \left(\frac{\text{exposure}}{400 \text{ kT yr}} \right), \quad (7.38)$$

Chapter 7. DM searches with neutrinos from the Sun

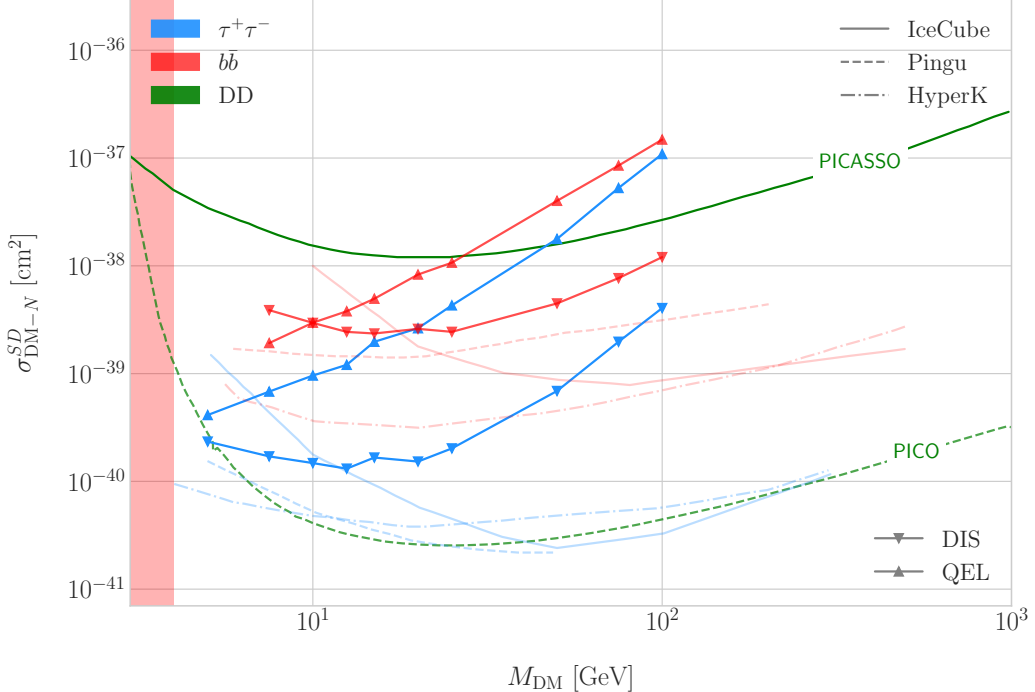


Figure 7.17: Projected 90% confidence level upper limit for DUNE (400 kT yr) on the spin-dependent DM-nucleon scattering cross section as a function of m_{DM} , for the annihilation channels $\tau^+\tau^-$ (blue) and $b\bar{b}$ (red) separated by interaction type (up triangles denote DIS interactions whereas down triangles represent QEL interactions). I also show the previous limits from IceCube [9] (solid lines) and the projected sensitivities for Pingu [10] (dashed lines) and Hyper-Kamiokande [11] (dash-dotted lines), as well as the direct detection limits from PICASSO [12] (solid green line) and PICO-60 C₃F₈ [13] (dashed green line).

2164 whereas for QEL events we have:

$$N_B^{QEL} \simeq \eta_B^{QEL} \times (2.248 \times 10^4) \times \left(\frac{\text{exposure}}{400 \text{ kT yr}} \right). \quad (7.39)$$

2165 Now, using these together with Eqs. (7.26) and (7.27) one can obtain the 90% C.L.
 2166 upper limit on the total annihilation rate at equilibrium for both kind of events. Then,
 2167 applying the computed DM-nucleons capture rates I can translate these into limits on
 2168 the DM-nucleon cross section by means of Eqs. (7.2), (7.5) and (7.6).

2169 Fig. 7.17 shows the obtained limits on the SD DM-nucleon cross section for DUNE,
 2170 using the DIS (up triangles) and QEL (down triangles) events both for the $\tau^+\tau^-$ (blue)
 2171 and the $b\bar{b}$ (red) samples, for an exposure of 400 kT yr. I also include the corresponding

7.7. Example: Leptophilic Dark Matter

2172 current limits from IceCube [9] (solid lines), as well as the projected sensitivities of Pingu
2173 [10] (dashed lines) and Hyper-Kamiokande [11] (dash-dotted lines). For comparison, I
2174 also show the reported direct detection limits from PICASSO [12] (solid green line) and
2175 PICO-60 C₃F₈ [13] (dashed green line).

2176 Notice that, for most of the mass range, the limits one can set by using the DIS
2177 events are stronger than those of the QEL interactions, except for the low mass part
2178 of both the $\tau^+\tau^-$ and the $b\bar{b}$ curves where the QEL events dominate. In general, the
2179 expected sensitivity of DUNE for DM masses $\lesssim 25$ GeV surpasses the stronger current
2180 indirect limits. However, experiments like Hyper-Kamiokande are foreseen to have an
2181 overall better sensitivity in this kind of searches, as they have a bigger active volume
2182 and accept a broader energy range.

2183 A pending question is what happens when we add the RES and MEC charged-current
2184 interaction contributions. In that case it would probably be more convenient to split
2185 the samples by final state interaction topologies. Also, another necessary improvement
2186 would be adding a full detector simulation and reconstructions. This will also require
2187 considering the effect of poorly reconstructed events or final states containing neutral
2188 particles such that they mimic the desired topology at the reconstruction level.

2189 7.7 Example: Leptophilic Dark Matter

2190 In general, the capture rate of DM particles by the Sun via interactions with electrons is
2191 several orders of magnitude smaller than the capture via DM-nucleus scattering. Thus,
2192 it would be sub-leading even when nucleon capture is loop suppressed. As I showed in
2193 Fig. 7.2, the capture rate via scattering off electrons only surpasses the capture rates
2194 via DM-nucleons interactions for DM masses $\lesssim 100 - 500$ MeV.

2195 However, if one considers a model where DM-nucleon interactions are forbidden even
2196 at loop level, then electron interactions will be the sole contributor to DM capture in
2197 the Sun. One can describe such scenario where the DM particles couple to leptons but
2198 not to the quark sector using effective operators.

Chapter 7. DM searches with neutrinos from the Sun

2199 In general, assuming that the DM particle is a Dirac fermion, the dimension six
 2200 operators describing the interaction between two DM particles and two leptons can be
 2201 written as:

$$\mathcal{L}_{eff} = G \sum_i (\bar{\chi} \Gamma_\chi^i \chi) (\bar{\ell} \Gamma_\ell^i \ell), \quad (7.40)$$

2202 where $G = 1/\Lambda^2$ is the effective coupling strength, Λ the cut-off of the effective field
 2203 theory and ℓ denotes any lepton. In principle, one should consider all the possible
 2204 Lorentz structures Γ_f^i in order to have a complete set of effective operators.

2205 However, some combinations will induce interactions with nucleons at loop level. As
 2206 we are specifically interested in interactions which forbid any communication with the
 2207 quark sector, I will not consider those [88]. In addition, some of the effective operators
 2208 give rise to velocity-suppressed scattering cross sections between DM particles and
 2209 leptons. I will also neglect those, as the suppression goes with the square of the DM
 2210 halo velocity which in units of the speed of light is $\sim 10^{-6}$.

2211 This way, the only Lorentz tensor structure that do not induce interactions with
 2212 quarks at loop level and gives a contribution to the scattering cross section that is not
 2213 velocity suppress is the axial-axial interaction. The effective Lagrangian is then given
 2214 by:

$$\mathcal{L}_{eff} = \frac{c_A^\chi c_A^\ell}{\Lambda^2} (\bar{\chi} \gamma^\mu \gamma^5 \chi) (\bar{\ell} \gamma_\mu \gamma^5 \ell), \quad (7.41)$$

2215 where c_A^χ and c_A^ℓ are the couplings for the different species. As the DM coupling appears
 2216 as a common factor for any lepton choice, I will redefine the corresponding coupling c_A^ℓ
 2217 to absorb c_A^χ . Also, for simplicity, I will assume that the couplings between the DM
 2218 particles and the leptons are flavour independent, i.e. I have just two couplings, c_A^e for
 2219 charged leptons and c_A^ν for neutrinos.

2220 In the case of a scalar DM particle, the lowest order effective interaction with
 2221 leptons happens through a dimension five operator, generating scalar and pseudoscalar
 2222 interactions. However, the former induces interactions with quarks at two loop level
 2223 whereas the latter gives a velocity suppressed scattering cross section.

2224 From the effective Lagrangian in Eq. (7.41) it can be shown that the axial-axial

7.7. Example: Leptophilic Dark Matter

contribution to the scattering cross section for the fermionic DM and a charged lepton is given by:

$$\sigma_{\text{DM}-e}^{AA} = 3(c_A^e)^2 \frac{m_e^2}{\pi \Lambda^4}. \quad (7.42)$$

If the DM interacts exclusively with fermions, then the only annihilation channels that will give us a measurable neutrino flux coming out of the Sun are $\tau^+\tau^-$ and $\nu\bar{\nu}$. The former channel, already explored previously in the more mainstream scenario of the DM capture via scattering off nucleons, is open only for $m_{\text{DM}} > m_\tau \simeq 1776.86 \pm 0.12$ MeV [89], a mass region where the solar DM capture by electrons is at least one order of magnitude smaller than the capture via interactions with nucleons. On the contrary, the latter allows us to explore a region where the capture rate via scattering off electrons dominates over the rest.

One downside of focusing in such low mass range is that it falls below the usual limit of $m_{\text{evap}} \sim 4$ GeV usually explored in the literature. The pretext to explore this region is the result discussed previously reported in Ref. [4], where DM evaporation in the Sun for the case of capture via electron scattering could be negligible for masses as low as $m_{\text{evap}} \sim 200$ MeV. This result is quite sensitive to the high velocity tail of the DM velocity distribution in equilibrium inside the Sun, and therefore full numerical simulations would be needed to assess the impact of this effect. However, this falls out of the scope of our work.

In this case, as I have a specific realisation of the interaction between the DM and leptons, one can estimate the relic density of our DM for different values of the couplings and the effective field theory scale Λ . The first step to do so is compute the self-annihilation cross section. Because I consider cold relics, at the freeze-out time our DM particles were non-relativistic and so one can expand the annihilation cross section in terms of the relative velocity v between two annihilating DM particles as [90]:

$$\sigma_{\text{ann}}^{AA}|v| \approx \frac{1}{2\pi\Lambda^4} \sum_\ell \left(c_A^\ell\right)^2 m_\chi^2 \sqrt{1 - \frac{m_\ell^2}{m_\chi^2} \left[\frac{m_\ell^2}{m_\chi^2} + \frac{1}{12} \left(2 - \frac{m_\ell^2}{m_\chi^2}\right) v^2 \right]}, \quad (7.43)$$

Chapter 7. DM searches with neutrinos from the Sun

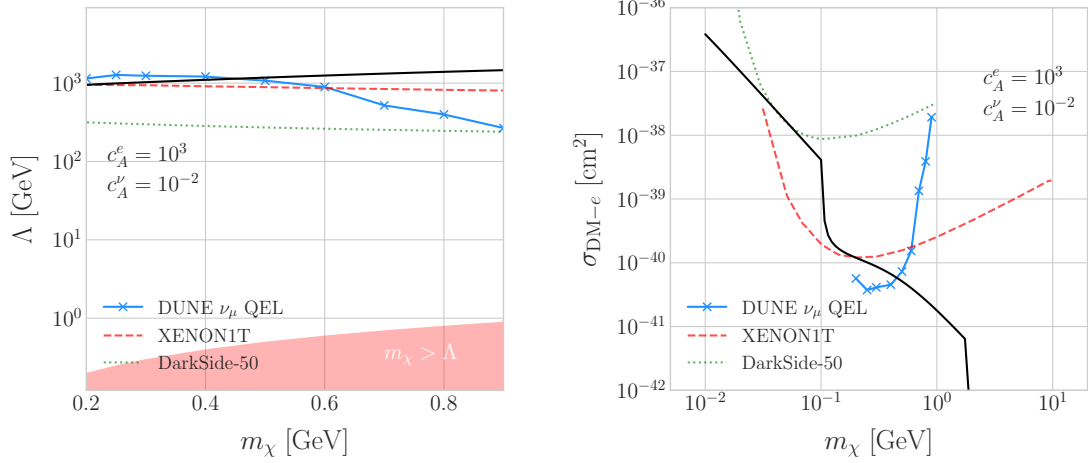


Figure 7.18: Left panel: Projected 90% confidence level sensitivity of DUNE (400 kT yr) to the scale Λ of an EFT containing only leptophilic DM axial-axial interactions (blue line). Right panel: In both cases the corresponding limits from DarkSide-50 [14] (dotted green line) and XENON1T [15] (dashed red line) are also shown, together with the configurations for which the correct relic density is achieved (black line), all for the coupling values $c_A^e = 10^3$ and $c_A^\nu = 10^{-2}$.

where the sum includes all the possible lepton final states with mass m_ℓ .
 Solving the Boltzmann equation for the evolution of the DM density gives as a solution a relic density of:

$$\Omega_\chi h^2 \approx \frac{(1.04 \times 10^9) x_F}{M_{Pl} \sqrt{g_*} (a + 3b/x_F)}, \quad (7.44)$$

where $x_F = m_\chi/T_F$ being T_F the freeze-out temperature, g_* the number of relativistic degrees of freedom at freeze-out and a and b the terms in the annihilation cross section expansion $\sigma_{ann}|v| \approx a + bv^2 + \mathcal{O}(v^4)$. Using the current best fit for the relic DM density $\Omega_\chi h^2 = 0.1198 \pm 0.0012$ [91] one can use these relations to compute the required effective theory scale Λ at which the correct density is achieved for any combinations of m_χ and c_A^ℓ .

As discussed before, in the low DM mass region QEL interactions dominate. Moreover, if I focus on direct annihilation to neutrinos, the energy of the muon neutrino flux is known as it must be equal to the mass of the DM particle, $E_\nu = m_\chi$. That way, now I do not need to use Eq. (7.33) in order to estimate the momentum transfer to the

7.7. Example: Leptophilic Dark Matter

2262 remnant nucleus, I can simply take:

$$\vec{p}_N = \hat{p}_\nu m_\chi - \vec{p}_\mu - \vec{p}_p. \quad (7.45)$$

2263 To estimate the signal efficiency and background rejection for this case I used again
2264 the MLP classifier from `scikit-learn`, using the same specifications as before. The
2265 only difference now is that I add also the reconstructed neutrino energy as one of the
2266 features to train the classifier with, because the characteristic monoenergetic flux for
2267 each m_χ value will help to distinguish between signal and background events.

2268 In this case, for masses below ~ 500 MeV I obtain a signal efficiency close to unity
2269 while keeping a background rejection of 99.9%. For bigger values of the mass, the signal
2270 efficiency drops significantly if I require to keep the background acceptance under 0.01%.
2271 However, because this kind of search is dominated by the background, sacrificing the
2272 signal acceptance to keep the background rejection to a minimum enhances the reach
2273 of the analysis. This way, for DM masses of the order of $m_\chi \sim 1$ GeV I end up with
2274 efficiencies as low as 1%.

2275 Now, estimating the number of background events using Eq. (7.39) one can go on
2276 and apply Eqs. (7.26) and (7.27) together with Eq. (7.42) to derive the sensitivity of
2277 DUNE to this kind of model. Fig. 7.18 (left panel) shows the potential reach of DUNE
2278 to constrain the EFT scale Λ this model containing only leptophilic DM axial-axial
2279 interactions (blue line), for a choice of couplings $c_A^e = 10^3$ and $c_A^\nu = 10^{-2}$. I also included
2280 the current limits on the DM-electron scattering cross section from DarkSide-50 [14]
2281 (dotted green line) and XENON1T [15] (dashed red line), reworked with Eq. (7.42) to
2282 show their implications for the EFT scale. The values of Λ for which the correct DM relic
2283 density value is achieved for each mass are also shown (black line). This tells us that,
2284 for that specific choice of couplings, DUNE would be sensitive to DM configurations
2285 allowed by the relic density constraint up to a mass of $m_\chi \sim 400$ MeV.

2286 In Fig. 7.18 (right panel) I show the same upper limits but for the DM-electron
2287 scattering cross section. From this view one can see that DUNE would be able to

Chapter 7. DM searches with neutrinos from the Sun

offer complementary information to the low energy DM-electron interaction searches performed by direct detection experiments, in a slightly higher mass range.

With the present example, although it focuses on a very specific realisation of the DM interactions, I show the potential of DUNE to constrain exotic DM scenarios. Thanks to its low backgrounds and superb angular resolution DUNE will be able to help with the systematic searches for dark sectors physics.

2294 Chapter 8

2295 Particle ID in GArSoft

2296 ND-GAr is a magnetised, high-pressure gaseous argon TPC (HPgTPC), surrounded by
2297 an electromagnetic calorimeter (ECal) and a muon detector (commonly refer to as μ ID).
2298 A detailed discussion on the requirements, design, performance and physics of ND-GAr
2299 can be found in the DUNE ND CDR [48] and the ND-GAr whitepaper (cite).

2300 In DUNE Phase II ND-GAr will fulfill the role of TMS, measuring the momentum
2301 and sign of the charged particles exiting ND-LAr. Additionally, it will be able to measure
2302 neutrino interactions inside the HPgTPC, achieving lower energy thresholds than those
2303 of the ND and FD LArTPCs. By doing so ND-GAr will allow to constrain the relevant
2304 systematic uncertainties for the LBL analysis even further.

2305 The goal of the present chapter is to review the requirements that the physics program
2306 of DUNE impose on ND-GAr, present the current status of its design and describe the
2307 GArSoft package, its simulation and reconstruction software.

2308 As decided during the DUNE Phase II workshop in June 2023 [reference], we want
2309 to build ND-GAr physics case by showing:

- 2310 • That ND-GAr can constrain systematic uncertainties that ND-LAr might miss.
- 2311 • The impact on the neutrino oscillation results if such systematic uncertainties are
2312 missed.
- 2313 • That ND-GAr is necessary to reach DUNE's main physics goals.

Chapter 8. Particle ID in GArSoft

2314 This way, the design of ND-GAr will be physics driven.

2315 In order to study the effects of final state interactions (FSI) in CC interactions,
2316 ND-GAr should be able to measure the spectrum of protons and charged pions at low
2317 energies. ND-GAr also needs to be able to measure the pion multiplicity, specially for
2318 energies above 100 MeV as at these energies the pions shower in the LAr, to inform the
2319 pion mass correction in the ND and FD LArTPCs.

2320 In order to correctly identify electrons, muons, pions, kaons and protons ND-GAr
2321 can use a combination of: dE/dx measurements in the HPgTPC, E_{ECAL}/p using the
2322 ECAL total energy and the momentum obtained from magnetic spectroscopy in the
2323 HPgTPC and penetration information through the ECAL and muon tagger.

2324 8.1 dE/dx measurement in the TPC

2325 Among the parameters extracted from the track fitting, ionisation is particularly useful
2326 for particle identification, as it is a function of the particle velocity. Although for the
2327 case of relativistic particles this dependence is not very strong, measuring the track on
2328 a large number of points may allow us to estimate the amount of ionisation accuratel.
2329 This, paired with a measurement of the momentum, may allow us to identify the particle
2330 type.

2331 The first calculation of the energy loss per unit length of relativistic particles using
2332 a quantum-mechanical treatment is due to Bethe [?]. Using this approach, the mean
2333 ionisation rate of a charged particle traveling through a material medium is (using
2334 natural units $G = \hbar = c = 1$):

$$\left\langle \frac{dE}{dx} \right\rangle = \frac{4\pi Ne^4}{m_e \beta^2} z^2 \left(\log \frac{2m_e \beta^2 \gamma^2}{I} - \beta^2 \right), \quad (8.1)$$

2335 where N is the number density of electrons in the medium, e the elementary charge, m_e
2336 is the electron mass, z the charge of the particle in units of e , β is the velocity of the
2337 particle, $\gamma = (1 - \beta^2)^{-1}$ and I denotes the effective ionisation potential averaged over
2338 all electrons. This relation is known as the Bethe-Bloch formula.

8.1. dE/dx measurement in the TPC

From Eq. (8.1) one can see that the ionisation loss does not depend explicitly on the mass of the charged particle, that for non-relativistic velocities it falls as β^{-2} , then goes through a minimum and increases as the logarithm of γ . This behaviour at high velocities is commonly known as the relativistic rise. The physical origin of this effect is partly due to the fact that the transverse electromagnetic field of the particle is proportional to γ , therefore as it increases so does the cross section.

It was later understood that the relativistic rise could not grow indefinitely with γ . A way to add this feature in the Bethe-Bloch formula is by introducing the so-called density effect term. It accounts for the polarisation effect of the atoms in the medium, which effectively shield the electromagnetic field of the charged particle halting any further increase of the energy loss [?]. Denoting the correction as $\delta(\beta)$, one can rewrite Eq. (8.1) as:

$$\left\langle \frac{dE}{dx} \right\rangle = \frac{4\pi Ne^4}{m_e \beta^2} z^2 \left(\log \frac{2m_e \beta^2 \gamma^2}{I} - \beta^2 - \frac{\delta(\beta)}{2} \right). \quad (8.2)$$

In general, the form of $\delta(\beta)$ depends on the medium and its state of aggregation, involving the usage of tabulated parameters and implicit relations [?].

Another standard method to compute the amount of ionisation a charged particle produces is the so-called photo-absorption ionisation (PAI) model proposed by Allison and Cobb [?]. Within their approach, the mean ionisation is evaluated using a semiclassical calculation in which one characterises the continuum material medium by means of a complex dielectric constant $\epsilon(k, \omega)$. However, in order to model the dielectric constant they rely on the quantum-mechanical picture of photon absorption and collision. Therefore, in the PAI model the computation of the ionisation loss involves a numerical integration of the measured photo-absorption cross-section for the relevant material.

In a particle physics experiment, the typical way of determining the energy loss per unit length as a function of the particle velocity is studying identified particles over a range of momenta. Once we have established this relation we can use it for other, unknown particles. In this sense, it makes sense to have a regular mathematical expression for this relation that one can use.

Chapter 8. Particle ID in GArSoft

2366 It happens that neither the Bethe-Bloch theory nor the PAI model from Allison and
2367 Cobb offer a close mathematical form for the ionisation curve. This is the reason why a
2368 full parametrisation of the ionisation curves can be useful. A parametrisation originally
2369 proposed for the ALEPH TPC [?] and later used by the ALICE TPC [?] group that
2370 manages to capture the features of the ionisation energy loss is:

$$f(\beta\gamma) = \frac{P_1}{\beta^{P_4}} \left(P_2 - \beta^{P_4} - \log \left[P_3 + \frac{1}{(\beta\gamma)^{P_5}} \right] \right), \quad (8.3)$$

2371 where P_i are five free parameters. Hereafter, we will refer to Eq. (8.3) as the ALEPH
2372 dE/dx parametrisation.

2373 8.1.1 Energy calibration

2374 In order to obtain the amount of energy loss by a charged particle due to ionisation
2375 in our TPC we need to determine the conversion between the charge deposited in our
2376 readout planes and the actual energy depositions. This procedure is known as energy
2377 calibration.

2378 In a general, the first step of the calibration involves a non-uniformity correction,
2379 to make sure that the detector response is uniform throughout the TPC. These are
2380 typically divided into three categories, non-uniformities in the transverse YZ plane,
2381 non-uniformities along the drift direction X and variations of the detector response
2382 over time (would not apply to us as the detector is not built yet). These would correct
2383 for effects such as electron diffusion and attenuation, space charge effects or channel
2384 misconfiguration. However, because at the moment I am only interested in making sure
2385 we recover a sensible result from our simulation, I will not apply uniformity corrections
2386 to our charge deposits.

2387 Other effects, like electron-ion recombination or ADC saturation, lead to a non-linear
2388 relation between the observed charge and the deposited energy in the detector, with the
2389 observed readout charge saturating at high ionisation energies. In this case, because we
2390 are dealing with gaseous argon and therefore recombination is not as important as in

8.1. dE/dx measurement in the TPC

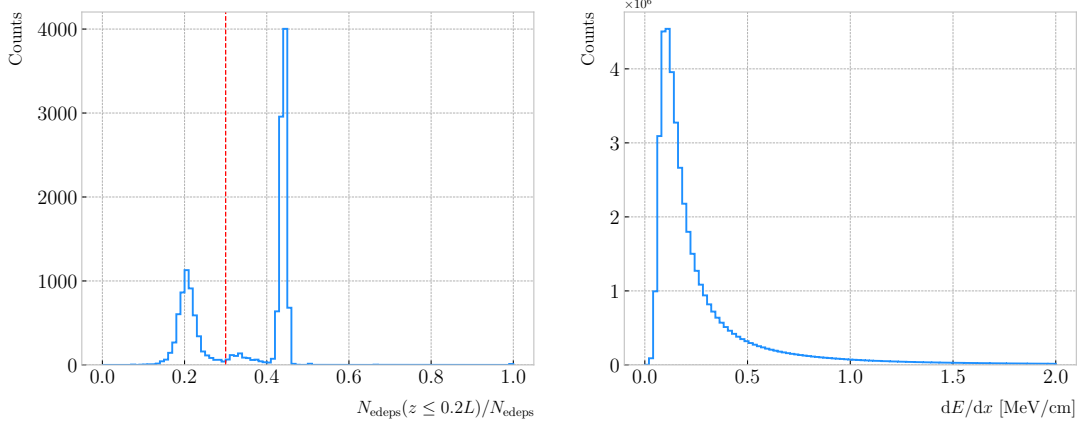


Figure 8.1: Left panel: distribution of the fraction of Geant4-level energy deposits per track with residual range less than 20% of the total track length, for the isotropic proton sample. Right panel: distribution of the ionisation per unit length of the energy deposits in the proton sample after removing the tracks with less than 30% of their energy deposits in the last 20% of the track.

2391 liquid, we do not simulate recombination effects in the TPC. Even so, the simulation of
 2392 the electronic response will still introduce charge saturation, and one needs to correct
 2393 for it in order to obtain the exact amount of energy loss due to ionisation.

2394 By default, the track fitting algorithm in GArSoft provides a `TrackIonization`
 2395 object associated to each reconstructed track. It contains two collections of charge
 2396 deposits, one for each fitting direction, consisting on pairs of charge values (dQ , in ADC)
 2397 and step sizes (dx , in cm).

2398 In order to estimate the ionisation loss in the ND-GAr TPC, I have used an MC
 2399 sample consisting of single, isotropic protons propagating in the TPC. The starting points
 2400 of the protons were sampled inside a $50 \times 50 \times 25$ cm box centered at $(100, -150, 1250)$,
 2401 and their momenta are uniformly distributed in the range $0.25 - 1.75$ GeV. I ran the
 2402 simulated sample through GArSoft's default detector simulation and reconstruction, and
 2403 then a custom analyser module that extracts the ionisation data together with other
 2404 reconstructed track information from the Kalman fit.

2405 For studying the energy loss of the protons I select the reconstructed tracks that
 2406 range out (i.e. slow down to rest) inside the TPC. A characteristic feature of the energy
 2407 loss profile of any stopping ionising particle is the so-called Bragg peak, a pronounced

Chapter 8. Particle ID in GArSoft

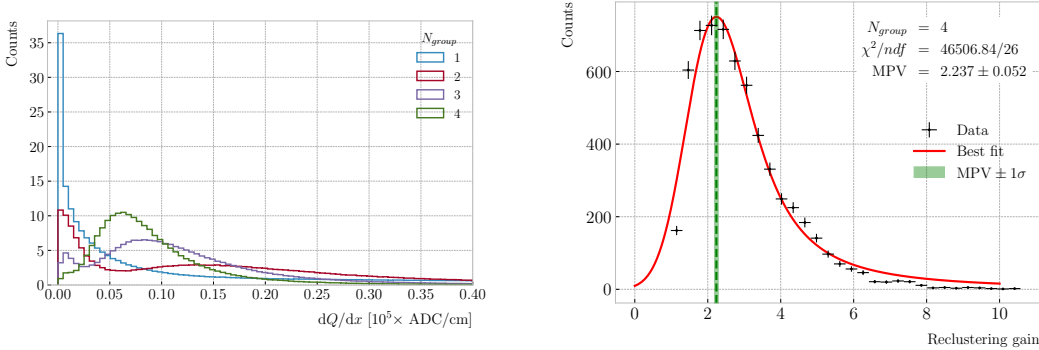


Figure 8.2: Left panel: distribution of the reconstructed ionisation charge per unit length for our MC stopping proton sample. The different colors indicate how many consecutive dQ/dx pairs were grouped together. Right panel: distribution of the median change in dQ/dx per track after $N_{group} = 4$ clusters were reclustered together.

peak that occurs immediately before the particle comes to rest. From Eq. (8.1) we can see that this behaviour is expected, as the energy loss for non-relativistic particles is inversely proportional to β^2 . In data, a way of identifying the Bragg peak, and thus select the stopping particles, is checking the number of energy deposits towards the end of the track. In this case, I count the fraction of the Geant4 simulated energy deposits with a residual range value (the distance from a given energy deposit to the last deposit in the track trajectory) less than a 20% of the corresponding track length¹. The distribution of this fraction of energy deposits for our proton sample is shown in Fig. 8.1 (left panel). We can clearly see two well separated peaks in this distribution, one centered at 0.2 and another, narrower, one centered at a higher value. The first one corresponds to non-stopping protons, as in that case the number of energy deposits towards the end of the track is uniformly distributed due to the absence of the Bragg peak. In that way, I apply a cut in this distribution, requiring that at least 30% of the simulated energy deposits sit in the last 20% of the tracks, to ensure that the Bragg peak is present.

Fig. 8.1 (right panel) shows the distribution of the energy loss per unit length for the Geant4 simulated energy deposits of the selected stopping protons. We can see that it

¹As we are applying this selection at the Geant4 level we could have simply selected the stopping protons using the `EndProcess` labels from the simulation. However, the Bragg peak identification method displayed here could serve as a starting point for a selection of stopping protons in real data.

8.1. dE/dx measurement in the TPC

follows the expected shape of a Landau distribution, which describes the fluctuations of the ionisation energy losses [?]. This distribution has a characteristic asymmetric PDF, with a long right tail that translates into a high probability for high-energy ionisation losses. The origin of these fluctuations is mainly the possibility of transferring a high enough energy to an electron, so it becomes a ionising particle itself.

Now, from the point of view of the reconstruction, the objects that we have available to extract the ionisation information for the different reconstructed tracks are the collections of dQ and dx pairs, as stated before. The dQ values come from adding up the amplitude of all the reconstructed hits in a cluster, which is the input object to the Kalman fit.

Fig. 8.2 (left panel) shows the distribution of the ionisation charge deposits per unit length for the track in the stopping proton sample (blue line). As one can notice, this distribution does not resemble the expected shape of the Landau PDF. This distribution peaks sharply at 0 and has a heavy tailed behaviour. Notice, however, how the distribution changes its shape as we group together N_{group} consecutive charge deposit pairs (red, purple and green lines). The distribution in the $N_{group} = 4$ case already has a shape which resembles that of the Geant4-level ionisation per unit length, so I will proceed using this amount of reclustering for the reconstruction-level depositions.

An extra factor I need to account for, when reclustering is applied, is how the overall dQ/dx per track changes. To do so, we can look at the ratio between the median dQ/dx after and before the reclustering. Fig. 8.2 (right panel) shows the median enhancement in dQ/dx per track for the stopping proton sample in the case $N_{group} = 4$. Fitting a Landau distribution convolved with a Gaussian², I estimate the most probable value of this ratio to be $G_{group} = 2.24 \pm 0.05$.

At this point, I am left with determining the conversion between the charge deposits per unit length dQ/dx and the energy deposits per unit length dE/dx . To this end, we need a way of comparing the two. I can use the residual range z to get a prediction of

²In the literature, this distribution is often referred to as Landau+Gaussian or langau. In the following, I will use LanGauss to refer to such PDF.

Chapter 8. Particle ID in GArSoft

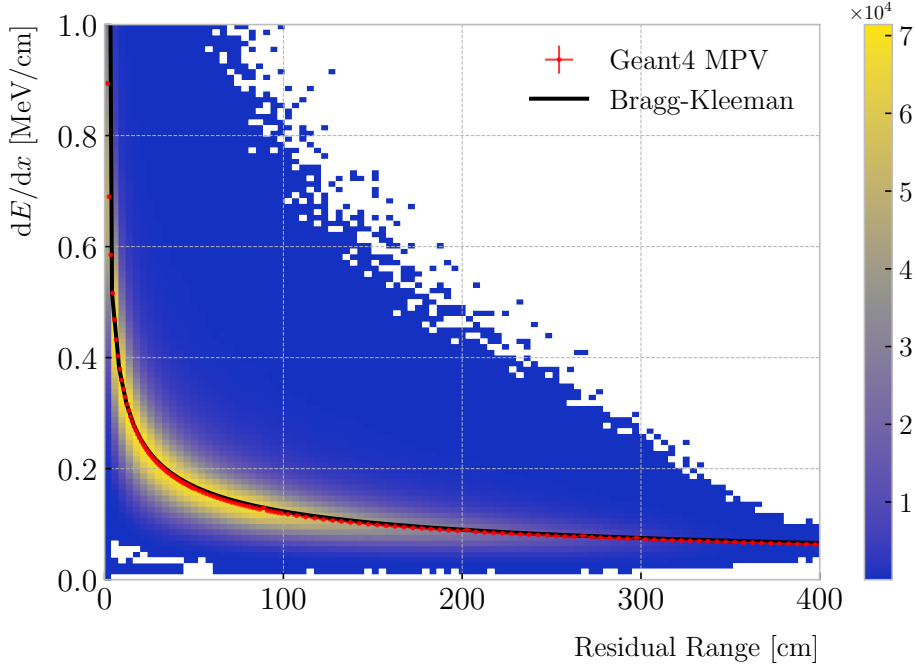


Figure 8.3: Distribution of the Geant4-simulated energy losses per unit length versus residual range for the stopping proton sample. The overlaid points represent the fitted most probable value of the dE/dx distribution in each residual range bin, whereas the curve is their best fit to the Bragg-Kleeman formula from Eq. (8.4).

2452 the most probable dE/dx by using the following empirical parametrisation [?]:

$$\frac{dE}{dx}(z) = \frac{z^{\frac{1}{p}-1}}{p\Lambda^{\frac{1}{p}}}, \quad (8.4)$$

2453 which is quoted in the literature as the Bragg-Kleeman formula. In order to obtain the
 2454 p and Λ parameters I perform a fit using the energy losses and the residual ranges given
 2455 by the Geant4 stage of our proton sample.

2456 Within our simulation, the residual range is sampled with a maximum size of
 2457 5 mm. Therefore, to perform the fit to the Bragg-Kleeman formula, we can use a
 2458 fine-grained residual range binning. For each of the residual range bins I extract the
 2459 dE/dx distribution and fit it to a LanGauss distribution, to obtain the value of the
 2460 most probable dE/dx in the bin together with a statistical uncertainty. I then fit Eq.
 2461 (8.4) to these most probable values and the centres of the residual range bins. This

8.1. dE/dx measurement in the TPC

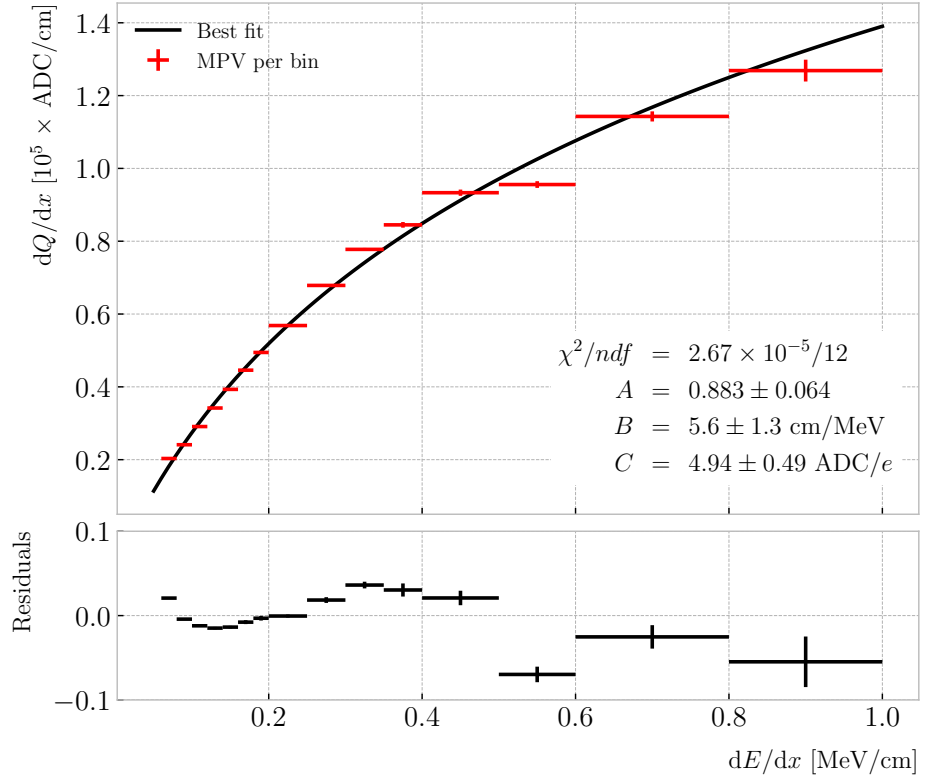


Figure 8.4: Fitted most probable dQ/dx values for each dE/dx bin (red points), obtained from the stopping proton sample. The overlaid curve (black line) represents the best fit to the logarithmic calibration function from Eq. (8.5).

procedure is depicted in Fig. 8.3, where I show the distribution of the energy loss per unit length versus the residual range, together with the most probable dE/dx values and their uncertainty in each bin (red points) and the curve with the best fit of the Bragg-Kleeman relation to those values (black line). The best fit is obtained for the parameter values $p = 1.8192 \pm 0.0005$ and $\Lambda = 0.3497 \pm 0.0008 \text{ cm/MeV}^p$ ³.

Having an analytical expression that relates the residual range to dE/dx , I can take our reconstruction-level residual ranges from the stopping proton sample and compute the most probable energy loss associated.

In order to parametrise the charge saturation, we can use the following logarithmic

³These strange units for Λ come from dimensional analysis, just to keep the Bragg-Kleeman formula (8.4) consistent.

Chapter 8. Particle ID in GArSoft

2471 function inspired by the modified box model for recombination:

$$\frac{dE}{dx} = \frac{e^{\frac{dQ}{dx}B\frac{W_{ion}}{G_{group}C}} - A}{B}, \quad (8.5)$$

2472 where A and B are the calibration parameters we need to determine, W_{ion} is the average
2473 energy to produce an electron-ion pair, G_{group} is the gain from the reclustering discussed
2474 above and C is the calibration constant to convert number of electrons to ADC counts,
2475 commonly refer to as gain (also to be obtained in the fit). In this case, I use a value for the
2476 electron-ion production energy of $W_{ion} = 26.4$ eV [?]. This value, used in our simulation
2477 as well, was measured for gaseous argon in normal conditions, and therefore should
2478 be checked in the future to describe correctly the high-pressure argon-CH₄ mixture of
2479 ND-GAr.

2480 For the calibration fit I follow a procedure similar to the previous one for Eq. (8.4).
2481 Binning the dE/dx range, I fit a LanGauss distribution to the corresponding dQ/dx
2482 distribution to obtain the most probable value. The resulting data points (red bars) are
2483 shown in Fig. 8.4 (top panel), the horizontal error bars depict the width of the dE/dx
2484 bin whereas the vertical bars represent the error associated to the most probable value
2485 estimation. A fit to the logarithmic function in Eq. (8.5) is also shown (black line).
2486 For this I weighted the data points using the inverse of their relative error, obtaining a
2487 reduced chi-square value of $\chi^2/ndf = 2.22 \times 10^{-6}$. The best fit parameters I found from
2488 this fit are $A = 0.883 \pm 0.064$, $B = 5.6 \pm 1.3$ cm/MeV and $C = 4.94 \pm 0.49$ ADC/e. In
2489 Fig. 8.4 (bottom panel) I show the residuals between the data points and the fit.

2490 The value for the gain I obtained from the fit is in reasonable agreement with our
2491 expectation. This value is set in GArSoft to 5 ADC/e by default.

2492 One interesting thing to check is what induces this non-linear relation between charge
2493 and energy. The only effects that modify the amount of electrons reaching the readout
2494 planes in the simulation are the transverse diffusion and the finite electron lifetime.
2495 Once the electrons reach the readout chambers, the pad response functions are applied,
2496 together with an electrons-to-ADC conversion and the ADC saturation limit.

8.1. dE/dx measurement in the TPC

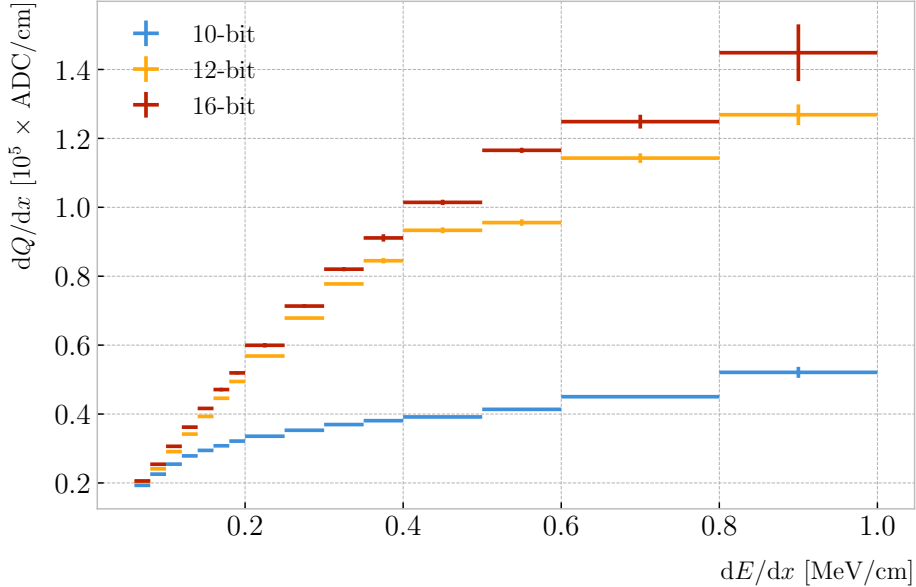


Figure 8.5: Fitted most probable dQ/dx values for each dE/dx bin for three different ADC bit limits, 10 (blue points), 12 (default, yellow points) and 16-bit (red points).

Table 8.1: Calibration parameters obtained from the fit of the ND-GAr simulated stopping proton sample to the calibration function from Eq. (8.5). The fits were performed for the 10, 12, and 16-bit ADC limits.

	χ^2/ndf	Best fit $\pm 1\sigma$		
		A	B (cm/MeV)	C (ADC/e)
10-bit	$1.83 \times 10^{-6}/12$	-9.3 ± 3.9	270 ± 69	27.1 ± 5.4
12-bit	$2.67 \times 10^{-5}/12$	0.883 ± 0.064	5.6 ± 1.3	4.94 ± 0.49
16-bit	$1.44 \times 10^{-5}/12$	0.949 ± 0.024	3.53 ± 0.58	4.52 ± 0.29

By default, GArSot applies a 12-bit ADC limit, which can be changed in the simulation configuration. However, it can only be increased up to 16-bit, as we represent the ADC collection as a `std::vector<short>`. This way, I tried to change the saturation parameter to see how it affects the relation between reconstructed charge and energy. Fig. 8.5 shows a comparison between the most probable dQ/dx for 10, 12 and 16-bit ADC limits. As expected, the lower the limit is the sooner the charge saturates. For higher ADC limits the relation between energy and charge remains linear up to higher dE/dx values, but even for the 16-bit limit the saturation is noticeable for values $\gtrsim 0.5$ MeV/cm.

In Tab. 8.1 I also show the results of fitting the samples with 10 and 16-bits ADC

Chapter 8. Particle ID in GArSoft

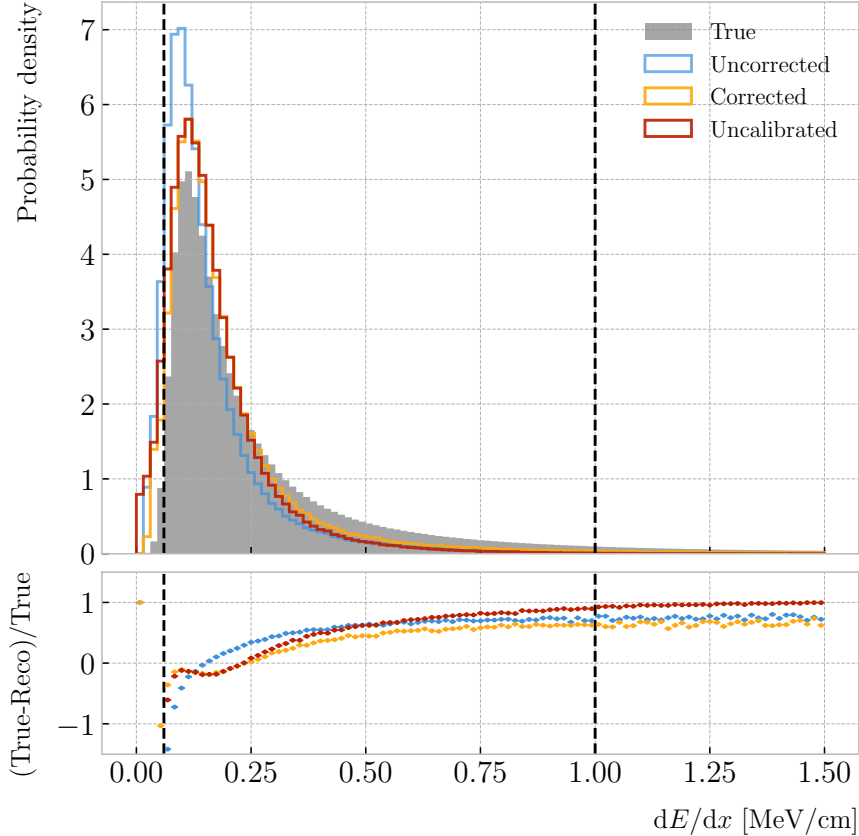


Figure 8.6: Top panel: area normalised dE/dx distributions for the true (solid grey) and the reconstructed energy deposits in the stopping proton sample, both after applying the calibration (blue) and the calibration and the normalisation correction (yellow). Also shown is the distribution obtained by applying a correction factor to the dQ/dx values but not the calibration (red). Bottom panel: fractional residuals for the uncorrected (blue), corrected (yellow) and uncalibrated (red) samples.

limits to the calibration function from Eq. (8.5), using the weights based on their relative error as described previously. One interesting feature to notice is how different the best fit points look for the 10-bit ADC saturation when compared to the other two, which are consistent with each other.

At this point we can compare the dE/dx distribution one gets from Geant4, i.e. the true energy loss distribution, and the distribution I found by applying the calibration function to our collection of reconstructed dQ/dx values. Fig. 8.6 (top panel) shows the true (solid grey) and reconstructed (blue, labeled as uncorrected) distributions together. The dashed vertical lines indicate the region of validity of the calibration fit, i.e. the left

8.1. dE/dx measurement in the TPC

and right edges of the first and last dE/dx bin respectively. Notice that these histograms are area-normalised, as the total number of true energy deposits is much higher than the number of reconstructed charge deposits. This is due to a combination of effects, like the finite spatial resolution of the detector, the hit clustering used in the track fitting and the reclustering we have applied here.

The two distributions are significantly different. That can be seen clearly when looking at the fractional residuals, shown in Fig. 8.6 (bottom panel). In particular, the position of the peak is off, which could bias the mean energy loss predictions. It seems like the difference between these may be due to an overall scaling factor. One possibility is to scale the most probable value of the reconstructed distribution to the most probable value predicted by Geant4. I do this by fitting both distributions using a LanGauss function, obtaining $dE/dx_{MPV, true} = 0.1145 \pm 0.0005$ MeV/cm and $dE/dx_{MPV, reco} = 0.0928 \pm 0.0005$ MeV/cm for the true and reconstructed most probable values respectively. These can be translated into a scaling factor $S = 0.579 \pm 0.006$.

The result of applying the scaling correction can be seen in Fig. 8.6 (top panel). The corrected dE/dx distribution (yellow, labeled as corrected) peaks around the same value the true distribution does, as expected. Moreover, the high energy region is also slightly better described. For low ionisations, below the lower limit of the calibration fit, the differences between true and reconstructed are still significant. This low energy excess may be migration of some events from the peak region. The overall effect of the correction can be seen in the fractional residual plot in Fig. 8.6 (bottom panel).

One can also check what happens if instead of applying the logarithmic calibration we simply scale the dQ/dx distribution (post reclustering) to have the same most probable value as the true dE/dx distribution. In this case, following an analogous procedure to the one described earlier, I found the scaling factor $S_{uncalibrated} = 0.414 \pm 0.002$ MeV/ADC⁴. The resulting distribution (red, labeled as uncalibrated) is also shown in in Fig. 8.6 (top panel). The behaviour of the new distribution is similar to the corrected case at low energy losses, around the peak of the true distribution, but it is worse at describing the

⁴Notice that now the scaling factor is not dimensionless, as it acts more like a conversion factor here.

Chapter 8. Particle ID in GArSoft

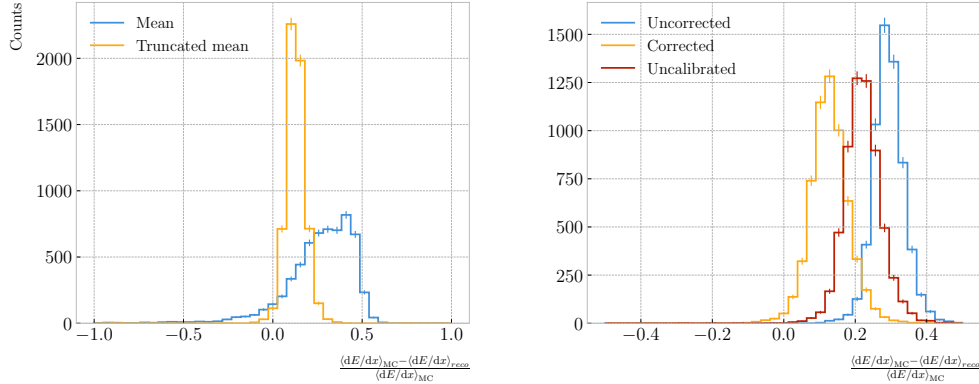


Figure 8.7: Left panel: fractional residuals between the true and the corrected dE/dx means (blue) and the 60% truncated means (yellow), for each event in the stopping proton sample. Right panel: fractional residuals between the true and the uncorrected (blue), corrected (yellow) and uncalibrated (red) dE/dx 60% truncated means, for each event in the stopping proton sample.

2543 high energy tail. This is expected, it is in the high ionisation regime where saturation
 2544 effects apply and therefore calibration is needed.

2545 8.1.2 Truncated dE/dx mean

2546 Once we have a collection of dE/dx values for each reconstructed track, we can compute
 2547 the corresponding most probable ionisation loss per unit length of the particle. This
 2548 is the value predicted by the Bethe-Bloch or the PAI models, and together with a
 2549 measurement of the momentum it allows for particle identification.

2550 However, estimating the most probable dE/dx value for each reconstructed track
 2551 is not a trivial task. As mentioned before, the dE/dx distributions follow Landau-like
 2552 distributions. Therefore, one should perform e.g. a LanGauss fit to correctly estimate
 2553 the most probable values. Automating this kind of fits is often problematic, as they
 2554 usually incur in convergence problems. Moreover, the reconstructed dE/dx distributions
 2555 we obtain tend to have relatively small statistics, which may also produce poor fits. In
 2556 practice, doing these unsupervised fits may degrade our performance, and a more robust
 2557 method is preferred.

2558 A possibility could be taking the mean of the reconstructed dE/dx distribution for

8.1. dE/dx measurement in the TPC

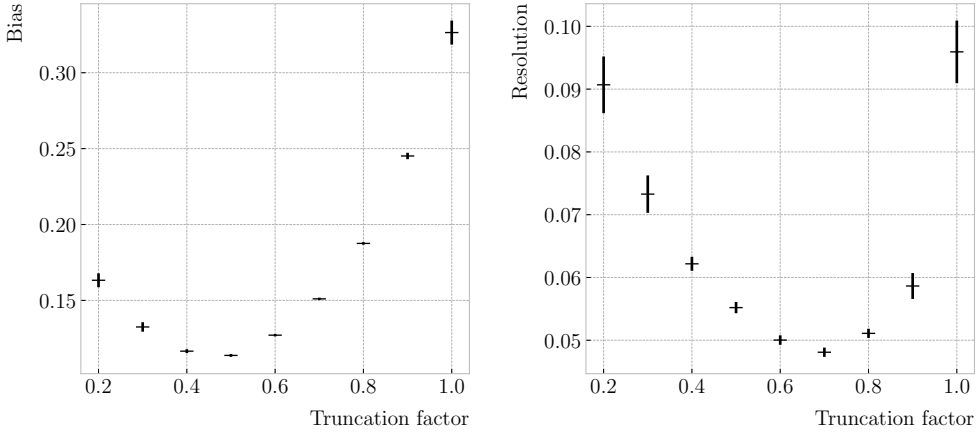


Figure 8.8: Estimated values of the mean dE/dx bias (left panel) and resolution (right panel) obtained using the corrected data from the stopping proton sample, for different values of the truncation factor.

each particle. The problem with this approach is that the high energy Landau tail, combined with our limited statistics, can induce large fluctuations in the computation of the mean. Imagine you have two protons with the same kinetic energy, but due to reconstruction problems in one case you did not get as many charge deposits reconstructed in its high ionisation loss region. If you do not remove the tails the computed dE/dx means will be significantly different.

In order to avoid those fluctuations, one can compute the mean of a truncated dE/dx distribution instead. By keeping only a given fraction of the lowest energy deposits we obtain an estimate of the mean energy loss that is more resilient to reconstruction inefficiencies and statistical effects. In Fig. 8.7 (left panel) I show a comparison between the $\langle dE/dx \rangle$ computed by taking the mean of the full distribution (blue line) and the 60% lowest energy clusters (yellow line), for the stopping proton sample. The fractional residuals are computed for each proton, taking the corresponding means using their collections of true and reconstructed energy deposits. One can see that using the simple mean translates into a high bias and uncertainty in the $\langle dE/dx \rangle$ estimation, whereas applying the truncation reduces both significantly.

Additionally, I performed a comparison between the 60% truncated mean dE/dx obtained using the different calibration methods discussed earlier, namely the uncorrected

Chapter 8. Particle ID in GArSoft

2577 (blue), corrected (yellow) and uncalibrated (red) distributions. The results are shown
 2578 in Fig. 8.7 (right panel). While the widths of these distributions are similar, the bias
 2579 obtained for the corrected sample, i.e. calibration function and correction factor applied,
 2580 is a factor of ~ 2 lower than in the uncalibrated case and almost three times smaller
 2581 than for the uncorrected sample.

2582 The next step is to optimise the level of truncation we are going to apply to our
 2583 data. To do so, I used different truncation factors, i.e. the percentage of energy-ordered
 2584 reconstructed energy deposits we keep to compute the mean, on the corrected dE/dx
 2585 sample of the stopping protons. Then, following the same procedure of computing the
 2586 fractional residuals as before, I fitted the resulting histograms using a double Gaussian
 2587 function. This is simply the sum of two Gaussian functions of the type:

$$g(x; \mu, \sigma, A) = A e^{-\frac{(x-\mu)^2}{2\sigma^2}}. \quad (8.6)$$

2588 I do not add the classical normalisation factor of the Gaussian, $1/\sqrt{2\pi}\sigma$, therefore
 2589 the amplitude A simply represents the maximum of the function. One of the two
 2590 Gaussian functions describes the core part of the distribution, while the other captures
 2591 the behaviour of the tails.

2592 For each truncation factor, I look at the bias and the resolution I obtain. I define
 2593 these as the weighted means of the corresponding parameters in the fits:

$$\bar{x} = \frac{A_{core} x_{core} + A_{tail} x_{tail}}{A_{core} + A_{tail}}, \quad (8.7)$$

2594 where A_{core} and A_{tail} are the amplitudes of the core and tail distributions respectively
 2595 and x is either the mean μ or the width σ of said distributions.

2596 Fig. 8.8 shows the bias (left panel) and the resolution (right panel) I obtained for
 2597 the stopping proton sample, using different values of the truncation. From these, it
 2598 can be seen that a truncation factor of 50% minimises the bias in the estimation, while
 2599 70% gives the best resolution. That way, I settled on the intermediate value of 60%

8.1. dE/dx measurement in the TPC

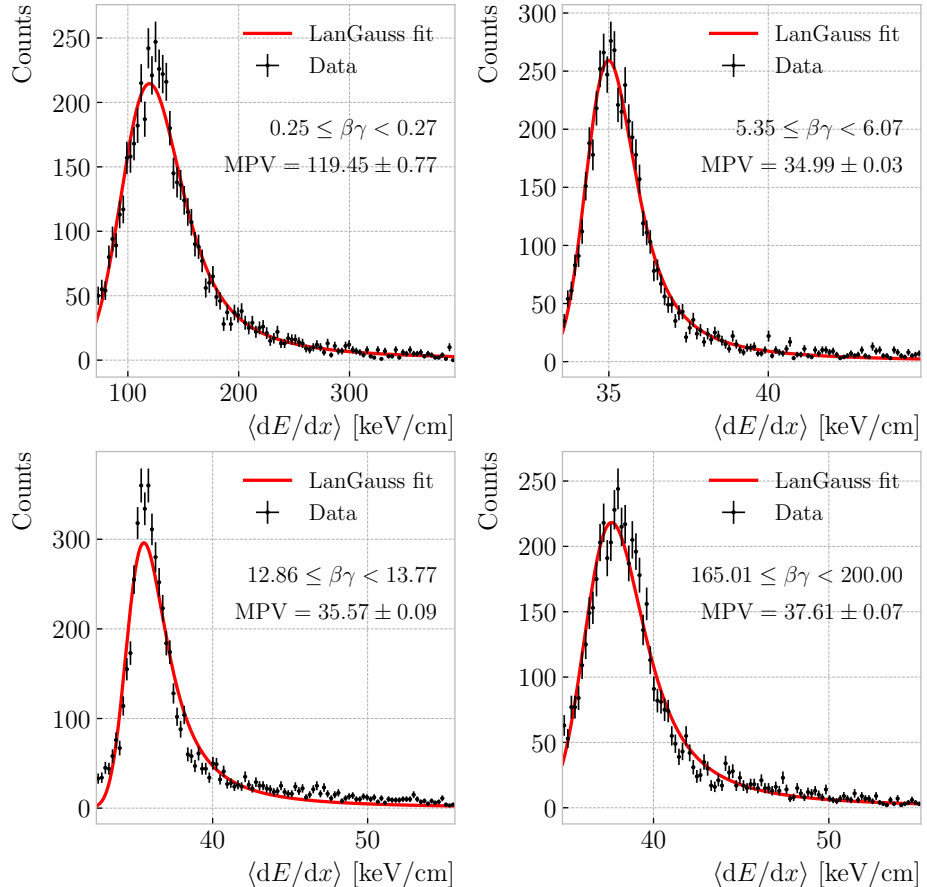


Figure 8.9: Examples of the truncated mean dE/dx LanGauss fits for various $\beta\gamma$ bins, from a simulated FHC neutrino sample.

truncation, which yields a $\langle dE/dx \rangle$ resolution of 5.00 ± 0.08 % for stopping protons.

8.1.3 Mean dE/dx parametrisation

Now that we have a way to estimate the mean energy loss of a particle in the HPgTPC, we can determine the value of the free parameters in the ALEPH formula, Eq. (8.3). For this, I used a sample of 10^5 reconstructed FHC neutrino events inside ND-GAr. In this case I cannot use the stopping proton sample, as we need to cover the full kinematic range of interest for the neutrino interactions in our detector.

The original data does not contain an estimation of the velocity of the tracks, instead the tracks have a value for the reconstructed momentum and the associated PDG code of the Geant4-level particle that created the track. Therefore, one can select some of the

Chapter 8. Particle ID in GArSoft

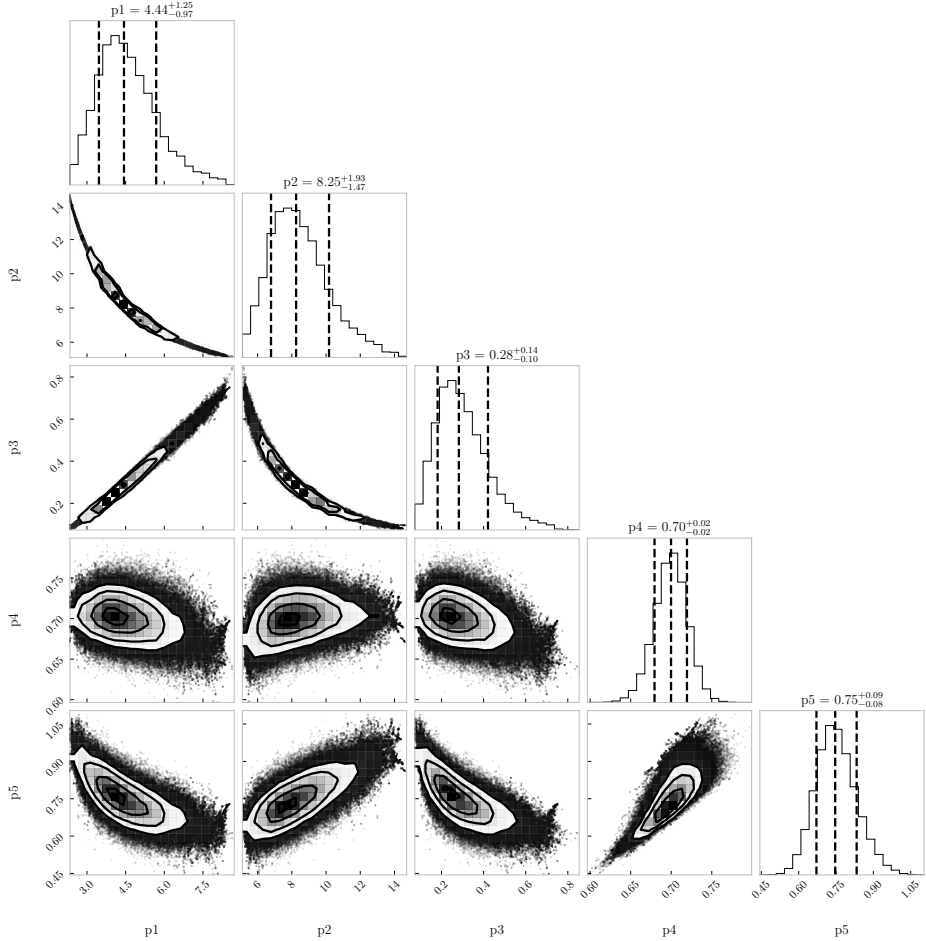


Figure 8.10: Resulting one and two dimensional projections of the posterior probability distributions of the ALEPH $\langle dE/dx \rangle$ parameters obtained by fitting the 60% truncated mean dE/dx values from a FHC neutrino sample in ND-GAr. The vertical dashed lines in the 1D distributions represent the 16th, 50th and 84th percentiles.

2610 particles in the data, in this case I selected electrons, muons, pions and protons, and
 2611 compute β and γ using the reconstructed momentum and their mass. In terms of $\beta\gamma$
 2612 the mean dE/dx does not depend on the particle species, so one can consider all the
 2613 dataset as a whole. For this fit, I will express β in terms of the $\beta\gamma$ product as:

$$\beta = \frac{\beta\gamma}{\sqrt{1 + (\beta\gamma)^2}}, \quad (8.8)$$

2614 which can be easily proven from the definition of γ .

2615 Next, I bin the data in $\beta\gamma$. I chose a fine binning so as to capture the different

8.1. dE/dx measurement in the TPC

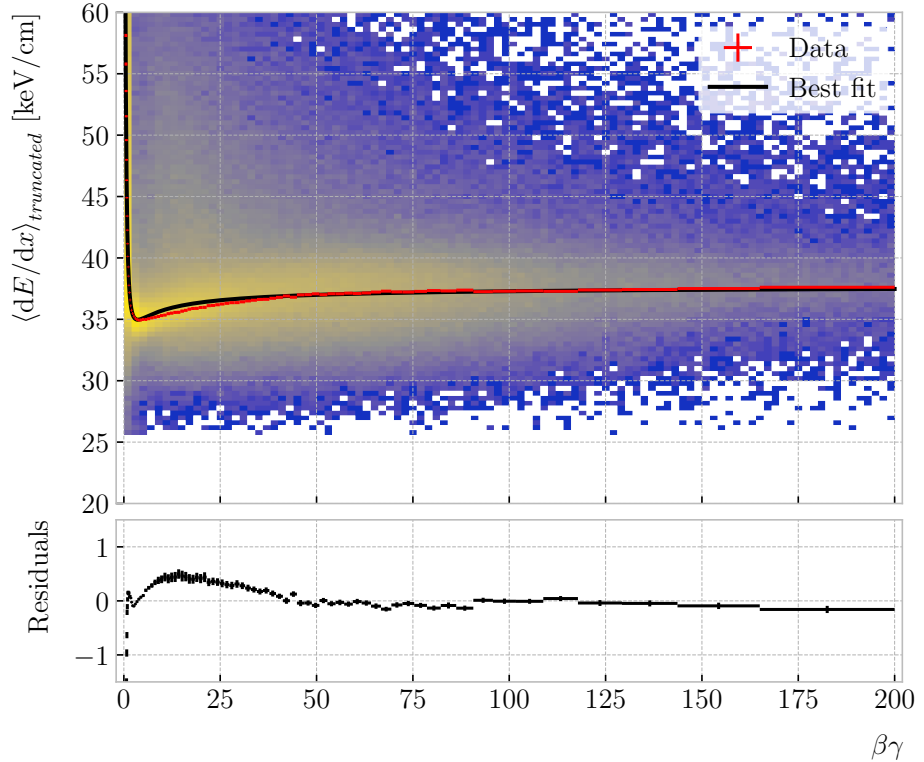


Figure 8.11: Truncated mean dE/dx obtained for the FHC neutrino sample as a function of the $\beta\gamma$ product (upper panel). Also shown are the fitted most probable values for each $\beta\gamma$ bin (red points) and the best fit obtained using the ALEPH parametrisation (black line). The residuals resulting from the fit are shown in the lower panel.

2616 features of the ionisation curve. Instead of fixing the bin width, I select them so each one
 2617 has approximately the same statistics. Then, for each $\beta\gamma$ slice, I compute the median
 2618 and the interquartile range (IQR) of the $\langle dE/dx \rangle$ distribution. Using these, I make a
 2619 histogram in the range [median – IQR, median + 5 IQR], which I fit to a LanGauss
 2620 function in order to extract the MPV. Using this range accounts for the asymmetric
 2621 nature of the distributions, while also helps avoiding a second, lower maximum present
 2622 at low $\beta\gamma$, probably a result of reconstruction failures.

2623 A few examples of these fits are shown in Fig. 8.9. The chosen values of $\beta\gamma$ sit in
 2624 very distinct points along the $\langle dE/dx \rangle$ curve, going from the high ionisation region at
 2625 low velocities (top left panel), to the minimum point (top right panel), the beginning of
 2626 the relativistic rise (bottom left panel), and the plateau produced by the density effect

Chapter 8. Particle ID in GArSoft

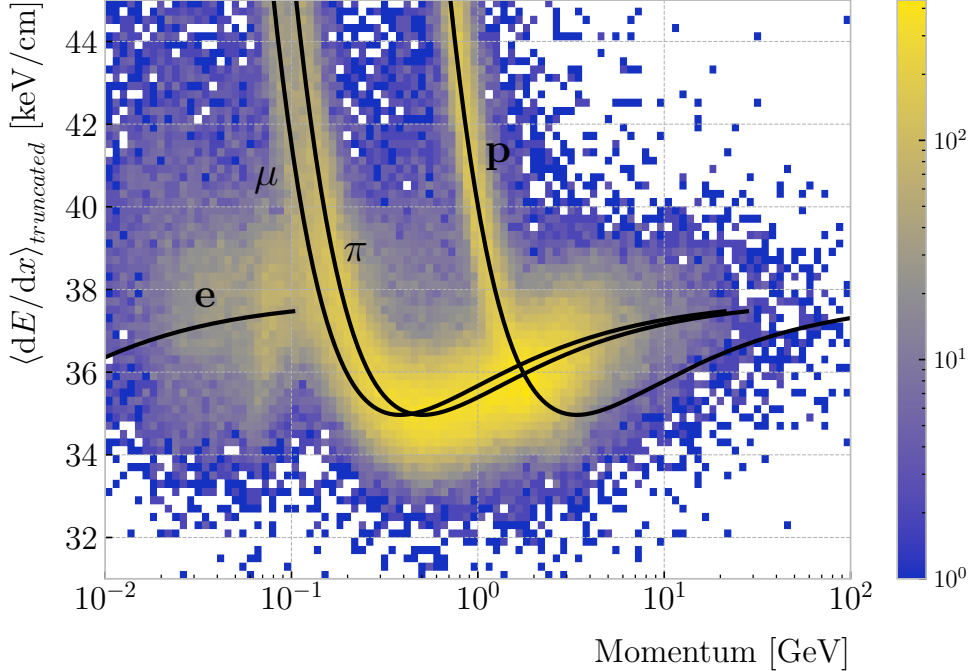


Figure 8.12: Distribution of the 60% truncated mean dE/dx versus reconstructed momentum for the FHC neutrino sample. The black lines indicate the predictions of the ALEPH parametrisation for electrons, muons, charged pions and protons.

2627 (bottom right panel).

2628 I used the resulting most probable $\langle dE/dx \rangle$ values and the centres of the $\beta\gamma$ bins as
 2629 the points to fit to the ALEPH formula. For this particular fit I used the least-squares
 2630 method to get a first estimation of the ALEPH parameters. Applying some uniform
 2631 priors, I then used these values as the starting point of a 100000 steps MCMC. In
 2632 Fig. 8.10 I show the posterior probability distributions I obtain for each parameter.
 2633 The reported best fit points are based on the 16th, 50th, and 84th percentiles in the
 2634 marginalised distributions.

2635 The resulting fit (black line), compared to the data points (red points) and the
 2636 underlying distribution is shown in Fig. 8.11 (top panel). The overall fit is good, with a
 2637 reduced chi-squared of $\chi^2/ndf = 1.02$. However, there are some regions where the fit
 2638 does not describe the data correctly, like the very low $\beta\gamma$ regime, where the fit severely
 2639 underestimates for energy losses $\gtrsim 50$ keV/cm, and the start of the relativistic raise,
 2640 where we have a slight overestimation. This is a result of those points having a larger

8.2. Muon and pion separation in the ECal and MuID

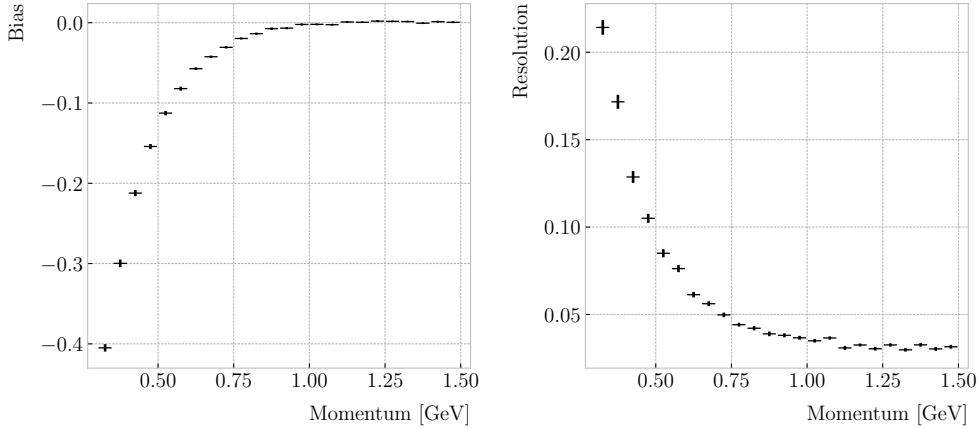


Figure 8.13: Estimated values of the mean dE/dx bias (left panel) and resolution (right panel) obtained for the true protons in a FHC neutrino sample.

uncertainty when compared to the ones around the dip or the plateau areas. These differences can be better seen in the residual plot, Fig. 8.11 (bottom panel).

8.1.4 Particle identification

8.2 Muon and pion separation in the ECal and MuID

As it could be seen from Fig. 8.12, it is not possible to separate muons and charged pions in the HPgTPC using dE/dx for momenta $\gtrsim 300 \text{ MeV}/c$. In ND-GAr, approximately 70% of the interactions in FHC mode will be ν_μ CC (compared to the 47% of $\bar{\nu}_\mu$ CC interactions when operating in RHC mode), while 24% are neutral currents. Out of these, around 53% and 47% of them will produce at least one charged pion in the final state, respectively. Fig. 8.14 shows a comparison between the spectra of the primary muons and the charged pions for ν_μ CC interactions in ND-GAr producing one or more charged pions. From this, one can see that (i) the majority of muons and charged pions are not going to be distinguishable with a $\langle dE/dx \rangle$ measurement, and that (ii) particle identification is necessary both to classify correctly the ν_μ CC events and identify the primary muon within them.

ND-GAr counts with two other subdetectors which can provide additional information for this task, namely the ECal and MuID. The current ECal design, described in (ref

Chapter 8. Particle ID in GArSoft

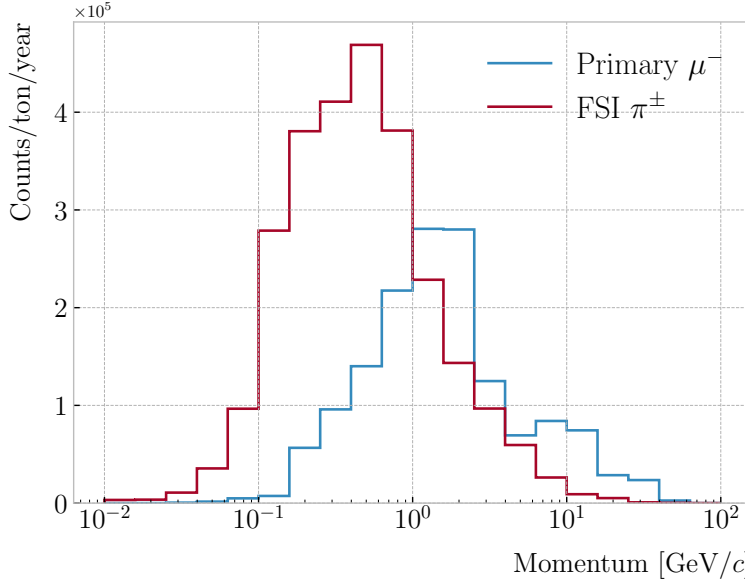


Figure 8.14: Momentum distribution for the primary muon in ν_μ CC $N\pi^\pm$ interactions inside the fiducial volume of ND-GAr (blue line), compared to the post FSI charged pion spectrum (red line).

section), consists of 42 layers, made of 5 mm of Pb, 7 mm of plastic scintillator and a 1 mm PCB board. The total thickness of this calorimeter is 1.66 nuclear interaction lengths or 1.39 pion interaction lengths. The MuID design is in a more conceptual stage, however it is envisioned to feature layers with 10 cm of Fe and 2 cm of plastic scintillator⁵. With its three layers, it will have a thickness of 1.87 or 1.53 nuclear or pion interaction lengths, respectively.

Because pion showers are dominated by inelastic nuclear interactions, the signatures of these particles in the calorimeter will look significantly different from those of muons. Although our ECal is not thick enough to fully contain the hadronic showers of the charged pions at their typical energies in FHC neutrino interactions, they can still be used to understand whether the original particle was more hadron-like or MIP-like. In Fig. 8.15 I have two examples of energy distributions created by a muon (left panel) and a charged pion (right panel) of similar momenta interacting in the ECal. These

⁵It is not mentioned anywhere, but I assume that there should also be another layer of PCB board of 1 mm. However, in this case its contribution to the total thickness of the sampling calorimeter would be negligible.

8.2. Muon and pion separation in the ECal and MuID

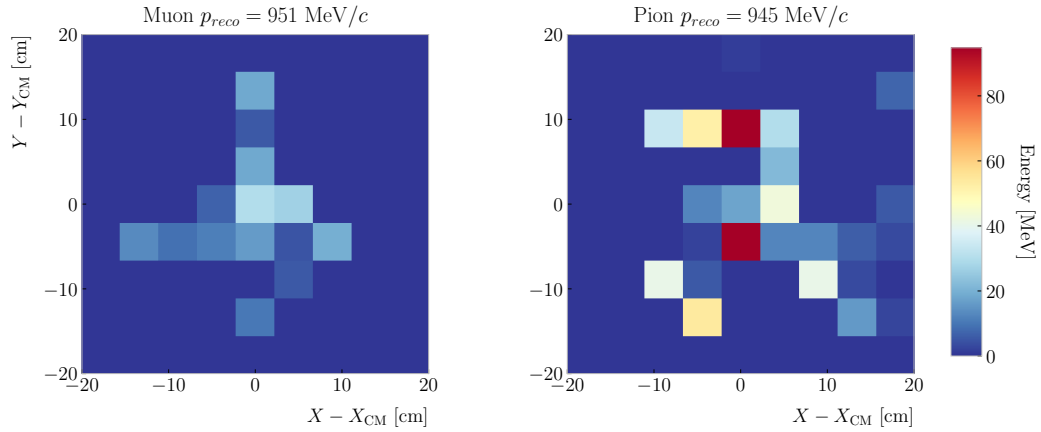


Figure 8.15: Distributions of energy deposits in the ECal for a muon (left) and a charged pion (right) with similar momenta. The energy is projected onto the plane perpendicular to the principal component of the hits, and the positions are relative to the center of the interaction.

2671 figures represent the transverse development of the interactions. For each of them, I
 2672 computed the principal component and centre of mass of the interaction, projecting
 2673 the position of the hits onto the plane perpendicular to that direction, and taking the
 2674 distances relative to the centre. It can be seen that the muon follows an almost MIP-like
 2675 behaviour, being the central bin in the histogram the one with the highest deposited
 2676 energy. On the other hand, the pion not only deposits more energy overall, but also this
 2677 energy is more spread-out among the different hits. It is this kind of information that
 2678 would allow us to tell apart muons from pions.

2679 This way, I identify three main action points that need to be addressed if one wants
 2680 to use these detectors to distinguish between muons and charged pions. These are:

- 2681 1. the way we make the associations between tracks in the HPgTPC to the activities
 2682 (what in GArSoft we call clusters) in the ECal and the MuID,
- 2683 2. what variables or features one can extract from the calorimeters that encapsulate
 2684 the information we are interested about,
- 2685 3. and how to carry out the classification problem.

Chapter 8. Particle ID in GArSoft

2686 8.2.1 Track-ECal matching

2687 One of the main players in the muon and pion separation is the way we associate clusters
2688 in the ECal to reconstructed tracks in the TPC. Missing some associations or making
2689 wrong ones can bias the ECal quantities that we can use for classifying particles. The
2690 current algorithm in GArSoft provides precise associations, i.e. most of the associations
2691 that it produces are correct, but it appears to miss an important number of associations
2692 (at least when using the default configuration).

2693 The current TPC track-ECal cluster association algorithm is divided in four parts.
2694 It first checks whether the track end point fulfils certain conditions to be extrapolated.
2695 There are two cut values in this step, one for the drift direction and other radial.

2696 If the point can be extrapolated, the code computes the coordinates of the centre
2697 of curvature using the Kalman fit estimates at the track end ($y, z, 1/R, \phi, \tan\lambda$). It
2698 then compares the distance between this and the cluster in the (z, y) plane with R . This
2699 introduces another cut in the perpendicular direction.

2700 The next step is different for clusters in the barrel or in one of the end caps. If it
2701 is a barrel cluster the algorithm extrapolates the track up to the radial distance of the
2702 cluster. There are three possible outcomes, the extrapolated helix can cut the cylinder
2703 of radius r_{clus} two, one or zero times. I get the cut point that is closer to the cluster and
2704 check that it is either in the barrel or the end caps. Computing the difference between
2705 the x coordinates of the cluster and the extrapolated point, the module checks that this
2706 is not greater than a certain cut. If the cluster is in an end cap, I propagate the track
2707 up to the x position of the cluster. Then, the algorithm computes the angle in the (z, y)
2708 plane between the centre of curvature and the cluster, α , and the centre of curvature
2709 and the propagated point, α' . A cut is applied to the quantity $(\alpha - \alpha')R$.

2710 If the cluster contains more than a certain number N of hits, I apply an extra cut to
2711 the dot product of the direction of the track at the propagated x value and the cluster
2712 direction.

2713 The code makes sure to only associate one end of the track (if any) to a cluster.

8.2. Muon and pion separation in the ECal and MuID

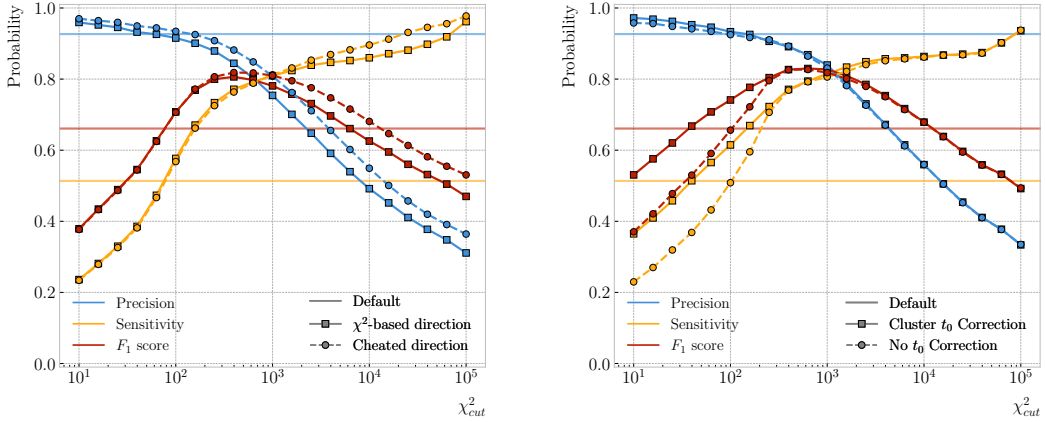


Figure 8.16: Left panel: comparison between the precision (blue), sensitivity (yellow) and F_1 score (red) obtained for the default (horizontal lines) and new algorithms, both with the χ^2 -based direction estimator (squares) and cheating the directions (circles), for different values of the χ^2 cut. Right panel: comparison of the performance of the new algorithm when applying the cluster t_0 correction (squares) and when (circles).

2714 However, it can associate more than one track to the same cluster. This makes sense,
2715 as different particles can contribute to the same cluster in the ECal, but it makes it
2716 difficult to quantify the relative contributions of the tracks to a certain cluster.

2717 As a way of comparing the performance of this algorithm, a new, simpler association
2718 module was written. The goal was to have a simple and robust algorithm, which depends
2719 on as few parameters as possible and that can produce a one-to-one matching between
2720 tracks and ECal clusters.

2721 For each reconstructed track, the new algorithms applies the same procedure to the
2722 forward and the backward fits irrespective of their end point positions. It first gets the
2723 Kalman fit parameters at the corresponding end point together with the X position, x_0 ,
2724 (y_0 , z_0 , $1/R$, ϕ_0 , $\tan\lambda$).

2725 For each ECal cluster, I compute the radial distance to the centre of the TPC and
2726 find the ϕ value in the range $[\phi_0, \phi_0 + \text{sign}(R)\phi_{max}]$ that makes the propagated helix
2727 intersect with the circle defined with such radius. The (x, y, z) position of the helix for
2728 the ϕ value found (if any) is then computed. In case there are two intersections, I keep
2729 the one that minimises the distance between (y, z) and (y_c, z_c) .

2730 I then calculate χ^2 value based on the Euclidean distance between the propagated

Chapter 8. Particle ID in GArSoft

2731 point and the cluster:

$$\chi^2/ndf = \frac{\sum_{n=0}^2 (x^{(n)} - x_c^{(n)})^2}{3}. \quad (8.9)$$

2732 If there was no intersection I store a -1 instead. In the end, for each reconstructed track
2733 in the event one ends up with two collections of χ^2 values, one for each ECal cluster
2734 and fit directions.

2735 The current code only supports having ECal clusters associated to one end of each
2736 track. We have two options to decide what track end to keep. The first one tries to
2737 cheat the selection, looking at the distance between the two track ends and the true
2738 start position of the associated MC particle. The second one keeps the track end with
2739 more χ^2 entries below the cut.

2740 This feature of only considering one track end limits the algorithm, making it not
2741 suitable for reconstructing events with particles originating outside the TPC. However,
2742 as for the moment the main concern of the group is the study of neutrino interactions
2743 off the gaseous argon, this is an acceptable assumption.

2744 In order to associate a cluster to a track, I take all clusters with a χ^2 value in the
2745 range $[0, \chi_{cut}^2]$. If a cluster has been assigned to more than one track we leave it with
2746 the one with the lowest χ^2 .

2747 This default behaviour of the algorithm can be modified to associate more than one
2748 track to each cluster. Not only that, but the χ^2 values can be used to assign relative
2749 weights to the different contributions.

2750 To evaluate the performance of the association method, I use a binary classification
2751 approach. In this case, I check the leading MC Track IDs associated to the reconstructed
2752 tracks and ECal clusters. I count an association as true positive (TP) if both Track
2753 IDs coincide. An association is considered false positive (FP) when the Track IDs are
2754 different. If a cluster has not been associated to any track but it shares the Track ID
2755 with a reconstructed track it is counted as a false negative (FN).

2756 For the testing, I used a sample of 10000 FHC neutrino events inside the HPgTPC.
2757 Fig. 8.16 (left panel) shows the precision (blue line), sensitivity (yellow line), and F_1

8.2. Muon and pion separation in the ECal and MuID

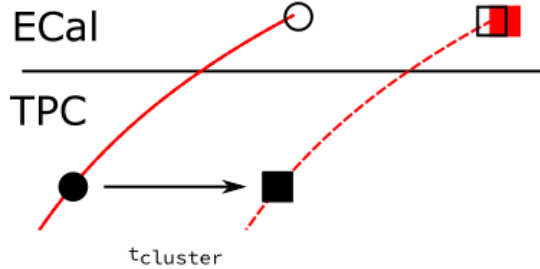


Figure 8.17: Schematics of a possible option to deal with track-ECal associations in non-zero t_0 neutrino interaction events, trying to correct for the drift direction uncertainty in a cluster-by-cluster basis using the cluster time, $t_{cluster}$.

2758 score (red line) I obtained for different values of χ^2_{cut} . For comparison, the same metrics
 2759 computed for the default algorithm with the current configuration are also shown (dashed
 2760 lines). In the case of the new algorithm, I used both the χ^2 -based method to estimate
 2761 the track direction described earlier (square markers) and the cheated direction from the
 2762 Geant-level information (circle markers). For either of these we achieve similar values of
 2763 the precision compared to the old code, while having a considerably higher sensitivity.
 2764 It can be seen that cheating the direction of the tracks only makes a difference at high
 2765 χ^2_{cut} , past the optimal value of the cut around the F_1 score maximum. Therefore, I set
 2766 the χ^2 method as the default.

2767 One of the possible weak points of this approach is that it relies on the position along
 2768 the drift direction to make the decisions. Within the current ND-GAr design implemented
 2769 in GArSoft, the timing information is provided by the ECal. That effectively means
 2770 that prior to make the track-ECal associations the reconstructed x positions of the track
 2771 trajectories differ from the simulated ones by an amount:

$$x_{reco}^{(n)} - x_{sim}^{(n)} = v_{drift} t_0, \quad (8.10)$$

2772 where v_{drift} is the mean drift velocity in our medium and the initial time is in the range
 2773 $t_0 \in [0, t_{spill}]$ where t_{spill} is the spill length. For a 10 μs spill this translates into a
 2774 maximum 30 cm uncertainty on the drift direction position.

2775 The current default in GArSoft sets $t_0 = 0$, but the functionality to randomly sample

Chapter 8. Particle ID in GArSoft

2776 this within the spill time is in place. Therefore, we need to understand what is the impact
2777 of a non-zero t_0 on the associations algorithm and foresee possible ways of minimising a
2778 loss in performance.

2779 Fig. 8.17 represents a possible option to tackle the association problem when having
2780 events with a non-zero initial time t_0 . The black and white circles represent the original
2781 points, whereas the squares indicate the corrected positions. The end points of the track
2782 and the propagated points up to the cluster radius are indicated using filled and unfilled
2783 markers respectively. The red square represents the position of the cluster.

2784 Here I try to correct for the drift coordinate position using the time associated to the
2785 cluster. Assuming that the drift time is much larger than the propagation time, $t_{cluster}$
2786 could be used as a good estimation of the t_0 . An alternative can be using the earliest
2787 time associated to a hit in said cluster. Doing this for each cluster before computing
2788 the χ^2 value could be used as an alternative to knowing the specific value of the t_0 , as
2789 when the association is correct this will provide the right correction but its impact is
2790 small enough to not change the position significantly in the case the cluster does not
2791 correspond to a given track.

2792 I tested the effect of this correction again using a sample of 10000 FHC neutrino
2793 events. Fig. 8.16 (right panel) shows the precision (blue line), sensitivity (yellow line),
2794 and F_1 score (red line) for the case the cluster t_0 correction is applied (square markers)
2795 and for the no correction case (circle markers), as a function of χ^2_{cut} . In this case, the
2796 differences are particularly notorious at low values of the cut. It makes sense, as the t_0
2797 effect becomes subdominant when the distance we consider grows large. Overall, the
2798 correction increases the sensitivity while keeping the precision almost unchanged. As a
2799 result, I apply the t_0 correction to the generated samples as the default.

2800 8.2.2 Feature selection and importance

2801 Boosted Decision Trees (BDTs) trained on a collection of ECal features allow for a track-
2802 by-track classification. A BDT is a good option for this classification problem, as they
2803 are easy to interpret and can handle data without any pre-processing.

8.2. Muon and pion separation in the ECal and MuID

2804 I am using samples with 100k FHC neutrino interactions, no truth cuts whatsoever.

2805 From the Geant4 I am only keeping the true momentum and PDG. From the track reco

2806 I keep the momentum (end momentum, both forward and backward fits).

2807 For the ECAL, I compute a series of variables per each reco track. As there can be

2808 more than one ECAL cluster associated to each track what I do is collect all associated

2809 clusters and compute my variables from the complete collection of hits associated to each

2810 track. I can roughly divide the variables in three types: energy-related, geometry-related

2811 and statistical.

2812 • Energy-related ECAL

2813 – ECAL total energy (ClusterTotalEnergy): sum of the energy of all the ECAL
2814 hits.

2815 – Hit mean energy (HitMeanEnergy): mean of the hits energy distribution.

2816 – Hit std energy (HitStdEnergy): standard deviation of the hits energy distribution.

2817 – Hit max energy (HitMaxEnergy): maximum of the hits energy distribution.

2818 • Geometry-related ECAL

2819 – Mean distance hit-to-cluster (DistHitClusterMean): mean of the distance
2820 distribution between the hits and the corresponding cluster's main axis.

2821 – RMS distance hit-to-cluster (DistHitClusterRMS): root mean square of the
2822 distance distribution between the hits and the corresponding cluster's main
2823 axis.

2824 – Maximum distance hit-to-centre (DistHitCenterMax): maximum of the
2825 distance distribution between the hits and the centre of the TPC.

2826 – Time-of-Flight velocity (TOFVelocity): slope obtained when fitting a straight
2827 line to the hit time versus hit distance to the centre (i.e. $d = v \times t$).

2828 • Energy and geometry ECAL

Chapter 8. Particle ID in GArSoft

- 2829 – Radius 90% energy (Radius90E): distance in the hit-to-cluster distribution
2830 for which 90% of the total energy is contained in the hits that are closer to
2831 the axis (i.e. radius that contains 90% of the energy).

2832 • Statistical ECAL

- 2833 – Number of hits (NHits): total number of hits associated to the track.
2834 – Number of layers with hits (NLayers): not really a count of all layers with
2835 hits but the difference between the last and the first layer with hits.

2836 For the MuID, now that the bug affecting the position of the reco hits has been
2837 solved (07/07/23) I also included some related quantities in the analysis ntuples. They
2838 also fall in the same classification I use for the ECAL variables and are also defined per
2839 reco track as there is also the possibility of having more than one MuID cluster for each
2840 track.

2841 • Energy-related MuID

- 2842 – MuID total energy (ClusterMuIDTotalEnergy): sum of the energy of all the
2843 MuID hits.
2844 – Hit MuID mean energy (HitMuIDMeanEnergy): mean of the MuID hits
2845 energy distribution.
2846 – Hit MuID std energy (HitMuIDStdEnergy): standard deviation of the MuID
2847 hits energy distribution.
2848 – Hit MuID max energy (HitMuIDMaxEnergy): maximum of the MuID hits
2849 energy distribution.

2850 • Geometry-related MuID

- 2851 – Max distance MuID hits (DistHitMuIDMax): maximum distance between
2852 pairs of MuID hits (not sure this is a good variable, distribution looks nuts).

8.3. ECal time-of-flight

- 2853 – Maximum distance MuID hit-to-centre (DistHitCenterMuIDMax): maximum
2854 of the distance distribution between the MuID hits and the centre of the
2855 TPC.

2856 • **Statistical MuID**

- 2857 – Number of hits (NHitsMuID): total number of MuID hits associated to the
2858 track.
2859 – Number of layers with hits (NLayersMuID): not really a count of all layers
2860 with MuID hits but the difference between the last and the first layer with
2861 MuIDhits.

2862 **8.2.3 Hyperparameter optimisation**

2863 **8.2.4 Probability calibration**

2864 **8.2.5 Performance**

2865 **8.3 ECal time-of-flight**

2866 **8.3.1 Arrival time estimations**

2867 **8.3.2 Proton and pion separation**

2868 **8.4 Charged pion decay in flight**

2869 As discussed previously, in GArSoft the TPC tracks are formed after a pattern recognition
2870 algorithm and a Kalman filter are applied to the TPC clusters. These two steps can
2871 find discontinuities in the track candidates (e.g. due to a particle decay) when these
2872 so-called breakpoints are large enough. However, for some, more subtle, cases they may
2873 miss them and form a single reconstructed track. It has been noted in the literature
2874 that Kalman filters offer, as a by-product, additional information to form test statistics
2875 to identify these breakpoints [?, ?].

Chapter 8. Particle ID in GArSoft

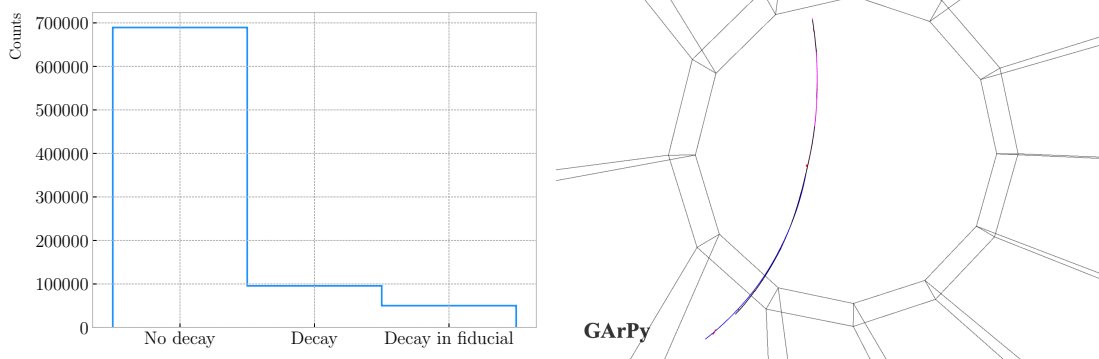


Figure 8.18: Left panel: number of non-decaying, decaying and decaying in the fiducial volume pions for a MC sample of 10^5 , $p = 500$ MeV isotropic positively charged pions inside the TPC. Right panel: event display for a positive pion decaying inside the fiducial volume, with a single reconstructed track for the pion and muon system.

2876 Considering the mean life of the charged pion, $\tau = (2.6033 \pm 0.0005) \times 10^{-8}$ s, one
 2877 can estimate that about 12% of the pions with momentum $p \sim \mathcal{O}(500)$ MeV (roughly
 2878 the peak of the pion momentum distribution in ν_μ CC interactions off argon) decay
 2879 inside the TPC. Fig. 8.18 (left panel) shows the amount of charged pions decaying in the
 2880 full TPC and fiducial volumes from an isotropic, monoenergetic sample of 10^5 negatively
 2881 charged pions with $p = 500$ MeV. We see that about 10% of those decayed, with more
 2882 than half of them decaying inside the TPC fiducial volume.

2883 Fig. 8.18 (right panel) shows an example event display of a charged pion (magenta
 2884 line) decays in flight inside the TPC, but because the angle of the muon (blue line) is
 2885 small both were reconstructed as one single track (black line). In this case, the composite
 2886 track reaches the ECal, where it undergoes a muon-like interaction, thus being classified
 2887 as a muon.

2888 A way to understand what decaying pion tracks were totally or partially reconstructed
 2889 together with the daughter muon is looking at the relative energy contributions to the
 2890 reconstructed track. In order to select a sample of such events, I require that a minimum
 2891 50% of the total energy comes from the pion and at least 20% from the muon.

2892 To identify potential decays we can use the information we obtain from the Kalman
 2893 filter at each step of the fitted track. The simplest test we can think about is computing

8.4. Charged pion decay in flight

2894 the χ^2 of the mismatch between all the parameters in the forward and the backward fits:

$$\chi_k^{2(FB)} = (\hat{x}_k^B - \hat{x}_k^F)^T [V^{(\hat{x}_k, B)} + V^{(\hat{x}_k, F)}]^{-1} (\hat{x}_k^B - \hat{x}_k^F), \quad (8.11)$$

2895 where \hat{x}_k^F , \hat{x}_k^B are the Kalman filter state vector estimates at step k in the forward and
 2896 backward fits and $V^{(\hat{x}_k, F)}$, $V^{(\hat{x}_k, B)}$ the covariance matrices of \hat{x}_k^F and \hat{x}_k^B respectively.
 2897 Using the values of the χ^2 at measurement k for the forward and backward fits we can
 2898 compute another χ^2 value that characterises the overall track fit:

$$\chi_{track}^2 = \chi_k^{2(F)} + \chi_k^{2(B)} + \chi_k^{2(FB)}, \quad (8.12)$$

2899 which remains approximately constant for all k .

2900 An alternative approach proposed in the context of the NOMAD experiment was
 2901 using a fit with a more elaborate breakpoint hypothesis, so we can perform a comparison
 2902 of the χ^2 with and without breakpoints. This can be achieved by using some alternative
 2903 parametrisation with extra parameters, which allows some of the track parameters to
 2904 be discontinuous at certain points. A decay changes the momentum magnitude and
 2905 direction, so we can use the new state vector:

$$\alpha = \begin{pmatrix} y, & z, & 1/R_F, & 1/R_B, & \phi_F, & \phi_B, & \tan\lambda_F, & \tan\lambda_B \end{pmatrix}^T. \quad (8.13)$$

2906 As we already have the estimates from the standard Kalman filter and their
 2907 covariance matrices at each point, we do not need to repeat the Kalman fit for the new
 2908 parametrisation. Instead, I can compute the values of α at each point k that minimise

Chapter 8. Particle ID in GArSoft

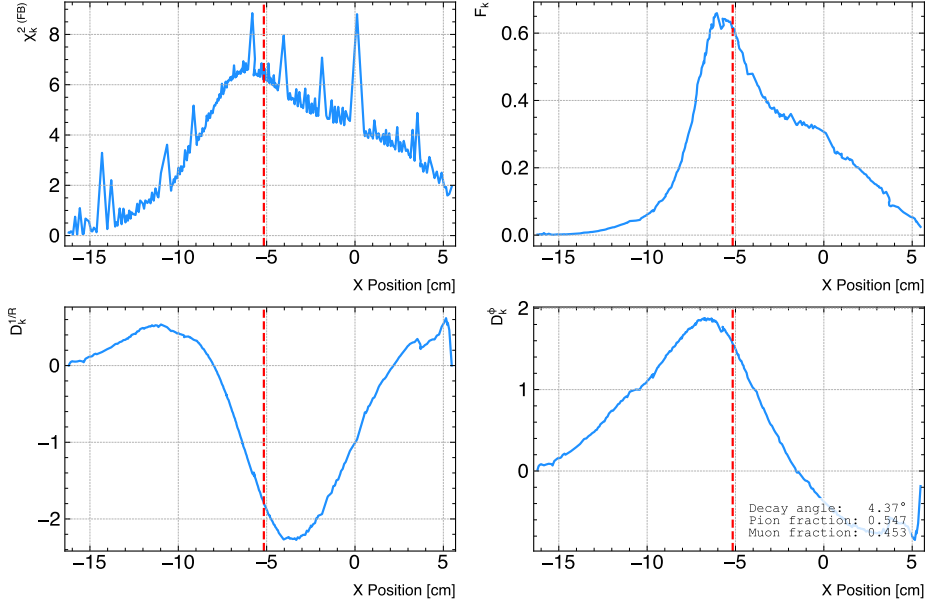


Figure 8.19: Values of $\chi_k^{2(FB)}$ (top left panel), F_k (top right panel), $D_k^{1/R}$ (bottom left panel) and D_k^ϕ (bottom right panel) versus position along the drift direction for a reconstructed track in a positive pion decay event. The vertical red dashed line indicates the true location of the decay point.

2909 the χ^2 resulting from comparing them to $\{\hat{x}_k^B, \hat{x}_k^F\}$. Introducing the two 5×8 matrices:

$$H^F = \begin{pmatrix} 1 & 0 & 0 & 0 & 0 & 0 & 0 & 0 \\ 0 & 1 & 0 & 0 & 0 & 0 & 0 & 0 \\ 0 & 0 & 1 & 0 & 0 & 0 & 0 & 0 \\ 0 & 0 & 0 & 0 & 1 & 0 & 0 & 0 \\ 0 & 0 & 0 & 0 & 0 & 0 & 1 & 0 \end{pmatrix}, \quad H^B = \begin{pmatrix} 1 & 0 & 0 & 0 & 0 & 0 & 0 & 0 \\ 0 & 1 & 0 & 0 & 0 & 0 & 0 & 0 \\ 0 & 0 & 0 & 1 & 0 & 0 & 0 & 0 \\ 0 & 0 & 0 & 0 & 0 & 0 & 1 & 0 \\ 0 & 0 & 0 & 0 & 0 & 0 & 0 & 1 \end{pmatrix}, \quad (8.14)$$

2910 we can write this as:

$$\begin{aligned} \chi_k^{2(FB)}(\alpha) &= (\hat{x}_k^F - H^F \alpha)^T \left[V^{(\hat{x}_k, F)} \right]^{-1} (\hat{x}_k^F - H^F \alpha) \\ &\quad + (\hat{x}_k^B - H^B \alpha)^T \left[V^{(\hat{x}_k, B)} \right]^{-1} (\hat{x}_k^B - H^B \alpha). \end{aligned} \quad (8.15)$$

2911 The minimum of $\chi_k^{2(FB)}(\alpha)$ is found when the measured new state vector takes the
2912 value:

$$\hat{\alpha}_k = V^{(\hat{x}_k)} H^T (V^{(\hat{x}_k)})^{-1} \hat{X}, \quad (8.16)$$

8.4. Charged pion decay in flight

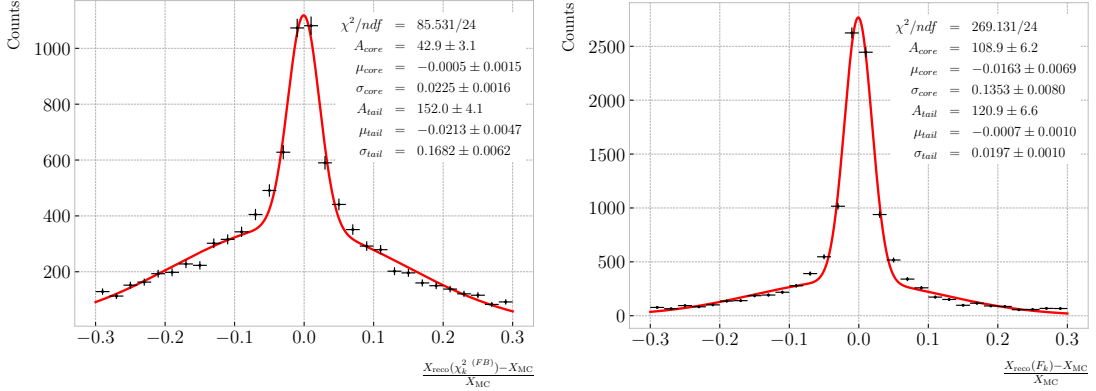


Figure 8.20: Fractional residual distributions of the true and reconstructed decay position along the drift coordinate, using the position of the maximum of $\chi_k^2(FB)$ (left panel) and F_k (right panel) as estimates of the decay position. Also shown are double Gaussian fits to these points (red lines).

where $\hat{\mathbf{X}} = \{\hat{\mathbf{x}}_k^B, \hat{\mathbf{x}}_k^F\}$, $V^{(\hat{\mathbf{x}}_k)}$ is the block diagonal matrix formed by $V^{(\hat{\mathbf{x}}_k, F)}$ and $V^{(\hat{\mathbf{x}}_k, B)}$ and $V^{(\hat{\alpha}_k)}$ is the covariance matrix of $\hat{\alpha}_k$, given by:

$$V^{(\hat{\alpha}_k)} = \left(H^T (V^{(\hat{\mathbf{x}}_k)})^{-1} H \right)^{-1}. \quad (8.17)$$

From these new fit estimates we can compute the F statistic, which tells us whether the model with breakpoint provides a statistically significant better fit:

$$F_k = \left(\frac{\chi_{\text{track},k}^2 - \chi_{\text{full},k}^2}{8-5} \right) / \left(\frac{\chi_{\text{full},k}^2}{N-8} \right). \quad (8.18)$$

One can also compute the signed difference of the duplicated variables divided by their standard deviation at each point. These represent how significant the discontinuity in each variable is. For any variable η we can write it as:

$$D_k^\eta = \frac{\hat{\eta}_k^B - \hat{\eta}_k^F}{\sqrt{\text{Var}[\hat{\eta}_k^F] + \text{Var}[\hat{\eta}_k^B] - 2\text{Cov}[\hat{\eta}_k^F, \hat{\eta}_k^B]}}. \quad (8.19)$$

In our case, the relevant ones to look at are $D_k^{1/R}$ and D_k^ϕ .

Fig. 8.19 shows the values of $\chi_k^2(FB)$, F_k , $D_k^{1/R}$ and D_k^ϕ as functions of the position along the drift direction, for an example reconstructed track with 55.5% of the energy

Chapter 8. Particle ID in GArSoft

coming from the charged pion and 45.5% from the daughter muon. The true position of the decay is indicated (dashed red lines). Notice how $\chi_k^{2(FB)}$ and F_k , $D_k^{1/R}$ reach their maxima near the decay point. In the former case this indicates a large forward-backward difference in the track fit. In the later it represents that the extended state vector improves the fit particularly around that point.

I can estimate the decay position finding resolution by computing the difference between the X position of the maxima of $\chi_k^{2(FB)}$ and F_k and the X position of the true decay. Fig. 8.20 represent the the fractional residual distributions for both cases, from the sample of tracks containing pion decays. Fitting a double Gaussian to the distributions (red lines) I find a resolution of 13.62% and 7.45% respectively.

In principle, the F -statistic should follow a Fisher distribution with $(8 - 5)$ and $(N - 8)$ degrees of freedom under the null hypothesis. In most of our cases $N \sim \mathcal{O}(100)$, so the probability density functions will look very similar. In this case, it is safe to take the limit $N \rightarrow \infty$ in the Fisher PDF:

$$\begin{aligned}\tilde{f}(x; a - b) &= \lim_{N \rightarrow \infty} f(x; a - b, N - a) \\ &= \frac{2^{-\frac{a-b}{2}}}{\Gamma(\frac{a-b}{2})} (a - b)^{\frac{a-b}{2}} x^{\frac{a-b}{2}-1} e^{-\frac{a-b}{2}x}.\end{aligned}\tag{8.20}$$

In our case $a - b = 8 - 5 = 3$, so we would obtain a p-value of 0.05 at $x = 2.60$.

Fig. 8.21 contains the distributions of the maxima of $\chi_k^{2(FB)}$, F_k and D_k^ϕ and the minima of $D_k^{1/R}$ for a sample of non-decaying pion tracks (blue) and another sample of reconstructed tracks containing part of the pion and the daughter muon from a decay inside the fiducial volume (red). Notice that, even though the values of $F_k^{(max)}$ for the decay sample are typically larger than for the non-decaying one, just a small fraction of the events go beyond the aforementioned value of $F = 2.60$. Therefore, from a practical point of view, it is not the most efficient variable to use for selecting the decay events.

However, looking at the $D_k^{1/R \text{ (min)}}$ distribution we can see there is a big difference between non-decaying and decaying events in this variable. One can use a combination of these four variables to distinguish between the pion decay events (signal) and the

8.4. Charged pion decay in flight

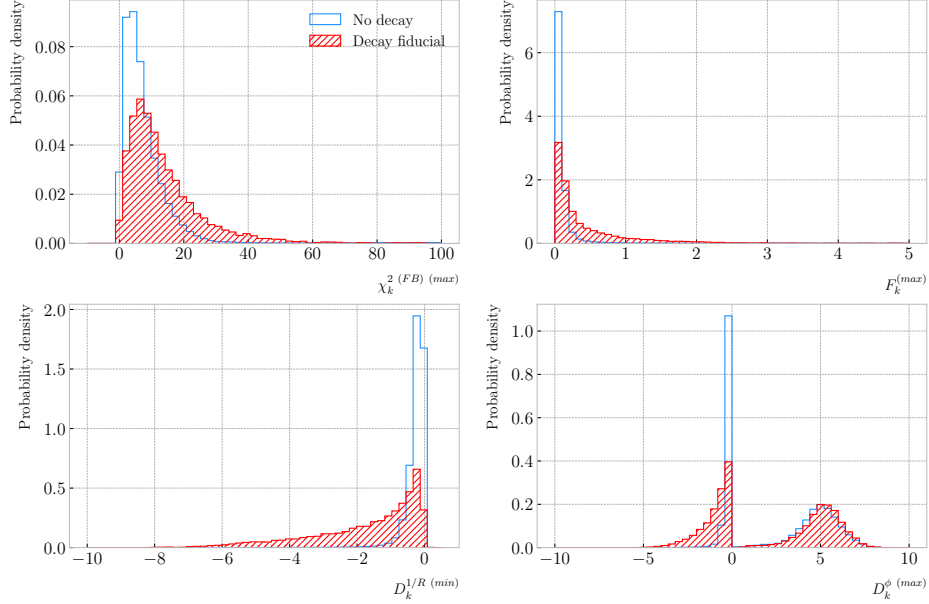


Figure 8.21: Distributions of the extreme values of $\chi_k^2(FB)$ (top left panel), F_k (top right panel), $D_k^{1/R}$ (bottom left panel) and D_k^ϕ (bottom right panel) for non-decaying reconstructed pion tracks (blue) and tracks which include the decay inside the fiducial volume (red).

2948 non-decaying pions (background).

2949 An approach to this classification could be using a boosted decision tree (BDT). One
 2950 of the advantages of BDTs is that they are easy to interpret and identify the relative
 2951 importance of the different input variables. Training a BDT with 400 estimators and a
 2952 maximum depth of 4 I can obtain an efficient classification without overtraining. Fig.
 2953 8.22 (left panel) shows the distribution of probabilities predicted by the BDT for a test
 2954 sample. The signal efficiency as a function of background acceptance, the so-called ROC
 2955 curve, is shown in Fig. 8.22 (right panel). With a relative importance of 0.83, the most
 2956 important variable turned out to be $D_k^{1/R}(\min)$.

2957 One thing we can check is how the resolution to the decay and the signal efficiency in
 2958 the classification changes with the true decay angle. Using an equal-frequency binning
 2959 for the decay angles, we can repeat the previous steps for each bin.

2960 Fig. 8.23 (left panel) shows the dependence on the decay angle of the decay finding
 2961 resolution. We can see that for the $\chi_k^2(FB)$ maximum location method the resolution

Chapter 8. Particle ID in GArSoft

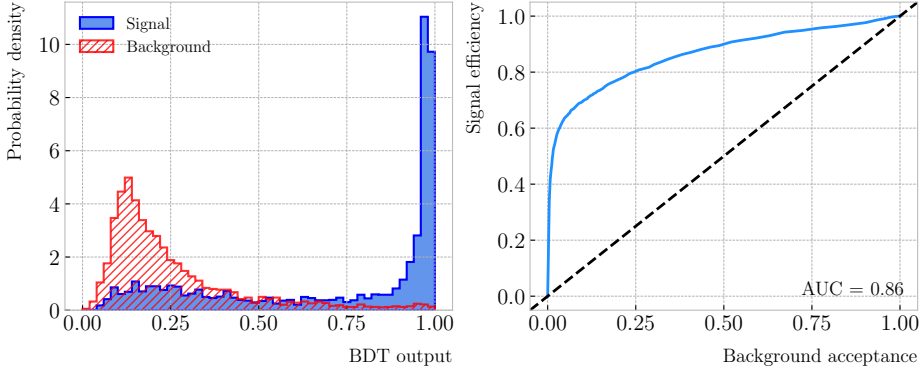


Figure 8.22: Left panel: distributions of the predicted probabilities assigned by the BDT classifier to a test sample of decaying pion+muon tracks (blue) and non-decaying pion tracks (red). Left: signal efficiency versus background acceptance (ROC curve) obtained from the BDT for the test sample.

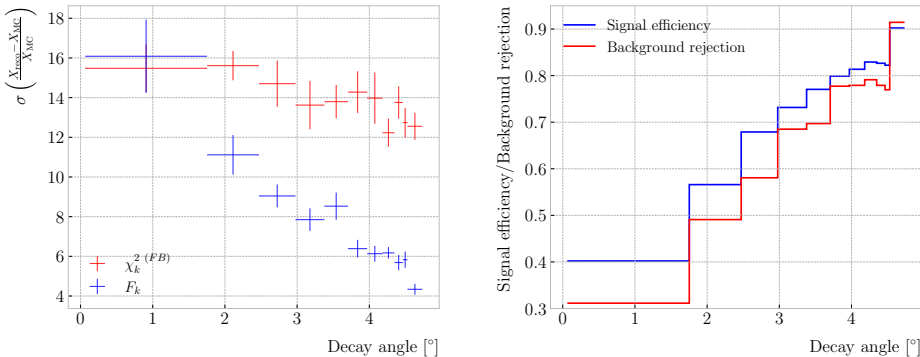


Figure 8.23: Left panel: dependence of the decay position finding resolution on the true value of the decay angle for the $\chi_k^2(FB)$ (red) and F_k (blue) methods. Right panel: signal efficiency (blue line) and background rejection (red line) from the BDT classifier versus true decay angle.

2962 consistently lies between 12 to 16%. However, the $F_k^{(max)}$ approach gives a significantly
 2963 better resolution for high angle values, reaching the 4 – 6% range for decay angles $\geq 4^\circ$.

2964 For the classification dependence on the angle, I use the same classifier I trained
 2965 before but evaluating the test sample for each individual angular bin. I compute the
 2966 signal efficiency in each bin for a fixed value of the background rejection, in this case
 2967 90%. Similarly, for the background rejection estimation I use a fixed signal efficiency
 2968 value of 90%. Fig. 8.23 (right panel) represents the change in signal efficiency (blue)
 2969 and background rejection (red) with the value of the true decay angles.

8.5. Neutral particle identification

2970 8.4.1 Track breakpoints

2971 8.5 Neutral particle identification

2972 8.5.1 ECal clustering

2973 Another important reconstruction item is the clustering algorithm of ECal hits in
2974 GArSoft. The default module features a NN algorithm that treats all hits in the same
2975 way, independently of the layer each hit comes from. However, the current ECal design
2976 of ND-GAr has two very different types of scintillator layers. The inner layers are made
2977 out of tiles, which provide excellent angular and timing resolutions. On the other hand,
2978 the outer layers are cross scintillator strips. That way, an algorithm that treats hits
2979 from both kinds of layers differently may be able to improve the current performance.

2980 Inspired by the reconstruction of T2K’s ND280 downstream ECal [?], the idea was
2981 to put together a clustering module that first builds clusters for the different ECal views
2982 (tiles, strips segmented in the X direction and strips segmented in Y direction), and
2983 then tries to match them together to form the final clusters.

2984 Working on a module-by-module basis, the algorithm first separates the hits depending
2985 on the layer type they come from. Then, it performs a NN clustering for the 3 sets of
2986 hits separately. For the tile hits it clusters together all the hits which are in nearest-
2987 neighbouring tiles and nearest-neighbouring layers, for strip hits it looks at nearest-
2988 neighbouring strips and next-to-nearest-neighbouring layers (as the layers with strips
2989 along the two directions are alternated). For strip clusters an additional cut in the
2990 direction along the strip length is needed.

2991 After this first clustering I then apply a recursive re-clustering for each collection
2992 of strip clusters based on a PCA method. In each case, we loop over the clusters with
2993 $N_{hits} \geq 2$, computing the centre of mass and three principal components. Propagating
2994 these axes up to the layers of the rest of the clusters, we check if the propagated point
2995 and the centre of mass of the second cluster are within next-to-nearest-neighbouring
2996 strips. An additional cut in the direction along the strip length is also needed. Moreover,

Chapter 8. Particle ID in GArSoft

2997 I require that the two closest hits across the two clusters are at most in next-to-nearest-
2998 neighbouring strips. I merge the clusters if these three conditions are satisfied. The
2999 re-clustering is repeated until no more cluster pairs pass the cuts.

3000 The clusters in each strip view are combined if their centres of mass are close enough
3001 and they point in the same direction. An alternative approach for the strip cluster
3002 merging could be to compute the overlap between the ellipsoids defined by the principal
3003 axes of the clusters, and then merge the pair if the overlap exceeds some threshold.
3004 Further study is needed to understand if this change would have an impact in the overall
3005 clustering performance.

3006 To merge the tile clusters to the combined strip clusters I propagate the principal
3007 axis of the strip cluster towards the inner layers, up to the centre of mass layer of the
3008 tile cluster. I merge the clusters if the distance between the propagated point and the
3009 centre of mass is below a certain cut.

3010 The last step is to check if clusters in neighbouring modules should be merged
3011 together, both across two barrel modules, across end cap modules and between barrel
3012 end cap modules. I check the distance between the two closest hits in the pair of clusters
3013 and merge them if it passes this and an additional direction cut.

3014 Fig. ?? presents an example of the clustering steps relevant for strip layer hits, from
3015 the input hits (top left panel) to the NN clustering (top right panel) and re-clustering
3016 (bottom left panel) for each strip view and the final merging strip clusters (bottom
3017 right panel). It shows the hits from a single ECal barrel module in a ν_μ CC interaction
3018 event with a neutral pion and a proton in the final state. The two clusters on the left
3019 correspond to the photon pair from the π^0 decay and the one on the upper right corner
3020 is associated to the proton.

3021 This algorithm has a total number of eight free parameters that need to be optimised.
3022 I used a sample of 1000 ν_μ CC interactions in order to obtain the optimal configuration of
3023 clustering parameters. This sample was generated up to the default ECal hit clustering
3024 level, so then I could run the new clustering algorithm each time with a different
3025 configuration of parameters. As the number of parameters is relatively large, I only

8.5. Neutral particle identification

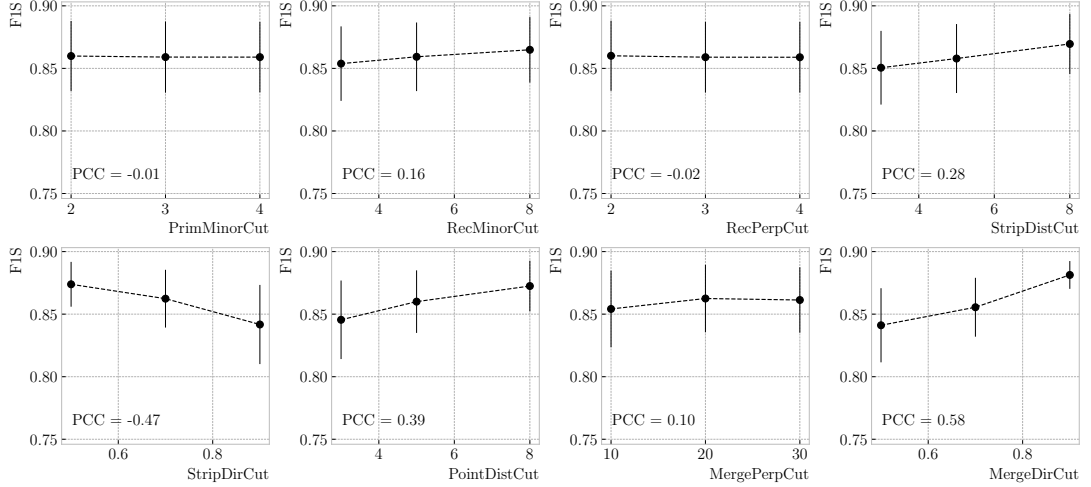


Figure 8.24: Mean values of the F_1 -score marginal distributions for the different free parameters of the new clustering algorithm, with the error bars representing one standard deviation around the mean. The F_1 -score values were computed for the 6561 possible parameter configurations using 1000 ν_μ CC interaction events.

Table 8.2: Summary of parameters and sampled values used in the optimisation of the clustering algorithm.

Name	Units	Sampled values	Description
PrimMinorCut	strips	2, 3, 4	Distance along strip length in NN clustering
RecMinorCut	strips	3, 5, 8	Distance between propagated point and CM along strip length in re-clustering
RecPerpCut	strips	2, 3, 4	Closest hit pair distance in re-clustering
StripDistCut	strips	3, 5, 8	Distance between CMs in strip cluster merging
StripDirCut	cos	0.5, 0.7, 0.9	Main axes direction cut in strip cluster merging
PointDistCut	tiles	3, 5, 8	Distance between propagated point and CM in strip-tile matching
MergePerpCut	cm	10, 20, 30	Closest hit pair distance in module merging
MergeDirCut	cos	0.5, 0.7, 0.9	Main axes direction cut in module merging

3026 performed a coarse-grained scan of the parameter space. Sampling each of the eight
 3027 parameters at three different points each I obtain 6561 different configurations. These
 3028 parameters, together with the used values, are summarised in Tab. 8.2.

3029 In order to measure the performance of the clustering, I use a binary classification
 3030 approach. For each formed cluster, I identify the Geant4 Track ID of the matching MC

Chapter 8. Particle ID in GArSoft

3031 particle and the energy fraction of each hit. Then, I assign to each cluster the Track ID
3032 with the highest total energy fraction. For each of the different Track IDs associated to
3033 the clusters, I select the cluster with the highest energy (only from the hits with the
3034 same Track ID). I identify such a cluster as the main cluster for that Track ID. I count
3035 as true positives (TPs) the hits with the correct Track ID in each main cluster. False
3036 positives (FPs) are the hits with the incorrect Track ID for the cluster they are in, not
3037 only main clusters. The false negatives (FNs) are the hits with the correct Track ID in
3038 clusters other than the main.

3039 Fig. 8.24 shows the computed F_1 -score values for the different cuts. In each case, the
3040 central value represents the mean of the F_1 -score distribution for the specified value of
3041 the corresponding variable and the vertical error bar represents one standard deviation
3042 around the mean. Also shown are the Pearson correlation coefficients of these central
3043 values. We can see that five of the variables have a sizeable effect on the F_1 -score, with
3044 an absolute difference between the last and first values as big as 4%.

3045 The working configuration is obtained as follows. I first select all configurations
3046 with purity $\geq 90\%$. Among those, I choose the combinations that yield the maximum
3047 F_1 -score. If more than one configuration remains I select the one with the highest
3048 sensitivity. Doing so, I end up with a parameter configuration with an efficiency of 88%
3049 and a 90% purity. Compared with the default algorithm, which gives an efficiency of
3050 76% and a purity of 91% for the same sample, I have managed to improve the efficiency
3051 by a factor of 1.16.

3052 8.5.2 π^0 reconstruction

3053 One of the potential applications of the new ECal hit clustering is the reconstruction of
3054 neutral particles, in particular pions. Neutral pions decay promptly after being produced,
3055 through the $\pi^0 \rightarrow \gamma\gamma$ channel ($98.823 \pm 0.034\%$) of the time. The photon pair does
3056 not leave any traces in the HPgTPC (unless one or both of them converts into an
3057 electron-positron pair), but each of them will produce an electromagnetic shower in
3058 the ECal.

8.5. Neutral particle identification

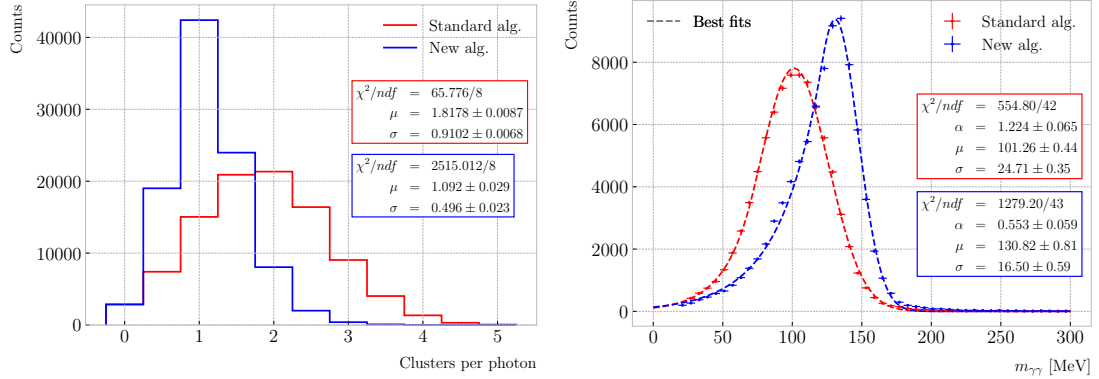


Figure 8.25: Left panel: distributions of the number of ECal clusters per photon from π^0 decays for the standard (red) and new (blue) clustering algorithms. Right panel: reconstructed invariant mass distributions for photon pairs from single π^0 events using the standard (red) and new (blue) ECal clustering algorithms.

3059 To test the potential impact of the new algorithm in π^0 reconstruction, I generated
 3060 a MC sample of single, isotropic neutral pions inside the HPgTPC. All pions were
 3061 generated with a momentum $p = 500$ MeV and their initial positions were uniformly
 3062 sampled inside a $2 \times 2 \times 2$ m box aligned with the centre of the TPC. I ran both the
 3063 default and the new clustering algorithms, using for the latter the optimised configuration
 3064 discussed above.

3065 The first thing to notice is that the number of clusters produced per photon has
 3066 decreased. Fig. 8.25 (left panel) shows these distributions for the default (red) and new
 3067 (blue) algorithms. Using a simple Gaussian fit, we see that the mean number of ECal
 3068 clusters per photon went from 1.82 ± 0.01 to 1.09 ± 0.03 . This effectively means that
 3069 with the new algorithm the ECal activity of one true particle is typically reconstructed
 3070 as a single object. From the reconstruction point of view this can be an advantage. As
 3071 now most of the photon energy ends up in a single ECal cluster, I can simply use cluster
 3072 pairs to identify the π^0 decay.

3073 In general, one calculates the invariant mass of the photon pair as:

$$m_{\gamma\gamma} = \sqrt{2E_1E_2(1 - \cos \theta)}, \quad (8.21)$$

3074 where E_i are the energies of the photons and θ the opening angle between them. In this

Chapter 8. Particle ID in GArSoft

3075 case I can use the energies deposited in the ECal and their incident directions. This
 3076 quantity is computed for all possible pairs of clusters, using their position together with
 3077 the true decay point. In a more realistic scenario, e.g. ν_μ CC interaction, one could use
 3078 the position of the reconstructed primary vertex instead. I also tried to use the principal
 3079 direction of the clusters, but that approach gave considerably worse results. For each
 3080 event I only keep the pair with an invariant mass closer to the true π^0 mass value.

3081 Fig. 8.25 (right panel) shows the invariant mass distributions for the photon pairs
 3082 we get using the default (red) and the new (blue) ECal clustering algorithms. For the fit
 3083 I used a modified version of the Crystal Ball function [?], obtained by taking the limit
 3084 where the parameter controlling the power-law tail goes to infinity:

$$f(x; N, \mu, \sigma, \alpha) = N \cdot \begin{cases} e^{\frac{\alpha(2x-2\mu+\alpha\sigma)}{2\sigma}}; & x \leq \mu - \alpha\sigma, \\ e^{-\frac{(x-\mu)^2}{2\sigma^2}}; & x > \mu - \alpha\sigma. \end{cases} \quad (8.22)$$

3085 Comparing the fitted mean and standard deviation values for the Gaussian cores, we
 3086 see that the distribution for the new algorithm is a 67% narrower and also peaks much
 3087 closer to the true m_{π^0} value, going from 101.3 ± 0.4 MeV to 130.8 ± 0.6 MeV.

3088 Chapter 9

3089 Conclusions

₃₀₉₀ Appendix A

₃₀₉₁ An appendix

₃₀₉₂

Bibliography

- ₃₀₉₃ [1] DUNE collaboration, *Deep Underground Neutrino Experiment (DUNE), Far*
₃₀₉₄ *Detector Technical Design Report, Volume I Introduction to DUNE*, *JINST* **15**
₃₀₉₅ (2020) T08008 [2002.02967]. 15, 41, 42, 43, 46, 47, 48, 54, 55, 56, 63, 64
- ₃₀₉₆ [2] DUNE collaboration, *Deep Underground Neutrino Experiment (DUNE), Far*
₃₀₉₇ *Detector Technical Design Report, Volume IV: Far Detector Single-phase*
₃₀₉₈ *Technology*, *JINST* **15** (2020) T08010 [2002.03010]. 15, 51
- ₃₀₉₉ [3] J.N. Bahcall, A.M. Serenelli and S. Basu, *New solar opacities, abundances,*
₃₁₀₀ *helioseismology, and neutrino fluxes*, *Astrophys. J. Lett.* **621** (2005) L85
₃₁₀₁ [[astro-ph/0412440](#)]. 21, 111, 113
- ₃₁₀₂ [4] R. Garani and S. Palomares-Ruiz, *Dark matter in the Sun: scattering off electrons*
₃₁₀₃ *vs nucleons*, *JCAP* **05** (2017) 007 [[1702.02768](#)]. 21, 109, 110, 112, 113, 114, 137
- ₃₁₀₄ [5] M. Honda, M. Sajjad Athar, T. Kajita, K. Kasahara and S. Midorikawa,
₃₁₀₅ *Atmospheric neutrino flux calculation using the NRLMSISE-00 atmospheric model*,
₃₁₀₆ *Phys. Rev. D* **92** (2015) 023004 [[1502.03916](#)]. 22, 117, 118
- ₃₁₀₇ [6] M. Colom i Bernadich and C. Pérez de los Heros, *Limits on Kaluza-Klein dark*
₃₁₀₈ *matter annihilation in the Sun from recent IceCube results*, *Eur. Phys. J. C*, **80** 2
₃₁₀₉ (2020) 129 **80** (2019) [[1912.04585](#)]. 22, 122
- ₃₁₁₀ [7] ANTARES collaboration, *Search for Dark Matter in the Sun with the ANTARES*
₃₁₁₁ *Neutrino Telescope in the CMSSM and mUED frameworks*, *Nucl. Instrum. Meth. A*
₃₁₁₂ **725** (2013) 76 [[1204.5290](#)]. 22, 122

BIBLIOGRAPHY

- 3113 [8] N. Deutschmann, T. Flacke and J.S. Kim, *Current LHC Constraints on Minimal*
3114 *Universal Extra Dimensions*, *Phys. Lett. B* **771** (2017) 515 [[1702.00410](#)]. 22, 122,
3115 123
- 3116 [9] ICECUBE collaboration, *Search for GeV-scale dark matter annihilation in the Sun*
3117 *with IceCube DeepCore*, *Phys. Rev. D* **105** (2022) 062004 [[2111.09970](#)]. 24, 134,
3118 135
- 3119 [10] C.-S. Chen, F.-F. Lee, G.-L. Lin and Y.-H. Lin, *Probing Dark Matter*
3120 *Self-Interaction in the Sun with IceCube-PINGU*, *JCAP* **10** (2014) 049 [[1408.5471](#)].
3121 24, 134, 135
- 3122 [11] N.F. Bell, M.J. Dolan and S. Robles, *Searching for dark matter in the Sun using*
3123 *Hyper-Kamiokande*, *JCAP* **11** (2021) 004 [[2107.04216](#)]. 24, 134, 135
- 3124 [12] E. Behnke et al., *Final Results of the PICASSO Dark Matter Search Experiment*,
3125 *Astropart. Phys.* **90** (2017) 85 [[1611.01499](#)]. 24, 134, 135
- 3126 [13] PICO collaboration, *Dark Matter Search Results from the Complete Exposure of*
3127 *the PICO-60 C₃F₈ Bubble Chamber*, *Phys. Rev. D* **100** (2019) 022001
3128 [[1902.04031](#)]. 24, 134, 135
- 3129 [14] DARKSIDE collaboration, *Constraints on Sub-GeV Dark-Matter–Electron*
3130 *Scattering from the DarkSide-50 Experiment*, *Phys. Rev. Lett.* **121** (2018) 111303
3131 [[1802.06998](#)]. 24, 138, 139
- 3132 [15] XENON collaboration, *Light Dark Matter Search with Ionization Signals in*
3133 *XENON1T*, *Phys. Rev. Lett.* **123** (2019) 251801 [[1907.11485](#)]. 24, 138, 139
- 3134 [16] P.F. de Salas, D.V. Forero, S. Gariazzo, P. Martínez-Miravé, O. Mena, C.A. Ternes
3135 et al., *2020 global reassessment of the neutrino oscillation picture*, *JHEP* **02** (2021)
3136 071 [[2006.11237](#)]. 29, 38, 43
- 3137 [17] W. Pauli, *Dear radioactive ladies and gentlemen*, *Phys. Today* **31N9** (1978) 27. 33

BIBLIOGRAPHY

- 3138 [18] F. Reines and C.L. Cowan, *Detection of the free neutrino*, *Phys. Rev.* **92** (1953)
3139 830. 33
- 3140 [19] ALEPH, DELPHI, L3, OPAL, SLD, LEP ELECTROWEAK WORKING GROUP,
3141 SLD ELECTROWEAK GROUP, SLD HEAVY FLAVOUR GROUP collaboration,
3142 *Precision electroweak measurements on the Z resonance*, *Phys. Rept.* **427** (2006)
3143 257 [[hep-ex/0509008](#)]. 34
- 3144 [20] SUPER-KAMIOKANDE collaboration, *Evidence for oscillation of atmospheric*
3145 *neutrinos*, *Phys. Rev. Lett.* **81** (1998) 1562 [[hep-ex/9807003](#)]. 34
- 3146 [21] B. Pontecorvo, *Inverse beta processes and nonconservation of lepton charge*, *Zh.*
3147 *Eksp. Teor. Fiz.* **34** (1957) 247. 34
- 3148 [22] Z. Maki, M. Nakagawa and S. Sakata, *Remarks on the unified model of elementary*
3149 *particles*, *Prog. Theor. Phys.* **28** (1962) 870. 34
- 3150 [23] L. Wolfenstein, *Neutrino Oscillations in Matter*, *Phys. Rev. D* **17** (1978) 2369. 36
- 3151 [24] B.T. Cleveland, T. Daily, R. Davis, Jr., J.R. Distel, K. Lande, C.K. Lee et al.,
3152 *Measurement of the solar electron neutrino flux with the Homestake chlorine*
3153 *detector*, *Astrophys. J.* **496** (1998) 505. 37
- 3154 [25] F. Kaether, W. Hampel, G. Heusser, J. Kiko and T. Kirsten, *Reanalysis of the*
3155 *GALLEX solar neutrino flux and source experiments*, *Phys. Lett. B* **685** (2010) 47
3156 [[1001.2731](#)]. 37
- 3157 [26] SAGE collaboration, *Measurement of the solar neutrino capture rate with gallium*
3158 *metal. III: Results for the 2002–2007 data-taking period*, *Phys. Rev. C* **80** (2009)
3159 015807 [[0901.2200](#)]. 37
- 3160 [27] G. Bellini et al., *Precision measurement of the ^{7}Be solar neutrino interaction rate*
3161 *in Borexino*, *Phys. Rev. Lett.* **107** (2011) 141302 [[1104.1816](#)]. 37

BIBLIOGRAPHY

- 3162 [28] SUPER-KAMIOKANDE collaboration, *Solar neutrino measurements in*
3163 *super-Kamiokande-I*, *Phys. Rev. D* **73** (2006) 112001 [[hep-ex/0508053](#)]. 37
- 3164 [29] SNO collaboration, *Combined Analysis of all Three Phases of Solar Neutrino Data*
3165 *from the Sudbury Neutrino Observatory*, *Phys. Rev. C* **88** (2013) 025501
3166 [[1109.0763](#)]. 37
- 3167 [30] SUPER-KAMIOKANDE collaboration, *Atmospheric neutrino oscillation analysis with*
3168 *external constraints in Super-Kamiokande I-IV*, *Phys. Rev. D* **97** (2018) 072001
3169 [[1710.09126](#)]. 37
- 3170 [31] ICECUBE collaboration, *Measurement of Atmospheric Neutrino Oscillations at*
3171 *6–56 GeV with IceCube DeepCore*, *Phys. Rev. Lett.* **120** (2018) 071801
3172 [[1707.07081](#)]. 37
- 3173 [32] KAMLAND collaboration, *Reactor On-Off Antineutrino Measurement with*
3174 *KamLAND*, *Phys. Rev. D* **88** (2013) 033001 [[1303.4667](#)]. 37
- 3175 [33] RENO collaboration, *Measurement of Reactor Antineutrino Oscillation Amplitude*
3176 *and Frequency at RENO*, *Phys. Rev. Lett.* **121** (2018) 201801 [[1806.00248](#)]. 37
- 3177 [34] DAYA BAY collaboration, *Measurement of the Electron Antineutrino Oscillation*
3178 *with 1958 Days of Operation at Daya Bay*, *Phys. Rev. Lett.* **121** (2018) 241805
3179 [[1809.02261](#)]. 37
- 3180 [35] K.J. Kelly, P.A.N. Machado, S.J. Parke, Y.F. Perez-Gonzalez and R.Z. Funchal,
3181 *Neutrino mass ordering in light of recent data*, *Phys. Rev. D* **103** (2021) 013004. 38
- 3182 [36] P. Dunne, “Latest Neutrino Oscillation Results from T2K.” Jul, 2020. 38
- 3183 [37] MINOS collaboration, *Combined analysis of ν_μ disappearance and $\nu_\mu \rightarrow \nu_e$*
3184 *appearance in MINOS using accelerator and atmospheric neutrinos*, *Phys. Rev. Lett.*
3185 **112** (2014) 191801 [[1403.0867](#)]. 38

BIBLIOGRAPHY

- 3186 [38] K2K collaboration, *Measurement of Neutrino Oscillation by the K2K Experiment*,
3187 *Phys. Rev. D* **74** (2006) 072003 [[hep-ex/0606032](#)]. 38
- 3188 [39] DUNE collaboration, *Long-baseline neutrino oscillation physics potential of the*
3189 *DUNE experiment*, *Eur. Phys. J. C* **80** (2020) 978 [[2006.16043](#)]. 38
- 3190 [40] HYPER-KAMIOKANDE collaboration, *Physics potential of Hyper-Kamiokande for*
3191 *neutrino oscillation measurements*, *PoS NuFact2019* (2019) 040. 38
- 3192 [41] DUNE collaboration, *Snowmass Neutrino Frontier: DUNE Physics Summary*,
3193 [2203.06100](#). 43, 44
- 3194 [42] DUNE collaboration, *Deep Underground Neutrino Experiment (DUNE), Far*
3195 *Detector Technical Design Report, Volume II: DUNE Physics*, [2002.03005](#). 43, 45,
3196 59, 61, 117, 126, 130
- 3197 [43] SUPER-KAMIOKANDE collaboration, *Search for Proton Decay via $p \rightarrow e^+ \pi_0$ and*
3198 *$p \rightarrow \mu^+ \pi_0$ in a Large Water Cherenkov Detector*, *Phys. Rev. Lett.* **102** (2009)
3199 [141801](#) [[0903.0676](#)]. 44
- 3200 [44] S. Raby, *Grand Unified Theories*, in *2nd World Summit: Physics Beyond the*
3201 *Standard Model*, 8, 2006 [[hep-ph/0608183](#)]. 44
- 3202 [45] KAMIOKANDE-II collaboration, *Observation of a Neutrino Burst from the*
3203 *Supernova SN 1987a*, *Phys. Rev. Lett.* **58** (1987) 1490. 45
- 3204 [46] R.M. Bionta et al., *Observation of a Neutrino Burst in Coincidence with Supernova*
3205 *SN 1987a in the Large Magellanic Cloud*, *Phys. Rev. Lett.* **58** (1987) 1494. 45
- 3206 [47] DUNE collaboration, *The DUNE Far Detector Vertical Drift Technology*,
3207 *Technical Design Report*, [2312.03130](#). 49, 50
- 3208 [48] DUNE collaboration, *Deep Underground Neutrino Experiment (DUNE) Near*
3209 *Detector Conceptual Design Report, Instruments* **5** (2021) 31 [[2103.13910](#)]. 53, 54,
3210 57, 61, 141

BIBLIOGRAPHY

- 3211 [49] J. Strait, E. McCluskey, T. Lundin, J. Willhite, T. Hamernik, V. Papadimitriou
3212 et al., *Long-baseline neutrino facility (lbnf) and deep underground neutrino*
3213 *experiment (dune) conceptual design report volume 3: Long-baseline neutrino*
3214 *facility for dune june 24, 2015*, 1601.05823. 58
- 3215 [50] DUNE DAQ, “dtp-firmware.”
3216 <https://gitlab.cern.ch/dune-daq/readout/dtp-firmware>, 2020. 73
- 3217 [51] DUNE DAQ, “dtp-simulation.”
3218 <https://gitlab.cern.ch/dune-daq/readout/dtp-simulation>, 2020. 76
- 3219 [52] DUNE DAQ, “dtpemulator.”
3220 https://github.com/DUNE-DAQ/dtpemulator/tree/fmlopez/filter_ana, 2022.
3221 76
- 3222 [53] J. McClellan and T. Parks, *A personal history of the Parks-McClellan algorithm*,
3223 *IEEE Signal Processing Magazine* **22** (2005) 82. 77
- 3224 [54] G. Turin, *An introduction to matched filters*, *IEEE Transactions on Information*
3225 *Theory* **6** (1960) 311. 80
- 3226 [55] J.W. Goodman, *Statistical Optics*, Wiley (1985). 82
- 3227 [56] B. Dwork, *Detection of a pulse superimposed on fluctuation noise*, *Proceedings of*
3228 *the IRE* **38** (1950) 771. 83
- 3229 [57] L. Wainstein and V. Zubakov, *Extraction of Signals from Noise*, Prentice-Hall
3230 (1962). 83
- 3231 [58] E.D. Church, *Larsoft: A software package for liquid argon time projection drift*
3232 *chambers*, 1311.6774. 86, 87
- 3233 [59] S.V. Stehman, *Selecting and interpreting measures of thematic classification*
3234 *accuracy*, *Remote Sensing of Environment* **62** (1997) 77. 100

BIBLIOGRAPHY

- 3235 [60] A.A. Taha and A. Hanbury, *Metrics for evaluating 3d medical image segmentation: analysis, selection, and tool*, *BMC Medical Imaging* **15** (2015) . 101
- 3236
- 3237 [61] J. Silk, K.A. Olive and M. Srednicki, *The Photino, the Sun and High-Energy Neutrinos*, *Phys. Rev. Lett.* **55** (1985) 257. 107
- 3238
- 3239 [62] M. Srednicki, K.A. Olive and J. Silk, *High-Energy Neutrinos from the Sun and Cold Dark Matter*, *Nucl. Phys. B* **279** (1987) 804. 107
- 3240
- 3241 [63] J.S. Hagelin, K.W. Ng and K.A. Olive, *A High-energy Neutrino Signature From Supersymmetric Relics*, *Phys. Lett. B* **180** (1986) 375. 107
- 3242
- 3243 [64] T.K. Gaisser, G. Steigman and S. Tilav, *Limits on Cold Dark Matter Candidates from Deep Underground Detectors*, *Phys. Rev. D* **34** (1986) 2206. 107
- 3244
- 3245 [65] N. Bernal, J. Martín-Albo and S. Palomares-Ruiz, *A novel way of constraining WIMPs annihilations in the Sun: MeV neutrinos*, *JCAP* **08** (2013) 011
- 3246
- 3247 [1208.0834]. 107, 108, 109, 115
- 3248 [66] C. Rott, J. Siegal-Gaskins and J.F. Beacom, *New Sensitivity to Solar WIMP Annihilation using Low-Energy Neutrinos*, *Phys. Rev. D* **88** (2013) 055005
- 3249
- 3250 [1208.0827]. 107, 114
- 3251 [67] C. Rott, S. In, J. Kumar and D. Yaylali, *Dark Matter Searches for Monoenergetic Neutrinos Arising from Stopped Meson Decay in the Sun*, *JCAP* **11** (2015) 039
- 3252
- 3253 [1510.00170]. 107
- 3254 [68] DUNE collaboration, *Searching for solar KDAR with DUNE*, *JCAP* **10** (2021) 065
- 3255 [2107.09109]. 107
- 3256 [69] G. Busoni, A. De Simone and W.-C. Huang, *On the Minimum Dark Matter Mass Testable by Neutrinos from the Sun*, *JCAP* **07** (2013) 010 [1305.1817]. 108
- 3257
- 3258 [70] V.A. Bednyakov and F. Simkovic, *Nuclear spin structure in dark matter search: The Zero momentum transfer limit*, *Phys. Part. Nucl.* **36** (2005) 131
- 3259
- 3260 [hep-ph/0406218]. 109

BIBLIOGRAPHY

- 3261 [71] A. Gould, *WIMP Distribution in and Evaporation From the Sun*, *Astrophys. J.* **321**
3262 (1987) 560. 110
- 3263 [72] J.N. Bahcall, M.H. Pinsonneault and S. Basu, *Solar models: Current epoch and*
3264 *time dependences, neutrinos, and helioseismological properties*, *Astrophys. J.* **555**
3265 (2001) 990 [[astro-ph/0010346](#)]. 112
- 3266 [73] T. Golan, J.T. Sobczyk and J. Zmuda, *NuWro: the Wroclaw Monte Carlo*
3267 *Generator of Neutrino Interactions*, *Nucl. Phys. B Proc. Suppl.* **229-232** (2012)
3268 499. 116
- 3269 [74] G. Cowan, K. Cranmer, E. Gross and O. Vitells, *Asymptotic formulae for*
3270 *likelihood-based tests of new physics*, *Eur. Phys. J. C* **71** (2011) 1554 [[1007.1727](#)].
3271 117
- 3272 [75] T. Kaluza, *Zum Unitätsproblem der Physik, Sitzungsber. Preuss. Akad. Wiss.*
3273 *Berlin (Math. Phys.)* **1921** (1921) 966 [[1803.08616](#)]. 119
- 3274 [76] O. Klein, *Quantum Theory and Five-Dimensional Theory of Relativity. (In*
3275 *German and English)*, *Z. Phys.* **37** (1926) 895. 119
- 3276 [77] T. Appelquist, H.-C. Cheng and B.A. Dobrescu, *Bounds on universal extra*
3277 *dimensions*, *Phys. Rev. D* **64** (2001) 035002 [[hep-ph/0012100](#)]. 119
- 3278 [78] N. Arkani-Hamed, S. Dimopoulos and G.R. Dvali, *The Hierarchy problem and new*
3279 *dimensions at a millimeter*, *Phys. Lett. B* **429** (1998) 263 [[hep-ph/9803315](#)]. 119
- 3280 [79] L. Randall and R. Sundrum, *A Large mass hierarchy from a small extra dimension*,
3281 *Phys. Rev. Lett.* **83** (1999) 3370 [[hep-ph/9905221](#)]. 119
- 3282 [80] G. Servant and T.M.P. Tait, *Is the lightest Kaluza-Klein particle a viable dark*
3283 *matter candidate?*, *Nucl. Phys. B* **650** (2003) 391 [[hep-ph/0206071](#)]. 119
- 3284 [81] H.-C. Cheng, K.T. Matchev and M. Schmaltz, *Radiative corrections to*
3285 *Kaluza-Klein masses*, *Phys. Rev. D* **66** (2002) 036005 [[hep-ph/0204342](#)]. 121

BIBLIOGRAPHY

- 3286 [82] M. Blennow, J. Edsjö and T. Ohlsson, *Neutrinos from WIMP annihilations using a*
3287 *full three-flavor Monte Carlo*, *JCAP* **01** (2008) 021 [[0709.3898](#)]. 121, 124
- 3288 [83] J. Edsjö, J. Elevant and C. Niblaeus, *WimpSim Neutrino Monte Carlo*. 121, 124
- 3289 [84] U. Haisch and A. Weiler, *Bound on minimal universal extra dimensions from*
3290 *anti-B → X(s)gamma*, *Phys. Rev. D* **76** (2007) 034014 [[hep-ph/0703064](#)]. 123
- 3291 [85] A. Freitas and U. Haisch, *Anti-B → X(s) gamma in two universal extra*
3292 *dimensions*, *Phys. Rev. D* **77** (2008) 093008 [[0801.4346](#)]. 123
- 3293 [86] C. Rott, D. Jeong, J. Kumar and D. Yaylali, *Neutrino Topology Reconstruction at*
3294 *DUNE and Applications to Searches for Dark Matter Annihilation in the Sun*,
3295 *JCAP* **07** (2019) 006 [[1903.04175](#)]. 126
- 3296 [87] F. Pedregosa, G. Varoquaux, A. Gramfort, V. Michel, B. Thirion, O. Grisel et al.,
3297 *Scikit-learn: Machine learning in Python*, *Journal of Machine Learning Research*
3298 **12** (2011) 2825. 132
- 3299 [88] J. Kopp, V. Niro, T. Schwetz and J. Zupan, *DAMA/LIBRA and leptонically*
3300 *interacting Dark Matter*, *Phys. Rev. D* **80** (2009) 083502 [[0907.3159](#)]. 136
- 3301 [89] PARTICLE DATA GROUP collaboration, *Review of Particle Physics*, *PTEP* **2020**
3302 (2020) 083C01. 137
- 3303 [90] M. Beltran, D. Hooper, E.W. Kolb and Z.C. Krusberg, *Deducing the nature of dark*
3304 *matter from direct and indirect detection experiments in the absence of collider*
3305 *signatures of new physics*, *Phys. Rev. D* **80** (2009) 043509 [[0808.3384](#)]. 137
- 3306 [91] PLANCK collaboration, *Planck 2018 results. VI. Cosmological parameters*, *Astron.*
3307 *Astrophys.* **641** (2020) A6 [[1807.06209](#)]. 138